University of South Wales
2053152

AN EXPERIMENTAL AND FINITE ELEMENT ANALYSIS OF THE THERMAL DEFORMATION OF AN OPEN SLEEVE PISTON

by

Mani Maran Ratnam

A thesis submitted in partial fulfilment of
the requirement of the Council for National Academic Awards
for the degree of Doctor of Philosophy

July 1991

The Polytechnic of Wales in collaboration with
Loughborough University of Technology and
AE Piston Products Limited

DECLARATION

This thesis has not been nor is currently submitted for the award of any other degree or similar qualifications.

(M.M.Ratnam)

ACKNOWLEDGEMENT

I would like to acknowledge with gratitude the guidance and encourgement offered by my Director of Studies, Dr.W.T.Evans and my Second Supervisor, Dr.J.R.Tyrer, throughout the period of this work.

I would also like to thank the Overseas Development Administration and the Polytechnic of Wales for the offer of the ODASS scholarship which enabled me to undertake and complete this study.

The consultation provided by AE Piston Products Limited is also gratefully acknowledged.

Abstract

This thesis presents the results of a comparative study on the thermal deformation of a bimetallic diesel engine piston using finite elements and holographic interferometry. As a result of the complexity of the piston design and the unknown in-built stresses certain assumptions were necessary in the generation of the finite elements model. By using the holographic technique for direct measurement of the deformation for a 45° sector of the piston surface it was possible to check the effects of these assumptions and to improve the accuracy of the model.

The comparison was carried out for two temperature ranges: 50°C to 60°C and 130°C to 140°C. At the lower temperature range the predicted profile was found to have a greater inward curvature at about mid-skirt height when compared to the measured profile. This was attributed to the assumptions made in the model with regard to the method of attachment of the steel sleeve insert to the piston skirt. At the higher temperature range, the original model was found to be incapable of predicting the true deformation profile. This is due to a separation that occurs between the insert and the skirt at a temperature above 130°C. Attempts made to match the predicted and measured profiles by releasing the insert from the skirt in the finite element analysis were only partly successful, suggesting that the true separation process is complex and may not be easily modelled. The holographic measurement, however, provided the true deformation profile of the piston at the two temperature ranges.

A comparative study on the use of the holographic method and ESPI (electronic speckle pattern interferometry) for the measurement of piston deformation has also been carried out. In this part of the study, a simplified ESPI method was used for measuring two displacement components simultaneously using an out-of-plane sensitive interferometer. A critical comparison of the two techniques as applied to the measurement of a thermally deforming piston has also been made.

CONTENTS Page

List of illustrations:

List of Tables

NOTATIONS

d	- displacement vector
D_{PP}	- distance from perspective plane to camera lens nodal point
G_r	- grey level of pixel at reference fringe
G_d	- grey level of pixel at datum line
G_P	- grey level of pixel at point P
N_1	- fringe order from direct view
N_2	- fringe order from reflected view
o	- unit observation vector
i	- unit illumination vector
n	- fringe order number
θ	- angle measured from gudgeon pin axis (clockwise when viewed from above piston crown)
λ	- wavelength of laser light (632.8nm)
Φ	- angle made by displacement vector with z-axis
σ	- angle made by mirror surface with z-axis
γ	- angle made by illumination vector with z-axis

CHAPTER 1

INTRODUCTION

Introduction

Petrol and diesel engine pistons are designed with low running clearances for several reasons. These are: (a) to reduce engine noise due to cold piston slap, (b) to reduce risk of lubrication break down and piston seizure, (c) to improve sealing abilities of the piston rings and (d) to improve the adaptability of the piston to increases in engine rating. Low running clearance can be achieved by controlling the expansion of the skirt. In a monometal piston this can be done by increasing the local flexibility of the skirt and reducing its temperature by introducing heat break slots between the piston crown and the skirt thrust areas. The presence of slots, however, can give rise to strength limitations with increased severity as the engine rating increases.

In order to achieve effective expansion control and maintain the rigidity with which the skirt is attached to the crown, a commonly accepted design is one that incorporates steel inserts cast into the piston during manufacture (Rhodes 1978). These inserts can take the form of continuous oval sleeves or two or more separate steel plates positioned in various locations of the skirt. The expansion behaviour of these pistons, however, depends largely on the design of the steel inserts used. In the open sleeve type of pistons (Figure 1.1), where the insert is exposed on the inner part of the skirt, a significant difference in the expansion behaviour at low and high temperatures was reported by the manufacturer, AE Piston Products Limited (Fletcher-Jones 1982). The insert was found to have full control over the expansion of the aluminium alloy skirt up to a temperature of 130°C. Above this temperature the insert loses control of the expansion of the skirt (see Figure 7.11, page 188). Although the open sleeve pistons have several advantages over pistons of other designs (see Chapter 3), large expansion of the skirt above 130°C will result in excessive wear, over-heating and under prolonged running conditions will possibly result in seizure. A method of understanding the thermal behaviour of the piston at different temperatures is therefore necessary in order to improve its design.

An important method for studying the deformation of pistons subjected to thermal and mechanical stresses is by using finite elements (e.g. Reipert and Buchta 1981 and Ruddy and Kinsella 1990).

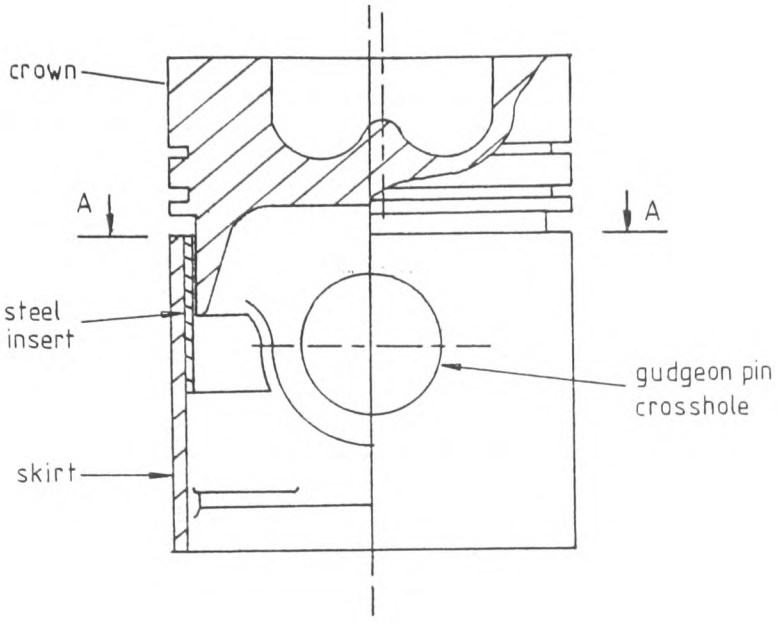

SECTION THROUGH PISTON

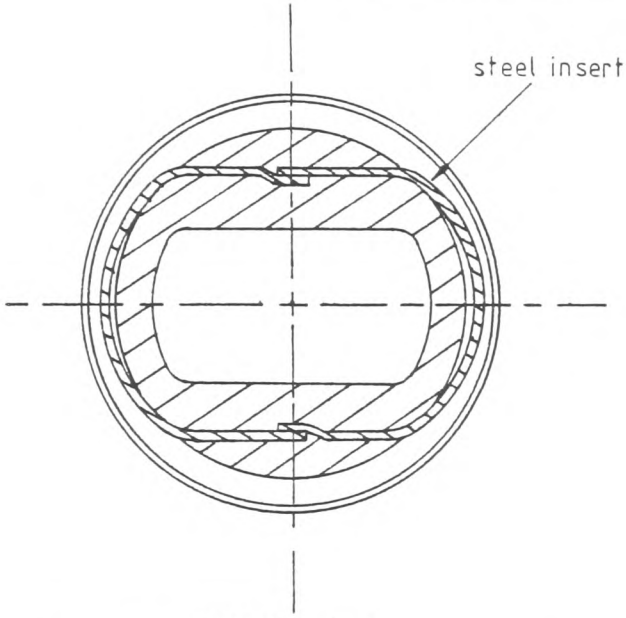

SECTION A-A

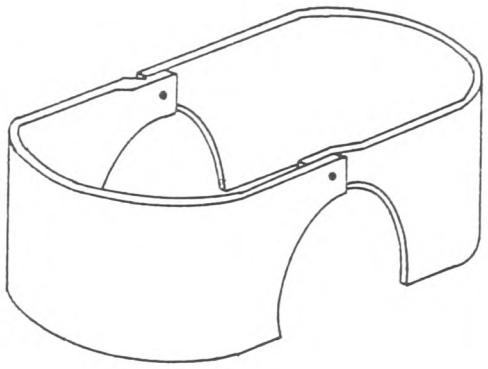

VIEW OF STEEL INSERT

Fi[illegible]

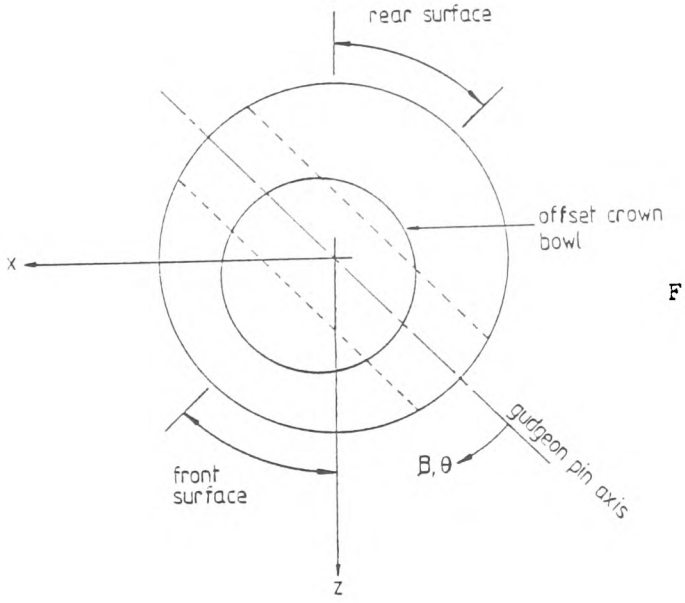

Figure 1.2 View above crown showing offset crown bowl

In this method a finite element mesh of the piston is generated and the loading conditions are simulated. The predictions of the model are experimentally verified in actual engine tests. In some situations, the piston may behave differently from the predictions and doubts on the accuracy of the model can arise. In such cases, the assumptions made in the generation of the model must be reconsidered. One simple technique of checking the accuracy of the model is to compare the predicted and the true deformation profiles. Since accurate measurement of the expansion is difficult to be carried out when the engine is running, such measurement can be made with the piston in a specially designed experimental rig. Such an approach has been used by the piston manufacturer. In their study, steady state thermal loading was applied and the diametral expansion was measured using dial gauges. Although this technique is simple to use, it provides deformation data at limited number of points and is of limited accuracy. In addition, physical contact with the piston surface can introduce heat sinks which can subsequently disturb the temperature distribution. Thus, a non-contact technique that can provide a whole-field deformation is necessary.

The aim of the present study is to make a quantitative comparison of the deformation profiles of an open sleeve piston predicted by a finite element model and those obtained by direct measurement using non-contact whole-field techniques. The effects of various assumptions made in the generation of the model on the predicted profile are investigated. Based on the measured data attempts are made to improve the accuracy of the model.

To achieve the above purposes a finite element mesh of the piston was generated based on drawings supplied by the piston manufacturer. The piston, which has an off-centred crown bowl (Figure 1.2), was assumed to be symmetrical in construction and therefore only a quadrant was modelled. Due to the unknown residual stresses within the piston certain assumptions were made as regard to the method of attachment of the insert to the skirt (see Chapter 3). The position of closure of the axial air gaps between the inner surface of the insert and the lower part of the crown was assumed to be at $\beta=40°$, measured clockwise or anti-clockwise from the gudgeon pin axis as viewed from above the crown (Figure 1.2). As will be shown in this thesis, the position at which the air gap closes is important in

predicting the deformed shape of the skirt and this position can be determined by comparing the measured and predicted profiles. The boundary conditions for the model were specified so as to reproduce the temperature rises measured in the experiments.

Two main optical techniques were considered for the experimental work: holographic interferometry and electronic speckle pattern interferometry (ESPI). Both these techniques are capable of providing full-field displacement data with a sensitivity of up to $\lambda/100$, where λ is the wavelength of laser light. A detailed theory of these techniques and some applications are discussed by Jones and Wykes (1989).

In the current work, three different holographic systems were developed to measure the deformation of the piston in the presence of rigid body displacement. The first rig devised is based on the multiple view method used by Evans and Russell (1983) (discussed in Chapter 2). An important feature of the new rig is the possibility of recording four instantaneous interferograms having different sensitivities on a single photographic film. This was achieved by using a system of mirrors mounted behind the holographic plate. The mirrors were inclined in a manner so that four images of the piston were visible from the view point of a single camera. Since all the four images were affected by perspective distortions and lateral inversions, a transformation algorithm for relating points on the individual interferograms with the corresponding points on the piston surface was developed. The algorithm is capable of operating on images arbitrarily inclined in space. An accurate technique of evaluating the equations of the surface of the mirrors has also been devised. The accuracy of the transformation has been verified by transforming grid points on a graph paper superimposed around a cylinder.

The technique developed for measuring the radial expansion of the piston using ESPI led to the development of the second and third holographic arrangements. In the ESPI system used, a vertical mirror was positioned adjacent to the piston so that two images of 45° sector of the front surface can be recorded together (Chapter 5). Two speckle fields having different sensitivities were thus imaged onto a single video frame for analysis. The interferometer used is one that was designed to measure only out-of-plane displacements. Here, it is

shown how such an interferometer can be used to measure two displacement components simultaneously by using a single recording system and without the use of expensive optical elements.

By omitting the axial component of displacement (i.e the component along the skirt) and measuring only the two vector components in the radial direction, effective usage of the available laser power was achieved in the second holographic arrangement. In addition, by imaging only two views of the piston on a single photographic film, high density fringes caused by a larger temperature rise (20°C) than that used with the four mirror method (8°C), could be recorded and analysed. This is because of the larger images obtainable when only two images are recorded, hence enabling one to obtain high density fringes resulting from a larger expansion (0.015mm to 0.020mm). Two reference beams were used to record two holograms of the piston before and after a specified temperature rise. This enabled the two holograms to be separated optically and any one to be used for the recording of live fringe formation in a repeated heating sequence. The results from the holographic and ESPI experiments were quantitatively compared. A critical assessment of the practical advantages and limitations of the two methods as applied to the study of a thermally deforming surface is presented.

Initial comparison of the holographic results and the predictions of finite elements for a temperature rise from 50°C to 70°C indicated a significant difference in radial expansion at the bottom of the skirt. A tilt was suspected to have occurred in the piston during the experiments and thus it was necessary to include the measurement at the rear surface. This led to the development of the third holographic arrangement (Chapter 6). Here, additional mirrors were positioned at the rear surface so that four images of the piston (two on each surface) could be recorded using a single holographic plate. A single reference beam was used due to the additional light required to illuminate the rear surface. The mean of the radial expansions at the two surfaces, which is free from body displacement and assumes a uniform heat input, was evaluated. The mean expansion could be compared accurately with the predictions of the symmetrical finite elements model.

The comparison between the predicted and the mean deformation have been made for two different temperature ranges : 50°C to 60°C

and 130°C to 140°C (Chapter 7). The first temperature range was selected well below the stress free temperature of 130°C so that the expansion of the skirt is fully restrained by the steel sleeve insert (Figure 7.4 of Fletcher-Jones et.al. 1982). The absolute temperatures are, however, not critical because of the linear diametral expansion of the skirt below the stress free temperature. The higher temperature range was selected so that a comparative study between holographic measurement and finite element predictions can be made after the steel insert has lost control over the expansion of the skirt.

The comparison at the 50°C to 60°C range showed that the predicted profile followed the measured profile closely at the top of the skirt when the position of closure of the axial air gap was assumed at $\beta=50°$. The predicted profile, however, was found to have a greater inward curvature at mid-skirt height when compared with the measured profile. This was attributed to the assumption in the model that the inner surface of the skirt and the outer surface of the insert are physically bonded. In the real situation complex residual stresses exist between the two surfaces as a result of the differential contraction between the steel sleeve and the aluminium alloy piston body. These stresses were partially relieved when the piston was heated hence imposing less restriction to the expansion of the skirt. At the higher temperature range the prediction of the model was similar to that at the lower temperature range. The measurement, however, showed a significant increase in the expansion along $\theta=90°$ to the pin axis. This observation is in agreement with the findings of Fletcher-Jones et.al.(1982) in which point-wise measurement was made. Here, a whole-field deformation was obtained and compared with the theoretical results. The separation between the skirt and the sleeve was confirmed by releasing the nodes at the sleeve-skirt interface and repeating the analysis. Attempts made to match the measured and predicted profiles by modifying the mesh were not totally successful, suggesting that the true separation process is complex and may not be easily modelled.

The comparative study has revealed the difficulties associated with the theoretical analysis of the complex thermal behaviour of the open sleeve piston. The predictions of the model was found to be influenced by the assumptions made in the generation of the mesh. It

was, however, possible to improve the accuracy of the model by comparing the predicted and measured profiles. At the higher temperature range, the original model is incapable of predicting the true deformation of the piston. The optical techniques used and the experimental methods developed as a result of the current work can, however, be used to measure the deformation profile accurately without having to consider the complex internal changes that occur when the piston is heated.

CHAPTER 2

LITERATURE REVIEW

2.1 Introduction

The application of predictive techniques such as the finite element method in the design and development of diesel engine pistons is well documented. However, there are only a few publications on the use of whole field experimental techniques to measure the deformed shape of a piston and its subsequent comparison with predictions of a finite element model. In this survey previous publications on the experimental and analytical study on pistons are considered with particular emphasis on the use of optical measurement methods. The development and some of the application of the two main optical techniques, holographic interferometey and ESPI, used in the current work are also reviewed. Comparative studies on experimental results obtained for other engineering components are briefly discussed.

2.2 Theoretical and experimental analysis of piston deformation

Combined theoretical and experimental analyses of the deformation of pistons using whole-field measurement methods have been published by relatively few authors. Besides the work carried out at the Polytechnic of Wales (Evans and Russell 1983, Evans and Premier 1989), there is limited published work on the use of such techniques for similar comparative studies. In the work described by Röhrle(1974) finite elements and photoelastic methods were used to analyse stresses and deformation of a piston resulting from pressure and heat. Although good correlation between analytical and experimental results were reported, the two-dimensional model used was suitable only for two-dimensional stress analysis and it was not possible to simulate heat loadings using a three-dimensional model. The photoelastic method is, however, not suitable for measuring three-dimensional surface displacements.

The theoretical predictions of stresses in a piston due to uniform pressure across the crown and axisymmetrical temperature distribution was verified experimentally by Johns et.al.(1973). Strain gauges and thermocouples were fitted in the region of the piston crown and recordings of strain and temperatures were made during operation of the engine. Good correlation between experimental

and theoretical results were reported. The experimental technique is, however, capable of providing strain values only at a few selected points on the piston surface.

Munro(1979) provided a general view of high speed diesel engine piston technology by selective consideration of new design features, analytical methods and research and development programmes. Emphasis was directed to the wider use of computer-assisted predictive methods and new experimental programmes. The use of predictive methods in several aspects of piston design such as cycle simulation, finite element analysis, transverse piston movement analysis and cooling oil flow were described. The advantages of using a short steel band in the open-sleeve 'isoformic' piston, similar to the one in the current study, are briefly discussed. The expansion control characteristics derived from a test rig for three types of piston design were compared along the major axis (90° to the gudgeon pin axis). The pistons used were :(a) a standard monometal piston, (b) a full length insert piston and (c) the 'isoformic piston'. The results showed that the 'isoformic' piston is capable of operating at the lowest cold diametral clearance of 0.0015in. when compared to the other two, which will result in reduced engine noise under operating conditions. Details of the test rig used for measuring the diametral clearance were, however, not given and no comparison with finite element predictions were discussed.

Some of the difficulties associated with the measurement of the whole-surface deformation of a piston has limited the experimental work in this area. In the technique used by Rhodes(1978), static test rigs were used for measuring the expansion of the skirt. In one of the rigs, steady-state thermal loading was applied by directing gas-heated air at the crown and the expansion was measured at diametrically opposite points using mechanical comparators. The expansions of various designs of petrol engine pistons were compared and one of these was the 'isoformic' piston. The comparison showed that high degree of control over the expansion of the skirt can be achieved in the 'isoformic' piston when compared to monometal pistons and other bimetallic pistons such as the 'pyrostrut'. As in Munro's paper (1979), no comparison with finite elements were made. Although the method of measurement described by Rhodes is simple to use, it is of limited accuracy and is capable of providing data at a few selected points.

Michael(1973) proposed how holographic interferometry could be used to measure the deformation of a piston. The expansion was assumed to be radial and the measured quantities at several selected points on the skirt were given. No details of the experimental work or comparison with theoretical predictions were discussed.

Work within the Department of Mechanical Engineering at the Polytechnic of Wales on the application of holographic interferometry to the measurement of piston deformation was initiated in the early eighties. The original aims of the project was to verify the accuracy of the finite element model of an open-sleeve 'isoformic' piston used by the piston manufacturer AE Piston Products Limited (formerly known as Wellworthy Limited) in their design and analysis work. This piston was used in the study due to the complexity of its design and the need to establish the hot shape of the piston above the stress free temperature. Although the original aims were not fully achieved, several major aspects of the work were accomplished to a satisfactory extent. An important achievement during the years 1981 to 1982 was the development of a software package that can be used for evaluating displacements merely by working from photographs of fringe patterns and recording of live fringe formation (Evans and Russell 1982).

The holographic arrangement developed by Evans and Russell(1982) consists of using three holographic plates and three cine-cameras for recording the live fringe formation (see Chapter 4). Although their technique provided a means of measuring all three Cartesian components of displacement simultaneously, the experimental work is tedious. Moreover, the method is capable of providing deformation at the front surface of the piston alone. The experimental arrangement developed by Evans and Premier(1989), however, enabled deformation at the front and rear surfaces of the piston to be measured so that the mean component, which is free from body displacement (see Chapter 6), can be used for comparison with the predictions of finite elements. Their measurement was limited to only two diametrically opposite points in spite of the whole-field capability of the holographic method. Nevertheless, their results were reported to be within 5% of the theoretical predictions.

Some of the work carried out by others on pistons were confined mainly to the development and/or application of sophisticated computing methods and design techniques to determine stress and

deformation. Reipart and Buchta(1981) described the details of an interactive piston development program using finite elements. Results of the analysis to obtain deformation due to thermal and mechanical loadings for truck diesel engine pistons were discussed. The predicted areas of maximum skirt distortion, which could result in increased surface pressure due to contact with the cylinder liner, was verified experimentally. Their experimental technique consists of placing a specially prepared pressure-sensitive sheet, which discolours according to the surface pressure, in between the piston skirt and cylinder liner. Good agreement between the experimental and finite element results were reported, though the former was purely qualitative.

Heitzman(1990) used 2-D and 3-D finite element method to optimise the design of an articulated piston for a diesel engine. Thermal and mechanical loadings were applied to determine the areas of maximum stress. Several modifications were made to the original model to improve its design. In order to reduce the piston crown temperature and increase oil life, a design option that consist of machining a hole in the strut wall connecting the crown to the pinbore was considered in the analysis. To fully qualify the piston a series of bench and engine tests were carried out. Since the pistons used by Reipart et. al. and Heitzmann were of monometal designs (i.e. without any cast-in reinforcements) their thermal behaviour could be accurately predicted. As will be shown in this thesis, the thermal behaviour of a bimetallic piston of the open-sleeve design is more difficult to predict using finite elements.

2.3 The whole-field methods

2.3.1 Introduction

Several whole-field methods are available for measuring strains and surface displacements : holographic interferometry, speckle pattern interferometry, moire' method, photoelasticity and brittle coatings. The first three techniques are usually applied to the measurement of surface displacements. Stress and strain can, however, be obtained by differentiating the data though this can result in a loss of accuracy. The last two techniques, photoelasticity and brittle coatings, are more suited for measuring stress and strains.

In this part of the literature survey, the above techniques are briefly reviewed with greater emphasis on their advantages and limitations, and the reasons for selecting holographic interferometry as the main measurement method in the current work is discussed. A theory of the holographic and ESPI techniques are given in Appendix A1.

The holographic technique relies on the interference of two wavefronts, one of which is holographically reconstructed (see Appendix A1). The interference gives rise to a fringe pattern whose sensitivity depends on the observation-illumination geometry. The main advantages of this technique are : (1) it is non-contacting and (2) it is capable of high accuracy (approximately 0.5 μm). Much higher accuracies can be achieved by using phase-stepping and heterodyne techniques. By using different observation-illumination arrangements, it is possible to measure all three Cartesian components of displacements and hence to define the movement of a surface point completely. The main disadvantage of this method is due to the difficulty associated with the experimental work when 3-dimensional measurement of a rapidly deforming surface is required (see Chapters 4 and 5). Recording of good quality holograms and wet processing of holographic plates can be time consuming. Thermoplastic recording materials can, however, be used as an alternative to the conventional photographic plates to save time, although this may results in increased cost.

Speckle pattern interferometry can be divided into two main classifications : speckle pattern correlation interferometry (SPCI) and speckle pattern photography (SPP). Both techniques rely on the speckle effect produced when a diffusely reflecting object is illuminated using expanded laser light. In the SPCI method, the illumination and observation directions can be arranged to produce fringes that are sensitive to pure in-plane or pure out-of-plane displacements (see Appendix A1). In the SPP method, two speckle fields, one scattered from the undisplaced and the other scattered from the displaced surface, are recorded on a single photographic plate. The speckle fields can be assumed to be identical except that one is displaced relative to the other by an amount which depends on the magnitude of the displacement and position of the recording plane. When the object is in focus, the image-plane speckle fields produce fringe patterns that are sensitive to in-plane displacement.

A main advantage of the SPCI method is that the speckle fields can be registered using a standard television camera and processed electronically to produce fringe patterns. This technique, which is known as electronic speckle pattern interferometry (ESPI), relies on video processing in order to generate the correlation fringes. A main feature of ESPI is the ease of obtaining and analysing fringes to obtain deformation (see Chapter 4).

The moire' method consist of using the moire' pattern to measure displacement or strains. Moire' patterns are formed when two gratings are superimposed. One of the gratings (known as the model or specimen grating) is used to characterise the state of deformation of a surface and the other is used as a reference grating. The moire' patterns are formed on the image plane of the observation system. The relationship between the model grating, the reference grating, the observation system and the surface under study must be known in order to determine displacement or strains. This relationship depends on the particular technique used. There are three basic techniques : intrinsic moire' method, projection moire' and reflection moire' method. Details of these techniques are discussed by Sciammarella(1982). In the intrinsic moire' method, the grating is fixed directly on the specimen surface, hence following the changes experienced by the surface. This method provides in-plane displacements. Out-of-plane displacements can be measured using the

projection moire' (or shadow moire') method. In this method, a reference grating is placed in front of the specimen and a collimated beam of light is directed at an oblique incidence through the reference grating onto the object surface. The shadow of the reference grating serves as the model grating. The reflection moire' method, on the other hand, provides the slope of the deformed surface. A technique for measuring in-plane and out-of-plane displacements simultaneously using the moire' method is described by Asundi et.al.(1989). Their technique consists of using two illuminations to superimpose a virtual grating on a specimen grating. Some of the applications of the moire' method are also discussed by Sciammarella(1982) and from this review, one will note that this technique can be used in a wide variety of problems in solid mechanics, both for static and dynamic conditions.

The method of photoelasticity is based on the changes in the optical behaviour of transparent non-crystalline materials which occur when the material is stressed. Such materials are optically isotropic when free from stress but become optically anisotropic and display characteristics similar to crystals when stressed. A detailed theory of this technique is described in several texts, e.g. Dally and Riley(1991). A main advantage of this method is the possibility to fabricate and investigate any section of a stressed component rapidly using pre-cast resin plates. Modification to the model can be made easily and their effect on the stress distribution can be determined by repeating the measurement. This method is, however, not suitable for studying three-dimensional surface displacement caused by thermal loads.

Brittle coatings can also be used to determine surface strains. In this method, the coating is usually air-sprayed until a layer of coating from 0.08mm to 0.225mm thickness has accumulated. After the coating has dried, the component is subjected to a system of loads which causes the coating to fail by cracking. Since the coating is thin relative to the thickness of the specimen, the surface strains occuring on the specimen can be assumed to be transmitted to the coating. The brittle coating fails when it is strained to a certain critical value called the threshold strain, which is determined by calibrating the coating. The advantage of this method is that objects of complex shapes can be studied. However, only in-plane strains can be measured.

The holographic method was used as the main measurement method in the current study due to several reasons. Among these are the possibility of measuring 3-D surface displacement on the entire surface of the illuminated area of the piston without contact and due to its high sensitivity. In addition, previous work carried out within the department has led to the development of an experimental technique and the associated computer programs which were used as the starting point for the current work. The ESPI method was used in part of the study in which a comparison between the two techniques were made. Since holography and ESPI were the main techniques used in the study, a review of the development and application of these techniques is given in the next section of the literature survey. A greater emphasis is laid on the simultaneous measurement of x, y and z components of displacements, thermal applications, problems of perspective distortions, rigid body motions, application to continuously deforming surfaces and some modern aspects of fringe analysis.

2.3.2 Holographic interferometry

2.3.2.1 Development of the technique

Holographic interferometry was first reported by R.L.Powell and K.A.Stetson at the Spring Meeting of the Optical Society of America in 1965 (review by Briers 1976). Their discovery originated from the problem of investigating and eliminating dark bands which appeared on superimposed reconstructed holographic images. They found that these bands were, indeed, interference fringes formed as a result of slight movement of the object during recording of the hologram. They later proceeded to show how these fringes could be used to analyse the vibrational modes of an object.

At about the same time another team at the National Physical Laboratory (UK) developed this technique independently for measuring displacements. Burch et. al.(1966) introduced the concept of multiple exposure holography with equal increments of strain between each exposure and the next in order to sharpen the fringes. A lack of sharpness indicates failure of Hooke's law. Burch and Ennos(1966)

later gave an account of the application of holographic interferometry to the comparison of cylinder bores.

Haines and Hilderbrand (Briers 1976) extended this technique to the analysis of simple translations and rotations, and of general deformations. The deformations were obtained by analysing the fringes resulting from an interference between the holographic image and the object itself (live-fringe method), or between two holographic images where the deformation is applied between the two exposures (double exposure method). They proposed a technique of interpreting fringe patterns for rotations about an axis in the plane of the object, and for in-plane translations.

Several methods of fringe interpretation were also put forward during the mid-sixties to the seventies. The fringe localisation technique is, historically, the first reported technique for interpreting holographic interferograms. This was the method proposed by Haines and Hilderbrand and it relies on the fact that, in general, fringes caused by the translation of the object are localised some distance behind the image. By identifying the plane of localisation and measuring its distance from the object it is possible to determine the in-plane components of translation. A main disadvantage of this technique is due to the difficulty in locating the plane of localisation of fringes which can lead to very poor accuracies.

In an alternative technique of interpretation proposed by Aleksandrov and Bonch-Bruevich (Briers 1976), known as the fringe counting technique, the observer counts the number of fringes that pass the point under consideration on the holographic image as he moves his head in a linear direction. In this technique the plane of localisation of fringes need not be known. The parallax between the fringes and the object is used rather than the actual position of the fringes in space. However, this method also gives only the in-plane components and relies on a change in viewing angle to determine the third component.

A third method, known an the 'zero-order fringe' method was introduced by Ennos in 1968. This method gives the component of displacement in a direction bisecting the illumination and viewing directions. In order to determine all three components of displacements, three separate holograms are made and fringe patterns from three directions are recorded for analysis. The fringes orders

are determined by counting the number of fringes from a stationary point of zero-order to the point whose displacement is to be evaluated. Among the three techniques of fringe interpretations, the zero-order fringe is the most widely used method (Briers 1976).

Sollid(1969) derived a general relation by which small displacements of a diffusely reflecting surface can be determined. A vector approach was used in the derivation. He applied the equation to three two-dimensional cases where the incident and scattered light are coplanar with the displacement vector and to a general three dimensional case. For the three dimensional case, the multiple hologram technique proposed by Ennos (zero-order fringe method) and the single hologram technique proposed by Aleksandrov and Bonch-Bruevich (fringe-counting method) were compared. The comparison showed that the Aleksandrov and Bronch-Bruevich method of fringe interpretation was severely limited by the solid angle subtended by the object at the hologram. As a result the line of sight component cannot be measured with any degree of accuracy.

A mathematical error in the derivation of the general equation by Sollid was pointed out later by Vest(1973). Vest suggested that the computation for displacement should be carried out in terms of the Cartesian components rather than the components along the three unit vectors used by Sollid.

Early experimental work using the zero-order fringe method proposed by Ennos and the vector theory proposed by Sollid was carried out by Shibayama and Uchiyama(1971) using a cantilever. In their experiments, three double exposure holograms of the cantilever were made and the fringes were recorded from three observation directions. Since the cantilever appeared in different perspectives, the corresponding points in the various views were identified by projecting a mesh pattern onto the surface of the cantilever. Their measurements were found to agree well with the theoretical results.

Although the set-up used by Shibayama produced a well conditioned geometrical matrix due to the large angles of separation (30° to 40°) between the various observation directions, the experimental set-up is relatively complex. The recording of three separate holograms requires the use of a large number of optical components and individual exposure and processing of the various plates. One

technique of simplifying the set-up is to use a single plate and to view the object through various parts of the same plate. This, however, will result in smaller angles of separation between the various observation directions (approximately 20° for a 4in.x 5in. plate and for object-to-hologram distance of 300mm) and hence a poorly conditioned geometrical matrix. A small error in the fringe count will therefore result in large errors in the displacement.

In order to solve the problems of poorly conditioned systems, Dhir and Sikora(1972) proposed the use of at least four observations through a single hologram to determine the phase shift at a particular point of interest and to solve the over-determined set of equations by using the method of least squares. They presented this technique based on the concept introduced by Aleksandrov and Bonch-Bruevich and demonstrated by analysing the three dimensional displacement fields of a beam under pure bending and a propeller blade under uniform pressure. When three of more equations were used to determine the three displacement components, their values were found to be reasonably consistent. However, the results obtained by using various combinations of exactly three equations were reported to differ in each case.

Although the Dhir and Sikora method provides improved accuracy, improper positioning of the various viewing stations can introduce significant errors in the displacement values. Hsu and Lewak(1984) found that when the viewing points were positioned in a vertical line large errors were encountered. A simple solution proposed was to move one of the observation points from the plane of the other three points.

2.3.2.2 Problems of perspective distortions

Although the multiple observation method can be useful in displacement measurement, the object appears in different perspectives and identifying the corresponding points in the various views becomes difficult. Matsumoto, Iwata and Nagata(1973) presented an alternative technique for solving this problem. In their arrangement instead of using virtual reconstructed images, real

images from the individual holograms were projected onto the object surface in the reconstruction process. To achieve this a conjugate of the reference beam was produced by positioning a mirror in the path of the reference beam, but on the opposite side of the hologram. The reflected beam then illuminates the hologram from the rear and the reconstructed wave forms a real image with fringes on the original surface. The fringes formed were photographed from a single recording direction. As a result the images have the same shape but superimposed by different interferograms corresponding to each observation direction and the corresponding points in each of the interferogram can therefore be identified easily.

An alternative method of overcoming problems relating to perspective distortions is to determine the 2-D coordinates of the points (at which deformation is required) on the interferogram in each of the views and to provide the geometrical positions separately for analysis by a computer (Ennos, Robinson and Williams 1985). However, this technique is not suitable in situations where deformation at large number of points are required because inputting the geometrical positions of each of these points into the computer can be tedious.

By using small angles of separation between the various observation directions, however, it is possible to obtain images that exhibit negligible perspective distortions. But in such an arrangement the fringes must be measured with very high accuracy, for instance, by using the heterodyne technique (Kakunai et.al. 1985). In this technique two reference beams are used to record a double exposure hologram, one for the unstressed condition and the other for the stressed condition. A small frequency shift is then introduced in one of the reference beams. The phase difference between the interfering wave is detected electronically as the phase difference of the beat signal. A single hologram and a single imaging lens are used to record three or more reconstructed images. The three components of the displacement vectors are obtained by imaging the interference fringes through three or more different parts of the hologram. Although this technique is capable of high spatial resolution and interpolation up to 1/1000 of a fringe spacing (Dandliker and Thalmann 1985) it requires sophisticated electronic equipment.

Another approach to the problem of perspective distortion is to use a similar arrangement as in heterodyne method but to measure the displacement vectors using the phase-shifting method (Kakunai and Hsegawa 1987). In this method the phase of one of the reference beam is shifted relative to the other, usually in 3 stages of 120°. The shift is normally introduced by using a mirror mounted on a piezo-electric translator and located in the path of the reference beam. The interferograms corresponding to each of the three views are digitised into a computer for analysis. This technique allows one to measure the interference phase with an accuracy of 1/100 of a fringe at any point on the digitised image. The phase-shifting method, however, has several other advantages besides its use for solving problems of perspective distortions and this will be discussed later (see Section 2.3.2.5).

A simple and cost effective method of handling perspective distortion in a multiple observations set-up is to use geometrical transformation routines to transform digitised fringes (in two-dimensions) back to the object surface (in three-dimensions). Such an approach was developed by Evans and Russell(1983). In their work a computer program has been developed that operates on fringe centrelines digitised manually from photographs of fringe patterns. A thermally deforming piston was used in their study (see Chapter 4). The movement of live fringes was recorded from three observation points simultaneously using three cine-cameras. The positions of the cameras relative to the piston were inputted into the program for the transformation which also takes into account the effects of perspective distortions. This technique was later used by Evans, Russell and White(1987) to measure the thermal deformation of a cylinder. Since it should be possible to describe the object surface in a mathematical form, the transformation routine is therefore limited to objects of simple shapes.

2.3.2.3 Measuring accuracy and error analysis

The measuring accuracy of the holographic technique was discussed by Matsumoto, Iwata and Nagata(1973). They derived equations for the allowable errors of the observation and illumination directions and of the order numbers for an allowable error in the displacement values. For a given accuracy of displacement component, the allowable reading error of order numbers and angular setting errors of observation and illumination directions increased with an increase in the angles between the various observation directions. The equations for the allowable errors were used in a later paper (Matsumoto et.al. 1974) in which they measured the deformation of a cylinder under concentrated loading with high accuracy (of the order of 0.0001mm). The fringe orders were read within an allowable error of 0.2 of a fringe spacing for a maximum error of 0.2μm in the displacement. Since a zero-order fringe was not identifiable, the fringe orders were determined by fixing one end of a flexible strip to the cylinder and the other end to a stationary point. A reliable zero-order fringe is then introduced into the interferogram and counting could be done from this fringe. Problems relating to perspectives distortion of the various images were overcome by using real images that were superimposed onto the cylinder before recording the fringes.

A similar error analysis was described by Nobis and Vest(1978). They presented a statistical analysis of the effect of measurement errors of the fringe orders and the illumination-observation geometry on the measured displacement. Their analysis was different from those of Matsumoto in the sense that the latter provides upper bounds for the errors. In addition, Matsumoto's arrangement requires three holograms and three observation points. The analysis given by Nobis and Vest is, however, based on a single holographic plate with three or more observations. A set of graphs were produced that enables one to estimate the magnitude of errors which are likely to occur in a given application of holographic interferometry. The expected errors were found to increase as the object-to-hologram distance is increased. This is caused by a convergence of the various observation vectors for large object-to-hologram distances. Very large errors also occur at small object-to-hologram distances ($<$100mm) in a

three-observations set-up. This is due to one of the observation vectors being almost normal to the line of sight component of displacement. Increasing the number of observation points to five and solving the over-determined set of equations by using the least squares method was reported to eliminate the singular behaviour at small object-to-hologram distances. At large object-to-hologram distances, however, only small reduction in errors occurs. Errors due to inaccurate measurements of system geometry were presented in a tabular form for various values of object-to-hologram and object-to-illumination source distances.

2.3.2.4. Problems of rigid body motions

A major problem associated with the holographic technique is rigid body movement. When an object under investigation is subjected to a stress, the object may undergo a rigid body movement besides the local deformation. Such a movement will give rise to fringes that can mask those due to a pure deformation and, in most situations, it is difficult to separate the two. Several papers were published on the type of fringes caused by rigid body movement, and various methods for eliminating them have been proposed.

Stetson(1974) discussed the fringes and fringe localisation associated with the rigid body motions and homogeneous deformations. Two types of rigid body motions were considered, i.e. rotations and helical motions. The observer-projection theorem is discussed in detail. This theorem states that fringes localised off the surface of the object can be projected to the surface of the object radially from the centre of transmittance of the aperture of the observing optical system.

A technique for producing an optical effect that is unaffected by rigid body motions was described by Hu, Turner and Taylor(1976) . Their method combines holographic interferometry and the moire' effect. Double exposure holograms are made from the front and rear of an object in a symmetrical optical arrangement using two light sources. The two sets of interferograms were treated as random grids and were superimposed to produce a moire' effect that is free from the effects of rigid body motion. Their proposed theory was confirmed

experimentally by working on a circular ring, a cantilever beam and a cylindrical pressure vessel. This technique was reported to have the same sensitivity as holographic interferometry. Precise alignment of the optics is, however, essential in order to minimise errors.

N.Abramson published a series of papers (e.g. Abramson 1979) on sandwich holography that not only enables one to compensate for rigid body motions but also to determine the direction of displacement of an object. In this technique two exposures of an object in the unstressed and stressed conditions are made on separate plates. By later recombining the two reconstructed images it is possible to study the interference fringes caused by dimensional differences of the object that have arisen between the exposures. In addition, the two images can be moved in relation to one another and, therefore, a movement of the object (i.e. body movement) can be compensated for so that the fringes caused only by local deformations are left. By extending the technique further it is also possible to record a number of holograms on different plates, each corresponding to a particular loading condition. Later, any two holograms can be recombined to study the deformation between the two exposures alone. The disadvantage of the sandwich holography is the need to reposition the plates with high accuracy in order to to assure correct results. In addition, change of plates in between exposures can result in errors caused by differences in plate thickness or plate inhomogeneities (Abramson 1981).

Some of the advantages of sandwich holography have been exploited by Kurtoglu, Abramson and Carlson(1988) on an investigation of an industrial robot. The direction of displacement is not known in some configurations of the robot but this information could be extracted from the sandwich pair. In situations where a large number of fringes appeared this technique enabled some of the fringes to be moved from densely covered parts onto a reference surface, and made the counting possible. The sandwich technique, however, needs more care when compared with other techniques.

Stimpfling and Smigielski(1985) devised a technique for compensating for complex rigid body motions. In their set-up a rigid connection between the reference point source and the hologram was established. By moving the whole reference source-hologram arrangement they showed how one can superimpose the object and the

reconstructed image and neutralise the effects of differences in the optical paths caused by a global movement of the object. They demonstrated the use of this technique both for the case of real-time and double exposure interferometry. In-plane translation of over 5mm has been compensated for using this method. Their technique is, however, unsuitable for a rapidly deforming body because of the finite time needed to shift the reference source-hologram arrangement carefully.

2.3.2.5 Some aspects of automatic fringe analysis

The automatic analysis of holographic fringes has gained wide attention from several researchers. Image processing and related techniques forms a specialised field of study and numerous papers have been published in this area (review by Reid 1987). Since automatic fringe analysis is considered to be outside the scope of the current study, an exhaustive survey will not be given. However, some of the more recent work is briefly reviewed.

The conventional technique of analysing fringes to obtain deformation consists of working on photographs of fringe patterns. The fringe centres are located manually and its true geometrical position are determined by suitable scaling using selected datum points. This technique is slow and tedious. When deformation over a large number of gridded points are required the fringes can be digitised into a computer by means of a digitising tablet for analysis. However, the digitising process can be time consuming.

For the holographic technique to gain wide acceptance in practical applications an automatic technique of analysing the fringes is necessary. Image analysis technique are commonly used to enable the semiautomatic or fully automatic analysis of fringe patterns. In these techniques the fringe pattern is directly digitised into a computer image memory via a television camera. A host computer can then be used to analyse the fringes to extract phase and deformation information.

Robinson(1983) presented an image processing algorithm that enables automatic analysis of fringes to be carried out with complex and noisy data. The application considered were strain measurement,

position location in spatial coordinates and fault detection in holographic non-destructive testing. The algorithms presented are capable of handling complex fringe patterns at high speeds.

In certain situations involving complex fringes patterns automated fringe analysis can be simplified by linearising the fringes. This can be achieved by introducing a carrier fringe pattern. This technique was used by Matthys, Gilbert and Dudderar(1988) on the measurement of surface deflections induced by internal pressure variations on a hermetically sealed package used to house microelectronic components. The carrier fringes were introduced by rotating the housing through a small angle. The introduction of a carrier fringe pattern results in straight fringes and these were perturbed or modulated by the application of internal pressure. The modulated fringes and the original carrier fringes are analysed separately and subtracted to obtain deformation caused solely by the internal pressure. The setback of this method when compared to that of Robinson's is the need to rotate the object accurately through a small angle in order to introduce the carrier fringes.

In the automated analyses of interferograms involving low fringe orders it is often necessary to interpolate in between fringe maxima (or minima) with high accuracy. In these cases, mathematical interpolation may not yield results of good accuracies. An alternative technique using a digital phase-measurement system was proposed by Hariharan et.al.(1982). In their system a diode array camera was used to image the interference pattern and the phase differences at 100 x 100 grid points were calculated by using digital electronics. The phase of the reference beam was shifted in 3 steps of 120° each by varying the voltage applied to an electro-optical modulator. Three images were digitised and analysed to provide the phase change at any particular point. This technique, which is also known as the phase-stepping method, allows measurement of the phase with an accuracy estimated at ±2°.

In another paper published by Hariharan(1983) an inexpensive system using a microcomputer which is fast enough to permit measurements on real time fringes to an accuracy of $\lambda/100$ is described. In the optical set-up developed, four illuminations were used (two in the horizontal and two in the vertical planes) to obtain

four equations in three unknowns. To evaluate the phase in an interference pattern three successive scans of the array were made, shifting the phase of the reference beam by 120° between each scan. A cantilever was used in their experiment and was deformed into an S-shape. Their results showed the capability of their system to deal with ambiguities arising from a change in the sign of displacement.

Hariharan extended the phase stepping method (also known as the quasi-heterodyne method) to holographic contouring in another publication (1985). Two basic method of contouring were discussed. The first is the two-wavelength contouring whereby the hologram is recorded at one wavelength and replayed at a different wavelength. In the second technique, known as two-refractive-index contouring, double exposure hologram of an object located in a cell filled successively with fluids having different refractive indices is recorded. By using electronic techniques to measure optical path differences directly at a uniformly spaced array of points, it was possible to increase the speed of analysis of the fringes.

In computerised analysis of holographic fringes the number of detector points available on the detector array usually sets a limit to the number of fringes which can be measured. Creath(1989) showed how it is possible to measure high density fringes using a Videk Megaplus camera with 1320 x 1035 detector elements. The system has been used to obtain deformation and surface contour of various parts. Because of the slow speed of the detector array and of reading the data into the computer, the object deformation must not change during the time required to take data.

2.3.2.6 Related techniques

A variety of techniques for obtaining deformation and strain information using holography were proposed by several authors. Here, we consider some of the pertinent published work that concerns these techniques.

The experimental implementation of the fringe vector theory of strain analysis of a cylinder was presented by Pryputniewicz(1978). The cylinder was subjected to rigid body rotation and thermal expansion. The fringe vector is defined as a vector which has a

direction normal to the fringe-locus plane, pointing in the direction of increasing fringe orders and whose magnitude is inversely proportional to the spacing between these planes. By observing the fringes, it is possible to determine the fringe vector. Since the fringes vectors are related to the sensitivity vectors by a matrix transformation that describes the strains, shears and rotations of the object, three or more such observations from different directions allow the determination of the desired matrix. Comparison of his experimental results with theory showed a difference of 2% for the case of rotation and between 10% to 32% for the thermal expansion. The large difference for the thermal expansion was related to the inaccurate assumptions made in the fringe vector theory on the formation of fringes, errors due to digitising and the limited solid angle subtended by the various observation vectors at the object.

In practically all applications of holographic interferometry in deformation analysis it is essential to know the position of the sensitivity vector. This can be determined by measuring the illumination and observation geometry but this method can be prone to errors. Pryputniewicz and Stetson(1980) proposed an alternative technique whereby the object is given a known rotation in between exposures and the sensitivity vectors are analysed from the interferograms. These vectors can, in turn, be used to analyse interferograms resulting from unknown motions of an object, providing the illumination and observation geometries remain the same. They showed that two rotations of the object alone are sufficient to provide data to solve for the sensitivity vectors.

Pirodda(1989) presented a technique using conjugate waves for measuring in-plane deformations. In his arrangement, the object is illuminated frontally by one plane wave and the scattered waves are recorded on two holographic plates positioned at equal angles to the illumination direction . The conjugate of these waves are then produced by positioning mirrors behind the hologram and they are made to impinge on the object, which in observed frontally. If the object is deformed, the reconstructed waves will also be distorted and its intensity distribution will map one in-plane component of the displacement. A practical implementation of this technique is given although calculations of the in-plane displacements are not provided.

In a multiple hologram arrangement to determine the vectorial object displacement three or more holograms must be recorded before the object is deformed. These must then be made to interfere with the object after deformation under the same illuminations. The phase distribution on each of the resulting interferograms can be determined using various techniques, e.g. the phase-stepping method. However, it is generally not possible to know how the phase at a point in one interferogram is related to the phase at the same point in another interferogram. Stetson(1990) presented two solutions to this problem. The first solution is to determine the displacement of the object points relative to some reference location. The second is to determine absolute displacement without knowledge of absolute fringe orders. In the first case, the sensitivity vector is assumed to be constant across the surface of the object. In the latter case he showed how the variations of the sensitivity vectors across the surface of the object can be used to make such measurements. To illustrate this, we consider an object that has undergone pure translation and, hence, generates a fringe pattern. The fringes will be uniformly spaced only if the sensitivity vector remains the same across the surface of the object. If the sensitivity vector varies across the surface the fringes will exhibit a gradual change in the spacing. Thus, if the variation of the sensitivity vector is known the absolute translation can be determined by analysing the fringes. This is the basis of the method proposed by Stetson. However, it requires at least four illuminations of the object and may not be applicable to a continuously deforming surface where a zero-order fringe is not present.

Hansche and Murphy(1974) presented a class of assumptions that reduces the number of views necessary to determine three-dimensional displacements form three to one. Knowledge of the expected motion of the object and geometry of the object surface are, however, required. Two internally pressurised spherical shells were used in their experiments and the mean radial deformation was converted into strains and compared with strain gauge measurements. Their holographic results showed good agreement with the strain gauge readings for one of the spheres. A larger difference was reported between the two results for the other sphere and this was associated with the non-uniform expansion of the sphere.

2.3.2.7. Applications

Holographic interferometry has been widely used in a variety of applications. In this survey we consider some of its important applications in the engineering field which are considered to have relevance to the current project. Particular emphasis is given on its application to the measurement of thermal deformation and comparative studies between holographic results and finite element analyses.

The possibility of using holographic interferometry in high temperature displacement measurement was demonstrated by Hsu and Moyer(1972). In their work a cantilever beam was located inside a modified furnace with a quartz window. Double exposure holograms of the cantilever were recorded at 400°C, 650°C, 700°C and 800°C and the fringes were analysed to obtain the deflection data. Their results showed that the measured deflection^3 were almost the same at all temperatures. The most disturbing factor seemed to be due to the light radiated by the specimen above 400°C. This was, however, overcome by using an emulsion (Kodak 649F) which is more sensitive to laser light than the light emitted by the glowing specimen.

In a later paper published by Hsu(1976) the thermal distortion characteristics of graphite-fiber and epoxy-resin laminated plates were studied. A multiple double exposure method was used to record fringes covering large temperature ranges on the same plate. Two methods were used to obtain the displacement data : out-of-plane displacement method (1-D) and general displacement method (3-D). The displacement was evaluated for seven points along the horizontal and vertical centrelines of the plate. The results were compared with theoretical calculations which showed a difference of about 40%. This difference was attributed to the temperature-sensitive properties of the material which was not taken into account in their theoretical analysis due to the limitations in their computer program. A marked difference from the theoretical results above a certain critical temperature was also reported. This was again attributed to changes in material properties of the epoxy resin as the temperature increased. Their results show that the holographic method is capable of providing the true deformation behaviour of composite materials which may not be predicted accurately using finite elements.

Hsu et.al.(1978) later demonstrated the possibility of using real-time holographic interferometry to monitor crack growth over a prolonged period of time and at elevated temperatures. A Vee-notched specimen was placed in an oven equipped with a glass window and the specimen was heated to 120°C and maintained for a maximum of 860h. The success of their experiment increased the possible scope of this technique to include measurement of strains over extended period of time and at high temperatures.

Gilbert and Vedder(1981) used holographic-moire' method to study thermally induced deformation in rock specimen. The concept of an optical rosette was introduced and used to measure principal strains and their corresponding directions. The values of thermal coefficients of expansion were evaluated and these were reported to be within the range of those documented by other investigators.

Goldberg(1975) applied the holographic technique to a slowly deforming rough surface. In his arrangement, two pairs of beams illuminated the object in two orthogonal planes. The subject used is a concrete specimen which expands due to absorption of water. A single observation was used and the object was illuminated with each of the four beams in turn. Because of the slow deformation of the concrete surface, it was possible to switch the object beams after photographing the fringe patterns without any significant loss of information due to continuous movement of fringes.

In a later publication, Goldberg(1982) presented a laboratory method using holographic interferometry to determine the magnitude and type of stress at points in the surface layer of a cast iron pipe in the vicinity of a screwed connection. Three illuminations and a single observation direction were used. A kinematic mount was used so that the specimen can be removed, stressed and returned to its original position with high accuracy. His results suggested that failure of a screwed connection of the type studied is mainly due to high tensile stress concentrated in the region around the boundary of the connection.

The need to verify and improve mathematical models for predictive analysis, such as the finite elements method, has developed much interest among engineers in the holographic technique. Miller et. al.(1988) used this technique to measure surface-crack-opening profiles in mortar and compared the results with the predictions of

the non-linear fracture model. The sandwich holography technique devised by Abramson was used to eliminate rigid body motion.

Maji and Shah(1990) measured the mixed-mode crack profiles using holography and also compared their results with the predictions of a finite elements model. They demonstrated the possibility of using an unexpanded reconstruction beam to produce the real image. The advantage of this method is that it is possible to pass an unexpanded beam through points of interest over a small area of the holographic plate. The laser power could be fully used to generate a bright image and the fringes can be conveniently counted on the real image when it is projected onto a screen. Their experimental results were found to be different from the predictions of the model and this difference was related to the assumptions made in the model.

An approach to applying the holographic technique for measuring large deformation was presented by Tatascoire and Schumann(1988). In their technique a modification to the set-up is proposed that makes the fringes that 'disappear' due to a large deformation to reappear, i.e., the mechanical object deformation is partly compensated for by optical means. It is, however, difficult to visualise how a compensation due to a non-uniform thermal expansion can be made.

The use of holographic interferometry in an industrial environment was described by Parker and Jones(1988). This technique was used to investigate the aerodynamic and mechanical behaviour of rotating fans for aeroengines. In the vibration analysis, the displacement of the blades of a model fan occuring during a short pulse interval was contoured. The holographic data was used to compare with and verify a finite element model of the fan. Good agreement between the predicted and measured vibration modes can be observed from their finite element plots and the holographic fringe patterns. Applications in the flow visualisation in rotating fans are also presented. In this case, the optical interference contours the change in density of the flow field between two exposures. The holographic results were again compared with a computed map of density predicted using flow modelling programs and good agreement between the results was also reported.

2.3.3 Electronic speckle pattern interferometry

2.3.3.1 Introduction

ESPI was first demonstrated by Butters and Leendertz (Jones and Wykes 1989) as a method of producing interferometric data without using the traditional holographic recording techniques. In this technique a video camera is used in place of a film to record a low spatial frequency 'hologram'. A reference hologram is stored as a video signal in a frame store and the incoming signals are electronically subtracted resulting in real-time correlation fringes. These fringes can be displayed directly upon a television monitor and digitised into a computer for analysis. Thus, photographic processing, plate relocation etc. associated with the holographic method are not necessary. The comparative ease of the use and of obtaining fringes has made the ESPI method an important test and measurement tool in the industrial community.

In this part of the literature survey we review some of the recent published work on ESPI. An exhaustive survey on this technique is not considered essential as it forms only part of the current study. As in holographic interferometry, a greater emphasis is laid on the applications of this technique and the comparison of the results with theoretical predictions. Some of the modern methods of analysis of ESPI fringes are also covered.

2.3.3.2 Some aspects of the technique

Three main types of measurement are possible using ESPI : in-plane displacements, out-of plane displacements and shape measurement. Details of the optical arrangement for these measurement and the theory involved are discussed by Jones and Wykes (1989). For the interest of completeness, the theory for the first two types of measurements which are considered relevant in the current study are covered in Appendix A1. Here, we briefly review the main features of the optical arrangement for these two measurements and discuss some of the papers that deal with the simultaneous measurement of several components of displacements.

In an out-of-plane sensitive interferometer, the illumination beam and the observation directions are set in-line. A smooth in-line reference beam is reflected off a beamsplitter, positioned in between the imaging lens and the image-plane, onto the light sensitive plate of a CCD camera (see Appendix A1 for details and diagrams). The reference beam is adjusted so that it appears to diverge from the centre of the viewing lens aperture.

In the in-plane configuration, two object beams are used to illuminate the object from equal angles to the observation direction, which is normal to the object surface. The in-plane component measured is one that lies in the same plane as the two illuminating beams.

The different optical arrangements necessary for the in-plane and out-of-plane sensitive interferometers makes it difficult to measure the two components simultaneously without using multiple recording systems and numerous optical components. Although in most applications one of the components (either in-plane or out-of-plane) is sufficient for the basic understanding of the behaviour of a stressed or vibrating object, it is sometimes essential to measure the various components simultaneously, especially in situations involving non-repeatable loading.

One method of measuring both horizontal and vertical in-plane components simultaneously was proposed by Moore and Tyrer (1990). Their technique consists of using beam pairs polarised in two orthogonal planes. A polarising beamsplitter was used to separate the two speckle fields into two separate television cameras. The nature of the specimen surface, however, affects the depolarisation of the scattered wavefront and this must be considered. In order to extend the technique to measuring the out-of-plane component, the authors suggested the use of a second wavelength illumination for one of the sensitivity vectors. This, however, may add complexity and cost to the experimental design and may therefore impose practical limitations to the technique.

Aswendt et.al.(1990) proposed an optical arrangement which allows measurement of in-plane and out-of-plane deformation 'almost simultaneoulsy'. In their technique, the optical system was initially arrangement to provide in-plane sensitivity. A rough-surfaced reference plate and an additional mirror were inserted rapidly into

the system to obtain out-of-plane sensitivity (see Section 2.3.3.4). This technique is, however, essentially sequential.

Jones(1976) proposed an optical arrangement for measuring total in-plane strains using two illuminations of the object. The beams were arranged in two orthogonal planes (x_1,x_2 and x_1,x_3), perpendicular to the plane of the object (x_2,x_3). In order to obtain the two illuminations necessary to measure in-plane displacements in the x_2- and x_3- directions, plane mirrors were placed in the x_1,x_2 and x_1,x_3 planes to reflect part of the beam onto the object surface. In this manner, the object can be illuminated from equal angles to the observation direction. The fringes are, however, recorded using one illuminated at a time, making the technique basically sequential.

The significance of measuring in-plane and out-of-plane components simultaneously has also been mentioned by Maji and Shah(1990) in their study on mixed-mode crack profiles. They, however, used holographic method with four illuminations and vectorially evaluated the unknown displacement components.

In many of the applications of the ESPI method described in Section 2.3.3.5, the in-plane and out-of-plane measurements were made separately. This could be due to the practical difficulties associated with measuring the various components simultaneously, mainly due to the different optical configurations of the in-plane and out-of-plane sensitive interferometers. Another reason is attributed to the wide application of ESPI in the analysis of vibrations. Since the vibrations are mostly steady-state, the various components can be measured sequentially by modifying the illumination geometry.

2.3.3.3 Analysis of ESPI fringes

One advantage of ESPI is that the interferograms, which exist as video signals, are easily amenable to automated analysis. Automated fringe analysis is, however, is a specialised area of study and is well documented (e.g. Chen and Taylor 1989, Kerr and Tyrer 1988, Kerr et.al. 1989). In this survey, we review some of the recent papers on the phase-stepping method of analysis. A brief theory of this method is given in Appendix A1.

An important development in the automated fringe analysis is the implementation of the phase-stepping method developed for holographic interferometry by Hariharan(1983). By introducing discrete shifts in the position of the fringes, this technique makes direct phase measurement possible. The phase of one of the beams, usually the reference beam, is shifted in several steps with respect to the other and the resulting interferograms are recorded for analysis. A phase map that can provide phase information at each point on the object surface is then calculated from the stored data. Creath(1985) presented the theory for this technique together with some experimental results. The application of this method to determine the disbonded area in a honeycomb structure brazed to aluminium plate is discussed.

In the usual implementation of the phase-stepping method, the phase of the reference beam is shifted in three stages of $2\pi/3$ each (Creath 1985). In some cases, four stages have been reported to be less sensitive to step errors (Hariharan 1983). Kerr, Mendoza Santoyo and Tyrer(1990) presented the single step method that has certain advantages over those that use more phase steps. This method increases the speed of analysis and is not greatly affected by environmental drift errors. Since only two phase shifted interferometric fringes are required, the host computer image memory needed for data storage is reduced by a factor of 3.

2.3.3.4 Applications

As in holographic interferometry, the ESPI method has been used in a wide range of applications. In this review, we consider some of these applications which are considered relevant to the present work.

Authors at Norwegian Institute of Technology used the ESPI method for several applications (O.J.Lokberg 1986). Their most common application is in the area of vibration analysis in which collaborative work with industry has been carried out. In these applications, pulse lasers were used to obtain the vibration in slow motion or to freeze them.

ESPI has also been used to study objects heated to very high temperatures. Malmo et.al.(1988) used this technique to monitor and

measure the surface behaviour of objects heated up to 3000°C. The possibility of analysing phase transition in materials is investigated. The problems of working at such high temperatures were reported to be due to the change in stability of the microstructure of the object, turbulence due to air currents and background radiation. The volume change that occurs due to transitions in material structure was reported to introduce anomalies in the fringe formation at certain temperatures. This was approximately equal to the temperature of phase transition for the iron samples used in their experiments. Although no quantitative information was extracted from the fringes, qualitative studies alone were found to provide valuable information.

Winther(1988) used ESPI for measuring 3-D strains in a pipe clamp. He adopted a set-up similar to a multiple illumination holographic arrangement. The object was illuminated from different directions using optical fibres. Although optical fibres gives the system a great degree of flexibility but this was at the expense of the available light. The optics were arranged so that the object wave and the reference wave were in-line. The video signal from the camera was digitised directly into a computer fitted with image processing facilities for analysis. A two beam contouring method was used to determine the shape of the object surface. In this technique, only one object illumination is used and between two successive exposures, the fibre end is given a small translation in the range of 0.1mm to 0.5mm. Each of the two exposures are stored and later subtracted, giving projected contouring fringes.

The use of ESPI in the design of loudspeaker chassis and cabinet was described by Tyrer(1989). In these applications the size of the components and its coating was reported to affect the laser power required. A 300mm diameter could be inspected by using a 10mW laser for the time-averaged analysis; larger areas requiring more laser power.

In a three dimensional vibration analysis, Shellabear and Tyrer(1989) used the ESPI method to measure three dimensional amplitude of single frequency harmonic vibrations. The steady state condition of the vibration made it possible to rearrange the illumination geometry so that the out-of-plane and the two in-plane components (horizontal and vertical) of displacement can be measured

sequentially. The object was mounted conveniently so that it could be rotated through 90° after measuring one in-plane component. In this manner, the two in-plane components can be measured without disturbing the illumination geometry or using additional optics. However, rotating the object is not always feasible in a practical situation.

A study on the thermal behaviour of dissimilar materials in a piston using ESPI was reported by Aswendt et.al.(1990). A marine diesel engine piston cast from aluminium-base alloy and fitted with a burning chamber made of heat-resistant ceramics was used in their study. In their optical arrangement, dual beam illumination was used to achieve in-plane sensitivity. A rough surfaced reference plate and an additional mirror were then inserted rapidly to obtain out-of-plane sensitivity. In this manner, the in-plane and out-of-plane components were measured sequentially with minimum time delay in between. The piston was heated using a 800W heating element mounted inside the piston. The fringes were observed while the piston was cooled from 590K. Their results showed that at above 500K, the aluminium body and the ceramic ring expands freely without interaction. The technique of mounting the piston and the effects of expansion of the piston support (which will introduce rigid body movement) are, however, not discussed in their paper.

2.4 Other comparison work

Comparative studies using experimental and analytical techniques on various engineering components have been carried out by a large number of authors (e.g. Yoon and Hong 1990, O'Toole and Santare 1990, Miniatt et.al. 1990). For simple homogeneous components, good correlation between experimental and theoretical results were reported in most cases. In this section of the literature survey, we consider some of these papers with emphasis on the use of other whole-field methods and the comparison with finite element analysis.

In an effort to develop a flaw detection system using computer vision, Peters et.al.(1989) analysed the displacement of a composite cylinder subjected to hydraulic pressure. In their system, the object was spray painted with 'white-light speckle' pattern. A camera was used to record this pattern as varying levels of gray. By comparing the patterns from the displaced and undisplaced object it was possible to determine the displacements. For comparison with theoretical calculations, the displacement fields for the surface of an unflawed and homogeneous cylinder were analysed. Comparison of radial displacement showed good correlation between experimental and theoretical results. A larger discrepancy was noted in the axial direction and this was attributed to rigid body translation. For the composite cylinder, however, no comparison with the theoretical results were given due to the unknown engineering properties of the composite material.

A study on the combined use of laser-speckle and finite elements method of stress analysis was described by Weathers et.al. (1985). The displacement data from the speckle technique was directly inputted to a finite element computer program for the determination of stresses. The displacement data was used as boundary conditions for the examination of subregion of structural components to be analysed. The calculated stress distributions for the combined laser-speckle/finite element method for a plate containing a circular hole was found to agree closely with the theoretical results. A substantial reduction in computational effort when compared with the conventional finite element analysis over the entire structure was reported. This approach, however, may not be readily applicable in situations involving components made up of composite materials which

are subjected to thermal loads. This is due to the difficulties in evaluating the deformation or stresses accurately using theoretical methods (Hsu and Lewak 1976).

Krishnakumar and Foster(1989) developed an optical method using photoreflective moire' method to measure the radial deformation of a cylindrical shell. In this method a conical mirror situated at the bottom of the vertical shell provided a complete view of the inner surface which was imaged into a camera using a 45° plane mirror at the top. Axial and circumferential grids were used to obtain sensitivity changes in slope along the two directions. Good agreement between theoretical and experimental results were reported.

2.5 Conclusions

The literature survey carried out shows that the two whole-field methods, holographic interferometry and ESPI, are gaining increasing importance as accurate measurement tools in the engineering field. Although more emphasis is now given to the ESPI method due to the ease of obtaining and analysing fringes, some of the inherent advantages of the holographic technique makes it useful in certain specific applications. As a result of the improvement in the fringe analysis methods, the two techniques of measurement have been successfully employed in industrial applications.

In spite of the vast amount of documented work on the application of the two techniques, their benefits have not been fully exploited and used in the design and analysis of bimetallic pistons. The abilities of the two techniques in providing the true deformation behaviour of thermally loaded composite structures, that cannot be modelled accurately using analytical methods, have not been fully explored and applied in this area of engineering. One reason could be due to the experimental difficulties associated with measuring the thermal expansion of the skirt in the presence of unknown rigid body movement and the problems associated with the finite element analysis of the complex structure of the piston. Another reason is possibly due to the lack of expertise among the piston manufacturers in the application of such measurement techniques.

CHAPTER 3

FINITE ELEMENTS MODELLING

3.1 The open sleeve 'isoformic' piston

The open sleeve 'isoformic' piston was introduced by AE Piston Products Limited (formerly known as Wellworthy Limited)(Rhodes 1978). In this type of piston, effective control over the expansion of the skirt is achieved by casting an approximately oval steel sleeve inside the piston during manufacture. The steel sleeve extends from the oil ring groove over approximately half the length of the skirt depth (Figure 3.1 (sleeve is shown shaded)). The sleeve is exposed in the groove in order to lower the expansion at the top of the skirt and it is shaped in such a way as to limit the arc over which it is exposed (Figure 3.2). The reinforcement provided by the steel sleeve allows a thinner skirt to be specified than in a monometal piston. This enables the sleeve to exert maximum control over the expansion of the skirt. In addition, the piston is lighter that other types of controlled expansion and monometal pistons.

In the design of certain types of pistons, including the open sleeve pistons, the skirt thrust areas are physically separated from the crown. This results in increased local flexibility and reduces skirt temperatures by creating a thermal barrier, with the effect that expansion is more positively controlled. In a monometal piston the separation is achieved by machining transverse slots whose geometry and location determine the extent of the resulting skirt flexibility. In the open sleeve piston, however, the separation is brought about by a natural mechanism arising from differential thermal contraction. During cooling after casting the insert contracts less than the piston alloy and therefore stretches the outer layer and separates the inner layer around the bottom edge of the crown (Figure 3.3). The separation process is technically completed by cutting the oil ring groove. As a result axial air gaps are formed over the full depth of the insert. The maximum width of the gap (at 90° to the gudgeon pin axis) typically varies from about 0.100mm to 0.150mm. The gap gradually closes along the circumference towards the pin axis (Figure 3.4).

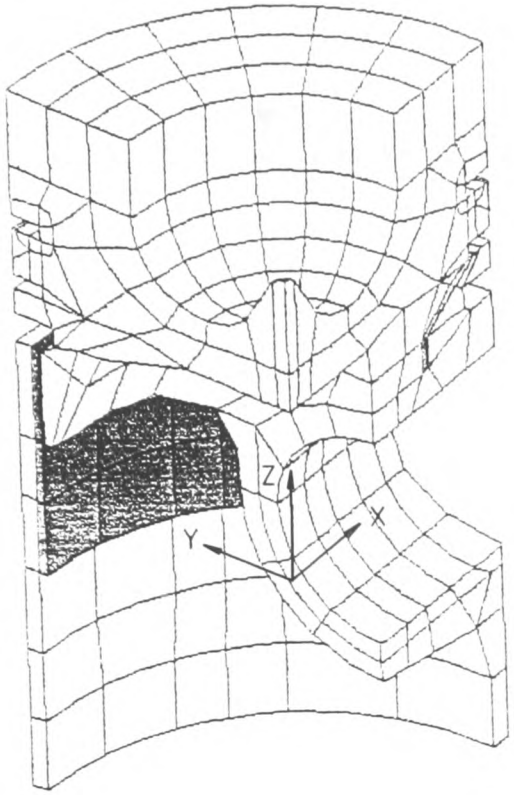

Figure 3.1. Original mesh generated in the current work (Mesh 1) (hidden details not shown)

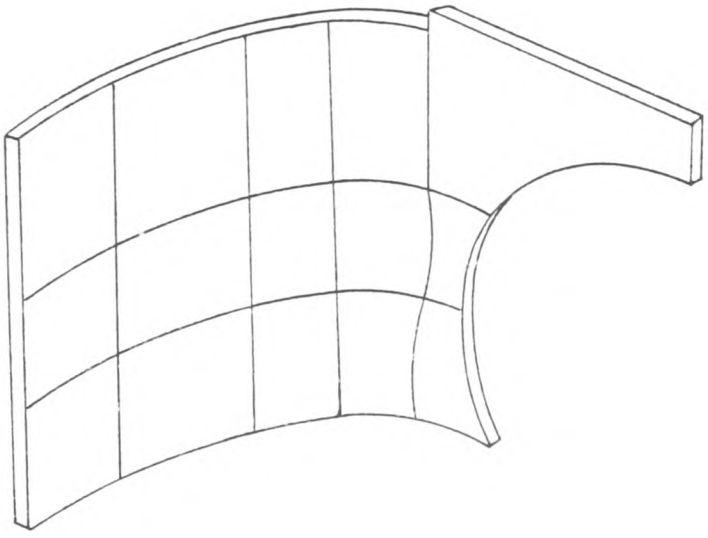

Figure 3.2. View of a quadrant of the steel insert

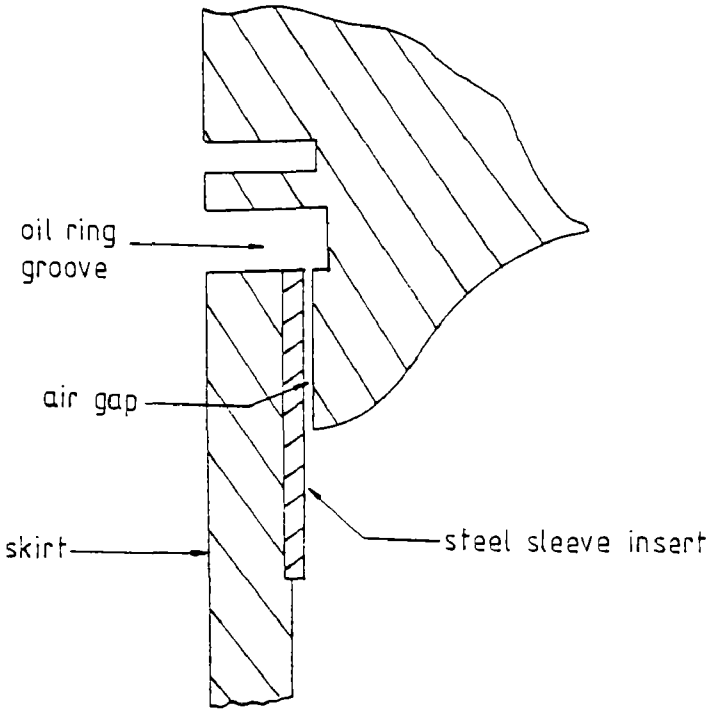

Figure 3.3. Section of piston showing position of axial air gap

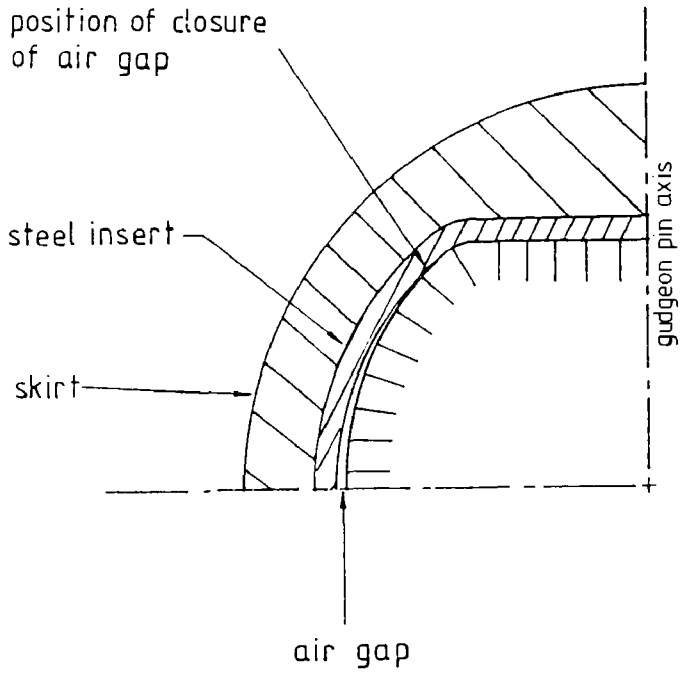

Figure 3.4. Section of piston showing approximate position of closure of air gap

3.2 Generation of the finite element mesh

The finite element mesh was generated by using PIGS (PAFEC Interactive Graphics System) program and was analysed by using the PAFEC software package. This software was selected so that the generated mesh could be transferred into the computers used by the manufacturer for checking purposes. Due to the limited flexibility of the PIGS program it was necessary the construct the entire mesh on a section by section basis. The completed mesh consisted of approximately 350 three dimensional elements and 3000 nodes. The elements were made up of twenty-noded isoparametric brick elements and fifteen-noded triangular prism elements.

The mesh was generated based on drawings and consultation provided by the manufacturer. The original mesh (Mesh 1) generated is shown in Figure 3.1. This mesh is basically same as the one created by the manufacturer and used in previous comparison work (Evans and Russell 1983). A wireframe drawing of the mesh is shown in Figure 3.5, indicating the complexity involved. The mesh was subsequently modified to investigate the effects of inclusion of a rib at the bottom of the skirt (Mesh 2)(Figure 3.6). The mesh was then further adjusted to approximate the true dimensions at the bottom of the skirt (Mesh 3)(Figure 3.7). The original mesh thus contained certain simplifications which were thought not to have significant effect on the expansion of the skirt. For the purpose of comparison of experimental results with theoretical predictions, however, it was necessary to create the model as accurately as possible. Nevertheless, the final model contained the following assumptions :
a) the axial air gap was assumed to close at 40° to the pin axis and
b) the outer surface of the steel sleeve and the inner surface of the aluminium alloy skirt were assumed to be bonded. This was represented by common nodes between the skirt-sleeve interface.

The first assumption was necessary because it is not possible to measure the exact position at which the air gap closes, i.e. the position at which the insert and the inner mantle below the crown regain contact. This uncertainty is due to the complex geometry of the piston (in the region of the air gap) resulting from the separation of the insert from the piston body. Hence, the position of the closure of the air gap is an unknown in the model. The effect of

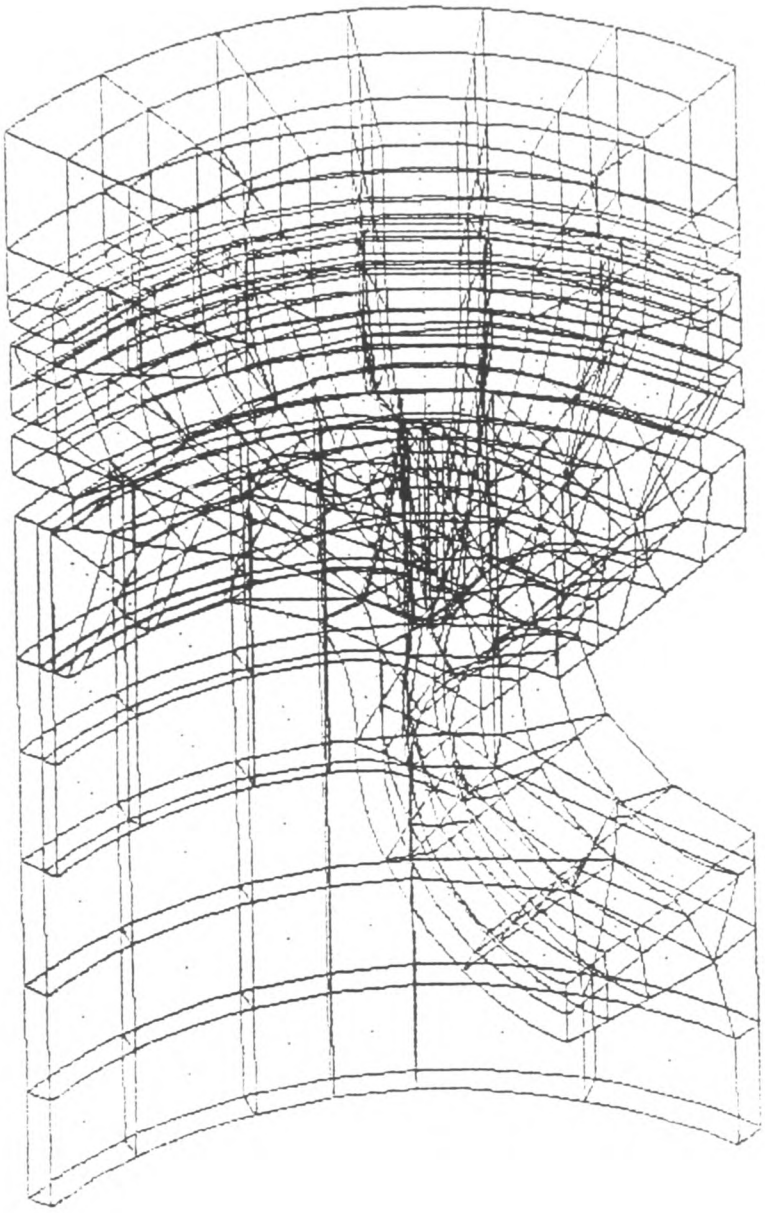

Figure 3.5. Wireframe drawing of the mesh

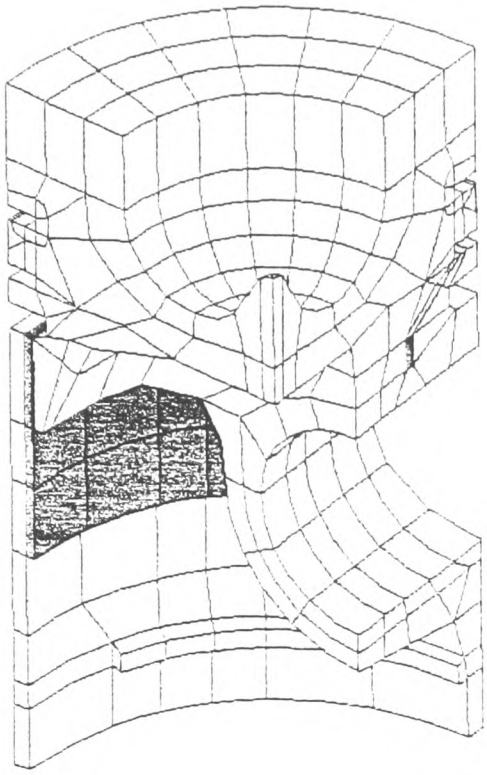

Figure 3.6. Mesh modified to include rib (Mesh 2)

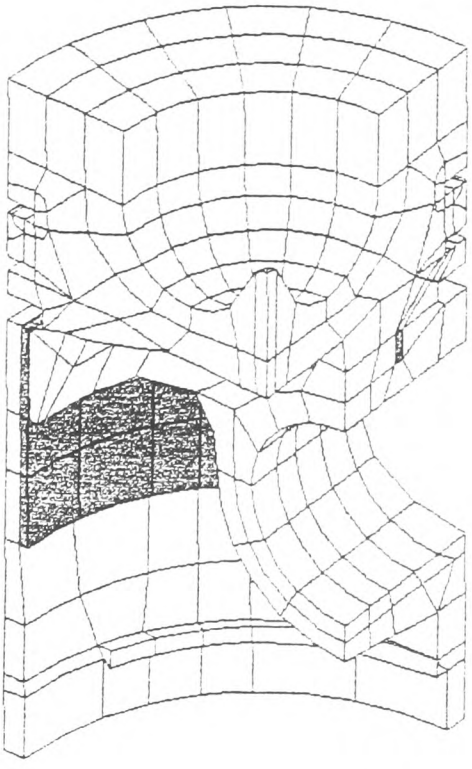

Figure 3.7. Mesh modified to approximate true dimensions at bottom of skirt (Mesh 3)

this assumption on the predicted profile has, however, been investigated and is discussed in Section 3.6.

The second assumption was made due to the unknown residual stresses that exist between the insert and the piston body as a result of the differential contraction of the two materials. Although these stresses can be modelled by assuming a 'stress free' condition at which they are relieved, the stresses present at room temperature will depend on the initial clearance specified between the insert and the piston. Due to the complex geometry of the piston and the insert, however, it will not be practical to determine this clearance accurately and therefore it may not be possible to model the residual stresses accurately. In addition, since the outer surface of the insert and the inner surface of the skirt are in contact, full thermal coupling between the two surfaces were assumed in the finite element model.

3.3 The analyses

3.3.1 Thermal analyses

Two types of thermal analyses were considered: steady-state and transient. In the steady state analysis appropriate boundary conditions were specified in a HEAT.TRANSFER module. Two separate thermal runs were carried out in order to reproduce the temperature rises measured at the twelve thermocouple points whose locations are summarised in Table 3.1. The first thermal run was for the lower temperature and the second was for the upper temperature. The temperature rises at the nodes at which the thermocouples were located were determined by subtracting the two. It was sufficient to consider only the temperature rises because the deformation due to a rise in datum temperature of 10°C or 20°C is of interest and not that at an absolute temperature. The absolute predicted temperature were, nevertheless, within 2°C of the absolute measured temperatures at the thermocouple points located at the skirt. The boundary conditions in the model were specified based on temperatures of air measured around the piston. Since these temperatures are only approximate, it was necessary to adjust the boundary conditions and to repeat the thermal

Thermocouple	Theta (degree)	Height above pin axis (mm)	Radius (mm)
T1	45	(bottom of bowl)	
T2	0	69.7	49.2
T3	90	41.1	49.2
T4	0	27.2	49.2
T5	90	27.2	49.2
T6	0	-50.8	49.2
T7	90	-50.8	49.2
T8	90	(see inset A)	
T9	0	(see inset B)	
T10	270	(see inset A)	
T11	(centre of underside of crown)		
T12	50	0	49.2

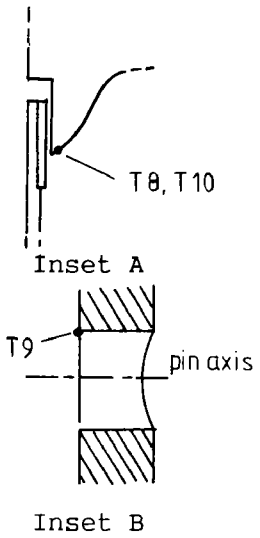

Table 3.1. Locations of thermocouples

Thermocouple	Measured rise (°C)	Predicted rise (°C)	Difference (°C)
T1	16.1	21.0	4.9
T2	21.9	20.2	-1.7
T3	20.1	20.4	0.3
T4	19.1	18.3	-0.8
T5	17.2	16.0	-1.2
T6	16.3	14.3	-2.0
T7	15.8	14.8	-1.0
T8	19.1	19.4	0.3
T9	19.2	18.7	-0.5
T11	20.0	20.9	0.9
T12	15.2	15.9	0.7

Table 3.2. Predicted and measured temperature rises for a datum temperature rise of 20°C for Mesh 1 (measured at T11)

Thermocouple	Measured rise (°C)	Predicted rise (°C)	Difference (°C)
T1	16.1	21.8	5.7
T2	21.9	21.9	0.0
T3	20.2	20.2	0.1
T4	19.1	17.9	-1.2
T5	17.2	13.9	-3.3
T6	16.3	14.4	-1.9
T7	15.8	14.0	-1.8
T8	19.1	18.8	-0.3
T9	19.2	18.8	-0.4
T10	20.0	21.7	1.7
T12	15.2	15.5	0.3

Table 3.3. Predicted and measured temperature rises for transient analysis

runs several times in order to obtain predicted temperature rises that matched as closely as possible with the measured rises, with each run taking approximately 30 minutes. The heat transfer coefficient was assumed to be 0.000409 W/mm^2 K all around the piston. Although this value actually depends on the surface temperature, this assumption will not affect the results because the combined effect of the specified temperature at the boundaries and the heat transfer coefficient H is to reproduce the temperatures at the measured points. The individual values of temperature and H are thus not critical. Typical set of values of the predicted and measured temperatures for a 20°C rise on the original mesh (Mesh 1) are shown in Table 3.2. The maximum difference is at the crown, close to the heating coil. This difference is not expected to influence the expansion at the skirt where the temperatures were made to match more closely (within 1.0°C at most of the points).

In the transient analysis, variable boundary conditions were specified and the predicted temperatures were outputted for every 50s of the analysis time over a period of 500s. The sets of temperature distribution which approximated the measured temperatures were selected and subtracted to determine the temperature rises. Although this type of analysis provides a closer approximation to the true situation encountered during the experiments, the analysis is tedious. The computing time taken for one set of thermal analysis was about 5 to 6 hours. Since a single transient thermal run would not necessarily produce the desired temperature rises, the analysis has to be repeated several times. This imposed practical limitations to the study due to time constraints. In addition, since in a steady state analysis the boundary conditions were specified in order to obtain a steady state temperature distribution that approximates the measured temperature distribution in the piston, the temperatures can be considered to be 'locked-in'. Thus, the boundary conditions need not vary with time in order to predict a temperature distribution that matches the measured distribution. Nevertheless, a comparison of the deformation obtained by using steady state and transient analyses has been made and is discussed in Section 3.4.

3.3.2 Stress analyses

For the purpose of the stress analysis, it was necessary to apply restraints at certain nodes to prevent them from moving in certain directions. Since the analysis was carried out on only a quadrant of the piston, restraints in the x-direction was applied at all the nodes along the face parallel to the y-z plane (Figure 3.1). Similarly, restraints in the y-direction was applied at all the nodes along the face parallel to the x-z plane. Restraints in the vertical direction (z) was applied at the point where the piston was supported. Since the mesh was originally created using thermal elements (which have only one degree of freedom at each nodes), it was not possible to create a RESTRAINT module for the stress analysis automatically. This was overcome by creating two RESTRAINT modules using thermal elements and altering the degrees of freedom appropriately. The files containing only the restrained nodes were merged with the original data file used for the stress analysis.

The properties of the material were specified in a MATERIAL module. The following values were required : Young's modulus, Poisson's ratio, density, coefficient of thermal expansion, thermal conductivity and specific heat. The values of these variables were supplied by the piston manufacturer.

As in the thermal analysis, two different stress analyses were necessary: one for the lower temperature and one for the upper. The deformation due to a rise between these temperatures were obtained by subtracting the absolute deformation at the two temperatures.

3.4 Comparison of transient and steady state analyses

The results of the steady state and transient analyses are shown in Figure 3.8. The measured and predicted temperatures for the transient analysis are shown in Table 3.3. The expansion along the length of the skirt at θ=50° for the two temperature conditions agreed to within 5%. The expansion along θ=90° shows a close agreement at the bottom of the skirt but a difference of 9% at 10mm above the pin axis. This difference can be attributed to a smaller predicted rise at this part of the skirt (T5 in Table 3.3). Thus if

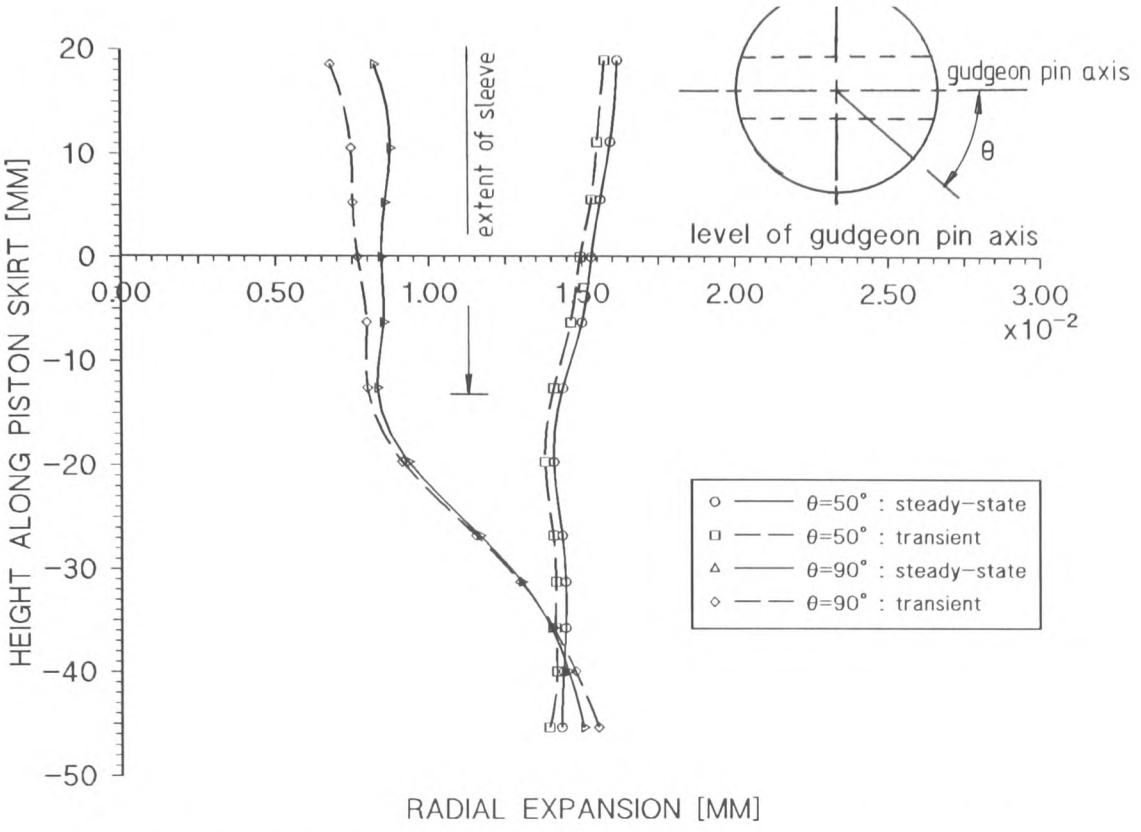

Figure 3.8. Comparison of steady-state and transient analysis for rise from 50°C to 70°C

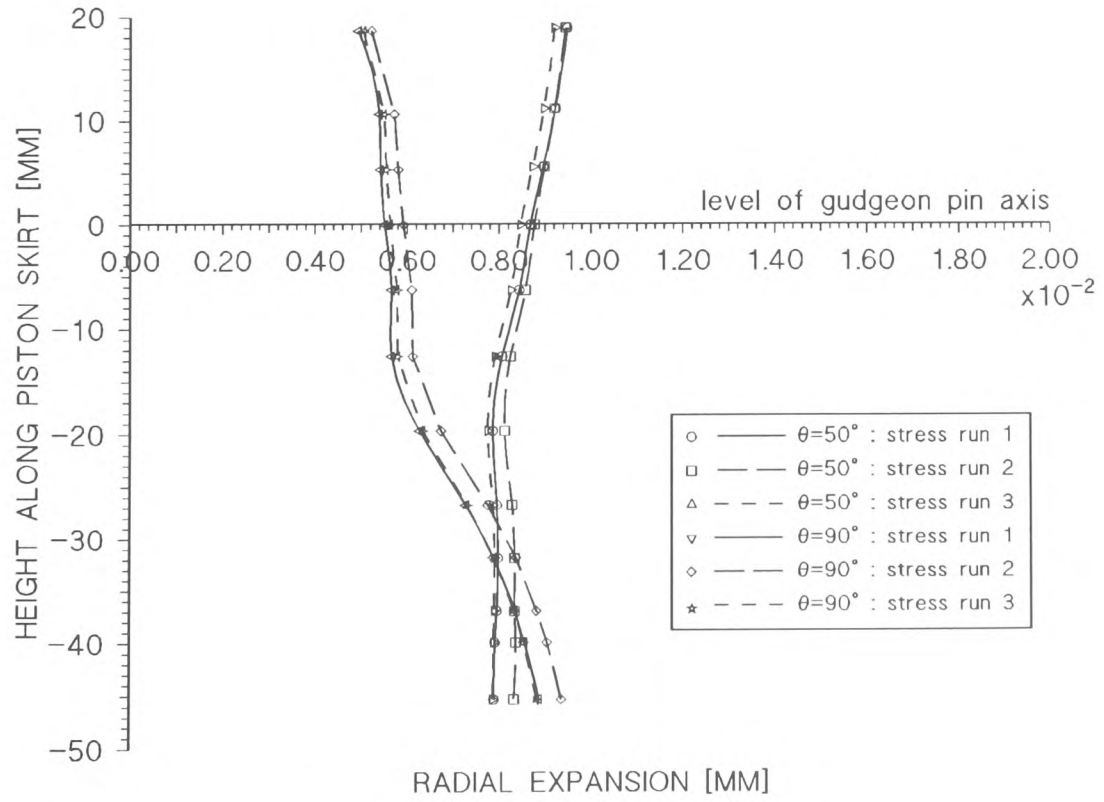

Figure 3.9. Effect of fluctuation in predicted temperatures on expansion profile (50°C to 60°C)

the boundary conditions are specified so that the transient analysis produces predicted temperature that agree closely with the measured values, it can be shown that the two types of analyses are capable of producing the same results.

3.5 Effects of fluctuations in predicted temperatures

The effects of fluctuation in predicted temperatures were investigated by changing the boundary conditions slightly so as to obtain predicted temperature rises that were within 0.6°C of the measured rises at the thermocouples located around the skirt. The analysis was repeated for three such cases and the results are shown in Figure 3.9. The predicted displacement deviates by about 9% at the top of the skirt and decreases to about 5% at the bottom of the skirt (measured at 90° to the pin axis). Due to such fluctuations, accurate comparisons between holographic and finite elements results can only be made after several repetitions of both holographic measurements and the finite element analysis and a statistical treatment of the data. This, however, has not been considered here due to time constraints. The results obtained for the purpose of the comparative study are, nevertheless, sufficient to enable one to appreciate how the steel insert affects the expansion profile of the piston and to study the effects of the assumptions made in the generation of the model.

3.6 Significance of position of closure of air gap

As mentioned earlier, the position of closure of the axial air gap was initially assumed at β=40° to the pin axis. The effect of this assumption on the expansion of the skirt was investigated by changing the position at which the air gap closes to β=50° and β=60° and repeating the analysis. The boundary conditions were altered so as to obtain predicted temperature rises that agreed closely to the rises measured during the experiments (see Chapter 6). The results are shown in Figure 3.10. The expansion at θ=90° increases by about

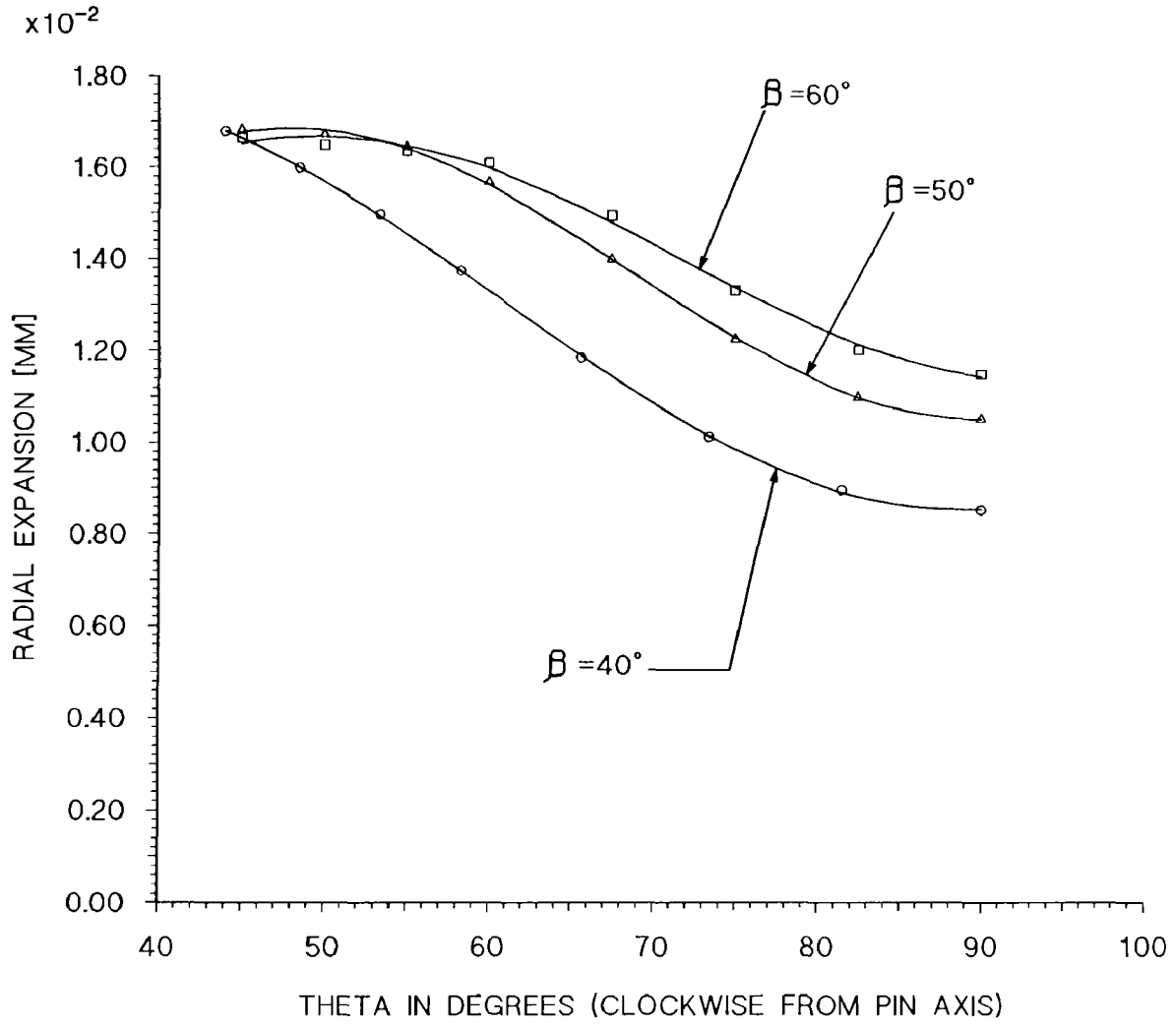

Figure 3.10. Radial expansion at 10.6mm above pin axis showing effect of change in position of closure of air gap (50°C to 70°C)

20% when the position of start of the gap was shifted to β=60°. This is due to the greater expansion of the inner aluminium mantle (below the piston crown) when compared to the steel sleeve hence pushing out the sleeve. The expansion along θ=50° is, however, not affected significantly. Therefore the only way of establishing the approximate position at which the air gap closes is to compare the predicted and measured profiles. This will enable one to improve the accuracy of the model (see Chapter 7).

CHAPTER 4

DEVELOPMENT OF A SIMPLIFIED HOLOGRAPHIC METHOD FOR SIMULTANEOUS MEASUREMENT OF X,Y,Z COMPONENTS OF DISPLACEMENT

4.1. Introduction

A technique for measuring all three Cartesian components of displacement simultaneously of a thermally deforming piston has been previously developed by Evans and Russell(1983). Their technique consists of using three holographic plates and three cine-cameras for recording the movement of live fringes from three observation positions. Photographs of initial and final fringe patterns were obtained from the live recording and these were digitised manually using a digitising tablet into a computer for analysis. They developed a program to transform the digitised data, which exist in two-dimensional coordinate system, into the three dimensional global coordinates used on the optical bench. Knowing the position of the fringes centres on the piston, it was then possible to determine the order numbers at superimposed mesh points by an interpolation technique using finite elements. The displacement could therefore be determined from knowledge of the order numbers and the illumination-observation geometry.

Evans, Russell and White(1987) later used this technique to measure the thermal deformation of a cylinder. In their paper, the part of the program that transforms the digitised points from the photograph and back to the original object surface and the part that calculates the displacements were verified by working on a 100mm diameter thin circular plate. The plate was rigidly clamped at its circumference and a displacement of 0.0038mm was applied at its centre. The fringes were obtained by doubly exposing the plate before and after applying the load. Their results showed that the maximum error in transforming the digitised points back to the surface of the plate was about 0.2 of a fringe spacing, which was considered acceptable. The displacement values evaluated showed good agreement with the theoretical predictions. They proceeded to use this technique to measure the thermal deformation of a cylinder. Three 4in.x 5in. holograms were used and the live fringes were recorded simultaneously using three cine-cameras. The reason for recording the movement of live fringes continuously was due to the absence of a zero-order fringe. The order numbers of the fringes were determined by replaying the fringe formation and counting the number of fringes crossing a reference point.

Although the set-up developed to date provides a means of measuring the x, y and z components of displacement simultaneously, the experimental set-up is complex and technique is tedious. The main reasons are due to the need to record three separate holograms simultaneously and to register the fringe formation from all the observation points simultaneously. The laser beam must be split into three reference beams and one object beam and this results in poor illumination of the piston, thus affecting the quality of the hologram and the contrast of the fringes. In addition, the three separate cine-cameras required to record the movement of live fringes makes the arrangement less cost-effective.

One simple technique of avoiding the use of three separate holograms is to record a single hologram and view the object through different parts of the same holographic plate (Vest 1976). This, however, will result in small angles between the various observation vectors thus leading to a poorly conditioned geometrical matrix, A, in the interferometry equation,

$$A.D = N.\lambda \qquad \ldots.4.1$$

where,

D = unknown displacement vector

N = fringe order number

λ = wavelength of laser.

In such cases, small errors in order numbers will be amplified and will lead to inaccurate values of displacement. However, the problem associated with poorly conditioned system can be overcome by using redundant data (Dhir and Sikora 1972). In this method a minimum of four observations are used and the overdetermined system of simultaneous equations are solved by the least squares method, hence, improving the accuracy of the results.

For cases involving continuous deformation where a zero order fringe is not present, it is necessary to record the movement of live fringes continuously from all the observation points. When four observations are used, however, four cine-cameras are required. This adds cost and complexity to the experimental design and a simplification of the arrangement would be beneficial. One method of achieving this is to position four small mirrors behind the

holographic plate and incline them in a manner so that all four images of the piston are visible from the view point of a single camera. The images will, however, appear too small on the recording and this may impose an upper limit to the density of the fringes and the displacement measured. In addition, since it is more practical to use video cameras instead of 35mm cine-camera, the quality of the images are sacrificed further. This may create difficulties in fringe tracking especially if the four interferograms are to be digitised simultaneously into a computer for subsequent analyses. One way of solving this problem is to photograph the live fringes from the four views using a high speed film in a plate camera. The movement of the fringes can be recorded by re-reflecting the four images by using a beam splitter in the view path of the plate camera. Such a technique has been devised here for measuring the deformation of the piston. In order to transform the digitised fringe centres from the photographs and back to the surface of the piston, a computer program based on a series of geometrical transformation was developed. An important feature of this program is the possibility of operating on fringes on an image of the piston which is inclined in an arbitrary position in space. This position is determined by the plane of inclination of the mirror. An accurate method of measuring the position of the mirrors has also been considered. The accuracy of the transformation was checked by transforming grid points on a high quality graph paper superimposed around a cylinder (see Section 4.4). The accuracy of the proposed technique was verified by measuring the deformation of a heated uniform cylinder and comparing the results with the predictions of a finite element model. Attempts were also made to extend the rig to include measurement at the rear surface of the piston.

4.2 Design of the holographic rig

A schematic layout and a photograph of the holographic arrangement are shown in Figures 4.1 and 4.2. The beam from a 50mW laser was split into object and reference beams. The object beam was initially used to illuminate the front surface of the piston alone. The reference beam was expanded at a sufficient distance from the 8in.x 10in. holographic plate so that the expanded beam covered the plate approximately uniformly. Four mirrors (of dimensions 4in.x 5in.) were rigidly mounted behind the holographic plate on a specially designed frame that allows the mirrors to be inclined in any arbitrary plane (Figure 4.3). The mirrors were inclined in a manner so that four views of the piston could be imaged onto a single photographic film. A 4in.x 5in. plate camera was used to photograph the fringes.

For the analysis of the interferograms the absolute position of the fringes on the piston surface must be determined from the photographs. Since the images on the photographs have perspective distortions and lateral inversions, a transformation routine is necessary to achieve this purpose. Such a routine has been developed and is described in Section 4.3.1. An important factor affecting the accuracy of the transformation is the accuracy of measurement of the mirror positions. In the technique employed, a laser beam was projected onto the front surface of the mirror and the coordinates of three points on the beam (one on the incident ray, one on the reflected ray and the other at the point where the beam meets the mirror surface) were measured. A program that makes use of these three points to determine the equation of the mirror surface and thus to evaluate the image coordinates of a given point has been developed. The operation of this program is described in Section 4.3.3.

The formation of live fringes were recorded on a video tape by positioning a 4in.x 5in. beam splitter in the view path of the plate camera and re-reflecting the four images onto a video camera. Correct alignment between the two cameras was achieved by using a laser beam (see Section 4.5).

In this arrangement although the angular spacing of the various mirrors (measured with respect to an object surface point) is small

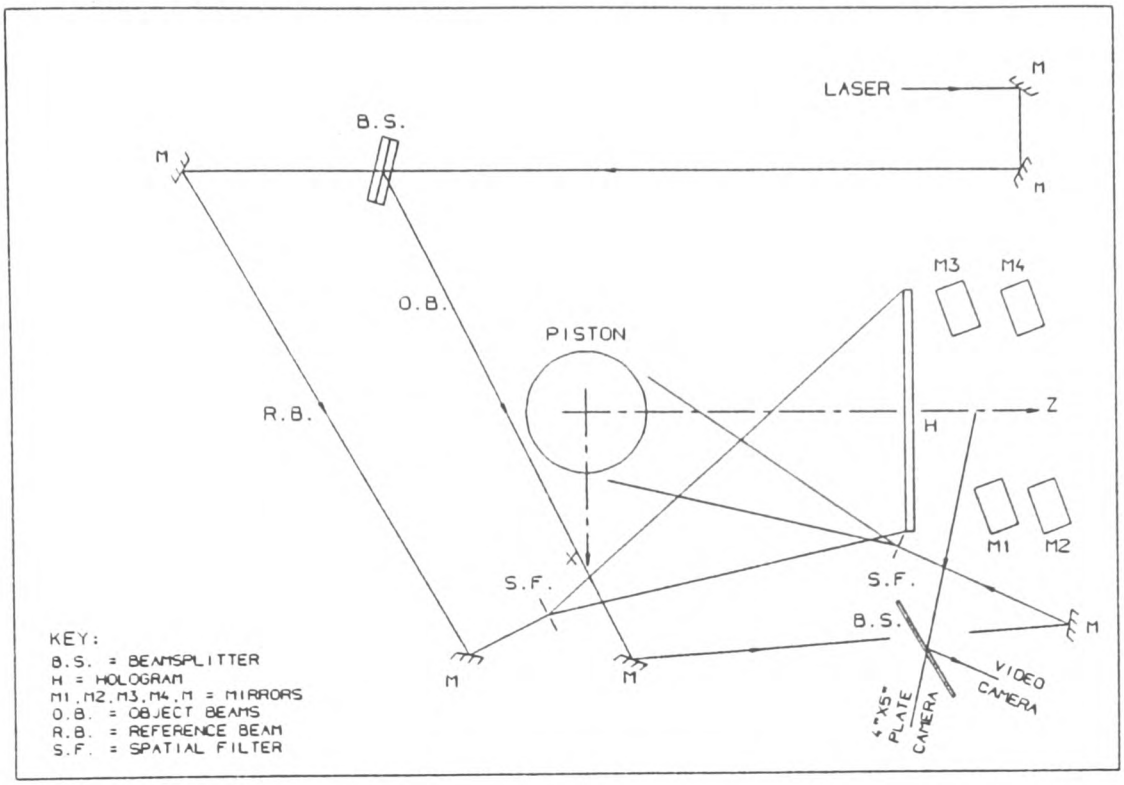

Figure 4.1. Schematic layout of the 4-mirror method

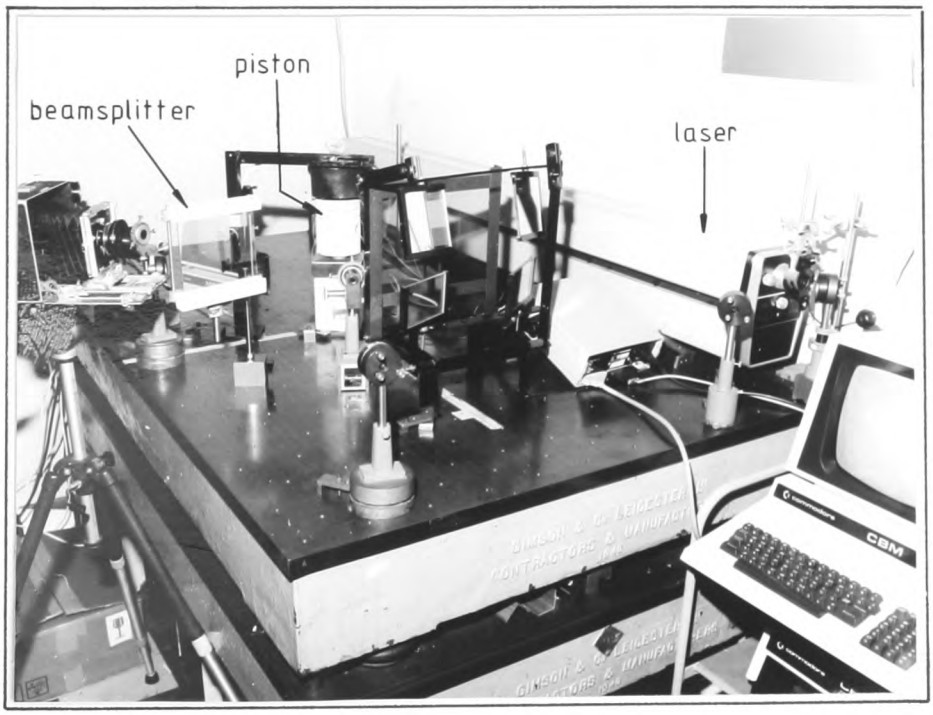

Figure 4.2. Photograph of the experimental set-up

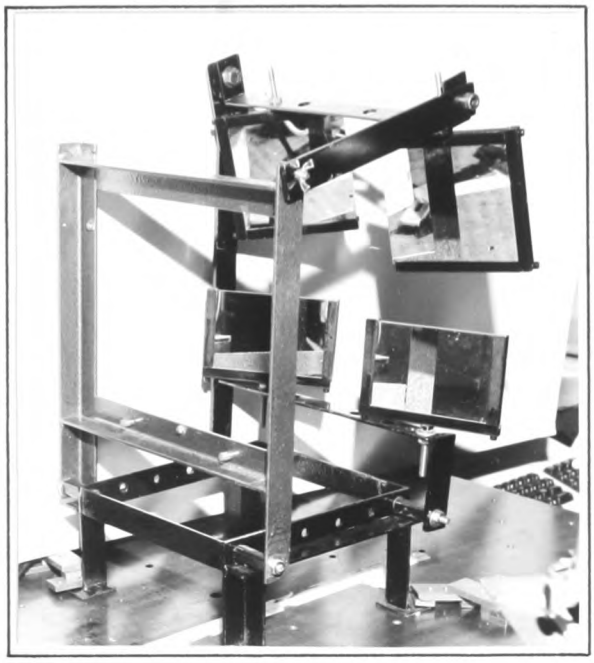

Figure 4.3. Mirror and holographic plate holder

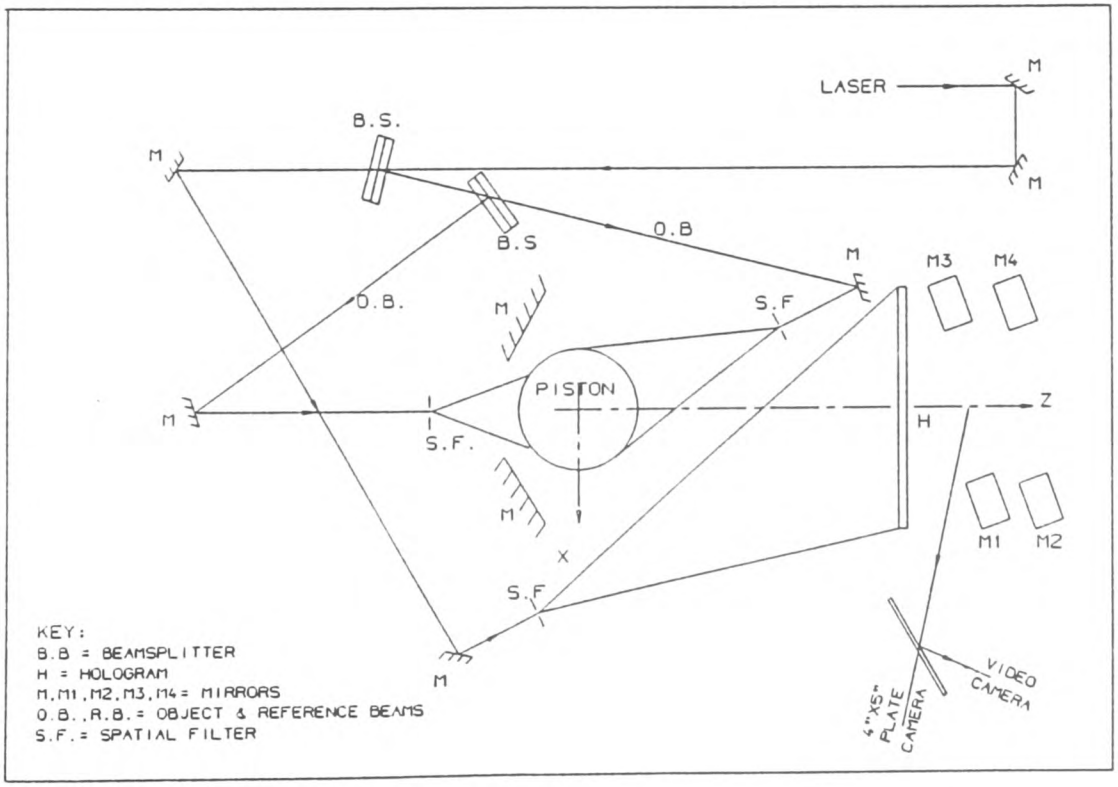

Figure 4.4. Extended rig to measure expansion at rear surface

(approximately 15°) and may lead to a poorly conditioned geometrical matrix, this setback was overcome by the use of redundant information. A least squares technique of solving the four equations was implemented by incorporating a NAG Fortran Library routine in a computer program. A listing of this program (named SOLVE1.FOR) is given in Appendix A2.

For the purpose of comparison of the measured results with finite elements, Evans and Premier(1989) showed that measurement of expansion on one surface alone is not sufficient. This was because of the different expansions undergone by the front and rear surfaces. Measurement at diametrically opposite points or sectors must therefore be made so that the mean expansion (which is free from body displacement) can be used for the comparison. This was also due to the assumption in model that the piston is symmetrical in construction and the heat input is central (Chapter 3). The current arrangement was therefore extended by using mirrors at the rear surface of the piston as shown in Figure 4.4. Four additional images of the rear view were imaged together with the front view, resulting in a total of eight images on the recording. Due to physical constraints, only a sector of about 25° of the rear surface was visible. However, the extended arrangement has several practical limitations and these are discussed in Section 4.6.

4.3 Geometrical transformation

4.3.1 Development of program CAMERA1.FOR

The program CAMERA1.FOR developed for transforming the digitised fringe centres from the photograph and back to the piston surface for the new arrangement is based on the concept of program CAMERA.FOR developed by Evans and Russell(1983). CAMERA.FOR transforms the 2-D coordinates of the digitised data into 3-D coordinates with reference to the optical bench axes by using a few selected datum points. In this program, the optical bench axes were initially rotated in such a manner so that the z-axis is in-line with the line of sight of the observer located at the camera nodal point N (Figure 4.5). The y-axis was maintained vertical when viewed from N.

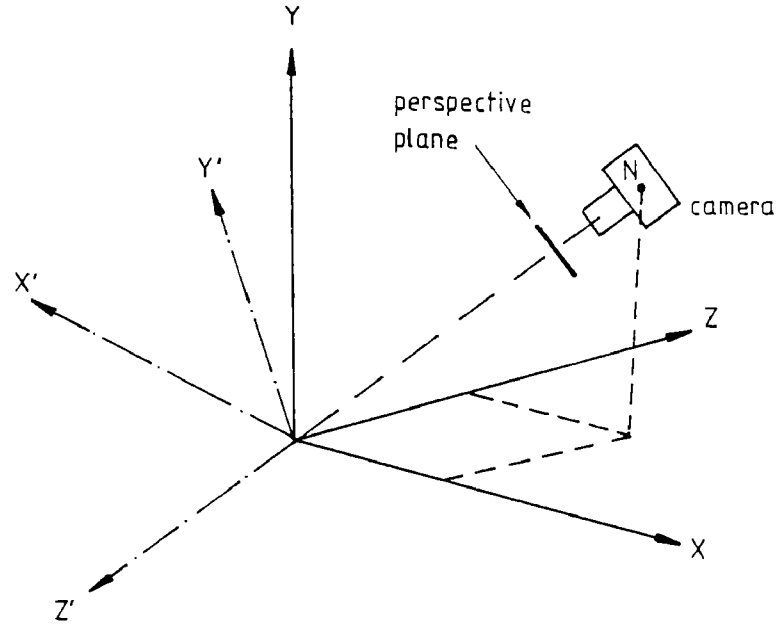

Figure 4.5. Transformation method used in CAMERA.FOR

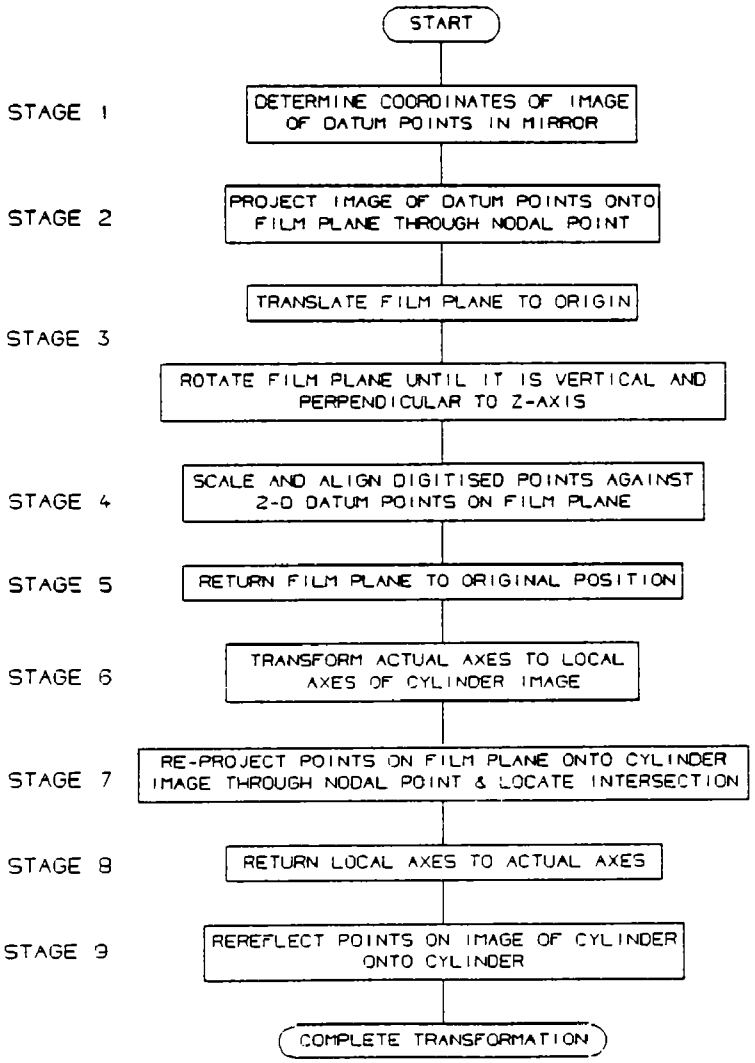

Figure 4.6. Flowchart showing various stages of transformation

The datum points (in 3-dimensions) were projected onto the resulting x-y plane. The projected datum points were scaled and further projected onto a perspective plane which is located at a distance equal to the distance between the film plane and the nodal point. This is equivalent to projecting the points onto the film plane. The program then takes the digitised datum points from the photograph and scales them against the projected datum points on the film plane. The program also determines the positional error correction factor and angles for alignment obtained by operating on the datum points. These variables are applied to all the digitised points on the fringes thus transforming these points from the coordinates of the digitising tablet into the local coordinates of the film plane. The transformed digitised points are then projected back onto the piston surface to determine their true global coordinates.

The operation of the new program is similar to that of CAMERA.FOR except for the following aspects:

(a) CAMERA1.FOR operates on images formed in mirrors inclined in any arbitrary plane in space. These mirrors are located behind the hologram. CAMERA.FOR works with images formed only in vertical mirrors located adjacent to the object.

(b) The principal axis of the camera lens can be directed towards any point in space whose coordinates are known. In CAMERA.FOR, the principal axis is directed towards the (vertical) y-axis of the optical bench.

c) CAMERA1.FOR allows four images of the piston to be photographed onto a single film thus reducing the number of cameras required to one. In CAMERA.FOR, the number of cameras required equals the number of observation directions.

The basic working sequence of CAMERA1.FOR has been divided into nine stages. The general flowchart in Figure 4.6 illustrates the various stages involved. In order to aid in the understanding of each of these stages, the transformations are illustrated by diagrams from Figures 4.7 to 4.10 . A listing of the program is given in Appendix A2. The operation of the program will be explained on a stage by stage basis and cross reference can be made to the program listing.

Stage 1

The program starts by requesting the names of files containing the digitised data (Data set 1), digitised order of datum points and

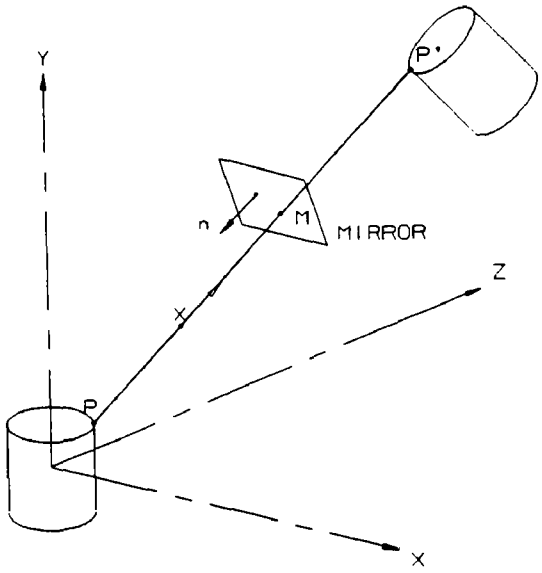

Figure 4.7. Reflection of datum points in mirror

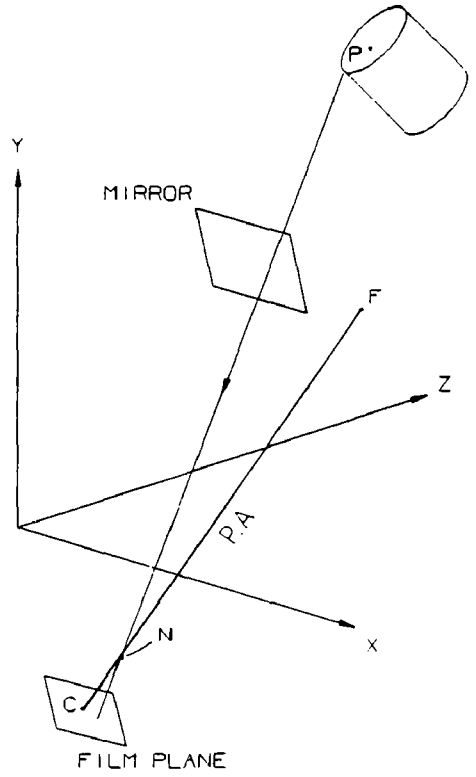

KEY:
N = NODAL POINT
C = CENTRE OF FILM PLANE
F = POINT OF FOCUS
P.A. = PRINCIPAL AXIS

Figure 4.8. Projection of image of datum points onto film

lines for alignment (Data set 2) and global coordinates of datum points (Data set 3). Data set 2 was extended to include the global coordinates of three points required for finding the equation of mirror plane. Additional information to be fed on request is the global coordinates of the point of focus of the camera as seen through the viewfinder. This point is later used to find the location of the principal axis and the equation of the film plane.

The main program calls subroutine IMAGE1 that determines the global coordinates of the image of datum points in the inclined mirror (Figure 4.7). The operation of this routine is explained in Section 4.3.3.

Stage 2

In stage 2, the image of the datum points, in global coordinates, are projected onto the 2-dimensional film plane (Figure 4.8). This is done by extending vectors from the datum point images through the nodal points until they intersect the film plane.

The equation of the film plane is first determined as follows.

Figure 4.11 shows the film plane and principal axis projected onto the x-z plane. F(XF,YF,ZF) is the point of focus, N(XN,YN,ZN) is the nodal point and C is the point of intersection between the film plane and the principal axis. N divides CF in the ratio a:b.

If (XC,YC,ZC) are the global coordinates of C then,

$$XC = \frac{(a+b)}{b}XN - \frac{a}{b}XF \qquad \ldots.4.2(a)$$

$$YC = \frac{(a+b)}{b}YN - \frac{a}{b}YF \qquad \ldots.4.2(b)$$

and

$$ZC = \frac{(a+b)}{b}ZN - \frac{a}{b}ZF \qquad \ldots.4.2(c)$$

Since N and F are known, the coordinates of C can be determined form the above expressions.

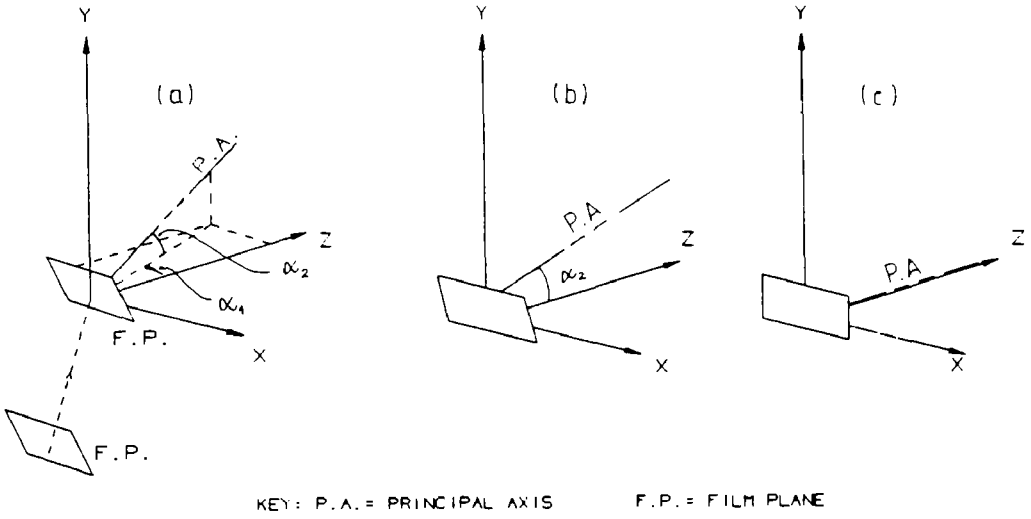

Figure 4.9. Conversion of '3-d' coordinates on film into 2-d coordinates

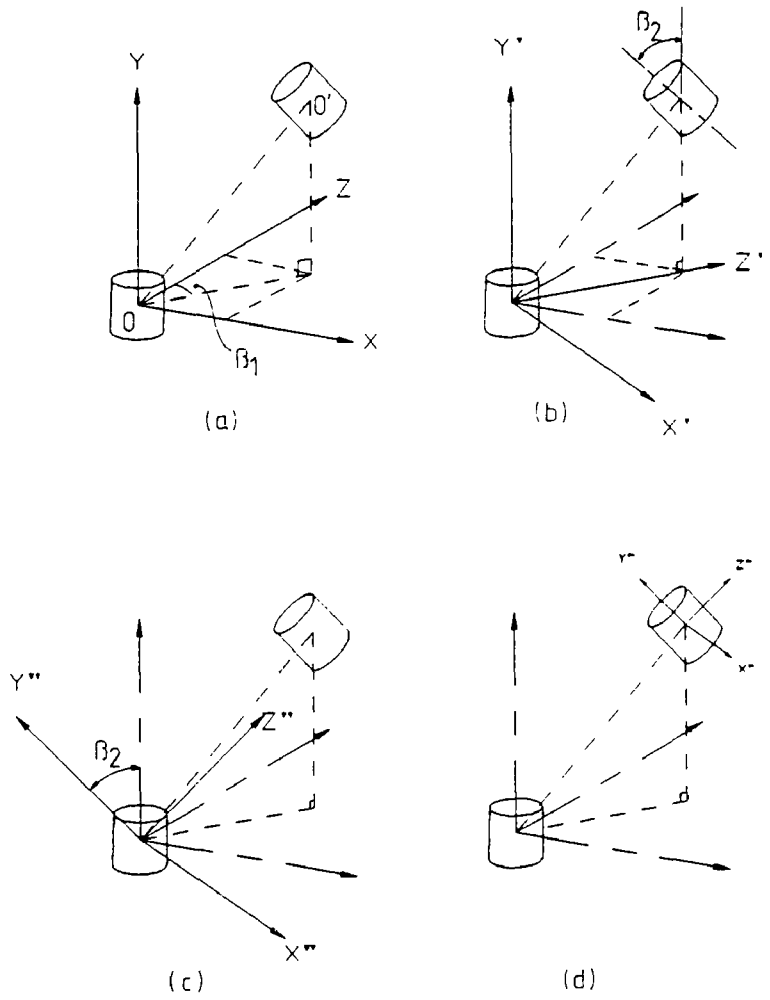

Figure 4.10. Conversion of global axes into local axes of image of cylinder

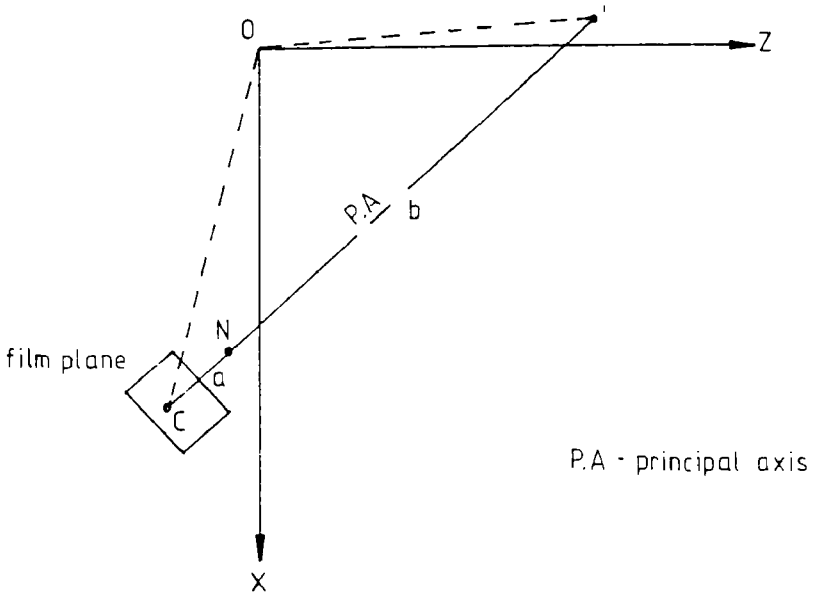

Figure 4.11. Location of principal axis of camera lens and evaluation of mirror equation

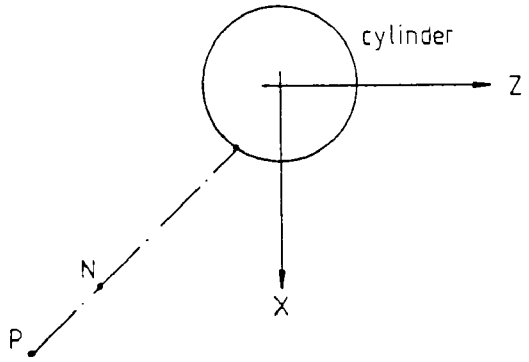

Figure 4.12. Projection of digitised points onto cylinder

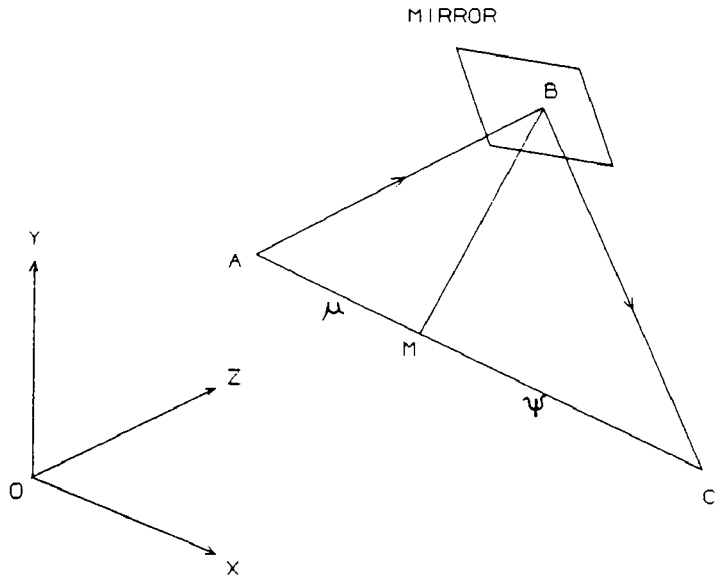

Figure 4.13. Laser beam method to measure position of mirror

The vector normal to the film plane is given by

$$\mathbf{NF} = \mathbf{OF} - \mathbf{ON}$$
$$= (XF - XN)\mathbf{i} + (YF - YN)\mathbf{j} + (ZF - ZN)\mathbf{k} \quad \ldots.4.3$$

For any point X(x,y,z) on the film plane,

$$\mathbf{XC} = \mathbf{OC} - \mathbf{OX}$$
$$= [(XC\mathbf{i} + YC\mathbf{j} + ZC\mathbf{k}) - (x\mathbf{i} + y\mathbf{j} + z\mathbf{k})] \quad \ldots.4.4$$

and since XC is perpendicular to NF, the dot product

$$\mathbf{NF} \cdot \mathbf{XC} = 0 \quad \ldots.4.5$$

Substituting 4.3 and 4.4 in 4.5, and after simplifying, we arrive at,

$$XC(XF - XN) + YC(YF - YN) + ZC(ZF - ZN) - \mathbf{NF}.\mathbf{OX} = 0$$

i.e.,

$$\mathbf{NF}.\mathbf{OX} = k \quad \ldots.4.6,$$

which gives the equation of the film plane.

In order to project a point P in space onto the film plane through N, it is necessary to determine the point of intersection between the line PN (after extension) with the film. This is achieved as follows.

The equation of line in space can be represented as

$$\mathbf{x} = \mathbf{b} + \sigma\mathbf{d} \quad \ldots.4.7$$

where for any two points $X1(x_1,y_1,z_1)$ and $X2(x_2,y_2,z_2)$,

$$\mathbf{b} = x_1\mathbf{i} + y_1\mathbf{j} + z_1\mathbf{k} ,$$
$$\mathbf{d} = (x_1 - x_2)\mathbf{i} + (y_1 - y_2)\mathbf{j} + (z_1 - z_2)\mathbf{k}$$

and

σ = constant

Since the point of intersection lies on both the plane and the line, σ can be determined by substituting 4.7 into 4.6,

$$\text{i.e.} \quad \mathbf{n}.(\mathbf{b} + \sigma\mathbf{d}) = k$$

$$\sigma = \frac{k - \mathbf{n}.\mathbf{b}}{\mathbf{n}.\mathbf{d}} \qquad \ldots.4.8$$

The coordinates of the point of intersection are then obtained by solving equation 4.7. In the program n.b, n.d and σ are designated by DOTNB, DOTND and RMU.

Stage 3

The images of datum points transferred onto the film plane in Stage 2 exist in 2-dimensions with respect to the local axes of the film plane itself. But, these points must be specified in terms of the x, y and z components when referred to the optical bench axes. This is due to the inclination of the film plane in the actual axes system. Therefore, in order to convert the '3-D' coordinates of the points on the film plane into 2-D coordinates with respect to the actual axes, three stages of transformation are employed (Figure 4.9).

a) The film is translated to the origin,

b) rotated about the y-axis through α_1,

c) rotated about the x-axis through α_2.

Stage 4

The digitised datum points are scaled, rotated and translated in order to match the global datum points on the film plane. Rotation is done by comparing the gradient (θ_1) of specified imaginary lines joining the digitised datum points with the gradient (θ_2) of the lines joining the corresponding transformed datum points. The digitised datum points are rotated through an angle ($\theta_1 - \theta_2$) about the local origin of the film plane. The digitised points are also corrected for positional errors. Scaling is performed by comparing the lengths of the corresponding lines joining the datum points. The scale factor, rotation angle and positional error correction factor are then applied to all the other digitised points thus transforming the 2-D coordinates of the digitising tablet to that of the film plane.

Stage 5

The film is returned to its original position by performing the reverse of the transformations in Stage 3.

Stage 6

With the film back in its original position, the points on it are transferred back onto the surface of the cylinder. The mathematics involved is simplified by first transforming the actual axes to the local axes of the cylinder image. This transformation, which consists of the following stages, is illustrated in figures 4.10(a)-(d).

i) Rotation about y-axis through β_1

ii) rotation about x-axis through β_2

iii) translation to O' (image of origin).

The transformation is applied to the nodal point and all the points on the film plane.

Stage 7

The points where the vectors from points on film plane through the nodal point intersect the cylinder is found by using the equation of the surface of the cylinder. When the cylinder is projected onto the local x-z plane, the problem simply becomes one of determining the point of intersection between a straight line and a circle. The y-component is then determined using similar triangles.

In Figure 4.12, for any point $P(x_1,y_1,z_1)$ on the film plane, the equation of line PN is given by

$$\frac{z - z_1}{x - x_1} = \frac{z_N - z_1}{x_N - x_1} = m_1 \qquad \ldots.4.9$$

$$z = (z_1 - m_1x_1) + m_1x \qquad \ldots.4.10$$

i.e., $$z = A_1 + m_1x \qquad \ldots.4.11$$

where $A_1 = z_1 - m_1x_1$.

The equation of the circle representing the projected cylinder is

$$x^2 + z^2 = R^2 \qquad \ldots.4.12$$

Substituting 4.11 into 4.12 and after simplifying we have,

$$A_2x^2 + A_3x + A_4 = 0 \qquad \ldots.4.13$$

where,

$$A_2 = 1 + m_1^2$$

$$A_3 = 2\,A_1m_1$$

$$A_4 = A_1 - R^2 \ .$$

Solving this,

$$x = [-A_3 \pm \sqrt{(A_3^2 - 4A_2A_4)}]/2A_2 \qquad \ldots.4.14$$

which yields two values of x, indicating that there are two points of intersection. In the analysis, the point which is closer to the nodal point is considered as the other will lie on the opposite side of the cylinder. By substituting 4.14 into 4.11, the z coordinate can be evaluated.

The y-component is determined by projecting the cylinder onto the y-z plane and is given by

$$y = (y_1 - m_2z_1) + m_2z \qquad \ldots.4.1.15$$

where m_2 is the gradient of the line PN in the y-z plane. Since the z coordinate of point I is known, the y component can be calculated from the above equation.

Stage 8

The coordinates of the points transferred onto the image of the cylinder in Stage 7 exist with respect to the local axes of the cylinder image. In this stage, the local axes are transformed to the actual axes of the optical bench by performing the reverse of the transformations in stage 6.

Stage 9

In this stage, the points on the image of the cylinder are re-reflected onto the cylinder by calling subroutine IMAGE1. This completes the transformation of the digitised points on the photographs and back to the surface of the cylinder.

By specifying different values of R, the above transformation routine can be used with cylinders or pistons of different diameters.

4.3.2. Evaluation of mirror surface equation

An important factor affecting the accuracy of the transformation is the accuracy with which the equation of the surface of mirror can be determined. To achieve this, a laser beam was directed onto a known point on the front mirror surface and the global coordinates of a point on the incident ray and one on the reflected ray were measured. The global coordinates of three points were used to determine the equation of the surface of the mirrors as follows:

In Figure 4.13, AB and BC are the incident and reflected rays respectively and M is a point on AC such that AM:AC equals $\mu : \mu+\psi$. From the laws of reflection it can be shown that the vector normal to the mirror plane at B passes through M.

If the coordinates of A,B and C are given, respectively by

A (x_1, y_1, z_1),
B (x_2, y_2, z_2) and
C (x_3, y_3, z_3),

by using geometry of 3-dimensional space, we can determine the coordinates of M as follows :

$$x_M = \frac{\mu x_3 + \psi x_1}{\mu + \psi} \qquad \ldots.4.16(a)$$

$$y_M = \frac{\mu y_3 + \psi y_1}{\mu + \psi} \qquad \ldots.4.16(b)$$

$$z_M = \frac{\mu z_3 + \psi z_1}{\mu + \psi} \qquad \ldots.4.16(c)$$

The value of μ and ψ can be determined from triangle ABM and line AC by using the sine rule.

For any point X on the mirror,

$$XB = OB - OX \qquad \ldots.4.17,$$

and since BM is perpendicular to XB, the dot product

$$XB.BM = 0 \qquad \ldots.4.18$$

gives the equation of the plane.

A subroutine named IMAGE1.FOR that uses the equation of the mirror surface to evaluate the image coordinates of a point when the object coordinates are given was written and incorporated into CAMERA1.FOR.

4.3.3. Operation of subroutine IMAGE1

A call to this subroutine is made by the statement

```
CALL IMAGE1(OA,OB,OC,X,Y,Z)   ,
```

where OA,OB,OC are one dimensional arrays assigned to the global coordinates of three points necessary for finding the equation of mirror plane. X,Y,Z are the coordinates of points whose image coordinates are to be determined. On return, X,Y,Z will be assigned to the coordinates of the image.

The program first evaluates the constants and coefficients in the equation of mirror plane by using the technique discussed in Stage 2 of Section 4.3.1. The vector XP, where X(x,y,z) is a point on the perpendicular line from a point $P(x_1,y_1,z_1)$ on the object surface to the mirror is then evaluated as follows.

In Figure 4.7, the perpendicular from P to the plane of mirror meets the latter at M.

Now,

$$OX + XP = OP$$

$$XP = (x_1 - x)i + (y_1 - y)j + (z_1 - z)k$$

Since XP is perpendicular to the plane,

$$XP = t(n) \qquad \ldots.4.19$$

where $n(n_1,n_2,n_3)$ is the vector normal to the plane determined from the equation of plane and t is a parameter.
In equation (4.19),

$$(x_1 - x)i + (y_1 - y)j + (z_1 - z)k = t(n_1i + n_2j + n_3k) \qquad \ldots.4.20$$

i.e.

$$x = x_1 - tn_1$$
$$y = y_1 - tn_2$$
$$z = z_1 - tn_3 \qquad \ldots.4.21.$$

Thus, at point M, if t = t', then,

$$x_m = x_1 - t'n$$
$$y_m = y_1 - t'n$$
$$z_m = z_1 - t'n \qquad \ldots.4.22.$$

If the equation of mirror plane can be written as,

$$Ax + By + Cz - D = 0 \qquad \ldots.4.23,$$

then,

$$PM = \frac{Ax_1 + By_1 + Cz_1 - D}{\sqrt{[A^2 + B^2 + C^2]}} \qquad \ldots.4.24.$$

Distance PM is also given by,

$$PM = \sqrt{[(x_1 - x_m)^2 + (y_1 - y_m)^2 + (z_1 - z_m)^2]} \qquad \ldots.4.25$$

Equating (4.25) and (4.25) and after replacing x_m, y_m and z_m by its parametric form (4.22), the resulting quadratic equation is then

solved for two values of t'. By substituting the value of t' into (4.22) the coordinates of M can be determined. Since M lies midway between P and P', the coordinates of P' are therefore given by,

$$x' = 2x_m - x_1$$
$$y' = 2y_m - y_1$$
$$z' = 2z_m - z_1 \quad .$$

Since the value of t' can be positive or negative, one of these will produce an image point which will lie on the opposite side of the mirror compared to $P(x_1,y_1,z_1)$. The program checks this by calculating the distances from M to P' for both values of t' and testing if the sign of the product of these distances is positive or negative. A positive will indicate that both points lie on the same side of the mirror and therefore, t' is set to -t' and the coordinates of the image of P' is evaluated.

4.4 Verification of accuracy of transformation

In order to check the accuracy of the transformation performed by CAMERA1.FOR, a high quality graph paper was superimposed around a 110mm diameter cylinder and photographed (Figures 4.14). Grid points on a 83° sector of the cylinder were digitised from the four photographs. These photographs were enlarged using the same magnification that would be used for the fringe patterns. The program was then used to transform these grid points (a total of 72) onto the surface of the cylinder. The positions of the mirrors were measured using the laser beam method and supplied to the program in a data file. The transformed points were then plotted onto the developed surface of the cylinder (Figures 4.15). Four datum points (numbered 1 to 4) were used to evaluate the scaling factor, rotation angles and positional error correction factors. The positional errors of the transformed points in the circumferential (Δs) and axial (Δy) directions were evaluated and summarised in Table 4.1. The number of points (in %) transformed within a positional error of 0.5mm and 0.8mm were calculated.

The analysis shows that the transformation can be achieved to a high degree of accuracy. Nearly all the points were transferred within a positional error of 0.8mm and, on the average, 85% of the points were transferred within a positional error of 0.5mm. The analysis thus validates the correct operation of CAMERA1.FOR and the results indicate that other errors, e.g. errors due to digitising and aberrations imposed by the mirrors affect the transformation in a manner so that the positional errors of the transformed points are within 0.8mm, which is considered acceptable. The effect of this positional error on the fringe orders and the displacement is discussed in Section 4.5.1.

		Within 0.5mm	Within 0.8mm
View 1	Δs	60	94
	ΔY	96	100
View 2	Δs	85	100
	Δy	100	100
View 3	Δs	93	100
	Δy	88	99
View 4	Δs	88	100
	Δy	99	100

Table 4.1. Percentage of number of points transferred to within 0.5mm and 0.8mm accuracies.

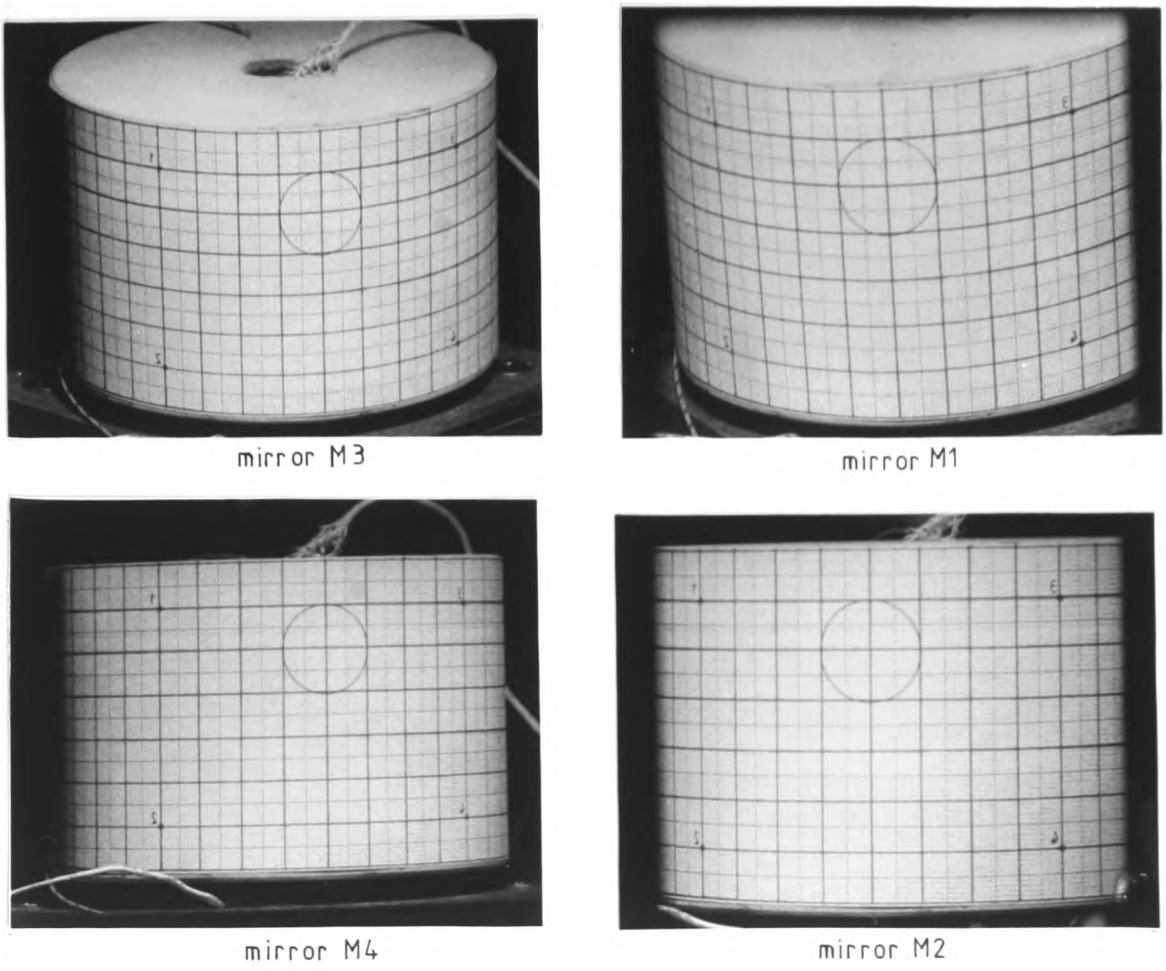

Figure 4.14. Various views of cylinder with superimposed grid points used for checking accuracy of transformation. (Mirror numbers correspond to those shown in Figure 4.1)

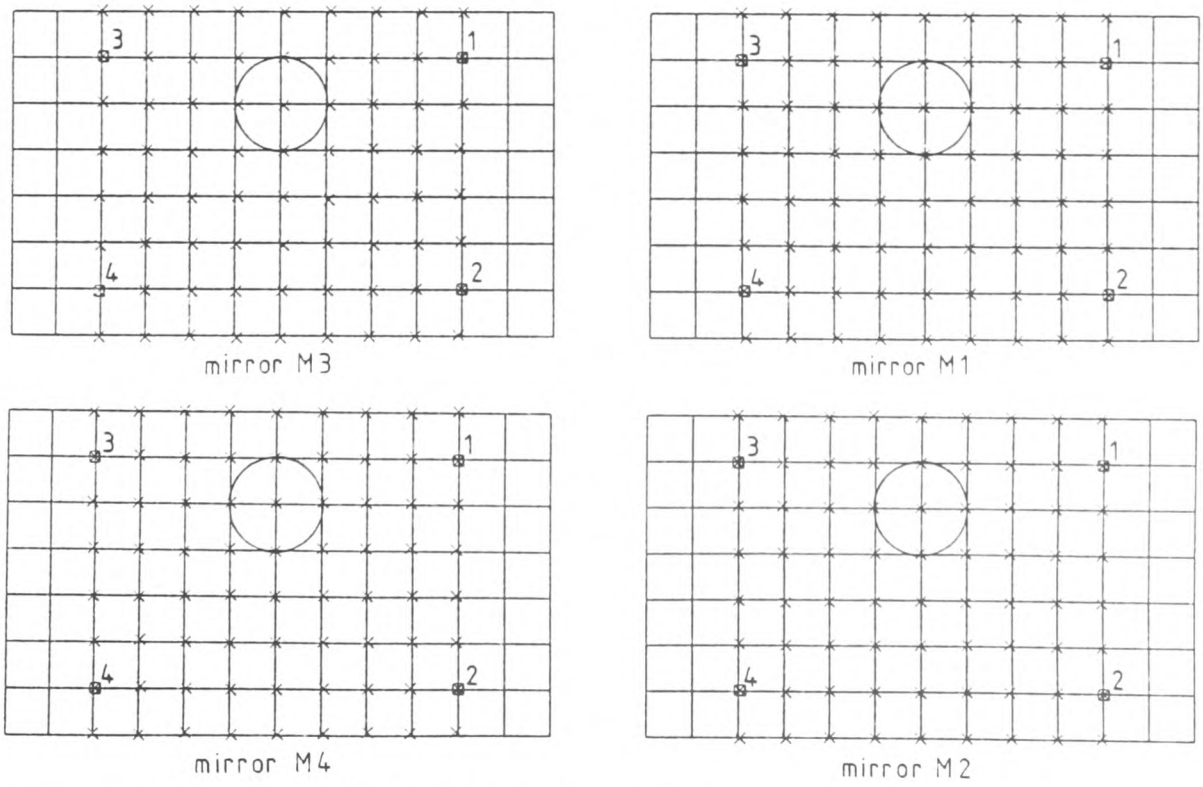

Figure 4.15. Plot of transformed grid points on developed surface of cylinder for views shown in Figure 4.14

4.5 Verification of the technique using a uniformly heated cylinder

4.5.1. The technique

The proposed method of measuring x, y and z components of displacements simultaneously was verified by measuring the thermal expansion of a uniform 110mm diameter solid cylinder. A $\frac{1}{4}$in. diameter hole was drilled at the axis and a 150W cartridge heating element was located for a length of 30mm inside the hole (Figure 4.16). The heat input was controlled by means of a variac. Temperatures were measured at four points on the surface of the cylinder by using thermocouples which were linked to a computer via an interface device.

The optical arrangement used is similar to the one shown in shown in Figure 4.1. The four mirrors were inclined in such a manner so that four images of the cylinder were visible from a single viewpoint of the plate camera. The camera was used to photograph the fringes at the start and end of the deformation. An aperture of f-11 was used to maintain sufficient depth of field so that all the images were reasonably in focus.

A hologram of the cylinder was recorded at room temperature (approximately 19°C). When the processed plate was repositioned in its holder, about four to five fringes appeared due to a change in ambient temperature (which rose to about 21°C). The cylinder was then heated from 22.5°C to 30.5°C and the fringes were recorded. The live fringes at these two temperatures were photographed (Figures 18 and 19) and the formation of the fringes were recorded on a video tape using the method discussed in Section 4.2. In order to synchronise the photographing and recording of live fringes, an alarm on the computer was set to sound at 22.5°C and 30.5°C. The audio signal of the alarm was also recorded onto the video tape so that the precise moment at which the counting of fringes should commence can be established.

The plate and the video cameras were aligned with the aid of a laser beam. To achieve this, the plate camera was initially focused onto a target point located among the four mirrors. The image of the target point was assured to be located centrally on the focusing plate at the back of the camera. A pendulum line was then hung about mid-way between camera lens and the target point so that its image

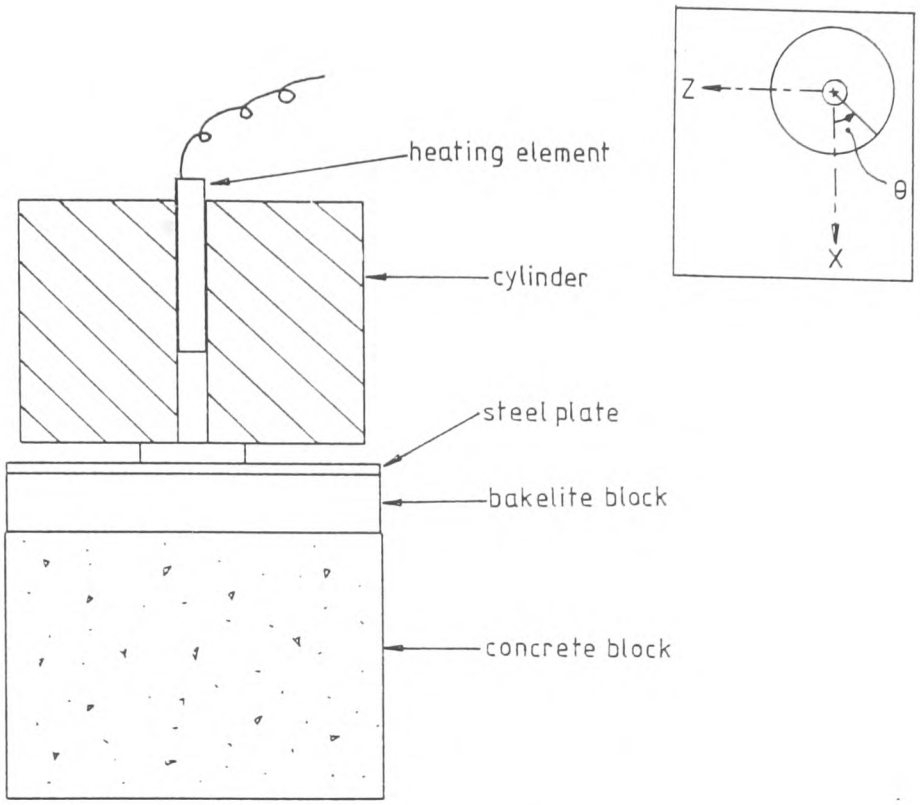

Figure 4.16. Arrangement of cylinder used for verification of the technique

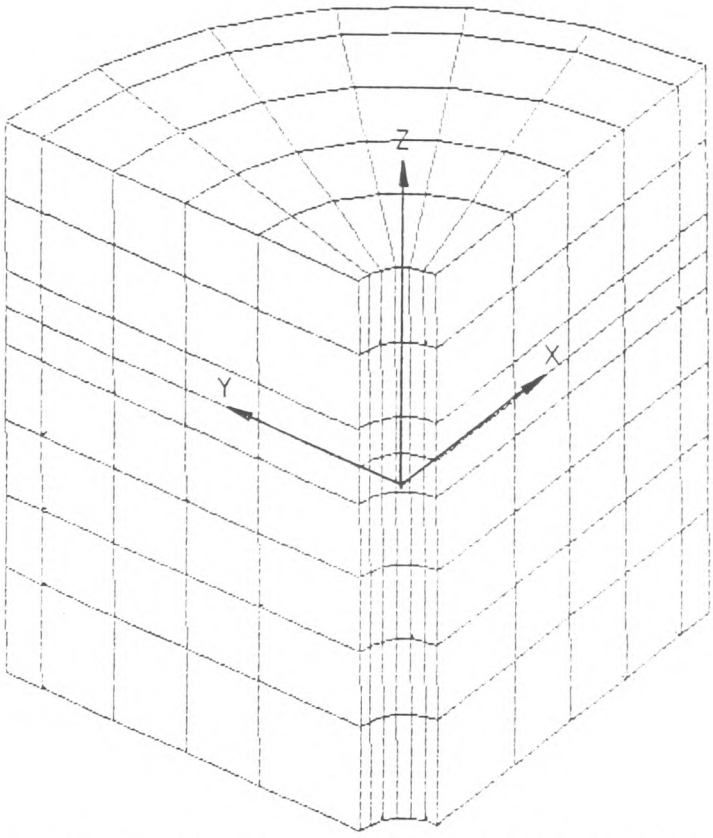

Figure 4.17. Finite element model of the cylinder

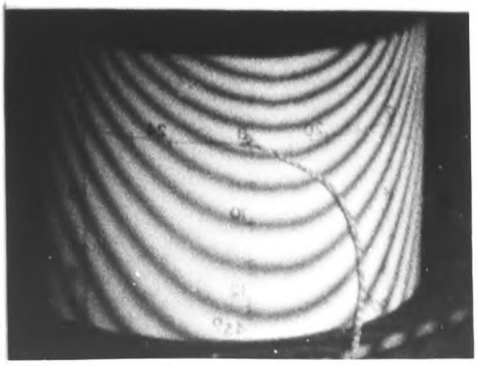

Mirror M3

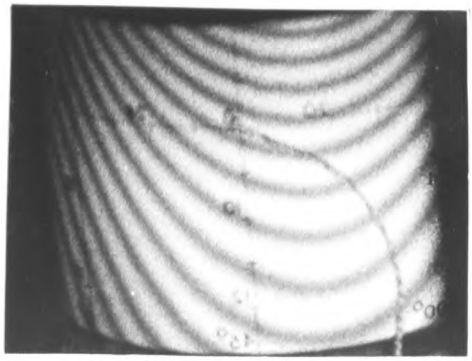

Mirror M1

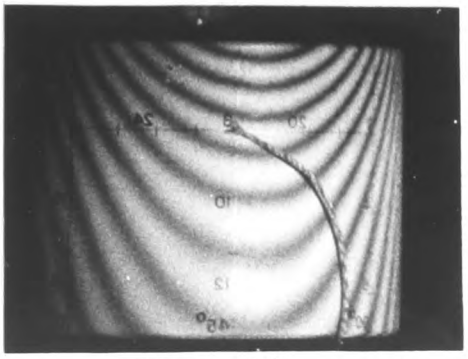

Mirror M4

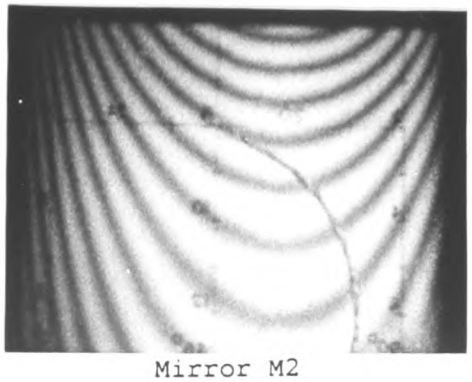

Mirror M2

Figure 4.18. Initial fringes on cylinder (at 22.5°C)

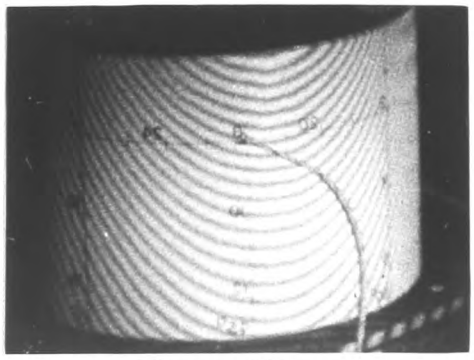

Mirror M3

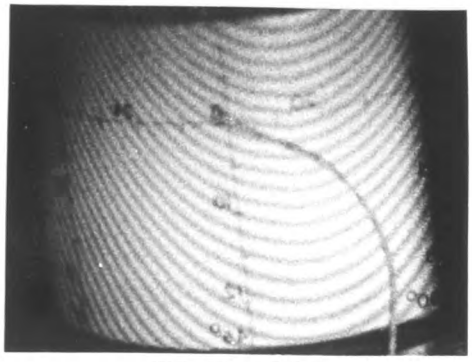

Mirror M1

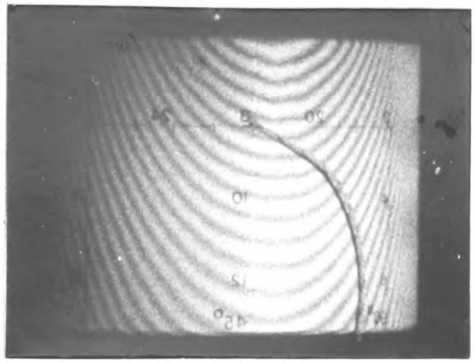

Mirror M4

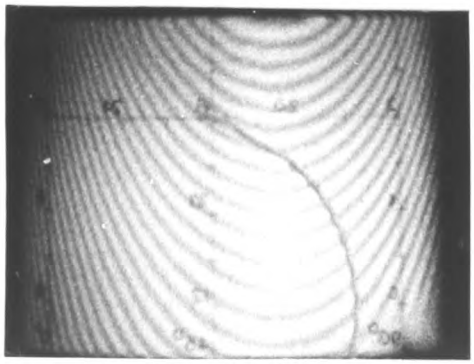

Mirror M2

Figure 4.19. Final fringes on cylinder (at 30.5°C)

(on the focusing plate) passed through the centre. A low intensity laser beam was then directed towards the lens in a manner so that it passes over the pendulum line. The height of the beam was adjusted so that its image is also focused onto the centre of the focusing plate. The position of the beam therefore represents the principal axis of the camera lens. A 4in.x 5in. beam splitter was then positioned at approximately 45° to the path of the laser beam and was located just in front of the plate camera. The position of the video camera was then suitably adjusted so that its lens was located along the path of the reflected beam. (The lens of the video camera was protected with a lens cap in order to avoid damage to the light sensitive elements during the alignment). Since this technique of alignment cannot guarantee very accurate results, a lateral misalignment of 20mm between the two cameras (assumed at the plate camera lens nodal point) has been considered for analysing the errors due to misalignment and is discussed in Appendix A3.

The fringe centres on the photographs were lined in manually and digitised into a Vax 11/785 computer system for subsequent analysis by using a digitising tablet. Although direct digitising of the fringe patterns into a computer using a scanner will increase the speed and accuracy of the analysis, the errors in displacement caused by errors in manual digitisation are small owing the high fringe orders. These errors can be estimated by applying the previous analysis (Section 4.4) to the fringe pattern photographs. The spacing of the fringes with lowest fringe orders is approximately 3mm. Thus a maximum positional error of 0.8mm due to digitising will cause a 4.4% error in fringe order (based on the lowest order number of 6) and this was considered acceptable.

The digitised points, which exist in two dimensions with respect to the local coordinates of the digitising tablet, were transformed into spatial coordinates with respect to the optical bench axis by using CAMERA1.FOR. The transformed digitised points were plotted onto the developed surface of the cylinder and an imaginary grid of 5mm intervals was then superimposed to determine the fractional fringe orders at the grid points. This was done with an interpolation technique using finite elements (Evans and Russell 1983). The fringe orders at the grid points for the initial and final fringe patterns were then subtracted. This was repeated for each of

the views and the resulting fringe orders were used in the interferometry equation (equation 4.1) in order to evaluate the displacements. The observation points for the four views were determined by reflecting the camera lens nodal point in each of the mirrors by using the program IMAGE1.FOR (Section 4.3.3). The four equations were solved using SOLVE1.FOR and the displacement was calculated for each grid point.

In order to confirm repeatability of the results, the measurement was repeated for a rise from 21°C to 29°C. Recording of the fringes was carried out two days after the first experiment, using the same hologram.

4.5.2 Finite element analysis

A finite element model for a quadrant of the cylinder was generated using the PAFEC Software Package (Figure 4.17). The base of the cylinder was assumed to be fixed. Suitable restraints were applied at the two vertical face parallel to the x-z and y-z planes to prevent movement in the y- and x-directions respectively. Appropriate boundary conditions were specified so as to produce temperature rises at the four thermocouple locations that agreed to within 0.8°C of the measured rises. A steady-state thermal analysis was carried out. The measured and predicted temperatures are given in Table 4.2. The mean difference between the predicted and measured temperatures is 0.2°C. The predicted temperatures were arrived at after about five different attempts, in each case of which the boundary conditions were altered appropriately. The predicted temperatures were then used in a stress analysis which were carried out separately at 22.5°C and 30.5°C. The deformation for a rise from the two temperatures were determined by subtracting the results.

The material properties used in the analysis are given in Table 4.3.

Thermocouple	Measured Rise (°C)	Predicted Rise (°C)	Difference (°C)
T1	9.6	9.6	0.0
T2	8.0	7.2	-0.8
T3	6.7	7.3	0.6
T4	5.1	4.5	-0.6

Table 4.2. Measured and predicted temperature rises for experiments using cylinder.

4.5.3 Results and discussion

The displacement along three different sections of the cylinder at $\theta=-36.5°$, $\theta=0°$ and $\theta=36.5°$ were compared with the finite element results (Figures 4.20(a)-(c)). For the holographic results the bottom the cylinder was found to have a slightly downward displacement of 0.0004mm. This value was added to the axial displacement at all points along the vertical surface of the cylinder so that the axial displacement at the base is zero, which corresponds to the assumption made in the model.

The plots in Figures 4.20(a) and 4.20(b) show good agreement between holographic and finite element results in the radial direction. The mean difference is about 7%. This difference could be due to the difference between the predicted and measured temperatures (Table 4.2) and an error of about 5% in the specified expansion coefficient of the material. The radial displacement for the repeated measurement also shows good agreement with the theoretical results (Figure 4.20(d)). The radial displacement in Figure 4.20(c) shows a good agreement (within 5%) at the top section of the cylinder but a greater difference at the lower part. This could be due to slight non-uniformity in temperature distribution and the effects of a small body displacement. The axial displacements show a greater deviation (up to 30%) between the two results at all sections of the cylinder. This result is in agreement with the findings of Evans, Russell and White(1987). The larger difference in the axial direction can be attributed to the poorer sensitivity of the arrangement to displacements in this direction. A small error in fringe order is suspected to have introduced large errors in displacement (Vest and Nobis 1978). This, however, can be overcome by tilting the cylinder either towards or away from the holographic plate so that the axial displacement will have a larger component along the sensitivity vectors. Since the radial components of displacement are more significant when compared to the axial component for the study on the piston, such an arrangement to improve the accuracy in the axial direction was not considered essential.

Young's modulus N/mm^2	Poisson's ratio	Coefficient of expansion /°C	Thermal conductivity W/mm K
206900	0.28	12.5E-6	0.00549

Table 4.3. Properties of mild steel.

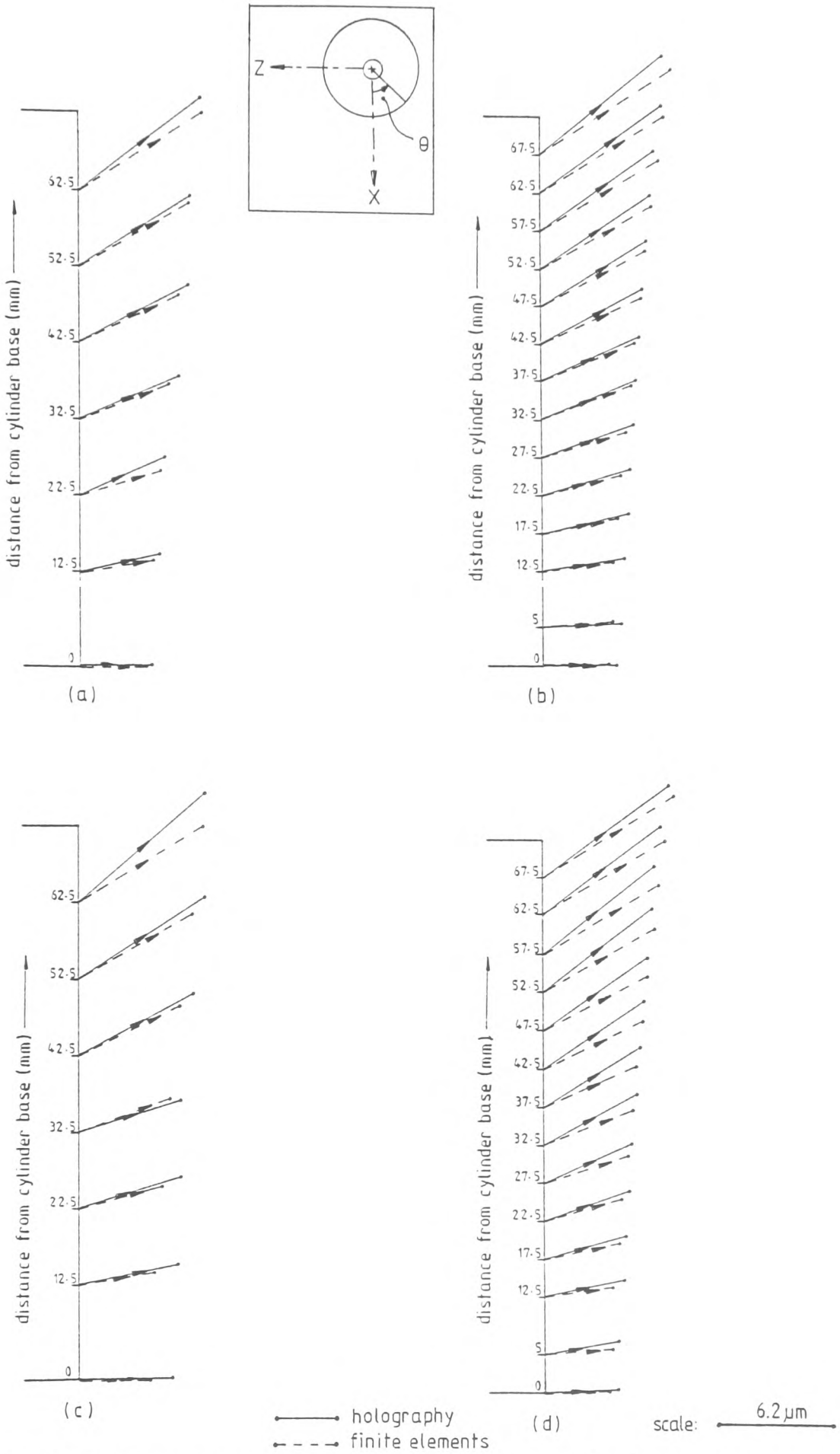

Figure 4.20 Displacement vectors at various sections of cylinder for comparison of experimental and finite results: along (a)θ=-36.5°, (b)θ=0°,(c)θ=36.5° and (d)θ=0° (repeat)

4.6 Application to the measurement of piston deformation

4.6.1 Experimental arrangement and technique

The piston and the heating arrangement are shown in Figure 4.21. The heat input, from a 800W heating coil, was controlled by using a variac and the temperature distribution at 12 points on the piston surface was measured by using type 'K' (copper-constantan) thermocouples (see Chapter 3 for details on thermocouple locations).

Attempts to measure the thermal expansion of the piston was initially carried out using the arrangement shown in Figure 4.4, which is essentially an extension of the arrangement shown in Figure 4.1. The two rear view mirrors enabled a sector of about 25° at the rear surface to be imaged together with the front surface of the piston. The object beam was split to illuminate the front and rear surfaces. The intensity of the beam at the rear surface had to be approximately 1.5 times the intensity at the front surface due to the longer path travelled by the light reflected from the rear surface.

Attempts to record the fringes at the front and rear surfaces simultaneously were made but without much success. This was due to the splitting of the main beam into several beams which resulted in an overall drop in the brightness of the illuminated piston. In addition, since the plate used was 8in.x 10in. and the observation points were effectively located close to the four corners, it was necessary to expand the beam sufficiently to cover the entire plate without a significant variation in intensity across the plate. Although the ratio of object to reference beam was maintained at 1:6, the overall intensity of light reaching the plate was low. Since the plate was exposed when the piston was continuously expanding, it was necessary to limit the exposure time to about 2 seconds. This resulted in the plate being underexposed. Increasing the developing time (which increases the effective speed of the film) did not sufficiently enhance the quality of the hologram. The resulting fringe were of poor contrast, especially at the rear surface. A typical photograph of the fringes at the front and rear surfaces for one of the views is shown in Figure 4.22. Although it is possible to digitise these fringes manually, the fringes orders cannot be determined accurately due to the much poorer contrast fringes on the

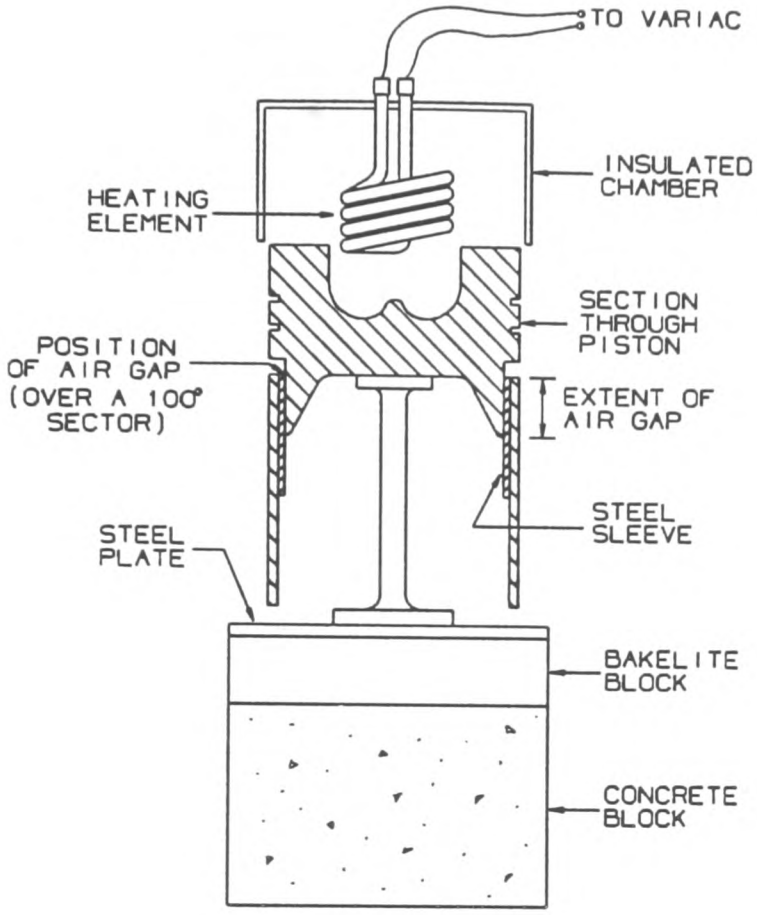

Figure 4.21. Piston and heating arrangement

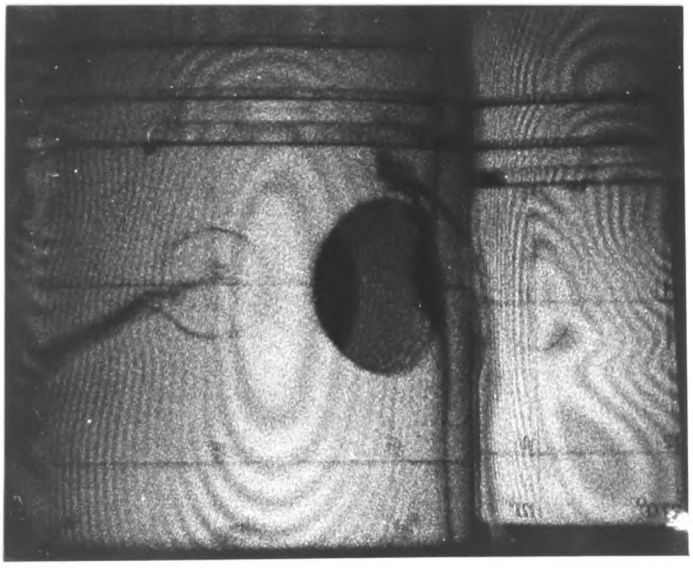

Figure 4.22. Photograph of fringes at front and rear surface of piston

video recording. This problem can be overcome by using a high power laser, such as an argon laser but this was not available. The measurement was therefore confined to the front surface only.

The deformation at the front surface was measured for a rise from 50°C to 58°C. The temperature rise was limited to 8°C to obtain fringes that can be easily resolved. The holographic plate was exposed at 50°C and the piston was allowed to cool to room temperature and then reheated for recording the fringes. The initial and final fringe patterns are shown in Figures 4.23 and 4.24. Although the initial fringes were photographed at a temperature that coincided with the plate exposure temperature, about 6 to 7 fringes were visible. These fringes were approximately straight suggesting that they are caused by a rigid body displacement. The piston support is suspected to have undergone a slightly different deformation during the first and second heating sequences, thus giving rise to the body movement. Since these fringes are dynamic in nature, it was not possible to adjust the plate at the exposure temperature so as to eliminate the tilt fringes. The initial fringes will, however, affect the final fringe pattern in a manner so that the difference between the two will be free from the effects of the fringes initially present. This can be checked by repeating the experiments and obtaining initial fringes that are different in number and geometry between successive experiments. In addition, the number of fringes crossing any point on the piston surface is a function of the change in path length resulting from the displacement of that point and should be independent of the initial fringe geometry. Several authors (e.g. Evans, Russell and White,1987 and Matthys et.al.,1988) have shown that by subtracting initial from final fringe orders, it is possible to obtain accurate displacement data. Here, however, this has been verified in the previous section using a cylinder.

The fringe centres on the photographs were digitised and transformed onto the piston surface using CAMERA1.FOR. Each of the views were considered separately, as in the case of the cylinder. Five datum points marked 'a' to 'e' were used for the purpose of the transformation. A typical plot of the initial and final fringes on the developed surface of the piston is shown in Figure 4.25(a)-(b) (the datum points are marked 'x'). The transformation has been

Mirror M3

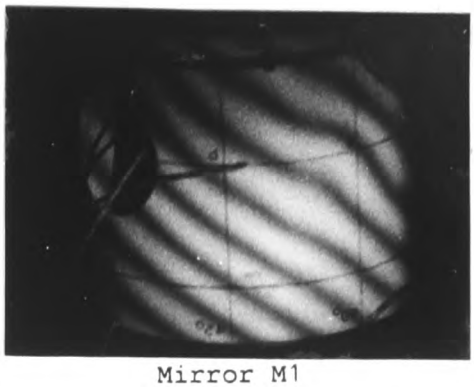

Mirror M1

Mirror M4

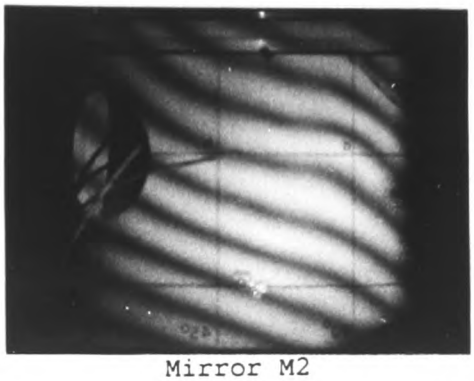

Mirror M2

Figure 4.23. Initial fringes on piston (at 50°C)

Mirror M3

Mirror M1

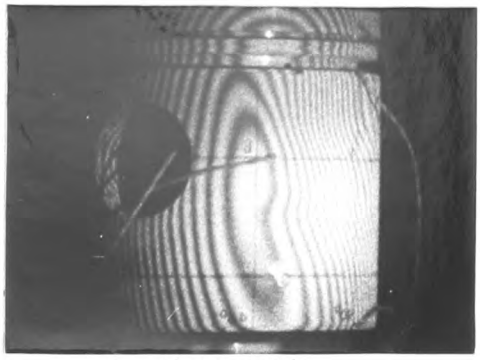

Mirror M4

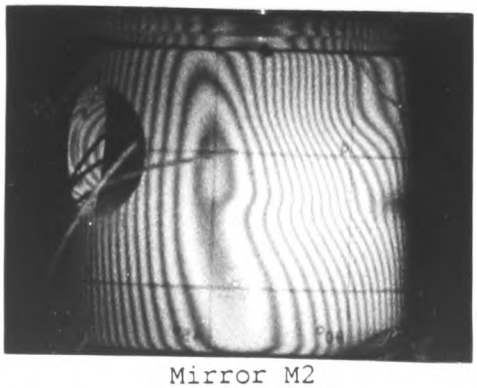

Mirror M2

Figure 4.24. Final fringes on piston (at 58°C)

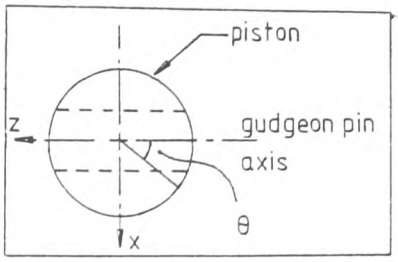

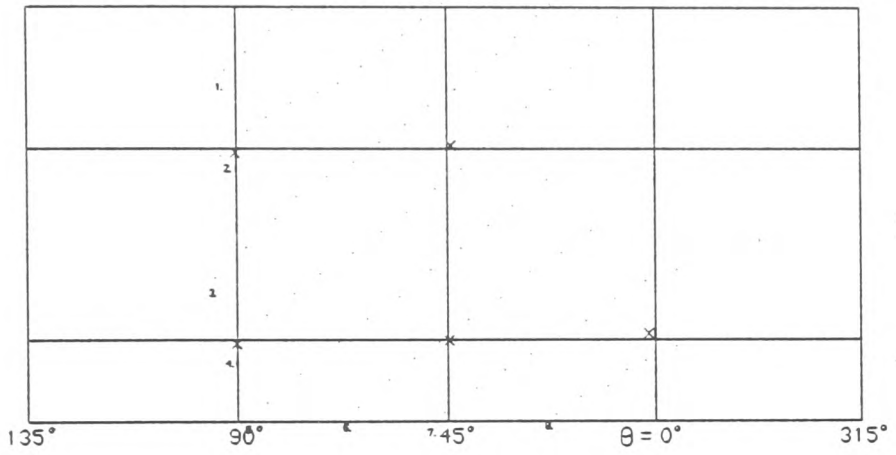

(a)

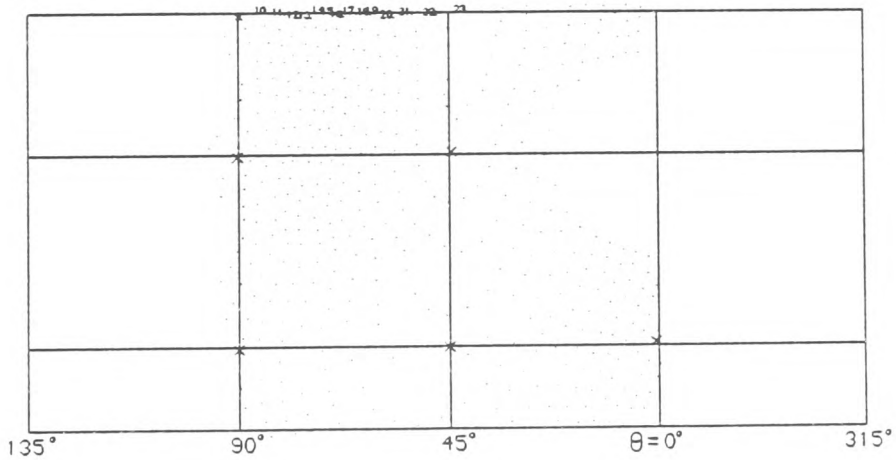

(b)

Figure 4.25. Digitised fringe centres transformed and plotted on developed piston surface (for view from mirror M1): (a) initial fringes, (b) final fringes

carried out accurately, complete with corrections for lateral inversions. The method of analysis to obtain deformation is similar to the one used for the cylinder. The recording and the analysis was repeated to confirm repeatability.

4.6.2 Results and discussion

A vectorial displacement plot for the piston is shown in Figure 4.26. The viewing position for this plot was located at (0,300,700) and it shows the presence of a body displacement towards the negative x-direction. The body displacement can be seen more clearly on the horizontal plot at 40mm below the pin axis for the two repeated experiments (Figures 4.27(a)-(b)). The radial expansion along θ=50° and θ=86° for the repeated measurement (Figure 4.28) show that the deformation profiles are similar but a difference of about 10% in the magnitude of displacement along θ=86° can be noticed. This difference is attributed to the slightly different body displacement undergone by the piston. Such a fluctuation was also observed when the measurement was carried out using a different experimental arrangement (see Chapter 6). As will be shown in Chapter 6 the body displacement has a larger component along the x-direction thus affecting the displacement at θ=86° more than that at θ=50°. The temperature rises for the two experiments (Table 4.4) show that the maximum difference is about 5%, which was considered acceptable.

The vertical displacement (y-direction) was found to vary by about 20% at 45mm below the pin axis between the two experiments. As described in Section 4.5 the greater fluctuation in the axial direction is due to the poorer sensitivity of the arrangement to movement in this direction.

Thermocouple	Temperature Rise for Expt.1 (°C)	Temperature Rise for Expt.2 (°C)
T3	7.5	7.7
T4	7.7	7.7
T5	7.2	6.8
T6	6.7	6.5
T7	6.8	6.5
T8	8.0	8.1
T9	7.9	7.9
T10	8.0	8.0
T11	8.0	8.0
T12	7.4	7.2

Table 4.4. Temperature rises for piston : Experiment 1 and Experiment 2 (repeat).

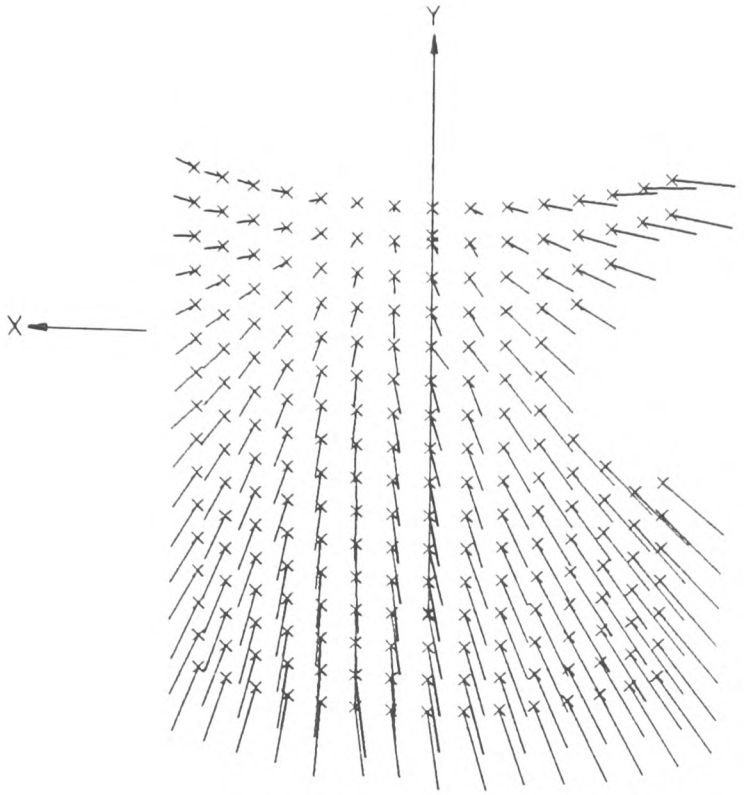

Figure 4.26. Vectorial displacement plot for piston

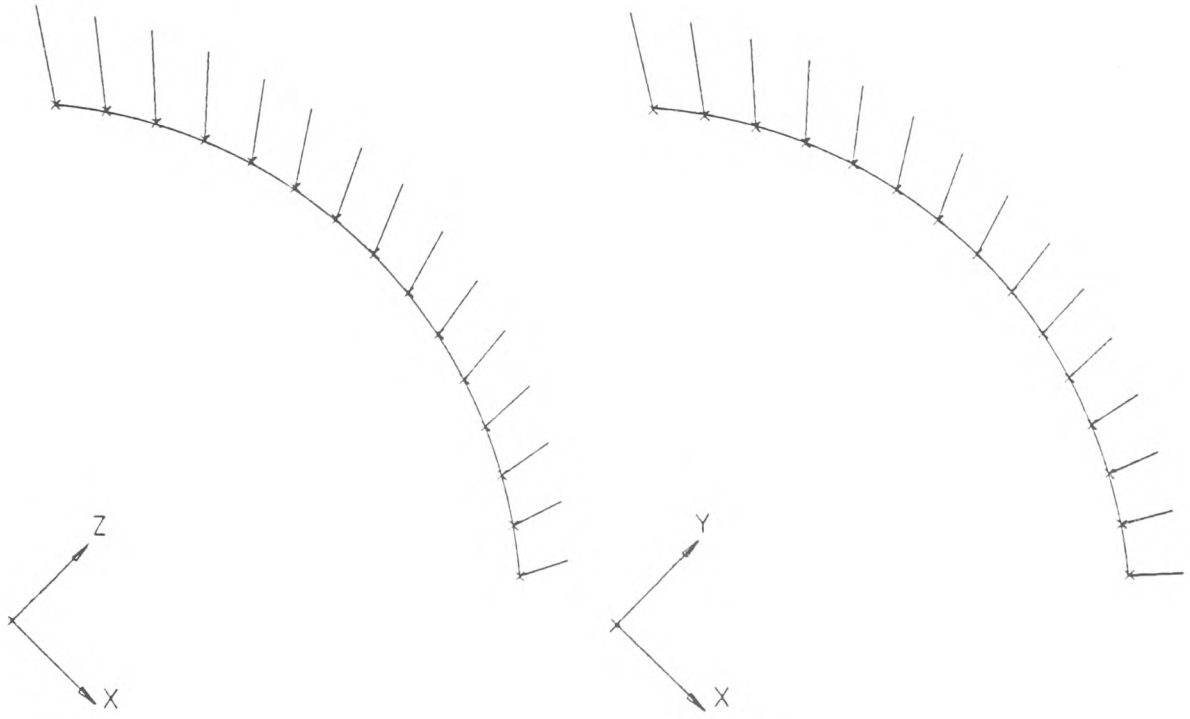

Figure 4.27. Vectorial displacement plot at 40mm below pin axis for (a) first and (b) second experiments

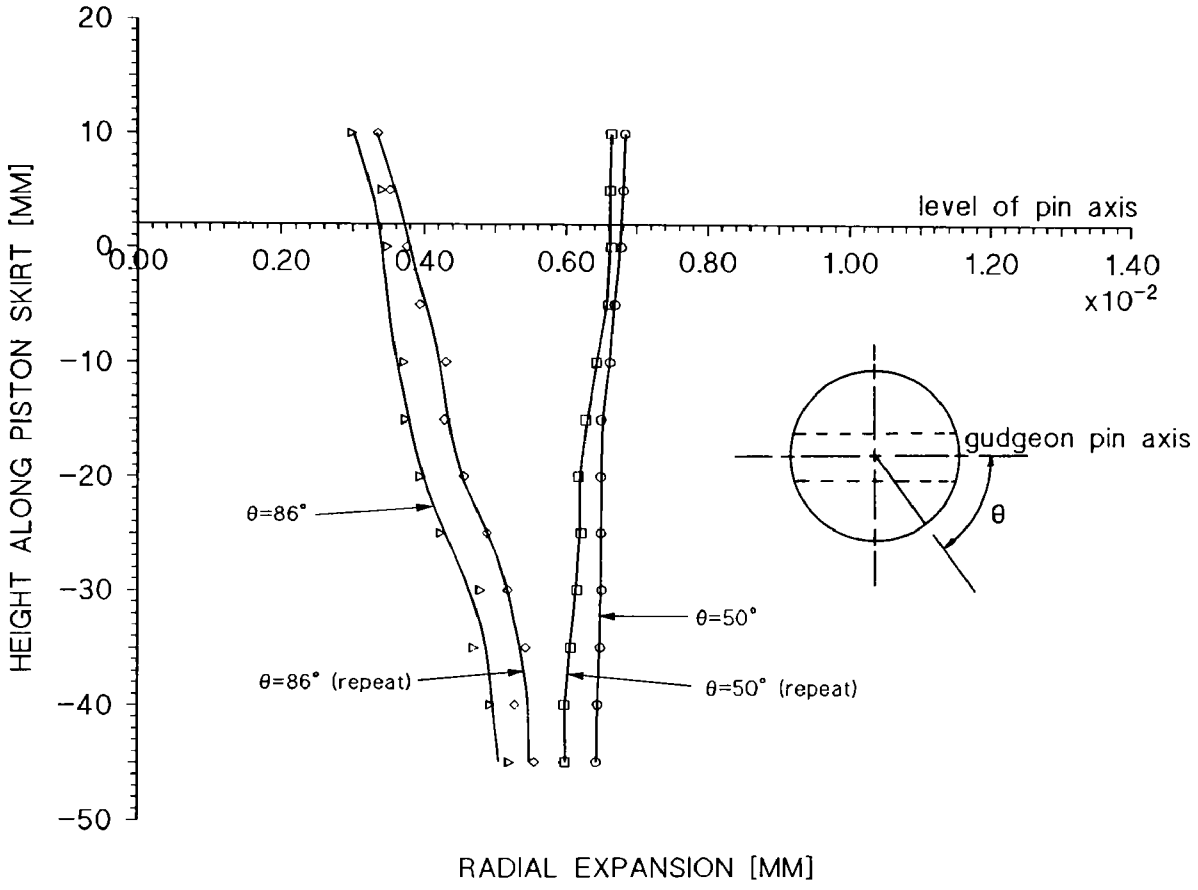

Figure 4.28. Radial displacement along skirt for a rise from 50°C to 58°C

4.7 Conclusions

A simplified technique for measuring the x, y and z components of displacement simultaneously has been developed in this part of the work. The accuracy of the transformation routine developed for relating points on the various interferograms to the corresponding points on the piston surface has been verified by operating on grid points superimposed on the surface of a cylinder. The validity of the technique has been verified by measuring the thermal expansion of a uniform cylinder and comparing the results with the predictions of a finite element model. This technique was then used to measure the expansion of the piston for a 8°C rise. The results indicated the presence of a rigid body movement, suggesting that it is not possible make accurate comparison between experimental and finite element results if the deformation on the front surface alone is considered. This is because, the finite element model was considered for only a quadrant of the piston, in which symmetrical conditions were assumed (Chapter 3). As will be shown in Chapter 6 the mean of the deformation at the front and rear surfaces is free from the effects of body displacement and also assumes symmetrical conditions and thus can be used for accurate comparison with finite elements predictions. However, attempts made to extend the present arrangement to include measurements at the rear surface was unsuccessful due to the limited laser power.

CHAPTER 5

COMPARISON OF MEASUREMENT OF RADIAL EXPANSION AT FRONT PISTON SURFACE USING ESPI AND HOLOGRAPHIC INTERFEROMETRY

5.1 Introduction

Both holographic interferometry (HI) and electronic speckle pattern interferometry (ESPI) are well established optical techniques in the field of surface metrology. ESPI, however, has several practical advantages over HI in terms of real-time observation, ease of obtaining fringes and processing the data. Some of the general applications and comparison between the two techniques have been given by Sharp(1989) and the limitations are discussed by Jones and Wykes(1989).

One of the advantages of ESPI over HI is the possibility of obtaining interferograms that are sensitive only to in-plane displacements. By maintaining the same observation direction it is possible to modify the illumination geometry to obtain complete out-of-plane sensitivity. This obviates the need to evaluate the in-plane and out-of-plane components from the interferometry equations, which may introduce errors as a result of the analysis. The two components can be measured simultaneously if required (e.g. in situations involving non-repeatable loading) by recording the fringes using multiple cameras. This can be achieved by using beams polarised in different planes and recording the various speckle fields into different video systems (Moore and Tyrer,1990). An alternative approach is to use beams of different wavelengths to record the various displacement components.

In this part of the work, a simplified technique using a plane mirror positioned adjacent to the piston was used to obtain two displacement components in the horizontal plane simultaneously. The two simultaneous equations were solved to obtain the magnitude and direction of the displacement vector, from which the radial expansion profile of the piston was determined. The self-contained ESPI rig used is one that was designed for measuring only out-of-plane displacements. No expensive optics or additional cameras were used and the technique developed enabled one to study a 45° sector of the piston surface under non-repeatable thermal loading. In order to compare the results from the ESPI experiments with holography, a holographic rig which is similar in concept to the ESPI rig was developed. A main advantage of this holographic arrangement when compared to the arrangement discussed in Chapter 4 is the possibility

of extending it to measure radial deformation at the rear surface. This will enable one to detect rigid body movement or unequal expansions at the two surfaces. The mean expansion can then be used for comparison with the predictions of a symmetrical finite element model of the piston. The experimental work using the extended arrangement is discussed in Chapter 6.

Comparison of the two techniques showed that the ESPI method has certain advantages over holography from an experimental point of view. These advantages are discussed and the limitations of both techniques are considered.

5.2 An electronic speckle pattern interferometer for simultaneous measurement of two displacement vectors.

5.2.1 Design of the experimental arrangement

A self-contained ESPI rig fabricated at Loughborough University of Technology was used in the measurement of radial expansion profile of the piston (Figure 5.1). The rig consists of a 10mW He-Ne laser, an optical system comprising of mirrors, prisms and beam splitters and a light sensitive CCD camera. The camera was linked to a frame grabber and a TV on which live correlation fringes were displayed. The self-contained rig was designed to measure out-of-plane displacements alone. Strictly speaking, the component measured is at an angle of about 3° to the observation vector. This is due to an offset between the illumination and observation vectors which should be in-line for truly out-of-plane measurements. In most situations where the object is located at more than 600mm from the optical head, the component measured can be assumed to be the out-of-plane component which is given by

$$d = N \lambda/2 \qquad \ldots.5.1$$

where,

N is the fringe order number,

λ is the wavelength of laser .

When the offset is taken into account the displacement will be given by

$$d = N \lambda/(1 + \cos\beta) \qquad \ldots.5.2$$

where,

β is the angle between the illumination and observation vectors.

Since β is small (approximately 7°) the displacements evaluated from equations 5.1 and 5.2 differ by only 0.4%.

In order to use this interferometer to measure two horizontal displacement components simultaneously, a plane mirror was positioned vertically adjacent to the piston and two views of the front surface

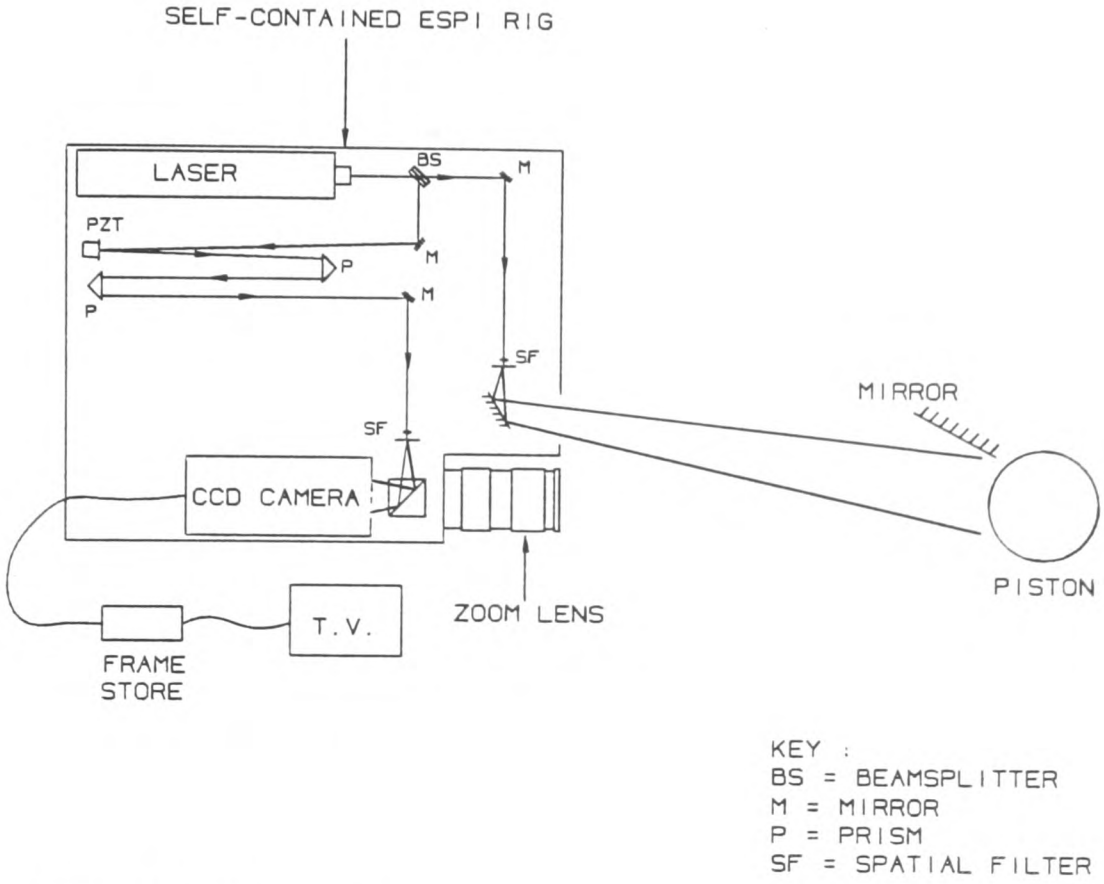

Figure 5.1. Schematic layout of the experimental arrangement for ESPI

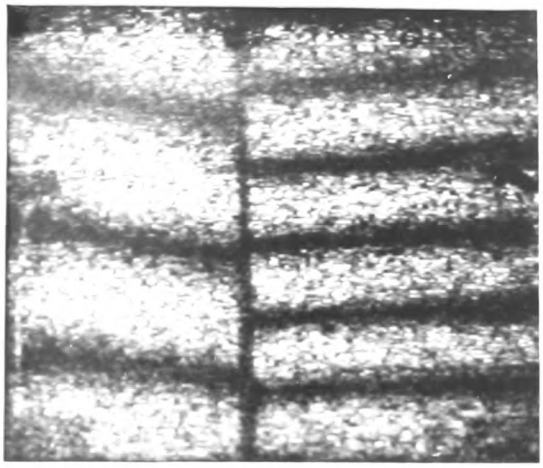

Figure 5.2 Tilt fringes used for calibration of piezo-translator

of the piston were imaged together onto a single video frame (Figure 5.1). Two speckles fields having different sensitivities were thus imaged together for analysis, each occupying approximately half the frame. One of the images (the direct view) gave an approximate out-of-plane component and the other provided a component at approximately 30° to the observation vector. The two components were recombined to give the radial expansion profile of the skirt. Since the object surface is curved, it was not necessary to measure the complete in-plane or out-of-plane component as these are more meaningful for flat surfaces. Thus, it was not necessary to separate the two by optical means. The in-plane and out-of-plane components can, nevertheless, be determined from the measured quantities.

This arrangement allowed one to study 45° sector of the front surface which was considered to be sufficient for the present aims. The vertical in-plane component (in the axial direction) was not measured as the other two components are more significant from a practical point of view. Although the expansion of the piston along the axis may affect the compression ratio of the engine, the general aim of the current study is to investigate how the skirt is deforming radially.

5.2.2 Phase stepping

A two-step phase shifting technique was used to obtain phase stepped fringes. To achieve this, a mirror mounted on a piezo-crystal translator (PZT) was positioned in the path of the reference beam (Figure 5.1). This translator was first calibrated by applying varying voltages in order to obtain the desired phase shift. For this purpose, tilt fringes were introduced into the system by positioning suitable weights at the base of the piston support (Figure 5.2). The voltage was varied between 4.0V to 4.5V and the shift of the fringes were noted in each case. The voltage required for shifting the fringes through 1/3 of a fringe spacing was approximately 4.3V. The maximum phase shift error is estimated to be 8%. A major problem encountered during the calibration was due to drift in fringes caused by external disturbances such as vibration and air movement. Thus, care was taken to ensure that the fringes that are compared to

determine the phase shift are those obtained immediately before and after the phase shift, without any time delay in between.

5.2.3 Technique of analysis

Two techniques of analyses were proposed for evaluating the radial displacements. In the first technique, the angles between the various illumination vectors (due to the non-collimated beam) and the observation vectors to each point on the piston surface were assumed to have negligible effect on the accuracy of the results. This is only true when the area under investigation is small and the object is positioned at a sufficient distance away from the illumination source and the camera. In this case, we have a single illumination vector I and two observation vectors O_1 and O_2 (Figure 5.3). If A is a point on the piston surface that is displaced to A' by a vector d at $\Phi°$ to the z-axis, then,

$$\mathbf{d} = d\sin\Phi\mathbf{i} + d\cos\Phi\mathbf{k}, \qquad \ldots.5.3$$

and the observation vectors for the direct and reflected views are given respectively by

$$O_1 = O_1\mathbf{k} \qquad \ldots.5.4$$

and

$$O_2 = O_2\sin 2\sigma\mathbf{i} + O_2\cos 2\sigma\mathbf{k} \qquad \ldots.5.5$$

where σ is the angle made by the mirror with the z-axis.

The illumination vector is given by

$$I = -I\mathbf{k} \qquad \ldots.5.6$$

Applying the interferometry relation,

$$[o - i].d = n.\lambda \qquad \ldots.5.7$$

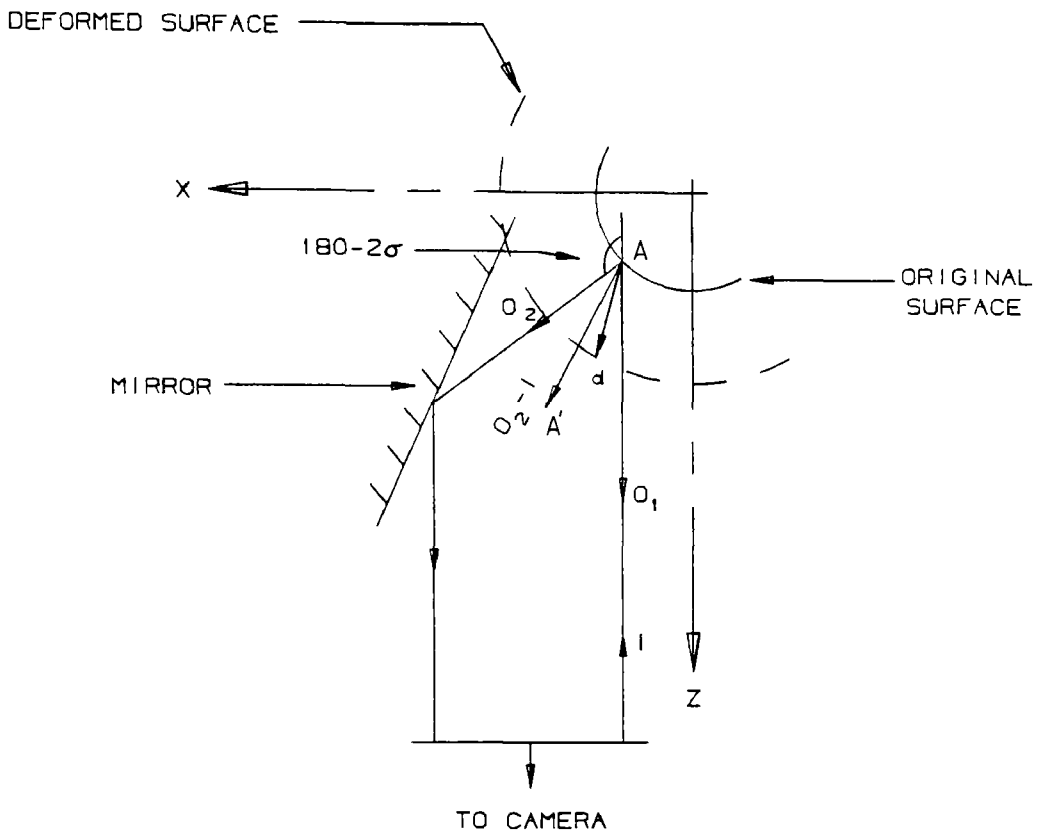

Figure 5.3. Observation and illumination vectors for the ESPI arrangement

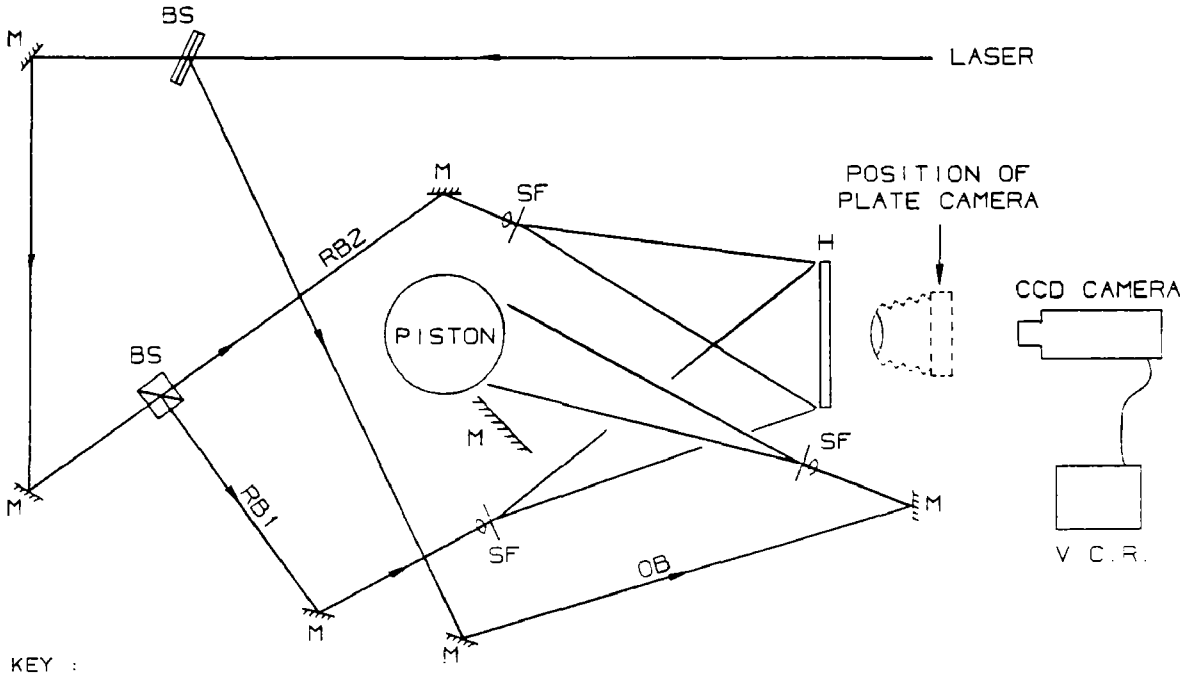

KEY :
BS = BEAM SPLITTER
H = HOLOGRAM
M = MIRROR
OB = OBJECT BEAM
RB1, RB2 = REFERENCE BEAMS
SF = SPATIAL FILTER

Figure 5.4. Schematic layout of the holographic rig for combined double exposure-live fringe method

for the direct view,

$$d(\mathbf{k} + \mathbf{k}).(\sin\Phi\mathbf{i} + \cos\Phi\mathbf{k}) = n_1\lambda \qquad \ldots.5.8,$$

which upon simplifying gives

$$d = (n_1\lambda/2\cos\Phi) \qquad \ldots.5.9.$$

For the reflected view,

$$d[\sin2\sigma\mathbf{i} + (\cos2\sigma + 1)\mathbf{k}].(\sin\Phi\mathbf{i} + \cos\Phi\mathbf{k}) = n_2\lambda$$

$$\ldots.5.10,$$

i.e.

$$d = n_2\lambda/[\sin2\sigma\sin\Phi + (\cos2\sigma + 1)\cos\Phi]$$

$$\ldots.5.11.$$

Equating 5.9 and 5.11 and after simplifying, we have,

$$\Phi = \tan^{-1}(2n_2/n_1 - \cos2\sigma - 1)/\sin2\sigma$$

$$\ldots.5.12.$$

The magnitude of displacement can then evaluated from (5.9) or (5.11). Thus by finding the order numbers at the corresponding points on the direct and reflected views of the piston it was possible to obtain the displacement vector in the horizontal plane. The in-plane and out-of-plane components can be evaluated from

$$d_x = d\sin\Phi \qquad \ldots.5.13(a)$$

and

$$d_z = d\cos\Phi \qquad \ldots.5.13(b),$$

from which the radial displacement can be determined.

In the second technique of analysis, two simultaneous equations were formed from the interferometry equation (equation 4.1) in two unknowns, i.e.,

$$\begin{bmatrix} o_1 - i \\ o_2 - i \end{bmatrix}\begin{bmatrix} D_x \\ D_z \end{bmatrix} = \begin{bmatrix} N_1 \\ N_2 \end{bmatrix}\lambda$$

$$\ldots.5.13(c)$$

In this technique, the illumination and observation vectors to each point on the piston were calculated individually. In both techniques, however, the sensitivity vector was assumed to lie in the horizontal plane (x-z) in order to simplify the arrangement. Such an assumption will affect both the ESPI and holographic results approximately equally and will still enable an accurate comparison between the two results to be made. A detailed discussion of the effects of this assumption on the measurement is given in Chapter 6.

The two equations were solved to obtain the two displacement components D_x and D_z. The displacement from the second technique (equation 5.13(c)) is expected to have a higher accuracy than the first (equations 5.11 to 5.12). The results obtained using each of the above techniques of analyses were, nevertheless, compared for a 5°C rise to give us an indication of the deviation in displacement due to the assumptions made in the first technique of analysis.

5.3 Holographic interferometer for measuring radial deformation

A schematic layout of the holographic arrangement used is shown in Figure 5.4. The arrangement of the piston, heating element and the mirror was similar to those used in the ESPI arrangement. The optics were arranged so that a two reference beam technique (Abramson 1981) can be used to record both double exposure and live fringes using a single 4in.x 5in. holographic plate for a 20°C rise. In order to confirm the results from this set-up a second holographic arrangement was used based only on the live fringe method where the final and initial fringes orders were subtracted for the analysis (Figure 5.5).

5.4 Verification of the mirror concept using a cantilever.

The mirror concept proposed for measuring two displacement components simultaneously was initially verified by using a cantilever. The verification was carried out for both ESPI and holographic techniques. The cantilever was positioned vertically with its fixed end at the base and its plane was inclined at ß (45° and 60°) to the observation direction along the z-axis (Figure 5.6). A

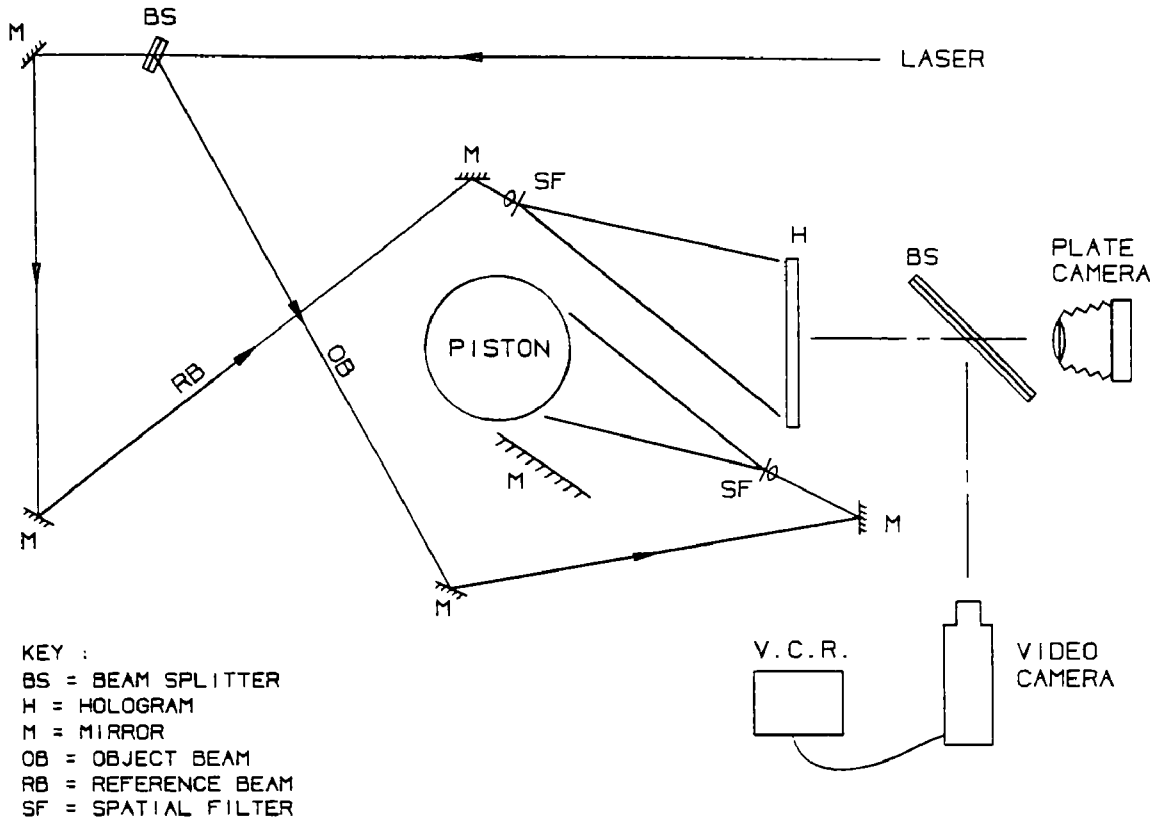

Figure 5.5. Schematic layout of the holographic rig for the live fringe method

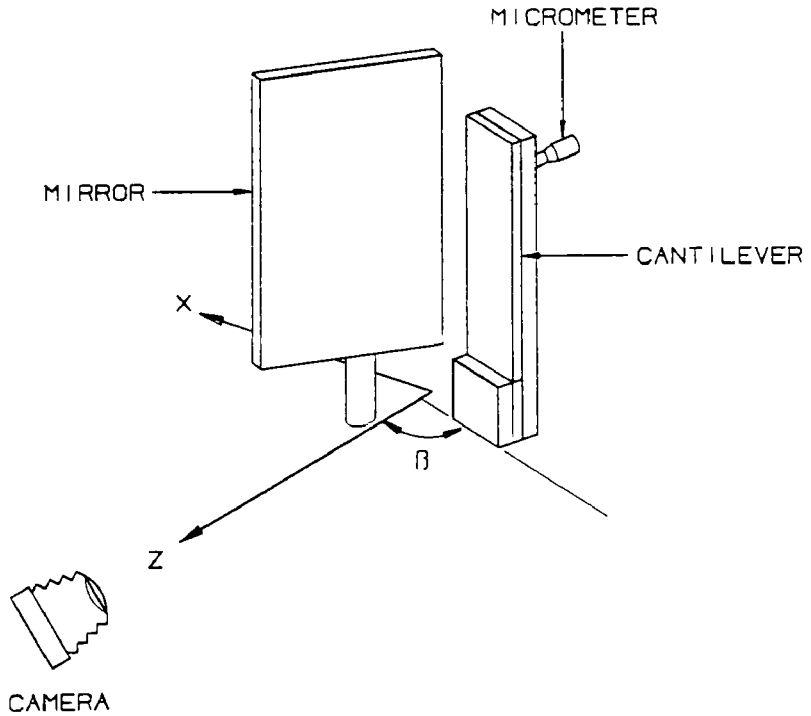

Figure 5.6. Schematic of cantilever arrangement to verify mirror concept

vertical mirror inclined at 45° (to the observation direction) was positioned adjacent to the cantilever. A point 100mm from the fixed end was displaced through 0.004mm by using a mounted precision micrometer.

The ESPI fringes were shifted in 3 steps and then analysed to obtain the phase maps. The raw and filtered fringes before the phase step for ß=45° are shown in Figure 5.7(a)-(b) and the phase map is shown in Figure 5.8. Due to drift in the fringes, a zero-order dark fringe was not always present at the fixed end. This did not introduce significant errors because the datum on the phase map was selected at the fixed end of the cantilever. The grey level intensity G_d along the datum line (at zero-order fringe) was evaluated. Thus, along the cantilever, the fringe order at any point P with grey level intensity G_p is given by,

$$N_p = (G_p - G_d)/255 + N \qquad ....5.14$$

where N (=0,1,2,..) is the lower order of the fringe adjacent to P. Since the cantilever was positioned at 700mm from the camera lens and the illumination source, the observation and illumination vectors can be assumed to be approximately in-line. The direction of movement of P is then given by,

$$\Phi = \tan^{-1} (2N_2/N_1 - 1) \qquad ....5.15$$

and the displacements is given, by

$$d = N_1 \lambda /2\cos\Phi, \qquad ....5.16$$

where N_1 is the order number at P on the direct view

N_2 is the corresponding order on the reflected view.

The in-plane and out-of-plane components were evaluated from equations 5.15 and 5.16.

The calculated displacements were plotted and compared with the predictions of the deflection theory obtained from,

$$y = - [P/EI](50x^2 - x^3/6) \qquad ....5.17$$

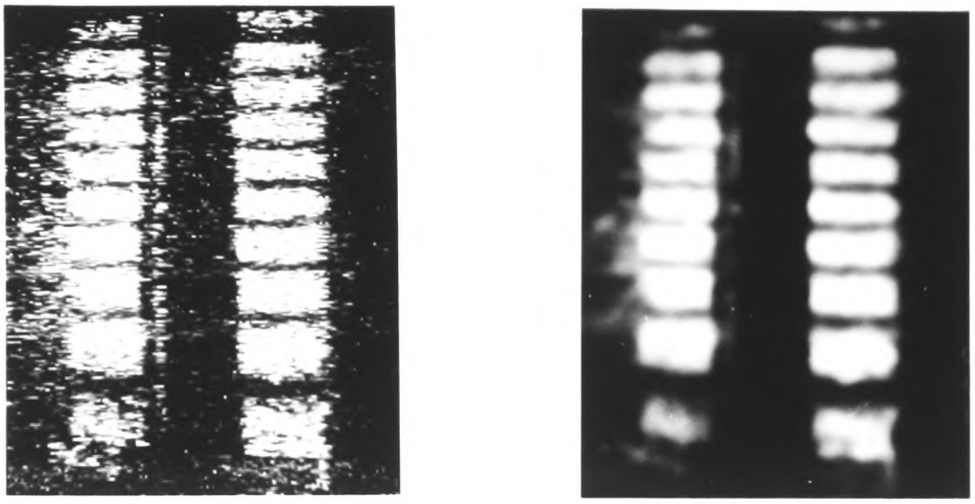

(a) (b)

Figure 5.7. ESPI fringes on cantilever for ß=45° :
(a) raw fringes (b) filtered fringes

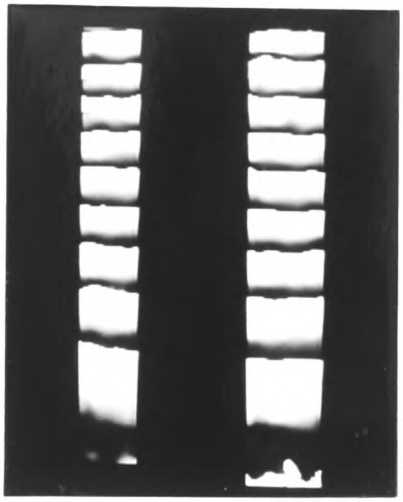

Figure 5.8. Phase map for cantilever

For the holographic analysis, it was necessary to introduce an angle γ between the illumination and observation vectors due to the physical arrangement of the optical components and the plate holder (Figure 5.9). Double exposure fringes on the cantilever and its (reflected) image were photographed for analysis (Figures 5.11(a)-(b)). The fringe centrelines were scaled from the photograph and the fractional order numbers at 10mm intervals along the cantilever were determined from plots of order numbers versus distance from fixed end. With reference to the vector diagram in Figure 5.9 and from equation (5.7) it can be shown that the direction of displacement of any point on the cantilever is given by,

$$\Phi = \tan^{-1} \frac{(1 + \cos\gamma)N_2/N_1 - \cos\gamma}{1 + \sin\gamma - (N_2/N_1)\sin\gamma} \qquad ....5.18,$$

and its magnitude by,

$$d = \frac{N_1\lambda}{\sin\gamma\sin\Phi + (1 + \cos\gamma)\cos\Phi} \qquad ....5.19$$

where,

Φ is measured from z-axis (Figure 5.9),

N_1 is the order number from the direct view,

N_2 is the order number from the reflected view,

γ is the angle made by the illumination vector with z-axis.

It can be noted that the equations (5.12) and (5.18) are the same when $\gamma=0°$ and $\sigma=45°$.

The experimental results for the cantilever were compared with those predicted by the deflection theory (Figures 5.10(a)-(c)). The close agreement between the results confirms the validity of the mirror concept for measuring in-plane and out-of-plane displacements simultaneously. The agreement of the results also shows that the experimental errors, including phase-stepping errors, in ESPI causes the displacement to differ by a maximum of about 7%.

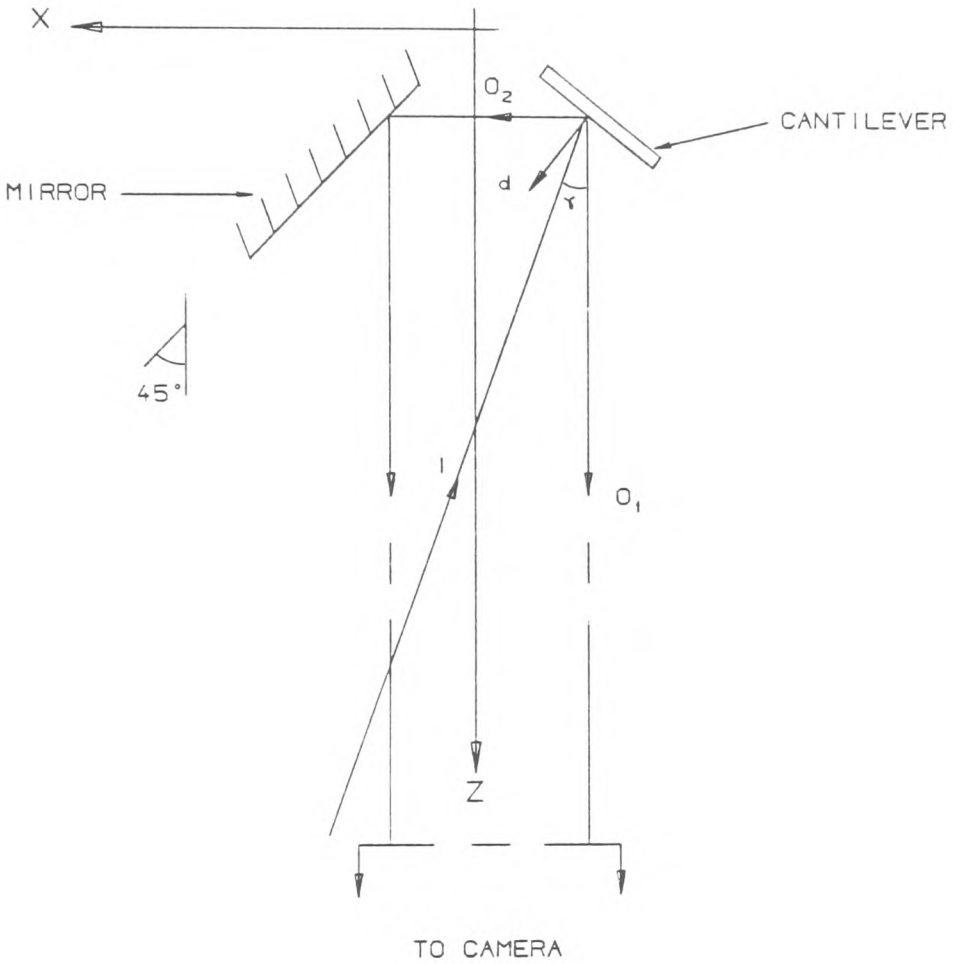

Figure 5.9. Observation and illumination vectors for cantilever arrangement in holographic experiments

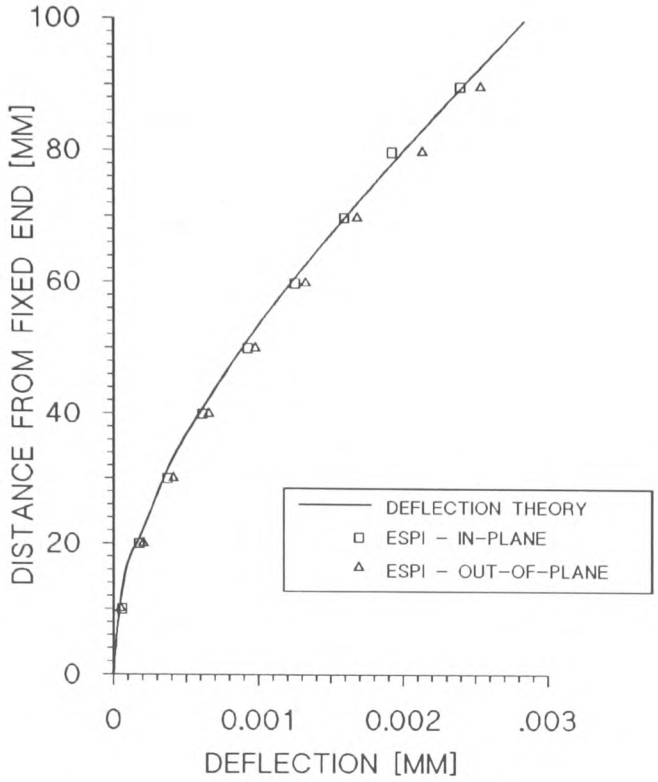

(a)

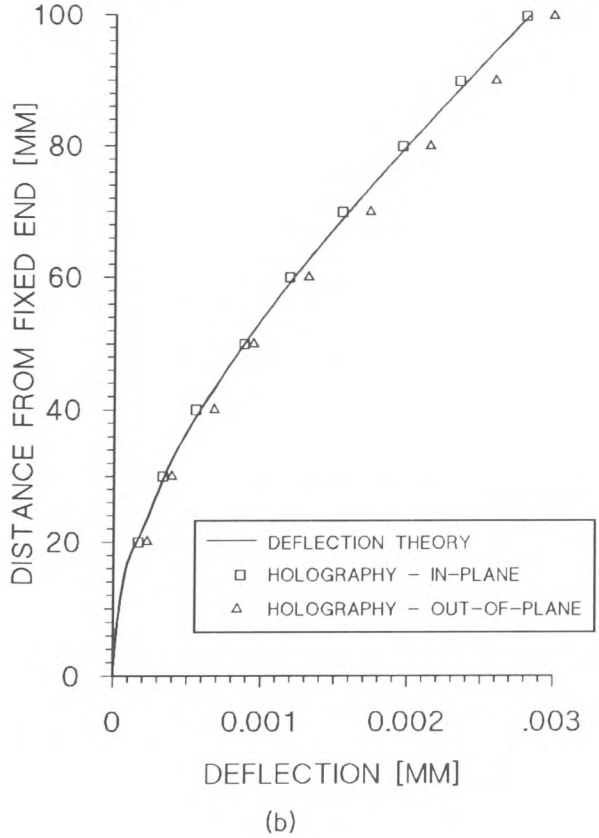

(b)

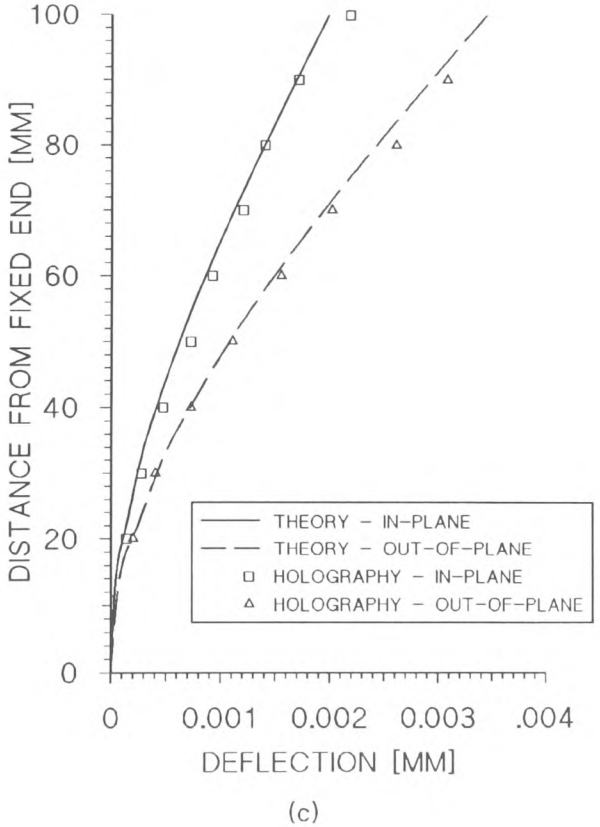

(c)

Figure 5.10. Comparison of experimental results with predictions of deflection theory for (a) ESPI (β=45°), (b) holography (β=45°) and (c) holography (β=60°)

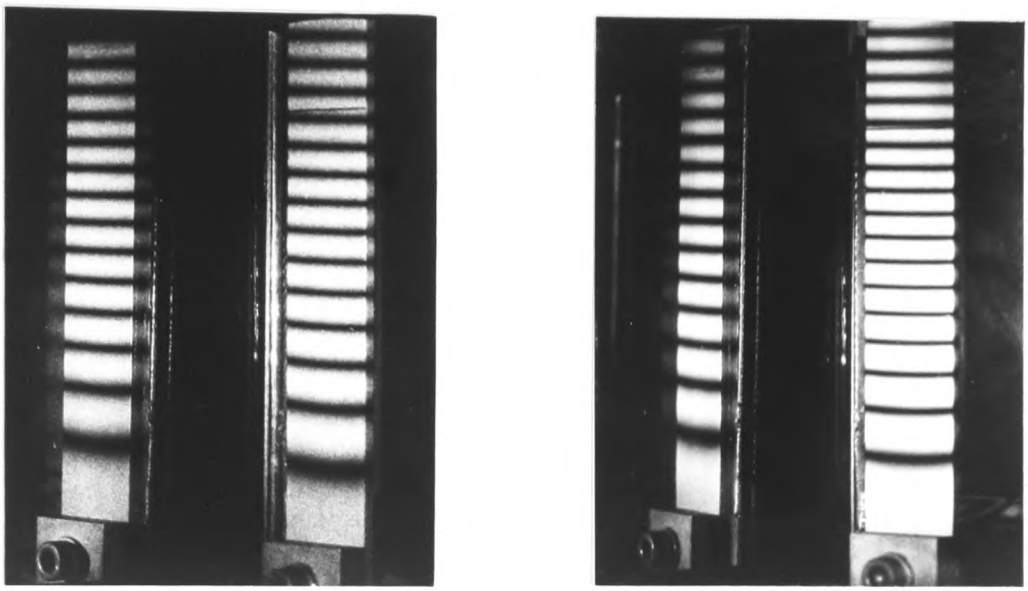

(a) (b)

Figure 5.11. Holographic fringes on cantilever inclined at (a) ß=45° and (b) ß=60°

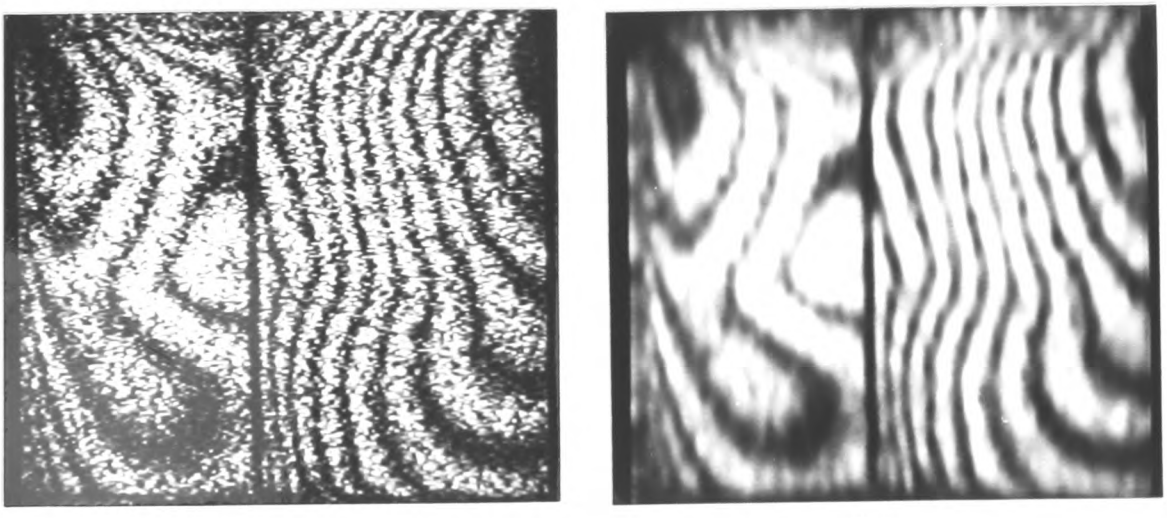

(a) (b)

Figure 5.12. ESPI fringes for 50°C to 55°C rise : (a) raw fringes, (b) low-pass filtered fringes

5.5 Measurement of radial deformation using ESPI

Before the start of the experiments, problems relating to the effects of thermal current on the ESPI fringes were investigated by using different heating rates. When the heating rate was set to a low value (<500W) the fringes appeared to shimmer as they moved and the effect increased when the heating rate was lowered further. After a series of tests, a heating rate of 600W produced fairly steady fringes which showed very little effect of thermal current. This observation can be attributed to the effects of changes in refractive index of the air surrounding the piston which is predominant when the expansion rate of the piston is low. When the piston expands rapidly due to a higher heating rate, the change in path length of the observation and illumination vectors due to expansion of the piston exceeds the path length variations due to changes in the refractive index of the air. Hence, the effects of thermal current are less at the higher heating rate. This condition was, however, achieved only in a carefully controlled laboratory environment where air movement was minimum. From the recording of live fringes the maximum shift in fringe position due to thermal effects is estimated to be 0.2 of a fringe spacing. For a 5°C rise in which 12 fringes were counted crossing a reference point, this introduces an error of less than 2%.

The measurement was carried out for a rise from 50°C to 70°C, measured below the crown (thermocouple T11). The phase of the fringes was stepped in three stages by applying -4.3V, 0V and 4.3V to the piezo-electric translator. The voltage was applied manually using a two-way switch while the live fringes were recorded. Preliminary tests with phase stepped fringes showed that when the rise in temperature exceeded 5°C, the phase fringes formed were discontinuous at certain points. This is due to the incorporation of two images (direct and reflected) on a single frame of the video monitor thus limiting the size of each image and hence the density of the fringes. Therefore, measurement for a 20°C rise was carried out in four stages of 5°C rise each, resetting the reference frame at the end of each stage (immediately after phase stepping). The phase stepped fringes were digitised into a Kontron image processor and low-pass filtered to remove the high frequency noise. A phase stepping routine developed at Loughborough University (Kerr and Tyrer 1988) was used

to obtain the phase maps from the filtered fringes. The raw ESPI fringes and the low-pass filtered fringes, before the phase step, for the first stage of temperature rise are shown in Figures 5.12(a)-(b). The phase maps for two of the stages are shown in Figures 5.13(a)-(b).

The order number at each of the grid points on the piston surface were determined from the grey level intensities of the phase map. This was done by first transforming the grid points, in global coordinates, into pixel coordinates. To achieve this the z-axis of the piston was initially translated so that it coincides with the principal axis of the lens. The grid points were then projected onto a two dimensional perspective plane located perpendicular to the principal axis and at an arbitrary distance from the nodal point N of the lens (Figure 5.14). The coordinates of the projected points (x_{PP},y_{PP}) were determined from the following expressions:

$$x_{PP} = (D_{PP} \times x')/(z_N - z')$$

$$y_{PP} = (D_{PP} \times y')/(z_N - z') \qquad \ldots.5.20$$

where,

D_{PP} = distance from perspective plane to nodal point of camera lens,

(x',y',z') = global coordinates of point on piston surface

z_N = z-coordinate of nodal point.

The distance D_{PP} merely controls the magnification of the projected image. Scaling is later performed by comparing the lengths of lines joining selected datum points on the perspective plane and the corresponding points in pixel coordinates, obtained from the computer screen with the aid of a cursor. In the case of the reflected view, the coordinates of the image of the grid points were first evaluated before projecting them onto the perspective plane. The position of the mirror was measured by using the laser beam method described in Chapter 4. The programs written to achieve the above transformation (TRANSGRDO.FOR and TRANSGRDI.FOR) are given in Appendix A2.

The projected grid points which have been scaled to match the local pixel coordinates were then plotted onto the phase map. An interactive technique was used to compute the order numbers at each

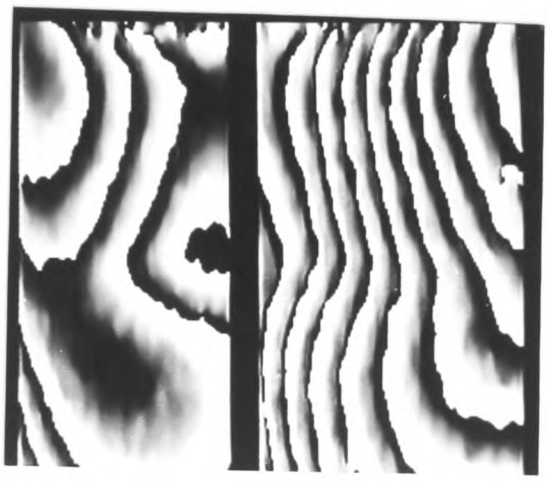

(a)

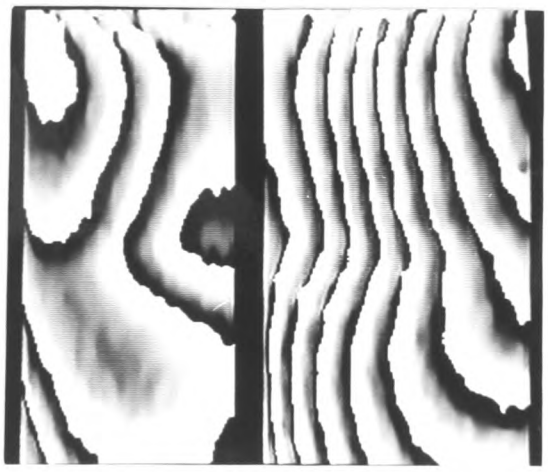

(b)

Figure 5.13. Phase maps for (a) 50°C to 55°C and (b) 55°C to 60°C rises

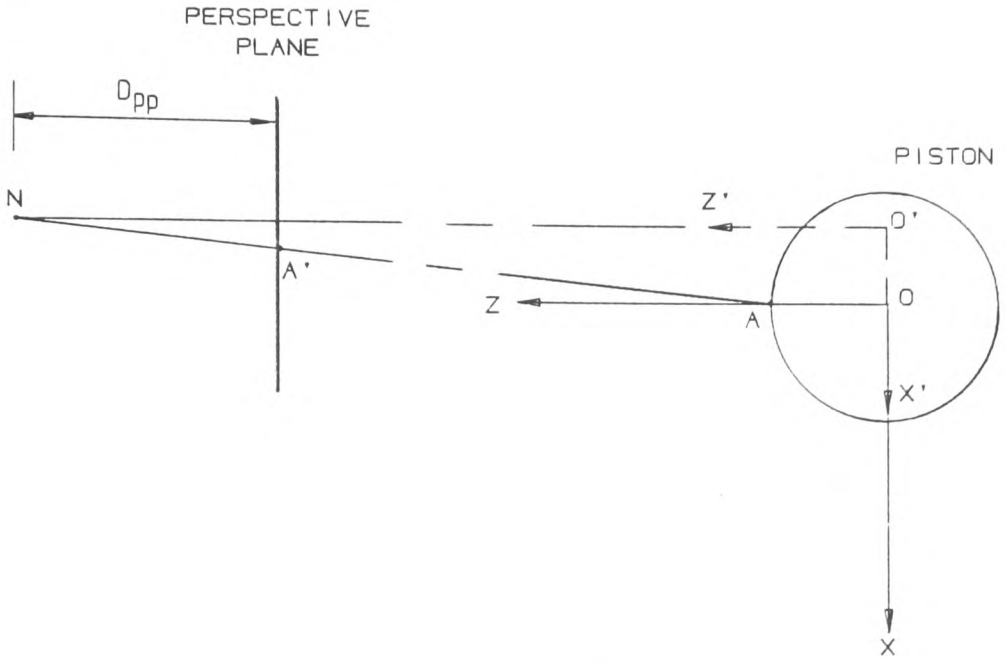

Figure 5.14. Transformation method for ESPI set-up

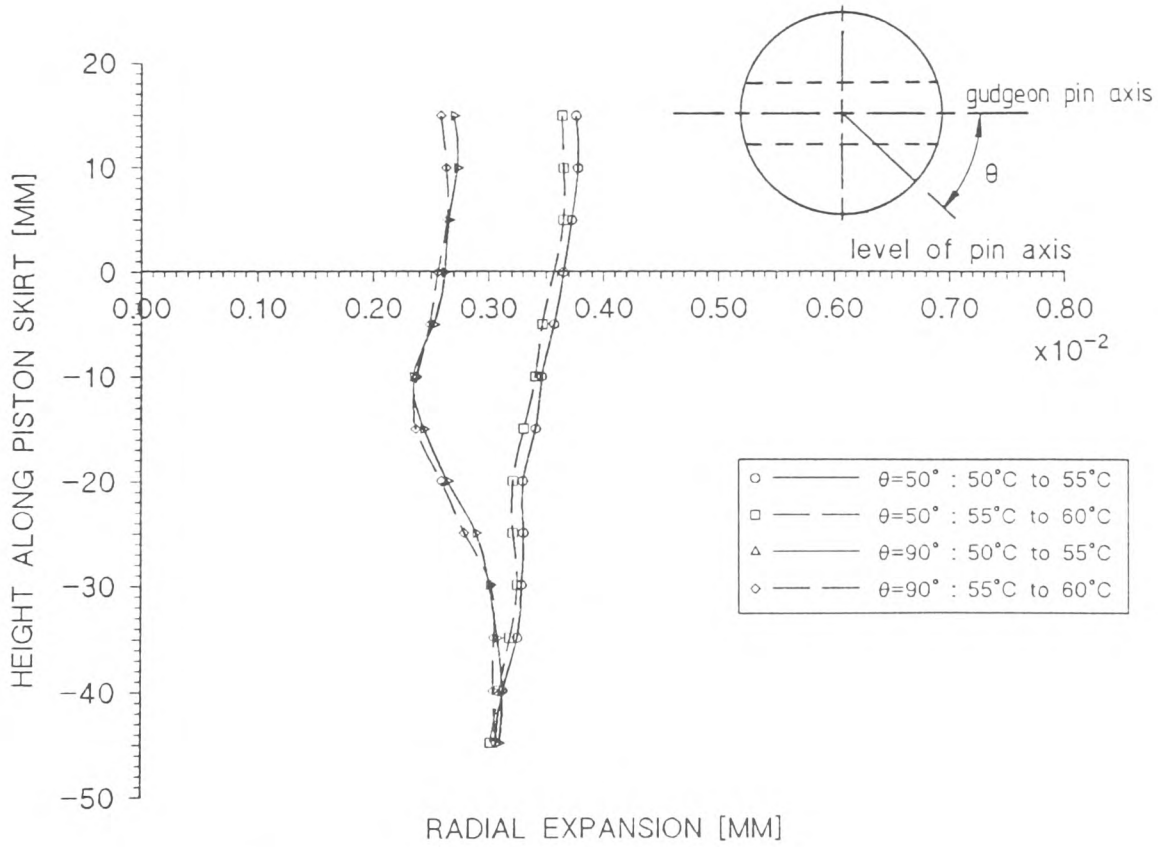

Figure 5.15. Repeatability check for ESPI results

of the grid points. In this technique, the location of a reference fringe whose order number is known was first established on the phase map. This was done by finding the pixel coordinates of six arbitrary points on the fringe centreline (on the raw fringe pattern before stepping) and their grey level intensities on the phase map. The grey level intensities were averaged and when this value is encountered while scanning across the phase map a change of one fringe order (i.e. a phase change of 2π) occurs.

In the computer algorithm developed for finding the order numbers from the phase map, the higher order number of a fringe located adjacent to the point (at which the order number is required) is supplied. If the grey level at this point is G_p, then, the order number is given by

$$O_p = O_h - G_p/255 - (255 - G_r)/255 \qquad ....5.21$$

where,

O_h = higher order number of adjacent fringe

G_r = grey level of reference fringe centreline (averaged over six points)

A setback of this technique is that the higher order number has to be supplied to the program at each grid point. Although a fully automatic method can be developed to scan the phase map and identify the order numbers at each of the grid points automatically, such a technique was not considered here because of time constraints. The present method, nevertheless, enabled the analysis to proceed without significant loss of time. The computer programs developed to determine the order numbers at each of the grid point (GETORDO.FOR and GETORDI.FOR) are also listed in Appendix A2.

Having determined the order numbers at each of the grid points for both the direct and reflected views, the displacement components were then evaluated from equations 5.12 to 5.14 (see program SOLVE2.FOR in Appendix A2). A total of 104 grid points covering a sector of 45° on the piston were used in the analysis and this was repeated for each of the four stages. The displacement from each stage was vectorially added to the next resulting in a total displacement for a 20°C rise .

Since each stage of the temperature rise can be assumed to be a repeat of the next (due to the linear expansion characteristic of the skirt below the stress free temperature (Fletcher-Jones (1982))) it was not necessary to repeat the measurement to confirm repeatability. It was sufficient to compare the displacement for one stage of temperature rise with the next. The comparison for the 50°C to 55°C and 55°C to 60°C rises are shown in Figure 5.15 in which good agreement between the two can be seen. The maximum deviation is estimated to be 4%.

5.6 Measurement of radial deformation using holographic interferometry.

A two reference beams double exposure technique was used in the holographic experiments. A 4in.x 5in. holographic plate was initially exposed at 50°C using reference beam RB1 (Figure 5.4) and finally at 70°C using reference beam RB2. Thus, when the processed plate was illuminated by RB1 and RB2 individually, reconstructed images of the piston at 50°C and 70°C were formed. When the plate was illuminated simultaneously by RB1 and RB2 a reconstructed image of the piston covered with fringes due to deformation from 50°C to 70°C was obtained. Since a zero-order fringe was not present, the fringe orders were determined by recording the movement of live fringes, on a video tape, obtained by using the hologram recorded at 50°C during a repeated heating sequence. The tape was replayed to count the number of fringes crossing a reference point.

The double exposure fringes were photographed by using the plate camera (Figure 5.16). By assuring large images on the film it was possible to work with high density fringes caused by deformation from 50°C to 70°C rise in a single stage. The centrelines of the fringes were digitised manually as in previous work and were transformed back onto the piston surface by using a slightly modified version of CAMERA1.FOR (see Chapter 4).

The transformed fringe centrelines were plotted on the developed surface of the piston and the fractional order numbers at the superimposed grid points were determined as in previous analysis (Chapter 4). The displacement was then evaluated using equation 5.14.

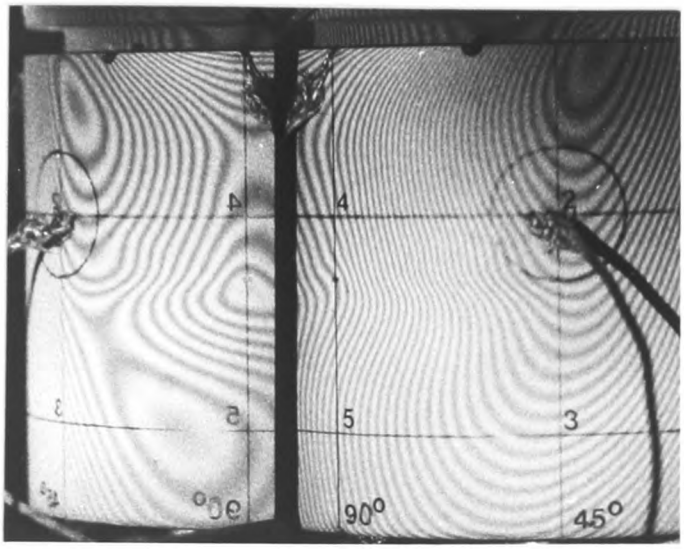

Figure 5.16. Double exposure holographic fringes for rise from 50°C to 70°C

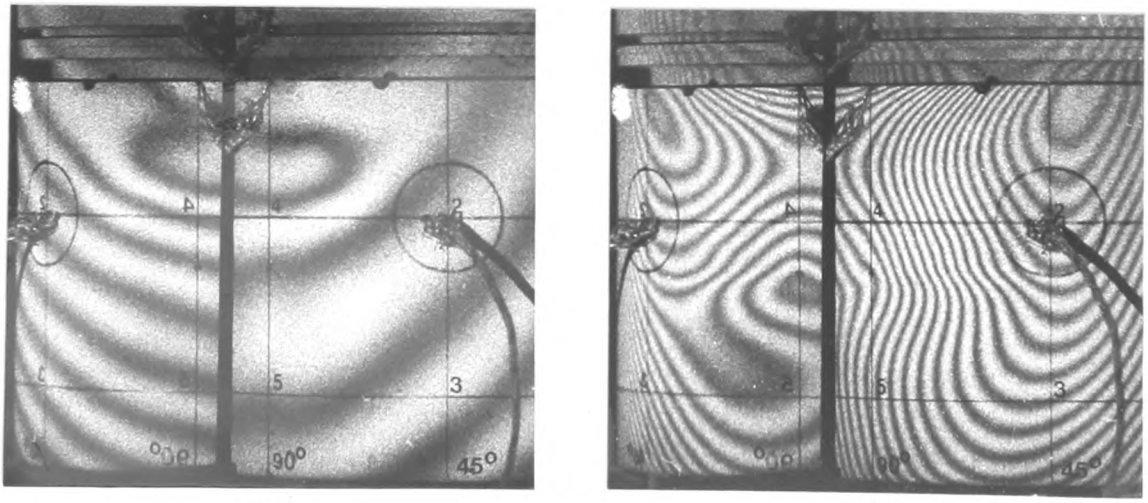

(a) (b)

Figure 5.17. Live holographic fringes at (a) 50°C (initial) and (b) 60°C (final)

The holographic measurement was repeated twice to confirm repeatability.

In the arrangement used the plate and video cameras were set in-line. After photographing, the plate camera was removed from its support to allow for the video recording. In this manner, high quality recordings can be assured on both the film and the video tape. Errors due to misalignment between the two camera have been accounted for in the analysis and are discussed in Appendix A3.

The results from the two reference beams double exposure technique were compared with those from the fringe order difference technique (set-up shown in Figure 5.5). In the second technique, initial and final fringe patterns at 50°C and 60°C, respectively, were photographed for analysis. The movement of live fringes was recorded simultaneously by reflecting the images in a beam splitter positioned in the view path of the plate camera. Absolute fringe orders on the photographs were determined from the video recording. The final and initial fringe patterns (Figures 5.17(a)-(b)) were digitised and the fringe orders were subtracted. The resulting fringe orders were then used in the evaluation of the displacement.

5.7 Discussion of results

5.7.1 Comparison of ESPI results from approximate and accurate solution.

Comparison of the results from ESPI for the two techniques of analysis (equations 5.11 to 5.12 and equation 5.13(c)) is shown in Figure 5.18. The radial deformation at 10mm above and 40mm below the gudgeon pin axis was found to differ by a maximum of 5% for the two types of analyses. Thus, for the ESPI arrangement, the errors due to the assumption that the sensitivity vectors to each point on the piston is constant is within the acceptable limits.

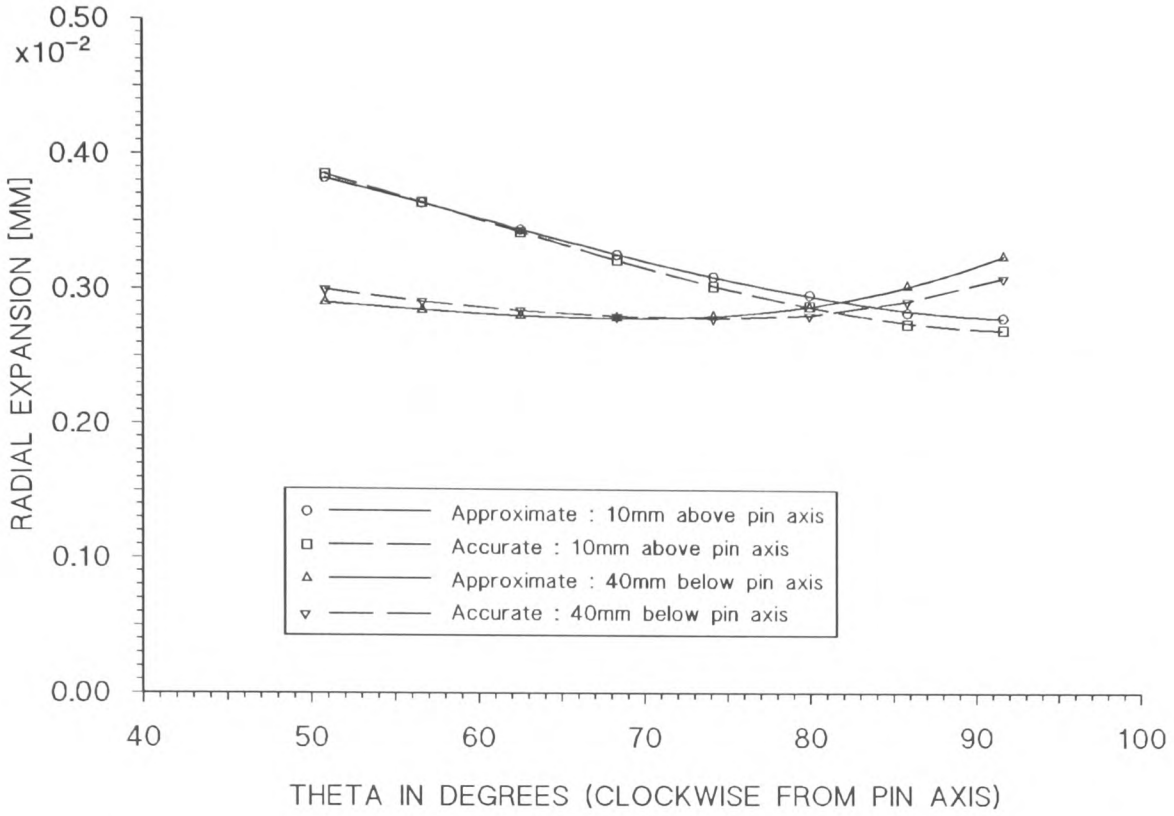

Figure 5.18. Comparison of ESPI results from approximate and accurate solutions (50°C to 55°C)

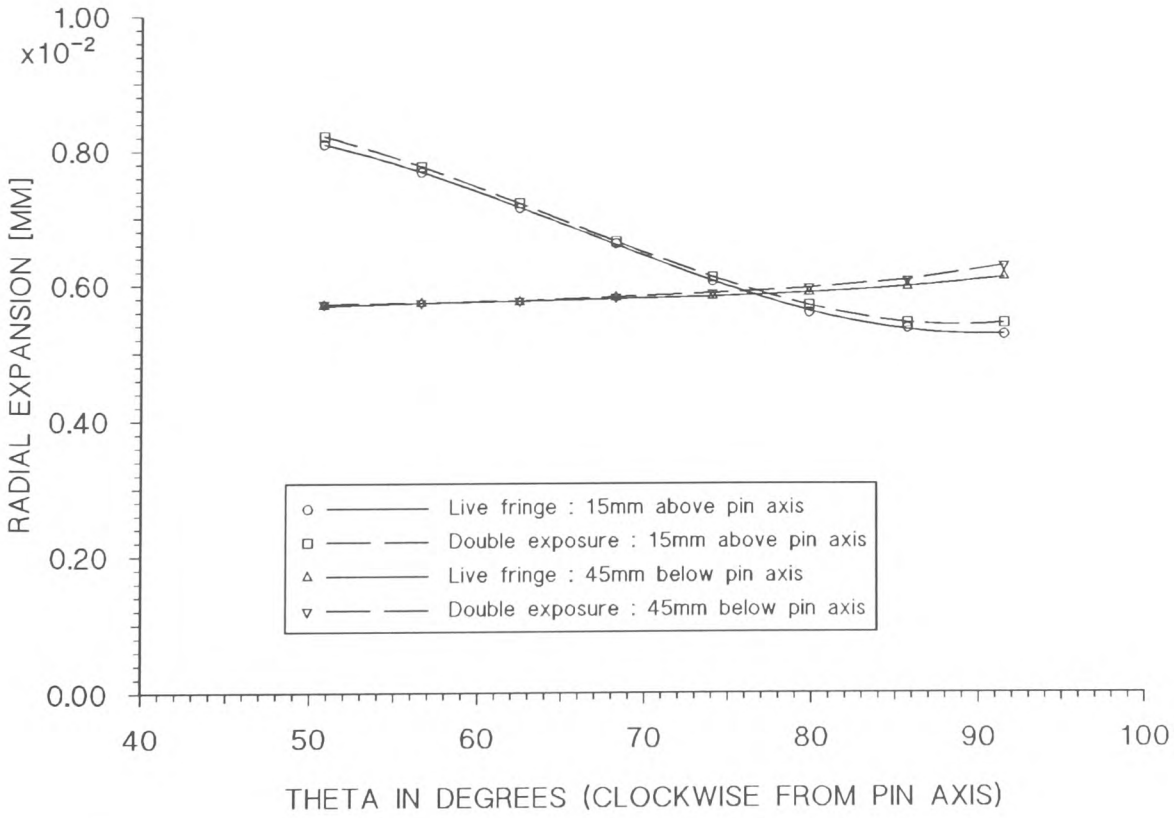

Figure 5.19. Comparison of radial expansion from double exposure and live fringe techniques (50°C to 60°C)

5.7.2 Comparison of holographic results for double exposure and live fringe techniques.

Figure 5.19 shows a comparison of the radial expansion plots from the double exposure and fringe order difference techniques. In this figure, the curve for the double exposure technique was obtained by taking half of the radial expansion for a 50°C to 70°C rise. The comparison indicates a difference of less that 4% between the results from the two techniques, suggesting that they are capable of producing similar results.

5.7.3 Comparison of repeated holographic measurements

The repeated holographic results show good agreement with one another along θ=50° (maximum deviation is 3%) and a deviation of about 7% along θ=90° (Figure 5.20). The greater deviation along θ=90° agrees with the results presented in Chapters 4 and 6 and is attributed to the different body displacements experienced by the piston.

5.7.4 Comparison of ESPI and holographic results

The radial expansion profiles of the piston in the horizontal planes at 45mm below and 15mm above the gudgeon pin centreline were plotted against θ for the results from ESPI and double exposure holography (Figure 5.21). The expansion profiles in the vertical planes along the skirt are shown in Figure 5.22, plotted along θ=50° and θ=90°.

Figure 5.22 indicates a similarity in the expansion profiles of the skirt for the results from ESPI and holography. The displacement measured using ESPI are, however, about 6% to 10% lower than those from holography at the top of the skirt, along θ=50°. The lower displacement measured using ESPI may be attributed to systematic errors in each stage of the analyses (four stages of 5°C rise each), resulting in a total displacement which is smaller than the displacement measured using holographic method. Such accumulated

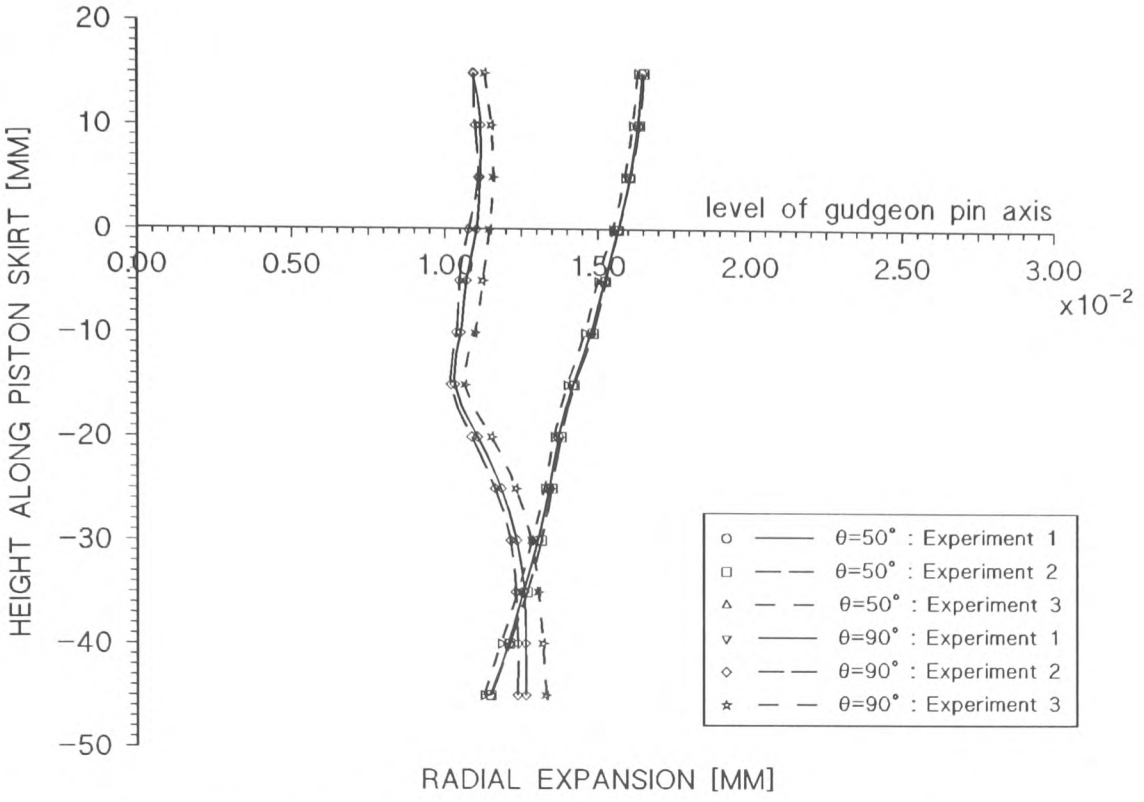

Figure 5.20. Comparison of repeated holographic results (50°C to 70°C)

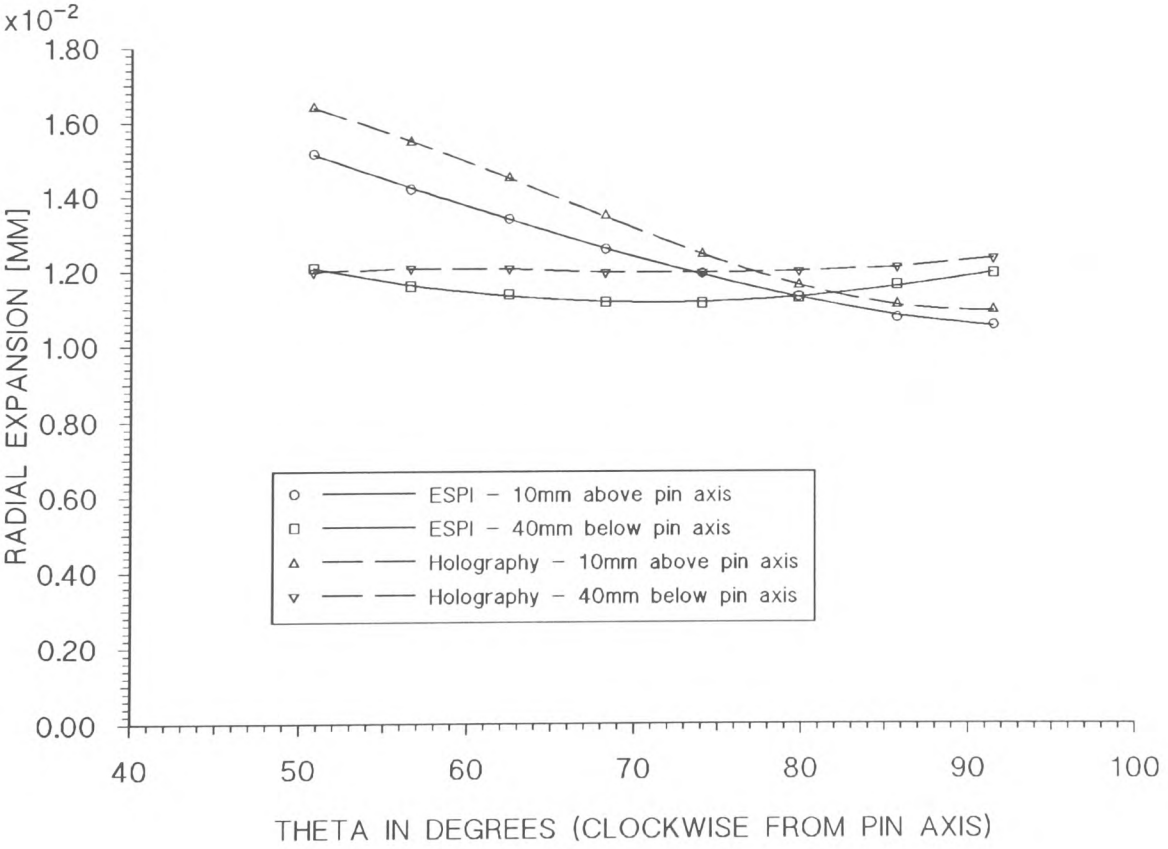

Figure 5.21. Comparison of ESPI and holographic results : radial expansion in the horizontal planes (50°C to 70°C)

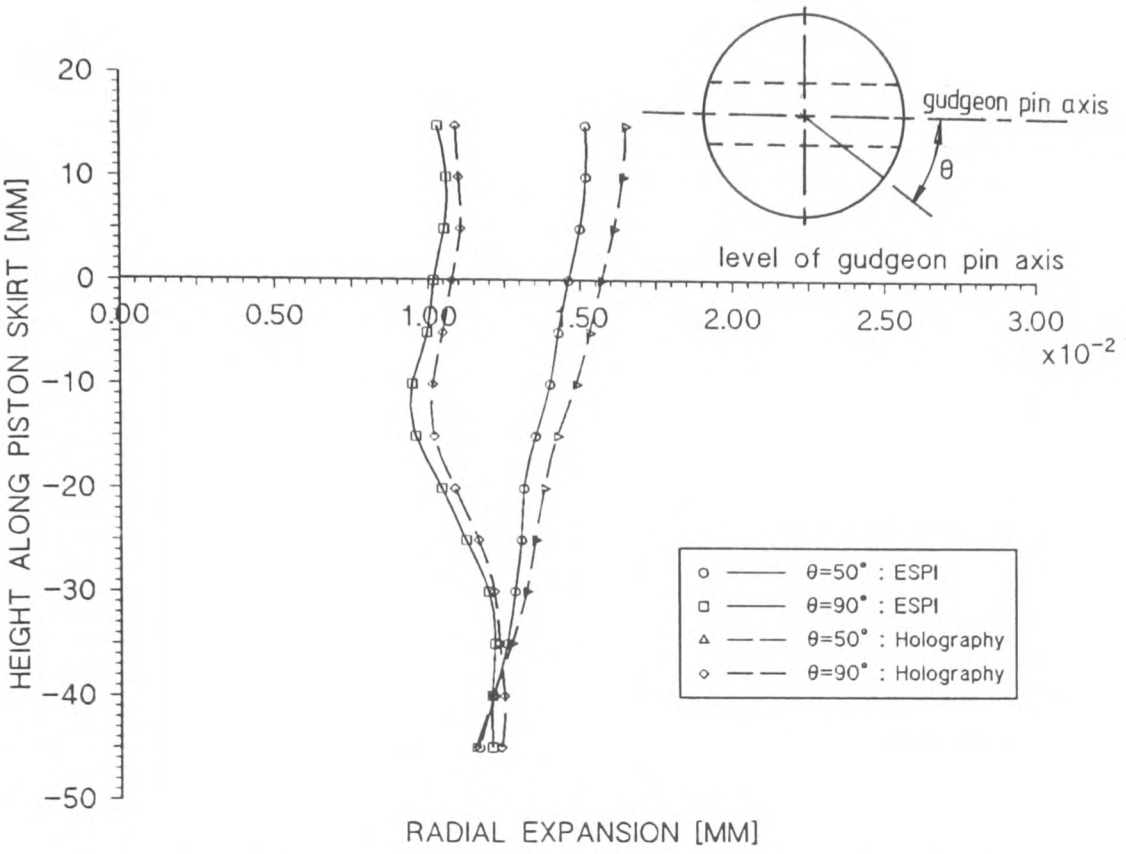

Figure 5.22. Comparison of ESPI and holographic results (50°C to 70°C)

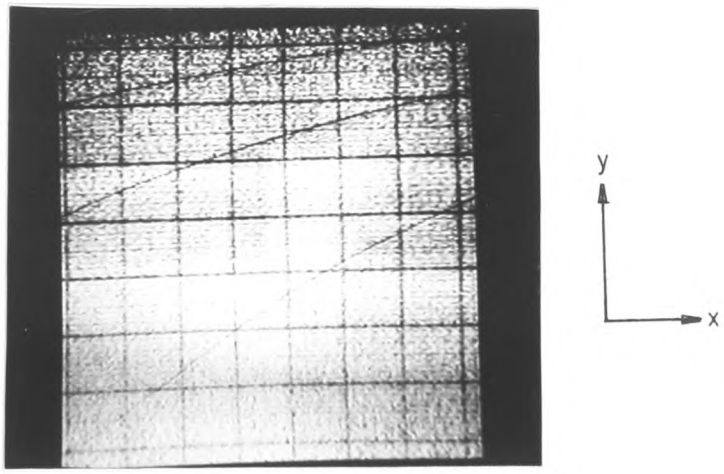

Figure 5.23. Grid on video image

errors are not present in the holographic measurement because the temperature rise was achieved in a single stage. These errors could be due to the following factors :

a) distortion in digitised images,

b) a delay between phase stepping and resetting of next video frame,

c) inaccuracies in the measurement of system geometry used for transformation purposes.

Distortion of video images is known to be a setback when accurate measurements are to be made (Winther 1988, Jones and Wykes 1989). The magnification can vary across the surface of the image and accurate calibration may be necessary. In such cases it is not possible to use simple mathematical transformations to relate points on the video image and the corresponding points on the object surface without a loss of accuracy. When a few datum points are used to achieve the transformation, the accuracy of the transformation of these datum points does not necessarily assure the accuracy of transformation of all surface points.

In the current application, the effects of video distortions were investigated by imaging a high quality graph paper and scanning the image in the horizontal(x) and vertical(y) directions to locate the positions of grid points in pixel coordinates (Figure 5.23). The scaling factor in the x- and y-directions were found to be 4.5 pixels/mm and 6.7 pixels/mm respectively. The maximum local distortion of pixel distances for 10mm grid intervals in the two directions were 2 pixels. This deviation could be due to distortion of the video image or due to the limited resolution of the cursor (which was 2 pixels wide) or a combination of both. The latter reason appears more likely due to the random variation of the distances between the grid points in pixels coordinates. Nonetheless, a local deviation of 2 pixels could cause a maximum deviation of 4 pixels in the lengths of lines joining selected datum points. Since these lines were used for scaling purposes, this could introduce an error in the transformation. This error can be determined by comparing the positions of the transformed datum points with the actual datum points on the screen. The maximum deviation was found to be 5 pixels, which corresponds to a positional error of 0.9mm on the piston surface. Since the fringe spacing is about 4mm, this positional error will introduce an error of about 3% to 4% in the displacement.

Although this error is small in a single measurement, repeated measurements with addition of displacement from several stages can cause this error to accumulate. A solution to the problem of image distortion is to use surface contouring techniques to relate the surface coordinates to the phase fringes.

Distortions in the photographs of the holographic fringes are, however, smaller when compared to the distortions in a video image. Hence, a simple perspective transformation routine can be applied to transfer fringe centrelines from the photographs and back to the piston surface accurately (see Section 4.4 of Chapter 4). The photographs are also capable of resolving high density fringes.

A time delay between the phase stepping at the end of the first stage of temperature rise and resetting of the reference frame for the following stage could result in a loss of fringes. In the current work, since the phase stepping and resetting of the reference video frame were carried out manually, a time delay of about 4s between first step and the appearance of the first fringe in the following stage exist. As the fringes on the direct view were moving at an average rate of about 0.32 fringes/second and those on the reflected view by 0.24 fringes/second, this time delay will result in a loss of approximately 1.2 and 1.0 fringes on the direct and reflected views respectively. The resulting displacement will therefore be smaller by 8% to 10%. This is the most probable reason for the smaller displacement measured using ESPI. The closer agreement at the bottom of the skirt, however, could be due to a non-linear effect of the loss of fringes, i.e. a loss of 8% of fringe orders at the top of the skirt need not cause a similar % loss at the bottom of the skirt, possibly, due to the complexity of fringe formation and movement in both views. The errors due to the time delay discussed here is a technique related error which can be overcome if the phase-stepping and resetting of a new reference frame were carried out automatically using a computer, and grabbing the images over 1/25 seconds.

Errors due to inaccuracies in measurement of system geometry used for transformation of surface points into pixel coordinates are difficult to separate from those due to distortion of video images and limited resolution of cursor. The combined error can, however, be checked from the accuracy of transformation of the datum points. As discussed earlier, this error is equivalent to a positional error of

approximately 0.2 of a fringe spacing, which was considered acceptable.

5.8 A critical comparison of the ESPI and holographic techniques

The main advantage of the ESPI method lies in the possibility of recording fringes using one heating cycle. The reference video frame can be reset when the fringe density increases beyond the resolving capability of the recording system and the recording can be continued. Problems relating to speckled nature of the fringes can be alleviated by using phase stepping methods which are also capable of high accuracies.

Poor fringe definition was found to limit the temperature rise in one set of analysis to 5°C using ESPI. Therefore, the measurement for a 20°C rise has to be carried out in several stages. Any systematic errors present may accumulate non-linearly to give an overall deformation which could be smaller than the actual deformation undergone by the piston. One possible source of error is due to distortion of video images which could affect the accuracy of the transformation of object points into pixel coordinates. Vertical body movement due to expansion of the piston support was found to cause speckle decorrelation and affect the contrast of the fringes.

The main advantage of the holographic method is the possibility of working with high density fringes caused by a rise of 20°C in a single stage. Small errors in fringe count would not affect the results significantly. When photographs are used for the analysis, perspective transformation routines can be employed to relate points on the object and the corresponding points on the fringe patterns accurately.

A major practical limitation of the holographic technique is, however, the need to record good quality holograms at elevated temperatures. A short exposure time must be used to avoid large expansion of the piston when the plate is exposed. The use of two reference beams to record two holograms on the same plate is done at the expense of the quality of the individual holograms. The contrast of the resulting fringes are poor and may not be easily amenable to automated analysis.

5.9 Conclusions

In this part of the study, a simple 'mirror' concept was used to measure the radial expansion of the heated piston. This concept was used in both ESPI and holographic arrangements. In the ESPI arrangement, a self-contained rig that enables one to measure only out-of-plane displacements was used for measuring two displacement vectors, simultaneously, in the horizontal plane. It was possible to separate the in-plane and out-of-plane components from the measured quantities. Perspective distortions of the direct and reflected images were accounted for in a transformation routine.

The radial deformation measured using ESPI was found to be 6% to 10% smaller than the holographic results. This difference was attributed to a time delay between phase-stepping and resetting of the next video frame which could have resulted in a loss of fringes. The possibility of distortions in the video images were also considered. The two displacement profiles, nevertheless, had similar shapes showing that both techniques are capable of producing the same results provided that the accuracy of the system is improved. This can be achieved in the following ways :

(a) by using an automatic phase-stepping and data acquisition technique. Since, the fringe movement is continuous, an automatic technique of resetting the reference frame immediately after the last phase-stepping should be incorporated.

(b) in order to relate object surface points to the corresponding points on the digitised video frame, surface contouring methods must be implemented. In the case where the points are related by mathematical transformations a study on the nature of the distortions, if any, is pertinent. A higher resolution computer system should be used to locate the datum points accurately.

In the analysis of the holographic fringes, the effects of distortions were found to be negligible. It was possible to transfer points on the photographs and back to the piston surface within a positional error of 0.8mm (which is equivalent to an error of 3% to 4% in displacement). Due the the high quality fringes, it also was possible to analyse high density fringe patterns. When a manual digitising technique is used contrast of the fringes is not a serious setback. The ESPI technique was, nevertheless, found to be a more practical technique to work with in terms of time consumed.

CHAPTER 6

MEASUREMENT OF RADIAL EXPANSION AT FRONT AND REAR SURFACES USING HOLOGRAPHIC INTERFEROMETRY

6.1 Introduction

The results of the investigation carried out by Evans and Premier(1989) showed that the expansion at diametrically opposite points on the skirt (at θ=45° and θ=225°) at the pin axis level differed by almost 15%. This discrepancy was attributed to a possible rigid body movement and the effects of eccentric heat input. The original piston support used consists of a 10mm diameter steel rod with a 3mm thick flange at one end. The end with the flange was fitted to the underside of the crown and the other end was fitted onto a base plate with a single 6mm screw, located axially. The method of securing the support to the base plate was thought to have caused a tilt in the piston hence giving rise to the different expansions at the two surfaces. The new support designed at the early stages of the project incorporated a 5mm thick flange (30mm in diameter) at the end that was connected to the base plate (Figure 4.21 of Chapter 4). Three 6mm screws were used to secure the support to the base plate and thus provided a rigid means of supporting the piston.

In spite of the precautions taken to mount the piston rigidly, a body displacement is suspected to have occurred during the experiments discussed in Chapters 4 and 5. This is due to a discrepancy of about 15% at the bottom of the skirt between the holographic measurement at the front surface of the piston and the predictions of the finite element model (see Chapter 7). Subsequent to the preliminary comparison between the two results, dial gauge measurements at θ=90° and θ=270° at 35mm below the gudgeon pin axis were carried out. The readings indicated a difference in expansion of about 40%, the expansion at θ=90° being smaller. The difference at the level of the pin axis was, however, approximately 8%. As will be shown later, the larger difference at the bottom of the skirt is due to two possible factors :

(a) a rigid body movement caused by tilt in the support (still present in spite of the improved support) and

(b) uneven expansion of the skirt.

In the presence of a body displacement, fringes caused by deformation alone will be manifested by tilt fringes and separating them is difficult in a dynamic situation such as the one in the

current study. None of the techniques proposed by several authors for compensating rigid body motion (Abramson et.al. 1979, Stimpfling et.al. 1985, Hu et.al. 1976) are readily applicable in the present situation.

As a result of the different expansions at the two surfaces it is not possible to use the expansion at one surface alone for comparison with the predictions of a finite element model. This is because in the generation of the model the piston was assumed to be symmetrical in construction and thus only a quadrant was considered (see Chapter 3). The heat input was assumed to be central. Therefore, for accurate comparison the mean of the expansions at the front and the rear surfaces must be considered. To achieve this the holographic arrangement developed in the previous work (Chapter 5) was extended to include the measurement at the rear surface. In the extended rig, mirrors were positioned behind the piston in a manner so that two additional views of the rear surface could be recorded using the same holographic plate used for recording the front surface. As will be shown in Section 6.5, the mean of the expansion at the two surfaces is free from the effects of body displacement and assumes symmetrical conditions, and thus provides an accurate means of comparison with finite element results. A detailed treatment of the various errors involved in the measurement is given. Attempts are also made to evaluate the magnitude and direction of the rigid body displacement vector.

6.2 Extension of experimental rig and program to include measurement of expansion at rear surface

The arrangement developed for measuring the radial expansion at the front surface was extended by using additional mirrors at the rear surface. A schematic layout of the new rig is shown in Figure 6.1. Mirror M2 was positioned at the rear surface so that two views of 45° sectors (225° to 270°) of the rear surface were visible from behind the piston. In order to record the two rear views using the same holographic plate used for recording the front direct and reflected views, a third mirror M3 was used to re-reflect the rear views towards the plate. Thus one of the rear views was obtained through a single reflection and the other through a double reflection. The four views were recorded using a single 4in.x 5in. holographic plate. The technique used for obtaining all the images on a single plate is illustrated in Figure 6.2.

In order to illuminate the rear surface a second beamsplitter BS was positioned in the path of the original object beam directed towards the front surface. The two rear view mirrors were positioned in a manner so that the expanded beam for the rear surface is just sufficient to illuminate a 45° sector. A collimating lens was positioned in front of the spatial filter to obtain a less divergent beam (i.e. not fully collimated) at the front surface. This was to optimise the usage of light. Although this resulted in a virtual shift in the illumination source origin, the assumption that the beam is fully collimated or fully divergent (i.e. non-collimated) does not affect the results significantly (see Section 6.4.2). This is because of the small variation in the illumination vector across the front piston surface. No collimating lens was used for the rear surface illumination due to space constraints.

The two reference beam method used in previous arrangement was not adopted here due to the additional light required to illuminate the rear surface (whose intensity is approximately 1.5 times that used for the front surface due to a longer path length travelled by the scattered light). Therefore, double exposure fringes were obtained by using a single reference beam and hence the two holograms were inseparable.

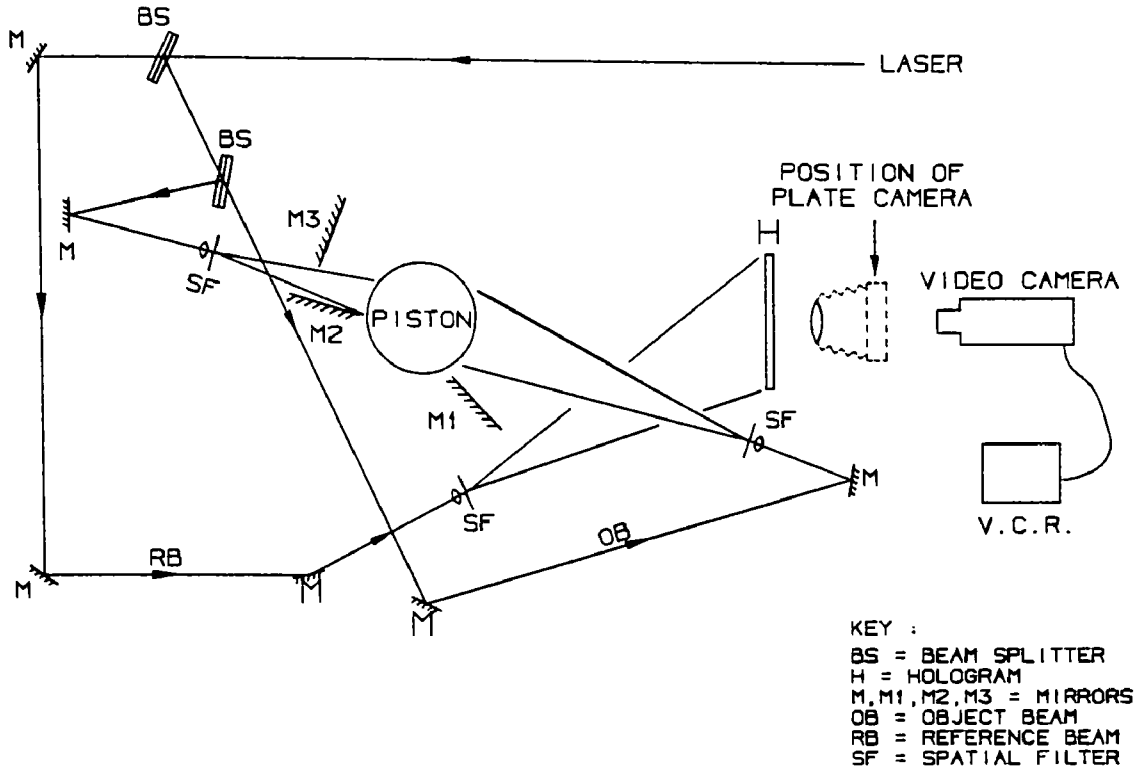

Figure 6.1. Schematic layout of the extended rig

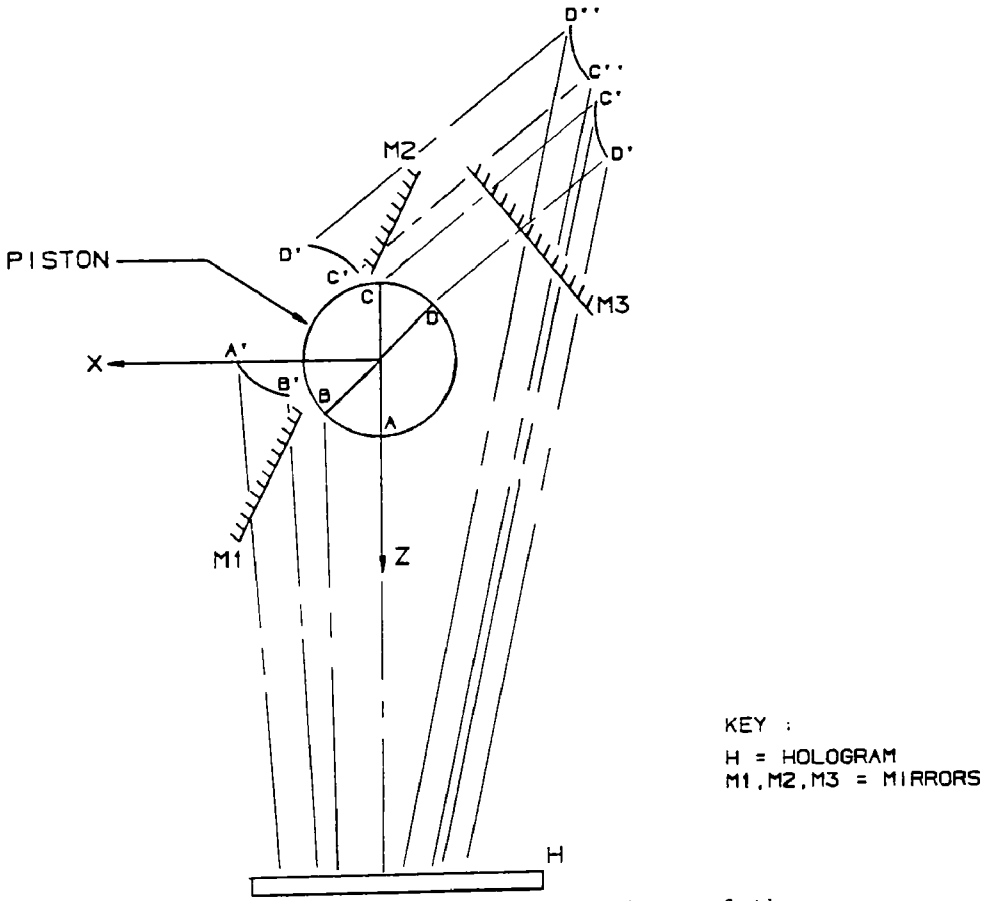

Figure 6.2. Technique of obtaining four views of the piston using a single plate

The computer program used for transforming fringes from the photographs and back to the piston surface was extended to handle multiple reflections in the rear view mirrors. Sector C''D'' was obtained by reflecting sector CD in M2 followed by a second reflection in M3 (Figure 6.2). Sector C'D' was obtained by a single reflection in M3. The positions of the mirrors were measured using the laser beam technique developed in previous work (Chapter 4). The verticality of each mirror was checked by projecting a horizontal beam and measuring the height of the incident and reflected beams from the surface of the optical bench.

6.3 Measurement of expansion for rise from 50°C to 60°C and 130°C to 140°C.

6.3.1 Experimental technique

As a result of the larger displacement at the rear surface it was necessary to limit the temperature rise to 10°C in order to obtain fringes which can be easily resolved. For the study at the lower temperature range the holographic plate was exposed initially at 50°C and then at 60°C using a single reference beam. Since the images at the rear views were located at a different position in space relative to the front views, the front and rear view images were photographed separately, refocussing the camera in between. The point of focus was, however, unchanged.

The fringe orders on the double exposure interferograms were determined by recording the live fringe formation using a second hologram exposed only at 50°C during a repeated heating sequence. Although it is possible to use a single hologram in a live fringe experiment for the measurement (similar to the arrangement using fringe order difference method discussed in Section 5.3) such an approach could have been made difficult by the limited laser power available. Since the repeated heating sequence produced temperature rises that differed only by a maximum of about 0.3°C, the combination of double exposure and live fringe method used here will produce an error of about 3% (due to temperature fluctuations). However, since the fluctuation in the temperatures will affect the initial and final

temperature approximately equally, the actual error would be less than this.

Although the initial arrangement allowed a sector of 45° at the rear surface to be viewed, accurate results were obtainable only for a 30° sector. This was due to the difficulty in transforming the fringes located at the sides of the piston as seen on the photograph and back to the rear surface of the piston accurately. For the purpose of comparison with finite elements, the expansion along the skirt at θ=60° and θ=240° has been considered. The holographic fringes due to a rise from 50°C to 60°C are shown in Figure 6.3(a) and 6.3(b).

In order to confirm that the expansion profile measured is not characteristic of a single piston but depends on the design of the piston, a second piston (piston No.2) of the same construction was used and the experiment was repeated. The rear view mirrors were adjusted so that 45° sector of the rear surface was sufficiently within the visible area so that fringes on the entire sector can be transferred accurately. This will enable comparison between holographic and finite element results to be made for a complete 45° sector. The expansion profiles along θ=60° for the first (piston No.1) and the second piston were compared.

The measurement on piston No.2 was carried out three times on consecutive days to confirm repeatibility, each time using a new hologram. Typical photographs of the fringe pattern for the experiments using the second piston are shown in Figures 6.4(a) and 6.4(b).

The measurement was repeated for a rise from 130°C to 140°C to investigate the expansion control characteristics of the steel insert and to determine the hot shape of the piston at temperatures above the stress free temperature (130°C). Due to a rapid expansion of the skirt at this temperature range it was necessary to expose the plate within two seconds. Due to the limited laser power available such a short exposure time resulted in the plate being under-exposed. Thus, the developing time was increased to about 6 minutes using fresh developer, though only slight improvement in the quality of the hologram was achieved. This problem could have been overcome by using a high speed film plate such as the 10E75 Holotest plates though this was not attempted. The present high resolution 8E75 plates used

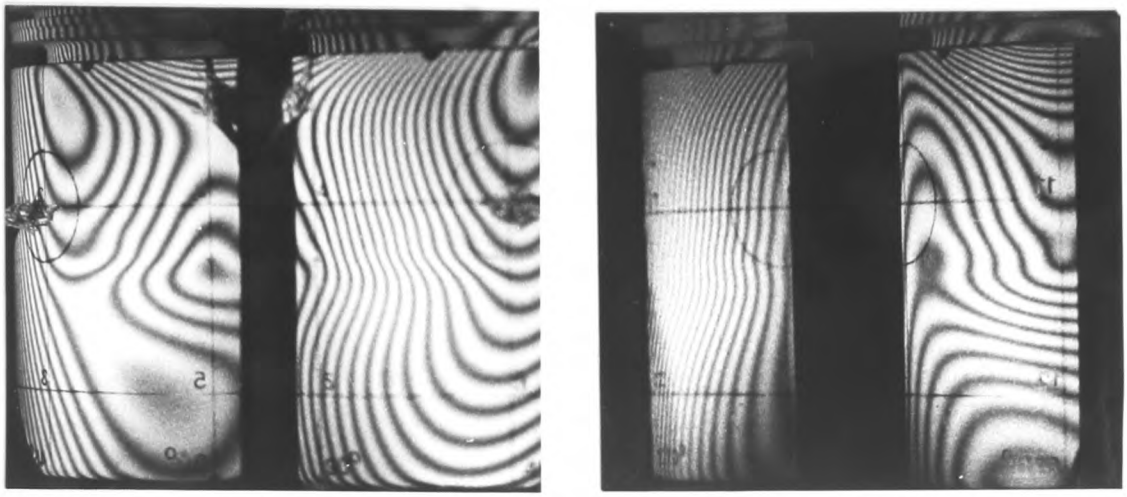

(a) (b)

Figure 6.3. Holographic fringes due to a rise from 50°C to 60°C for piston No.1 at (a) front surface and (b) rear surface

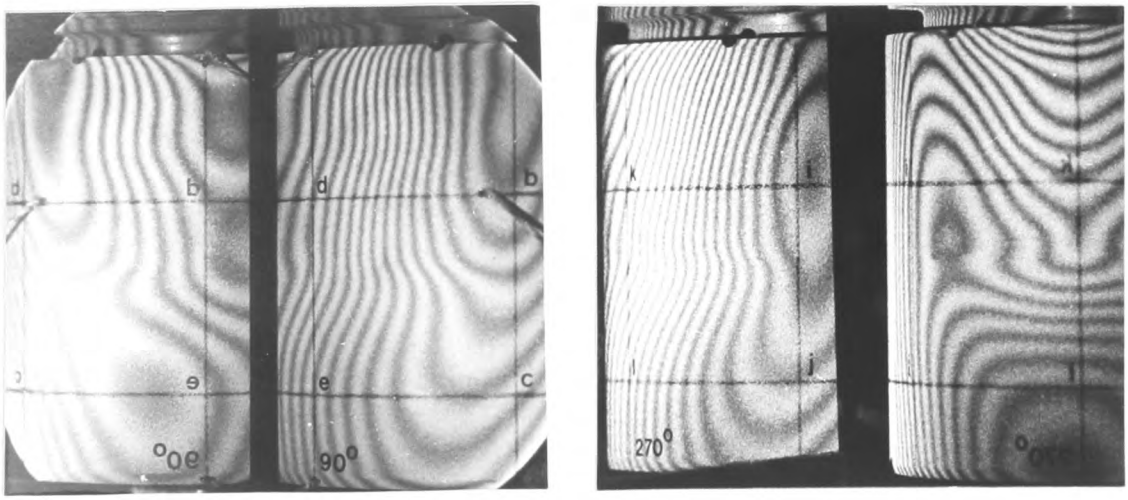

(a) (b)

Figure 6.4. Holographic fringes due to a rise from 50°C to 60°C for piston No.2 at (a) front surface and (b) rear surface

enabled holograms of reasonable quality to be recorded. The contrast of the fringes were improved by positioning polarisers in front of the cameras as in previous recordings.

The measurement at the higher temperature range was repeated using a new hologram to confirm consistency of the results. Typical photographs for the 130°C to 140°C rise are shown in Figures 6.5(a) and 6.5(b). Comparison of the fringe geometries in Figures 6.4 and 6.5 shows that the piston is expanding differently at the two temperature ranges.

The effects of thermal current have also been considered. When the fringe density was at its lowest, the fringes appeared to shimmer as they moved but at other instances they were more stable. Since whole number of fringes were counted crossing a reference point, the fractional order number variation due to thermal currents (estimated to be 0.2 of a fringe spacing) will not significantly affect the results. However, a maximum error of 0.5 of a fringe spacing has been considered in the errors analysis and the sensitivity of the solution to this error has been investigated (Section 6.4). Since the thermal current will not affect the results of the three repeated experiments in identical manner, it is possible to check its effect on the displacement by comparing the mean of the expansions obtained from the three experiments.

6.3.2 Technique of analysis

The fringes on the photographs were manually digitised into a VAX 11/785 computer for analysis as in the previous work. Since the fringes were located visually, it was possible to digitise low contrast fringes. (The contrast of the fringes for the extended set-up were poorer than the previous set-up (Chapter 5) due to the additional light used for illuminating the rear surface). The presence of dark areas at the top of the skirt (Figure 6.5) which are indicative of a movement of the object during exposure (due to continuous expansion of the piston) did not create specific problems in digitising. However, one could expect certain difficult in automatically locating the fringe centres if these interferograms were digitised using a scanner or video frame grabber. As encountered

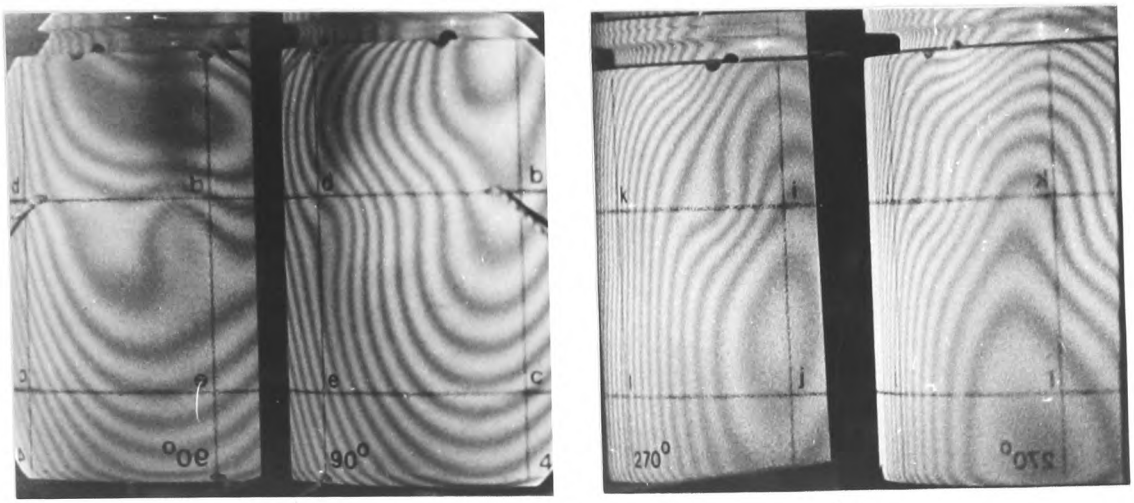

Figure 6.5. Holographic fringes due to a rise from 130°C to 140°C at (a) front surface (b) rear surface

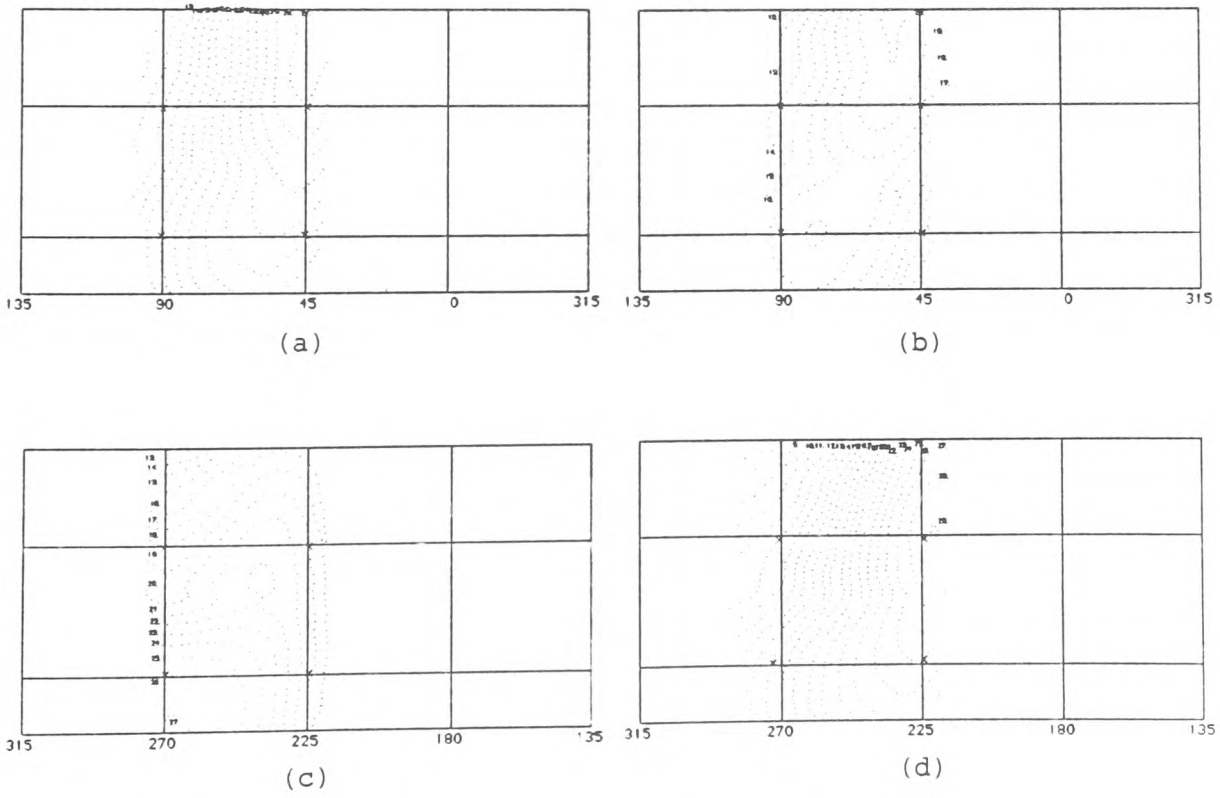

Figure 6.6. Plot of transformed digitised fringe centres on the developed piston surface for (a) front direct view (b) front reflected view (c) rear : single reflection (d) rear : double reflection

with the ESPI fringes, if the phase stepped analysis is performed on poor contrast fringes then the phase fringes formed would be discontinuous along certain parts of the fringes. In addition, the resolution of the video system can limit the density of the fringes that can be analysed automatically. Moreover, other than digitising and automatic analysis to obtain order numbers at specified grid points (or phase unwrapping), the rest of the analysis including correction for perspective distortions, lateral inversions and scaling follows a sequence similar to that used when working with the photographs.

The technique of transforming digitised fringe centres back to the piston surface was similar to that described in Chapter 4. The transformed points were plotted onto the developed surface (Figures 6.6(a)-(d)) and the fringes orders at the grid points were determined by interpolation. The camera lens nodal point was reflected in the rear view mirrors to take into account the change in the positions of the sensitivity vectors. The displacement were evaluated from equations 5.13(c).

6.4 Analysis of errors

6.4.1 Sensitivity of solution to errors in order numbers.

Errors in fringe orders can arise from the following factors :
(a) assignment of fringe orders on double exposure interferogram from live fringe formation,
(b) inaccuracies of transformation of fringe centres from photographs to piston surface,
(c) fluctuations in temperatures due to ambient air movement and
(d) misalignment between video and plate cameras.
The effects of each of the above errors are discussed in sequence:
(a) In the experimental technique developed the fringe orders on the double exposure interferograms were determined from a recording of the live fringe formation. The number of fringes N crossing a reference point P was counted and the fringe adjacent to P on the double exposure interferogram (moving away from P) was assigned the order N. In such a technique a maximum error of half fringe order is

possible because only fringes that cross the reference point P were considered and those that may have moved close to P but have not crossed it are not counted.

(b) The errors in the transformation of fringe centres were estimated to be 0.2 of a fringe spacing at the front surface and 0.5 of a fringe spacing at the rear surface (Figures 6.6(a)-(d)). The larger error for the double reflection at the rear surface is due to the need to reflect this surface twice, which magnifies slight inaccuracies in measurement of mirror positions.

(c) Fluctuations in temperatures can affect the actual deformation undergone by the surfaces and thus causing a fluctuation in order numbers. Since the temperature rises during separate heating sequences were found to differ by a maximum of 0.3°C and since the deformation is proportional to the temperature rise, a deviation of approximately 3% in the evaluated displacements can be expected. The effect of this error on the fringe orders can be seen as follows.

For a fixed illumination-observation geometry, the relationship between the displacement and fringe order number is given by the interferometry relation,

$$s.d = n.\lambda \qquad \ldots.6.1$$

where $s = o - i$ is the sensitivity vector.

Considering a section of the piston where the sensitivity vector lies in the x-z plane, equation 6.1 can be rewritten as

$$(s_1 i + s_2 k).(d_x i + d_z k) = n.\lambda \qquad \ldots.6.2.$$

For radial expansion whereby the x-component is in-line with the z-axis, the above equation reduces to

$$s_2 d_z = n.\lambda \qquad \ldots.6.3$$

For a variation of Δd_z in d_z, if Δn is the corresponding variation in n, then

$$s_2 (d_z + \Delta d_z) = (n + \Delta n)\lambda \qquad \ldots.6.4.$$

From equations 6.3 and 6.4,

$$\Delta d_z/d_z = \Delta n/n \qquad \ldots.6.5$$

i.e. a variation of 3% in the radial expansion will cause a similar % variation in the fringe orders. Since the fringe count varies between 20 to 30 fringes for a 10°C rise, the fluctuation in temperature will not cause the fringes to vary by more than one. Moreover, the maximum fluctuation of 0.3°C was observed at only one or two thermocouple points and the mean fluctuation is much lower (less than 0.2°C).

(d) The errors due to misalignment between the plate and video cameras for recording fringes on the front surface were discussed in Section 5.6. Here, we consider the effects of similar errors for the rear surface. The analysis, which is given in Appendix A3, showed that the maximum deviation in fringe order for a 20mm lateral misalignment is in the single reflection. The error in fringe order is 1.6% and is considered acceptable.

The effects of thermal current was found to be more visible when the density of the fringes is low but is more difficult to notice when the fringes are closely spaced together. However, when interferograms of high fringe densities are analysed the errors due to thermal drift is expected to be smaller than when the analysis is carried with low density interferograms, providing that the drift causes fringes to move by equal amounts in both cases. Here, the errors due the thermal currents can be checked by noting the mean of radial expansions at the front and rear surfaces for the three experiments. Since the mean displacements agreed to within 3% (see Section 6.5.2), the errors caused by thermal current fall within this range. In addition, the video recording of live fringes show that the fringes move steadily without significant effect of thermal current. This can be attributed to the high rate of heat input (see Chapter 4). The maximum drift in the fringes is estimated to be 0.2 of a fringe spacing, which was considered acceptable.

The sensitivity of the solution to errors in order numbers due to the various factors discussed above has been investigated by varying the fringe orders at the front and rear views and repeating the analysis. Eight different variations in order numbers were considered and these can be grouped into two main categories :

a) An increase (or decrease) in fringe order by 1 on both views for each surface. This variation was considered because the recording of live fringes on each of the two views at the front and rear surfaces were carried out simultaneously on a single video frame. Thus, an error amounting to an increase (or decrease) in the fringe order on the direct view will cause a similar variation for the reflected view at the front surface. A similar situation can be expected for the rear surface.

b) An increase of 0.5 fringe on one view and a decrease of 0.5 fringe on the other view on each surface and vice-versa. The reason for this variation is because a maximum error of 0.5 fringe can occur in assigning fringe order on the double exposure fringes from the live recording. It is clear that in the analysis the extreme cases have been considered.

The details of the analyses, which were carried out for four 'corner' points on the area under study, are given in Appendix A4.

From the analyses the effects of the errors due to factors described in (a) caused a maximum deviation of 7.6% in the calculated absolute displacement. The maximum deviation in the direction of displacement Φ is 5.4° (at θ=270°, 45mm below pin axis), which caused a deviation of 2.6% in the radial displacement.

The effect of the errors described in (b) resulted in a maximum deviation of 5.7% in the absolute displacement. The deviation in the direction of displacement (8.6°) is higher than in the analyses described in (a) because the variations in fringe orders were considered having opposite signs. This deviation causes a 8.5% variation in the radial displacement (at the front surface at θ=90°). The above analyses, however, represent an upper limit estimate of the errors involved.

6.4.2 Errors due to assumption that sensitivity vectors remain constant along piston skirt

In the evaluation of displacements from equations 5.13(c), the sensitivity vector was assumed to lie in a horizontal plane (see Chapter 5). This assumption was necessary in order to simplify the arrangement in which the vertical component was not measured. Such an assumption is expected to introduce some errors in the displacement due to the actual variation of the sensitivity vector along the piston skirt. In this part of the analysis the maximum error introduced as a result of the assumption made is evaluated.

For the arrangement used, fringes on two views on each surface of the piston were recorded for analysis. This results in two simultaneous equations in three unknowns :

$$s_{x1}d_x + s_{y1}d_y + s_{z1}d_z = n_1\lambda \qquad ....6.6$$

$$s_{x2}d_x + s_{y2}d_y + s_{z2}d_z = n_2\lambda \qquad ....6.7$$

where s_{x1}, s_{y1}, s_{z1} and s_{x2}, s_{y2}, s_{z2} are unit sensitivity vector components for the first and second views respectively, and n_1 and n_2 are the fringe orders for the two views.

In the analysis, s_{y1} and s_{y2} were assumed to be negligible so that equations 6.6 and 6.7 reduce to

$$s_{x1}d_x' + s_{z1}d_z' = n_1\lambda \qquad ....6.8$$

$$s_{x2}d_x' + s_{z2}d_z' = n_2\lambda \qquad ....6.9$$

From equation 6.9 we have

$$d_x' = (n_2\lambda - s_{z2}d_z')/s_{x2} \qquad ....6.10$$

Substituting 6.10 into 6.8 and after simplifying,

$$d_z' = (s_{x2}n_1 - s_{x1}n_2)\lambda/(s_{x2}s_{z1} - s_{x1}s_{z2}) \qquad ....6.11$$

In order to investigate the effects of the assumptions, we let $d_y = kd_z$ and repeat the analysis.
Thus, from equation 6.6 :

$$d_x = [n_1\lambda - (s_{y1}k + s_{z1})d_z]/s_{x1} \qquad ....6.12$$

Substituting 6.12 into 6.7 and after simplifying,

$$d_z = (s_{x1}n_2 - s_{x2}n_1)\lambda/A \qquad ....6.13$$

where $A = (s_{x1}s_{y2} - s_{x2}s_{y1})k + s_{x1}s_{z2} - s_{x2}s_{z1}$.

Dividing 6.11/6.13 and simplifying, we arrive at,

$$\frac{d_z'}{d_z} = \frac{(s_{x1}s_{y2} - s_{x2}s_{y1})k}{(s_{x2}s_{z1} - s_{x1}s_{z2})} - 1 \qquad ....6.14.$$

The maximum error is expected to occur at a level of the skirt at which the angle made by the sensitivity vector with the horizontal is maximum. For the estimation of the errors, points located at P1(0,-45,49.2) and P2(0,-45,-49.2) for the front and rear surfaces, respectively, have been considered. A third point P3(0,-30,49.2) located on the front surface have been considered to see how this error decreases further up the skirt. The fringe orders and the components of the sensitivity vectors for the three points are given in Table 6.1.
At P1, substituting the relevant variables taken from Table 6.1 into equation 6.14 and simplifying gives

$$d_z'/d_z = -0.091k - 1,$$

the % difference in $d_z = -9.1k$ %.
The value of k at P1 can be estimated from the results using four-mirror method (see Chapter 4) and its approximately value is -1.2. Hence, a maximum error of 10.9% occurs at 45mm below the pin axis.

Similarly at point P2,

$$d_z'/d_z = 0.092k - 1.0$$

The % variation in d_z = 9.2k %. The corresponding error in d_z is 11%.

At the third point P3, located at 30mm below the pin axis,

$$d_z'/d_z = -0.058k - 1.$$

The % variation in d_z = -5.8k %.

At P3, k is approximately -0.94, thus the % variation in d_z is 5.4%.

The analysis shows that the maximum error due to the assumption considered is about 5% for 50mm of the skirt length (measured from the top of the skirt). The error at the remaining 20mm of the skirt are higher (the maximum is about 11%). Although this analysis gives an estimation of the errors expected, the actual errors at the bottom of the skirt at the front surface are lower. This is because of the use of a collimating lens which shifts the effective illumination source origin further from the piston surface, thus decreasing the angle made by the sensitivity vector with the horizontal.

6.4.3 Errors due to measurement of observation and illumination vectors

The errors in displacement resulting from errors in measurement of observation and illumination vectors can be checked by comparing the measurement with theoretical results for simple components such as a cantilever and a uniform cylinder. The comparison has been carried out in previous work (Chapters 4 and 5) in which an agreement to within 5%-7% was observed. Since the technique of measuring the observation and illumination geometry in all the experiments were the same (i.e. by using triangulation) the errors in displacement is therefore expected to be within this range.

6.5 Discussion of results

6.5.1 Comparison of expansion profiles for different pistons of the same design.

The geometry of the fringe patterns in Figures 6.4 and 6.5 show that the two pistons are undergoing similar deformation. In both cases, a 'kink' in the fringes at about mid-skirt level can be seen. This is the approximate level at which the steel sleeve terminates. The effect of the insert on the fringe geometry is clearly visible. The fringes originated at the top of the skirt and moved downwards as the piston was heated.

The plots of radial expansion along $\theta=60°$ and $\theta=240°$ for the two pistons show a significant difference in the expansion at the two surfaces (Figure 6.7). This shows that the two pistons are undergoing different types of rigid body movement. This body movement could be due to several factors (see Section 6.5.3). One of these could be due to the non-uniform heat input at the crown resulting in an uneven expansion of the support flange attached below the crown. The support is suspected to have induced a tilt in the piston. As will be shown in Section 6.5.3 the mean of the expansion at the two surfaces is free from the effects of body movement and provides an accurate means of comparing the expansion profiles of the two pistons. The mean expansions in Figure 6.7 show a similarity suggesting that the expansion profile is characteristic of the design of the piston. The expansion of the second piston is, however, about 10% larger than that of the first. This is due to a larger temperature rise for the second piston, the maximum difference being 0.9°C.

6.5.2. Experiments to confirm repeatability

The expansion profiles on the front and rear surfaces and the mean of the two from the three repeated experiments (Experiments 1, 2 and 3) for Piston No.2, for the 50°C to 60°C rise, are shown in Figure 6.8(a)-(b). The expansion at the front surface deviates by a maximum of 10% between Experiments 2 and 3 and at the rear surface the corresponding maximum deviation is about 8% (Figure 6.8(b)). The

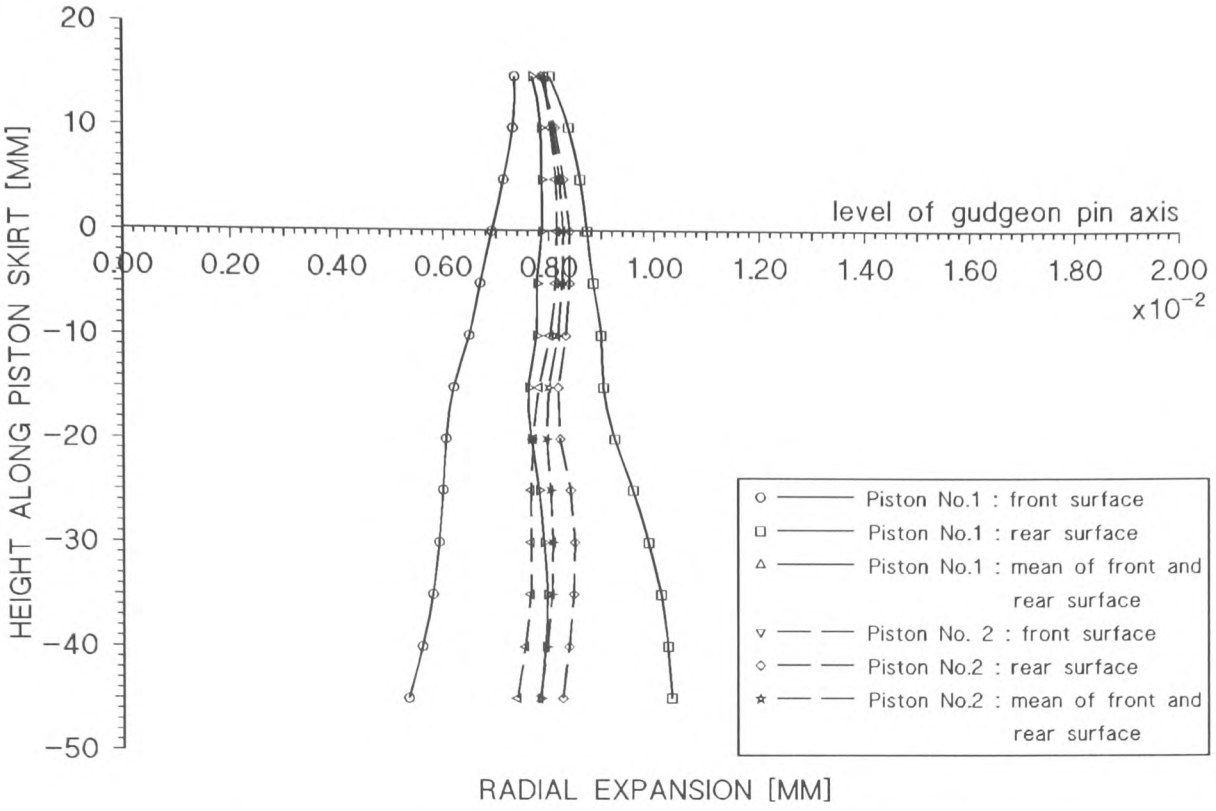

Figure 6.7. Comparison of radial expansion for two pistons of the same design (50°C to 60°C)

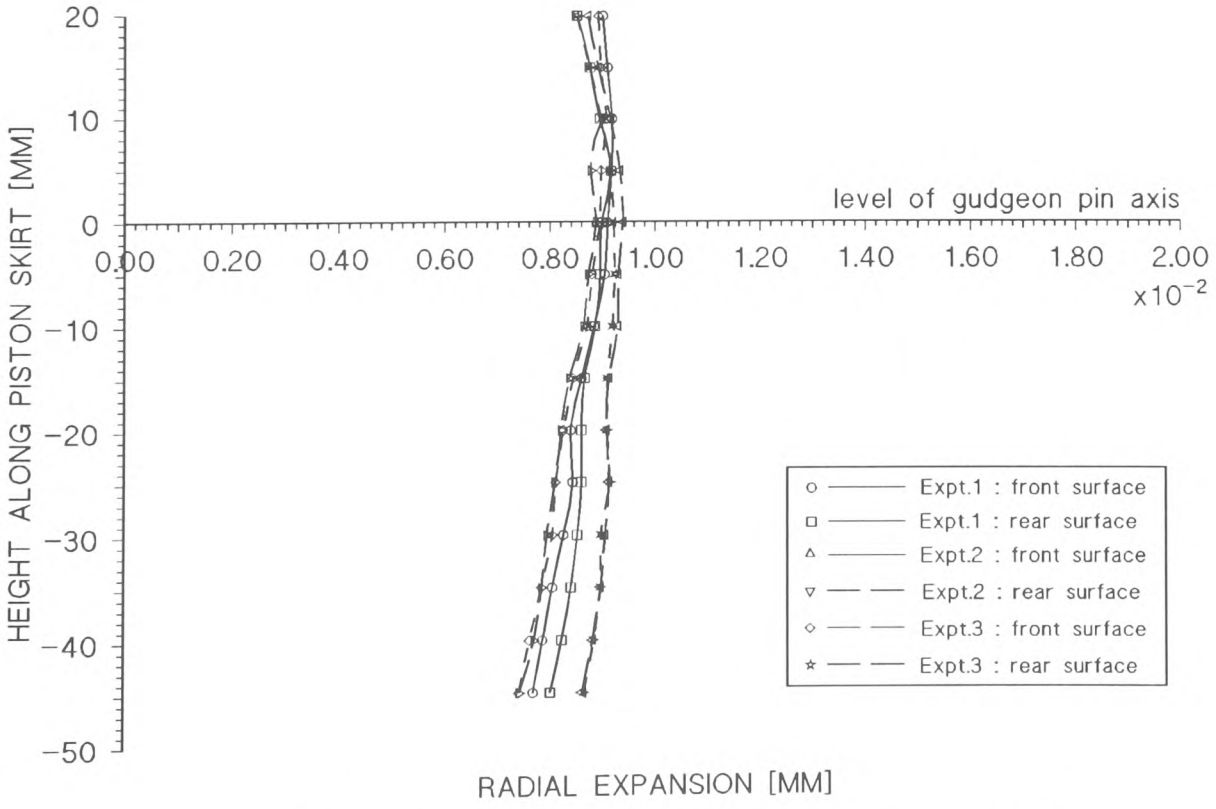

Figure 6.8(a). Radial expansion at front and rear surfaces along θ=50° to confirm repeatability (50°C to 60°C)

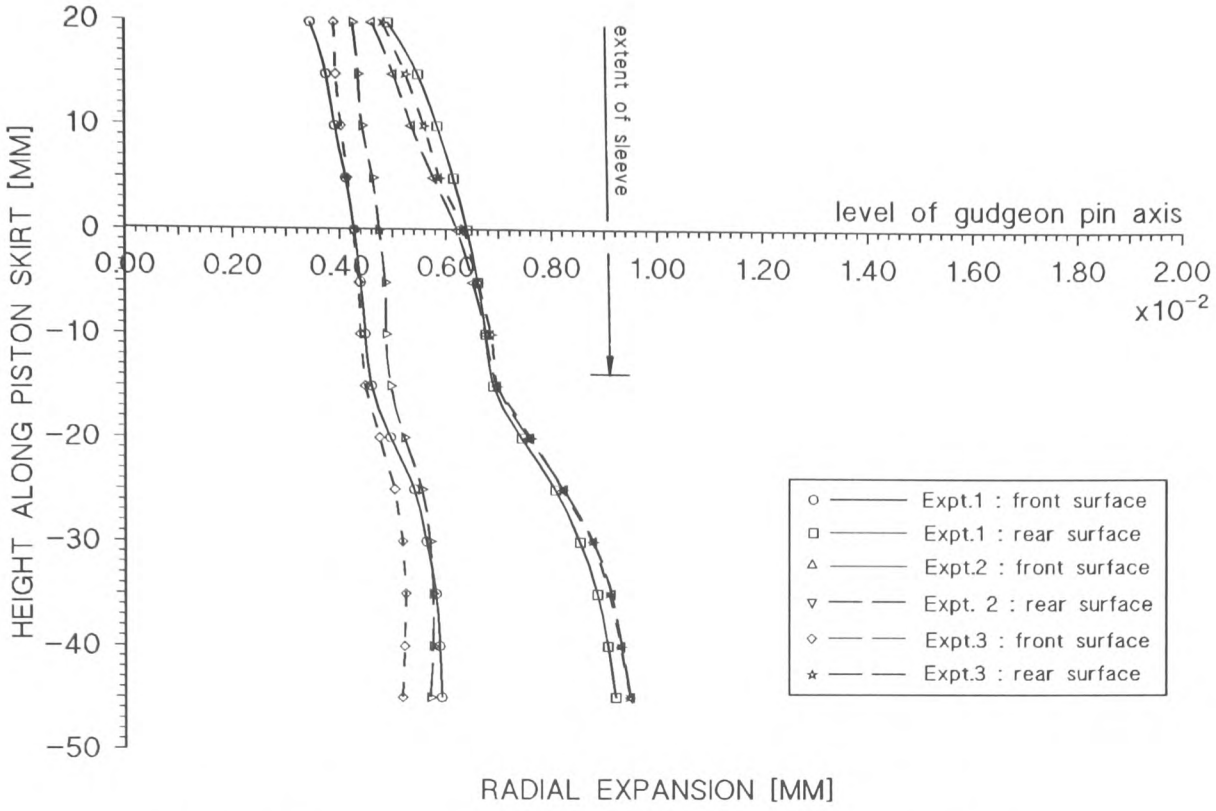

Figure 6.8(b). Radial expansion at front and rear surfaces along θ=90° to confirm repeatability (50°C to 60°C)

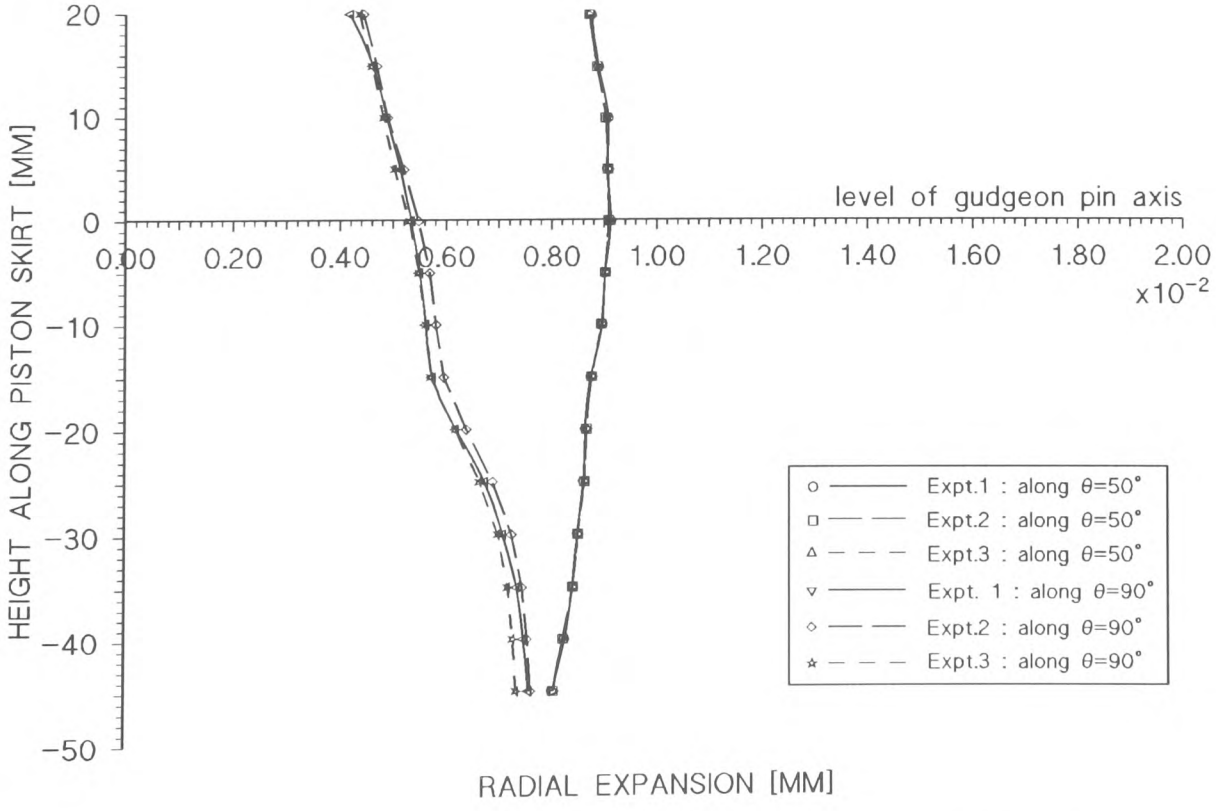

Figure 6.9. Mean of radial expansion for repeated experiments (50°C to 60°)

mean of the expansion at the two surfaces, however, agreed to within 3% for the three experiments (Figure 6.9). The deviation in expansion at the individual surfaces show that the piston is undergoing slightly different rigid body movement in each case. Since the mean displacements are unaffected by the rigid body movements (see Section 6.5.3), they therefore show close agreement with one another. In addition, close agreement of the mean expansions also indicate that the effects of the errors (discussed in Section 6.4) are within the acceptable limits (5%) and that the experimental results are reproducible.

The measured temperature rises for the three experiments showed a maximum deviation of 0.3°C and this was considered acceptable (Table 6.2).

The results of the repeated measurement at the higher temperature range (130°C to 140°C) are shown in Figure 6.10. From these plots a variation of about 8% in the radial expansion at the front and rear surfaces between the two experiments can be observed. The mean expansion agrees to within 2%, again suggesting that the variation is due to different rigid body movement. As for the lower temperature range, any one of the mean expansions can be used for comparison with finite elements.

6.5.3 Comparison of expansion profiles at front and rear surfaces

Table 6.3 summarises the difference in expansion between the front and rear surfaces taken at 15mm above and 45mm below the pin axis. The results show a significant difference in expansion at the front and rear surfaces at θ=90°. This difference can be attributed to the following factors :

a) a rigid body movement

b) unequal expansion at the two surfaces due to different gap geometries and non-symmetry in piston construction,

c) a combination of (a) and (b).

Along θ=50° and θ=90° a variation in the difference in expansion at the two surfaces along the skirt was observed. If the body displacement is a pure translation in the horizontal plane the difference in the expansion would remain the same along the skirt.

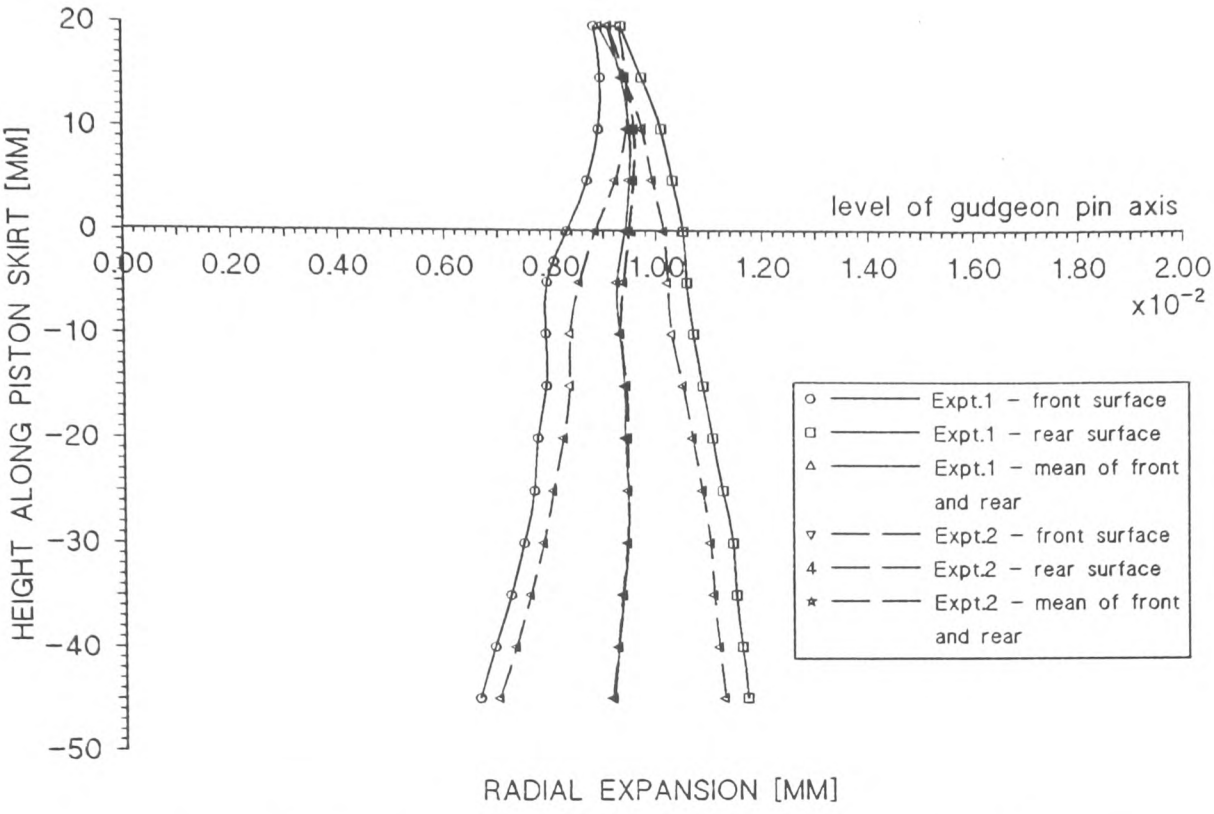

Figure 6.10. Radial expansion at front and rear surface along θ=90° to confirm repeatability (130°C to 140°C)

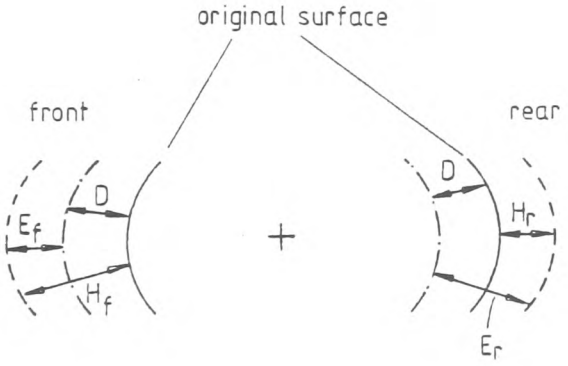

Figure 6.11. Part of piston in the horizontal (x-z) plane

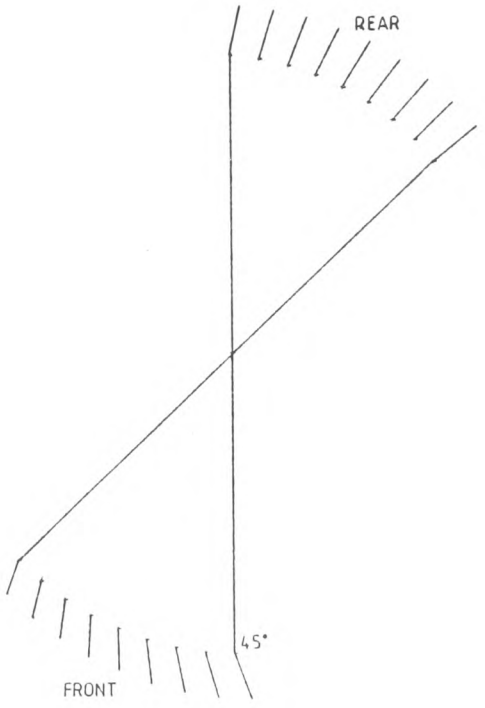

Figure 6.12. Vectorial plots of expansion in the horizontal plane at 45mm below pin axis

	P1	P2	P3
S_{x1}	0.471	-1.371	0.471
S_{y1}	0.187	0.178	0.119
S_{z1}	1.876	-1.266	1.881
S_{x2}	1.290	-0.109	1.293
S_{y2}	0.176	0.177	0.112
S_{z2}	1.438	-1.856	1.442
n_1	20.75	19.87	22.93
n_2	12.00	25.3	13.98

Table 6.1. Components of sensitivity vectors and order numbers at points P1, P2 and P3

Thermocouple	Measured rise (Expt.1) °C	Measured rise (Expt.2) °C	Measured rise (Expt.3) °C
T2	14.9	15.0	14.3
T3	10.5	10.4	10.5
T4	10.1	10.1	10.1
T5	8.8	8.9	8.9
T6	8.2	8.3	8.4
T7	7.9	8.0	8.2
T8	10.2	10.2	10.1
T9	10.1	10.2	10.2
T11	10.0	10.0	10.0
T12	8.8	9.0	9.0

Table 6.2. Measured temperature rises for repeated experiments for a datum rise from 50°C to 60°C (at T11)

Height from pin axis (mm)	θ from pin axis (Degree)	$Expansion_{rear}$ - $Expansion_{front}$ (mm)
15	50°	-0.000332
15	90°	0.00173
-45	50°	0.000326
-45	90°	0.003307

Table 6.3. Difference in expansion between front and rear surfaces along θ=50° and θ=90°.

However, in this case a tilt is more likely. This can be explained as follows :

Figure 6.11 shows part of the piston in the horizontal plane where,

D = body displacement

$E_{f,r}$ = thermal expansion at front(f) and rear(r) surfaces

$H_{f,r}$ = holographic measurement at front and rear surfaces.

Now,

$$H_f = E_f + D \qquad \ldots.6.15(a)$$

$$H_r = E_r - D \qquad \ldots.6.15(b)$$

where only the absolute displacements are considered.

Subtracting the above two equations at 15mm above and 45mm below the pin axis we have, respectively,

$$(H_f - H_r)_{15} = (E_f - E_r)_{15} + 2D_{15} \qquad \ldots.6.16$$

$$(H_f - H_r)_{-45} = (E_f - E_r)_{-45} + 2D_{-45} \qquad \ldots.6.17$$

From finite elements analysis it was shown that the geometry of the air gap has negligible effect on the expansion along $\theta=50°$ (see Chapter 7). Also, the temperatures at $\theta=50°$ and $230°$ were found to differ by less than 4%, thus, along this section of the skirt the following assumptions can be made,

$$(E_f - E_r)_{15} \approx 0 \qquad \text{and}$$

$$(E_f - E_r)_{-45} \approx 0 \quad .$$

Hence subtracting 6.17 from 6.16,

$$(H_f - H_r)_{15} - (H_f - H_r)_{-45} = 2(D_{15} - D_{-45}) \qquad \ldots.6.18$$

From Figure 6.8,

$$(H_f - H_r)_{15} \neq (H_f - H_r)_{-45},$$

hence from equation 6.18,

$$D_{15} \neq D_{-45} \quad ,$$

i.e. the body displacement at the bottom and top of the skirt are not the same, suggesting that it is a tilt.

It was shown in the finite elements analysis that the expansion along $\theta=90°$ is affected by the position at which the air gap was assumed to start. Since it is possible for the air gaps at the two sides of the piston to have slightly different geometries (i.e. they may not close at the same angular positions measured from the pin axis), the expansion at the two surfaces can be affected differently. Thus the difference in expansion along $\theta=90°$ can be due to a combined effect of tilt and different gap geometries. The effects of slight non-symmetry in the piston construction could also be present though this is difficult to verify.

The presence of tilt can also be identified by observing the vectorial displacement plot on the horizontal plane at 45mm below the pin axis (Figure 6.12). From these plots we observe that the direction of displacement at the two surfaces are affected similarly due to the body displacement. The magnitude and direction of the body displacement can be estimated using a vector approach and this is given in Appendix A5. From the calculations the following results were obtained:

$d_{-45} = 0.00178\text{mm}$ at $\Phi = 80.4°$ and

$d_{15} = 0.000602\text{mm}$ at $\Phi = 72°$,

where,

d_{-45}, d_{15} are the absolute body displacement at 45mm below and 15mm above the pin axis, respectively,

Φ is the angle made by d with the z-axis.

The body displacement was found to be greater at the bottom of the skirt again confirming that it is a tilt. At 45mm below the pin axis, the x-component of body displacement is larger than the z-component and this partly accounts for the larger difference in expansion between the two surfaces along $\theta=90°$ and $\theta=270°$ when compared with the expansion along $\theta=50°$ and $\theta=230°$.

Since all the points along the circumference at a certain level of the piston will experience similar rigid body movement due to the tilt, it is possible to estimate the difference in expansion along $\theta=90°$ due to factors other then body movement. This is based on the body displacement vector obtained at $\theta=50°$. These displacements are given by,

$$e_{fx} = h_{fx} - d_x$$
$$\text{and} \quad e_{fz} = h_{fz} - d_z \qquad \ldots.6.19$$

for the front surface and by

$$e_{rx} = h_{rx} - d_x$$
$$\text{and} \quad e_{rz} = h_{rz} - d_z \qquad \ldots.6.20$$

for the rear surface. Based on the mean of the three experimental results, the corresponding radial expansions are

$e_{f\ radial} = 0.007947mm$ and
$e_{r\ radial} = 0.006011mm.$

Thus the difference in radial expansion is estimated to be 0.00084mm. This difference could be due to the effect of different gap geometries and non-symmetry in piston construction.

The presence of rigid body displacement was also investigated using in-plane ESPI. In this investigation, the top piston surface was illuminated using two beams at equal angles to the observation direction with the aid of a mirror positioned above the crown (Figure 6.13). The piston was initially heated to about 70°C and was allowed to cool to 50°C before recording of the fringes was commenced. The fringes were recorded for a 5°C drop in temperature. The low rate of temperature drop (approximately 0.3°C/min) and disturbances due to thermal current made the investigation difficult. The fringes were observed to be approximately straight (Figure 6.14) suggesting that the expansion is mainly radial. It was, however, difficult to detect the presence of a rigid body displacement using this arrangement, possibly due to the small magnitude of this displacement at the top piston surface (less than 0.001mm).

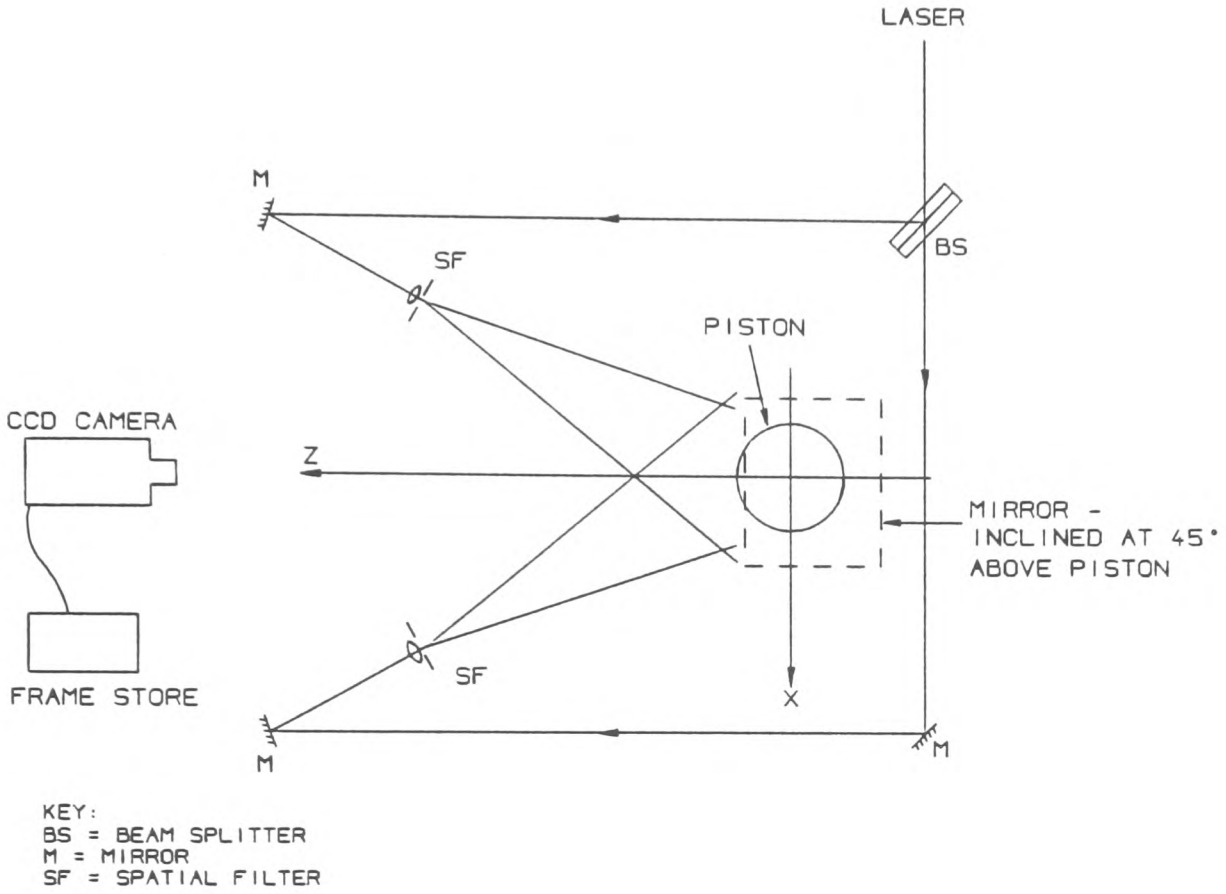

Figure 6.13. In-plane ESPI arrangement for measuring rigid body displacement at top piston surface

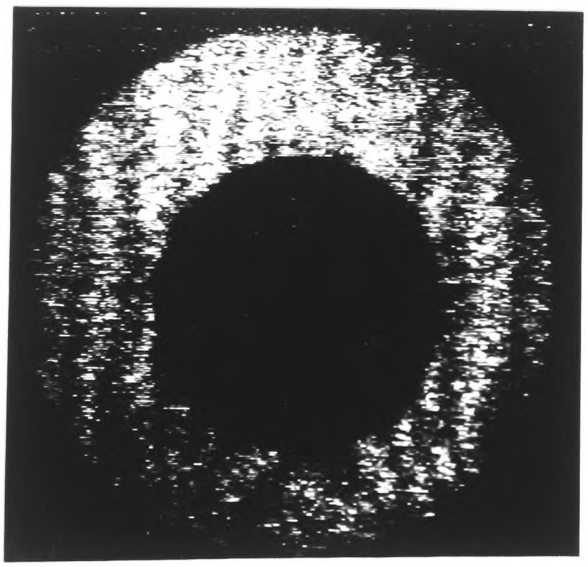

Figure 6.14. ESPI fringes on top piston surface (50°C to 45°C drop)

6.5.3 Evaluation of radial expansion for comparison with finite elements

For the comparison of experimental results with finite elements predictions the mean of the expansion at the two surfaces were evaluated. The mean expansion is free from body displacements as shown in the following calculations :
Adding equations 6.15(a) and 6.15(b) for any level of the skirt,

$$H_f + H_r = E_f + E_r \qquad \ldots.6.21$$

i.e.

$$(H_f + H_r)/2 = (E_f + E_r)/2 \ , \qquad \ldots.6.22$$

Thus, when the holographic results for the two surfaces are averaged we obtain the mean thermal expansion which is unaffected by body displacement. This can be seen from Figure 6.9 which shows that the mean expansion from the three experiments have a maximum deviation of 3%. The mean expansion also assumes a symmetrical piston construction with uniform heat input and thus could be used for accurate comparison with the predictions of the finite element model.

6.6 Conclusions

In this chapter, the experimental arrangement used for measuring the radial expansions at the front and rear surfaces of the piston was described. This arrangement is an extension of the arrangement developed in previous work (Chapter 5). The mean of the expansions at the two surfaces was evaluated and shown that the maximum deviation between the repeated measurements is 3%. This suggest that the deviation in radial expansion at the front and rear surfaces are due to different rigid body movements experienced by the piston. The mean expansion is shown to be free from effects of rigid body movement and assumes symmetrical conditions. An analysis of the various error involved has also been carried out.

CHAPTER 7

COMPARISON OF FINITE ELEMENTS AND EXPERIMENTAL RESULTS

7.1 Comparison of expansion at piston front surface.

Preliminary comparison between holographic and finite elements results was carried out for the expansion at front surface alone due to a rise from 50°C to 70°C. The results were obtained from the experiment discussed in Chapter 5. At the initial stage of the comparison a tilt in the piston was not suspected due to the improved method of supporting the piston. The expansion at the front surface alone would then provide an approximate comparison with the predictions of the first finite element model, which is simplified when compared to the piston geometry (see Chapter 3).

The radial expansion profiles of the piston along the skirt for the holographic and finite elements results for a rise from 50°C to 70°C at θ=50° and θ=90° are shown in Figures 7.1. The model (Mesh 1) used for the predictions is shown in Figure 3.1 of Chapter 3. In this model, the following assumptions and simplifications were made :

a) the axial air gap was assumed to close along θ=40°,

b) the rib at the bottom of the skirt was assumed to have negligible effect on the expansion of the skirt and was, therefore, omitted,

c) the thickness of the skirt was assumed to be constant at all positions along the circumference.

The effect of including a rib was investigated by modifying the mesh and repeating the analysis. The boundary conditions were appropriately specified so as to produce temperature rises that agreed to within 1°C of the measured rises at atleast 90% of the thermocouple points located along the skirt. The modified mesh (Mesh 2) is shown in Figure 3.7 of Chapter 3. The expansion profiles obtained for the modified mesh have been included in Figure 7.1. These figures show that for Mesh 1 the radial deformation from the holographic results along θ=50° agreed to within 5% of the predictions but differed by 25% along θ=90°, both measured at the top of the skirt. The effect of including a rib can be seen from these figures. A 9 % reduction in the predicted expansion is noticeable at the bottom of the skirt, at 90° to the pin axis. At θ=50°, the reduction is smaller (approximately 5%) due to the lower flexibility of the skirt in this region. Nevertheless, the predicted expansion is

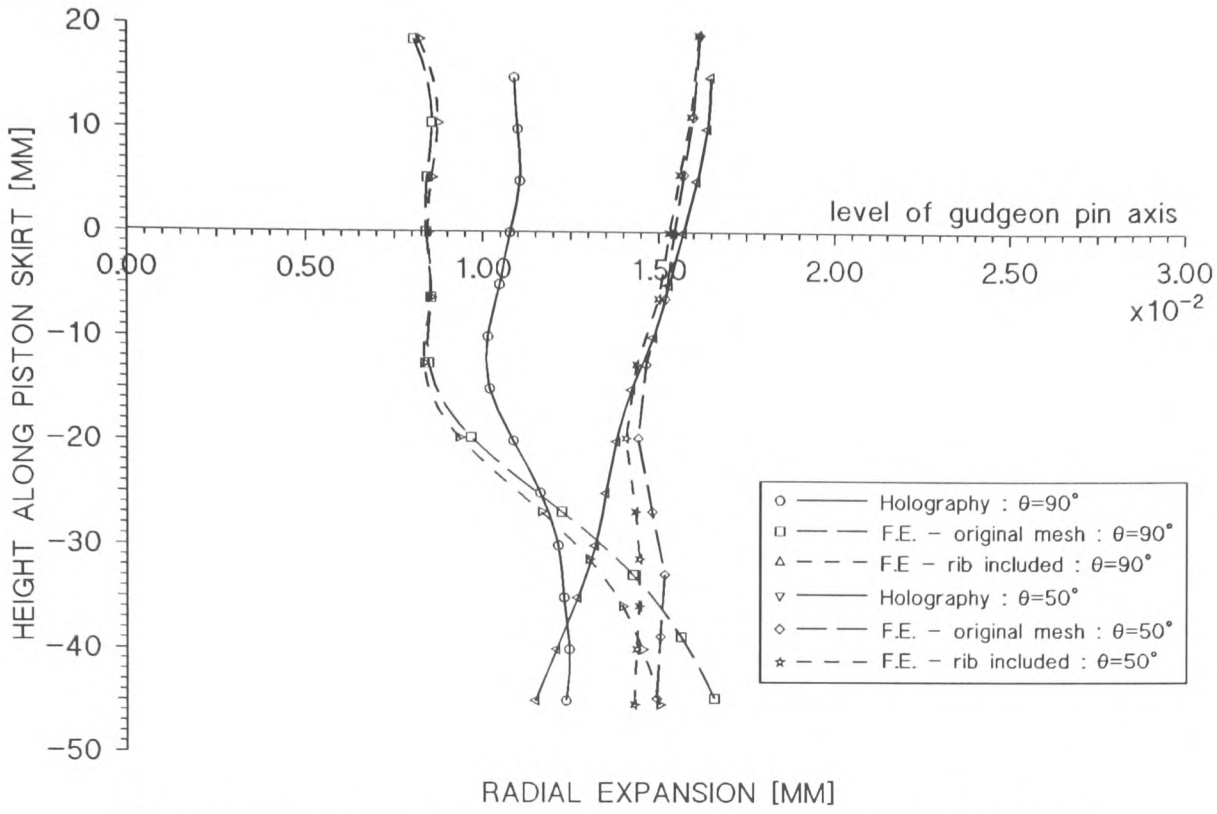

Figure 7.1. Comparison of holographic and finite element results for 50°C to 70°C rise (effect of including rib at bottom of skirt is shown)

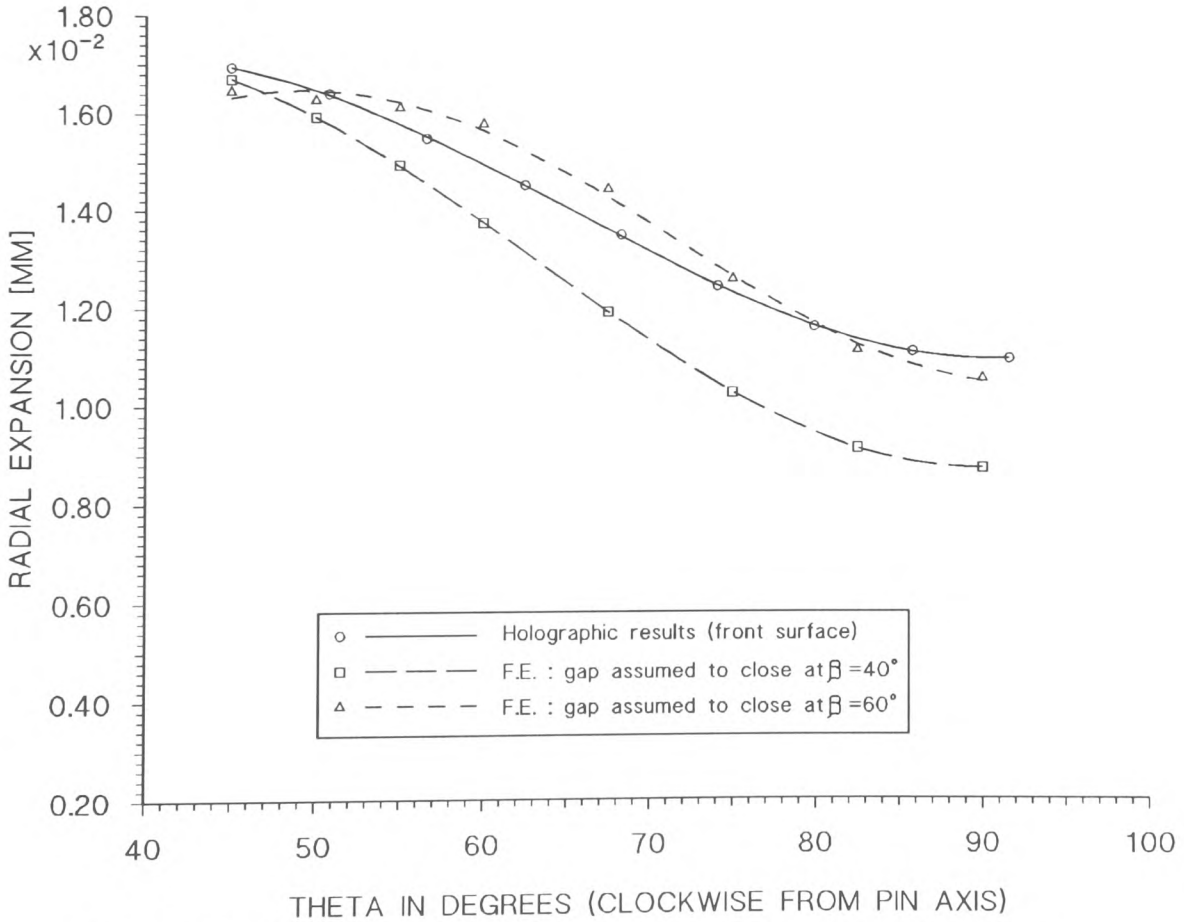

Figure 7.2(a). Comparison of holographic and finite element results at 10mm above gudgeon pin axis (50°C to 70°C)

larger that the experimental results by almost 17% at the bottom of the skirt.

The smaller predicted expansion at the top of the skirt at θ=90° was attributed to the incorrect assumption with regard to the position of closure of the axial air gap in the model. This position was previously shown to affect the expansion profile of the skirt (Chapter 3). Thus, in order to establish an accurate position where the gap closes, the model was modified by shifting the position of closure of the gap to β=60° (see Chapter 3) and the analysis was repeated. The boundary conditions in the modified mesh were altered appropriately in order to predict temperature rises that were once again within an allowable range of the measured rises. This will result in an expansion that not only indicates the effects of the modification but also includes the effects of changes in the boundary conditions. This was, however, acceptable for the comparison because the experimental results were being compared with the predictions of a model whose accuracy is not known. Thus the boundary conditions must be specified so that the predicted and measured temperature rises match, irrespective of the nature of modification made to the model.

Plots of radial expansion in the horizontal plane at 10mm above the pin axis for the two models with different positions of closure of the gaps is shown in Figure 7.2(a). The comparison shows that a better correlation between the experimental and predicted profiles can be achieved when the gap is assumed to close at β=60°. As will be shown later, a more accurate comparison can be made when the mean of the expansions at the front and rear surfaces is considered instead of expansion at the front surface alone. However, since dial gauge measurements at the pin axis level at diametrically opposite points at θ=45° and θ=225° showed a deviation of only about 8% (Chapter 4), the effect of the tilt is not significant at this level of the skirt. Hence, the present comparison is not grossly inaccurate.

The gradient of the profile from the experimental results can be seen to have a smoother variation when compared with the predicted curve. This is because the effect of closure of the air gap along the circumference during heating was not considered in the model (see Chapter 8). The measured and predicted profiles along the skirt at θ=90° now shows a closer agreement for a length of about 40mm of the

skirt (Figure 7.2(b)). Lower down the skirt, however, the measured displacement is larger than that predicted by about 25%. The expansion along $\theta=50°$ is not affected significantly by the change in position of closure of the air gap due to the lower flexibility of the skirt at this region.

The reasons for the large difference at the bottom of the skirt were suspected to be due to inaccuracy of the model in this area and possibly due to body displacement resulting from the non-central heat input. The first effect was investigated by revising the model so that the thickness of the skirt around the lower region matched as closely as possible to the true dimensions of the piston. A step, forming part of the rib, was introduced at the base of the pin-hole boss and the inner and outer radii of the skirt were varied to approximate the true complex geometry of the piston (Figure 3.8 of Chapter 3). The analysis was repeated using the new model (Mesh 3) with suitable boundary conditions so that once again the predicted rises in temperatures at the thermocouple points in the area under investigation agreed as closely as possible with the measured values. The measured and predicted temperatures for Mesh 3 are given in Table 7.1. The results are shown in Figure 7.3. From this figure we observe a smaller difference in expansion between the holographic and finite element results at the bottom of the skirt along $\theta=90°$ when compared to the previous case. The flexibility of the skirt in the revised mesh is less than that in the original mesh and therefore forms a closer approximation to the dimensions of the actual piston used in the experiments. The modification does not, however, affect the expansion along $\theta=50°$. Nevertheless, the difference between the two results at the bottom of the skirt was still large (approximately 15%). This difference was suspected to be due to a tilt in the piston and in order to confirm this the expansion at the front and rear surface were measured (see Chapter 6).

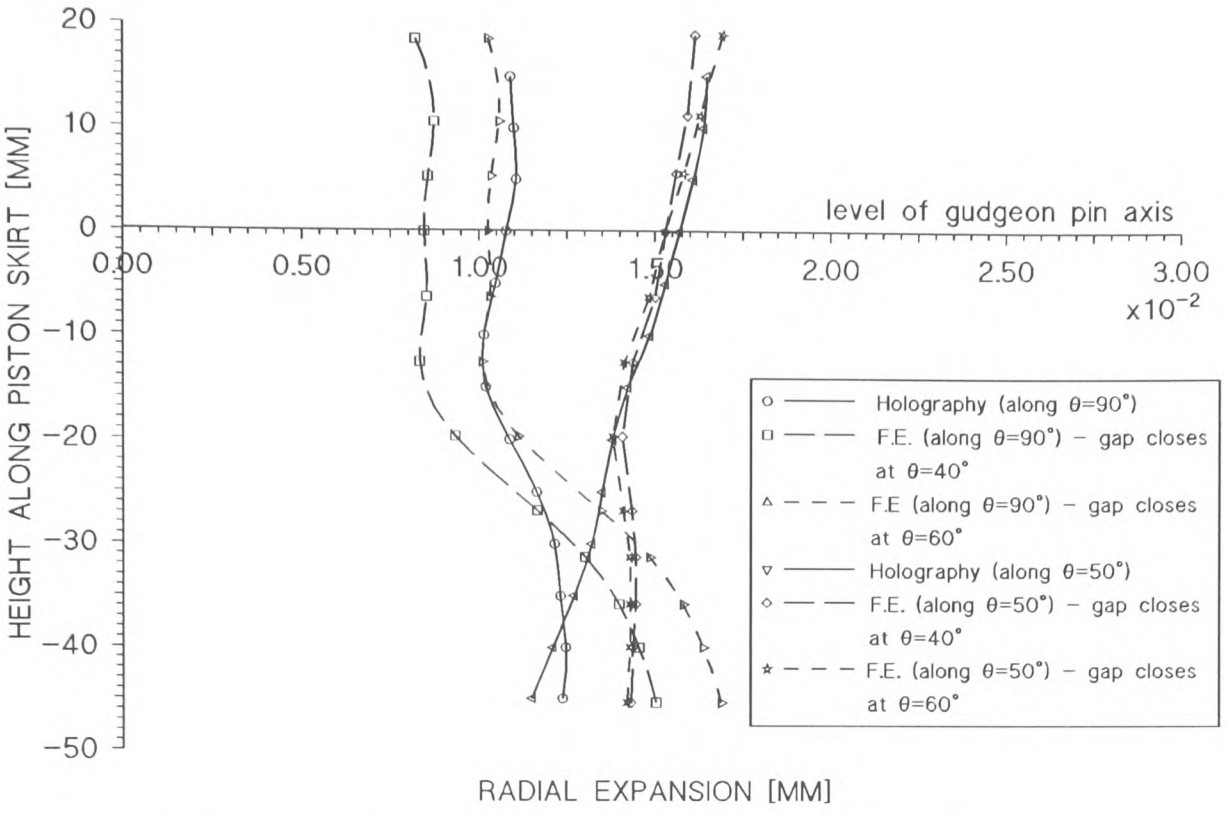

Figure 7.2(b). Comparison of holographic and finite element results along skirt showing effect of changing position of closure of air gap (50°C to 70°C)

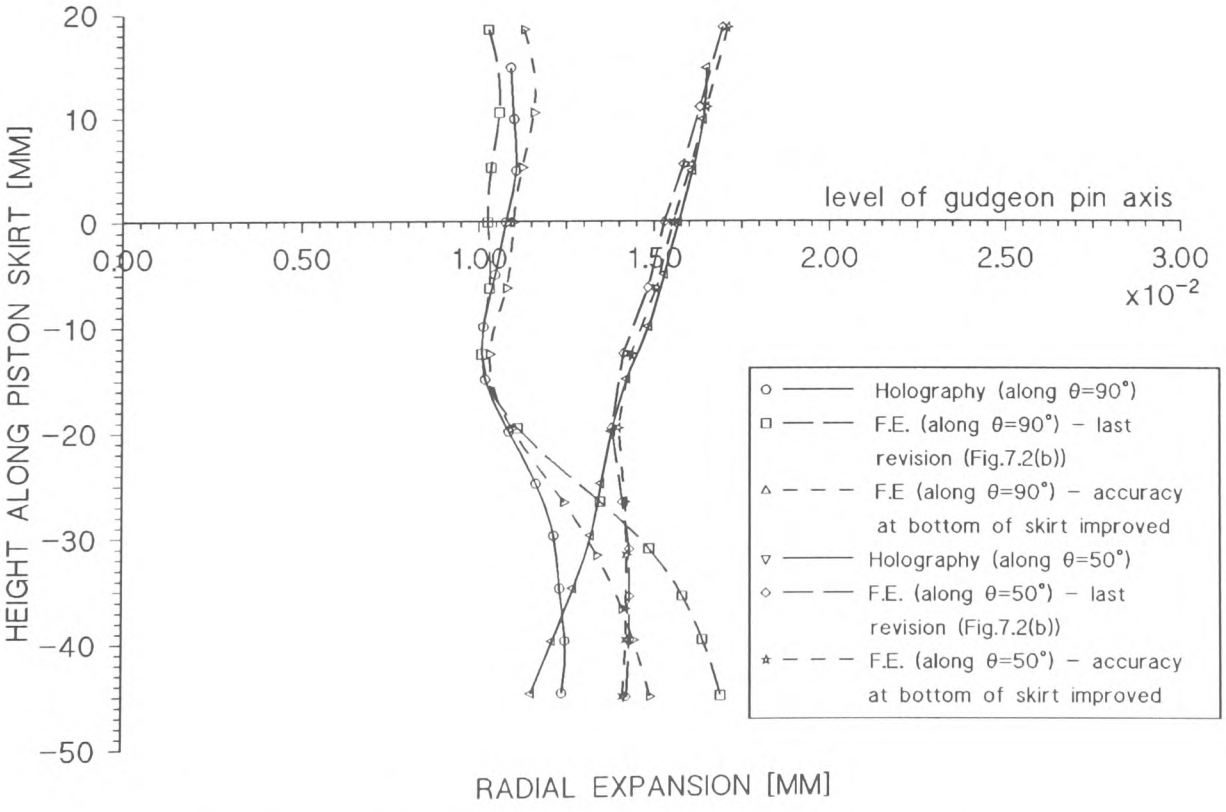

Figure 7.3. Comparison of holographic and finite element results showing effect of improving accuracy at bottom of skirt (50°C to 70°C)

Thermocouple	Predicted rise (°C)	Measured rise (°C)	Difference (°C)
T2	19.8	21.9	-2.1
T3	19.9	20.1	-0.2
T4	18.2	19.1	-0.9
T5	17.7	17.2	0.5
T6	14.4	16.3	-1.9
T7	14.3	15.8	-1.5
T8	19.1	19.1	0.0
T9	18.5	19.2	-0.7
T11	20.6	20.0	0.6
T12	16.6	15.2	1.4

Table 7.1. Predicted and measured temperature rises for Mesh 3 for datum rise of 50°C to 70°C (at T11)

Thermocouple	Predicted rise (°C)	Measured rise (°C)	Difference (°C)
T2	11.0	9.5	1.5
T3	10.9	10.2	0.7
T4	9.8	10.0	-0.2
T5	10.0	9.4	0.6
T6	9.0	9.1	-0.1
T7	9.4	8.9	0.5
T8	10.1	10.1	0.0
T9	9.9	10.1	-0.2
T11	9.8	10.0	-0.2
T12	9.6	9.5	0.1

Table 7.2. Predicted and measured temperature rises for Mesh 3 for datum rise of 130°C to 140°C (at T11)

7.2 Comparison of expansion at front and rear surfaces for 50°C to 60°C

7.2.1 For Piston No.1

The comparison of the mean of radial expansions at the front and rear surfaces with finite elements is shown in Figure 7.4. The comparison was made along the skirt at θ=60° for reasons discussed in Chapter 6. A close agreement at the top and bottom of the skirt can be seen. The predictions of the model are, however, smaller than the measurement by about 10% at 20mm below the pin axis.

The predicted expansion was shown (in Chapter 3) to fluctuate with the predicted temperatures. Since the maximum difference between the predicted and measured temperatures for the experiment using Piston No.1 for a rise from 50°C to 60°C was 3% (0.3°C), the predicted deformation can be expected to fluctuate by a similar amount and this was considered acceptable.

The predicted profile can be seen to have a greater inward curvature at about mid-skirt level when compared to the measured profile. The smaller predicted expansion at this level of the skirt can be attributed to the assumption that the inner surface of the skirt and outer surface of the sleeve were bonded. This was represented by common nodes between the two surfaces in the model. In the real situation, the skirt is in tension and the sleeve is in compression as a result of the differential contraction between the two during cooling after casting. This resulted in in-built stresses which were partially relieved when the piston was heated, thus imposing less restriction to the expansion of the skirt.

7.2.2 For Piston Number 2

The mean of the expansions at the two surfaces was found to have negligible deviation for the three repeated experiments. Thus, it was sufficient to consider any one of these for comparison with finite element results. However, the effect of a maximum difference of 0.6°C between the predicted and measured temperatures must be considered in the comparison. As discussed in Chapter 3 (Section 3.5), a

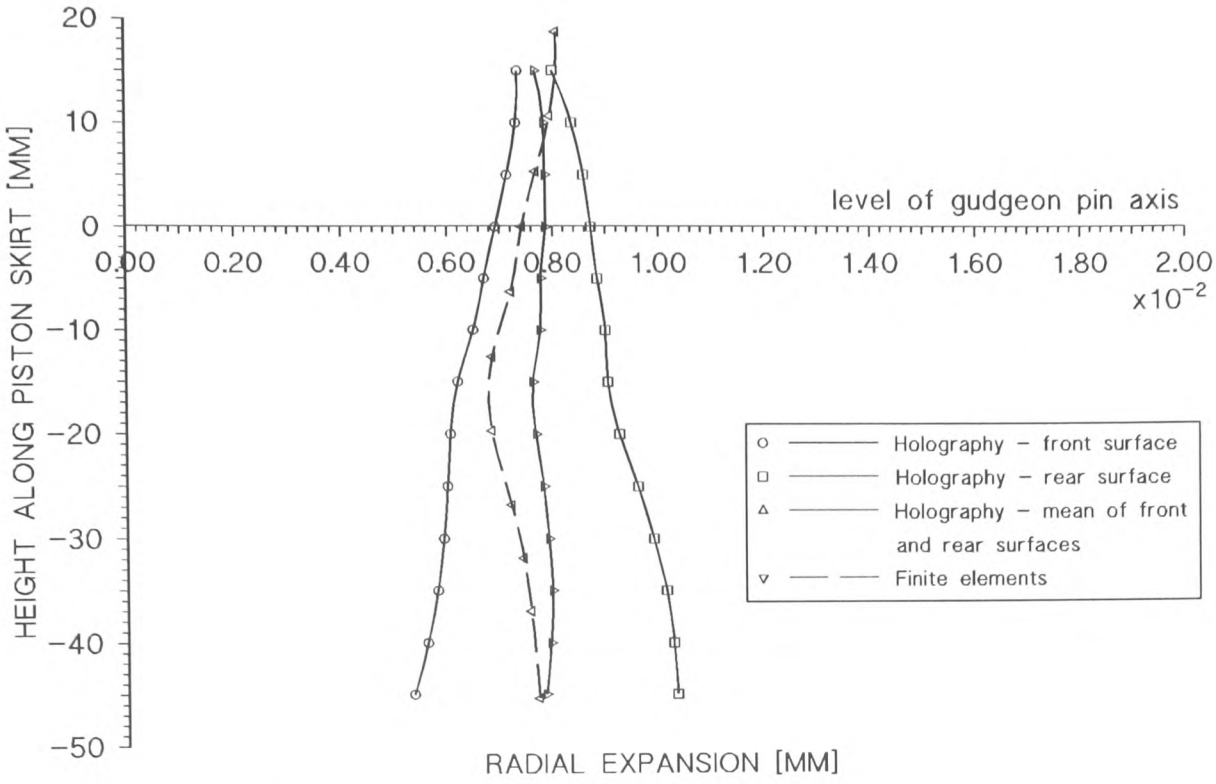

Figure 7.4. Comparison of holographic and finite element results for Piston No.1 (50°C to 60°C)

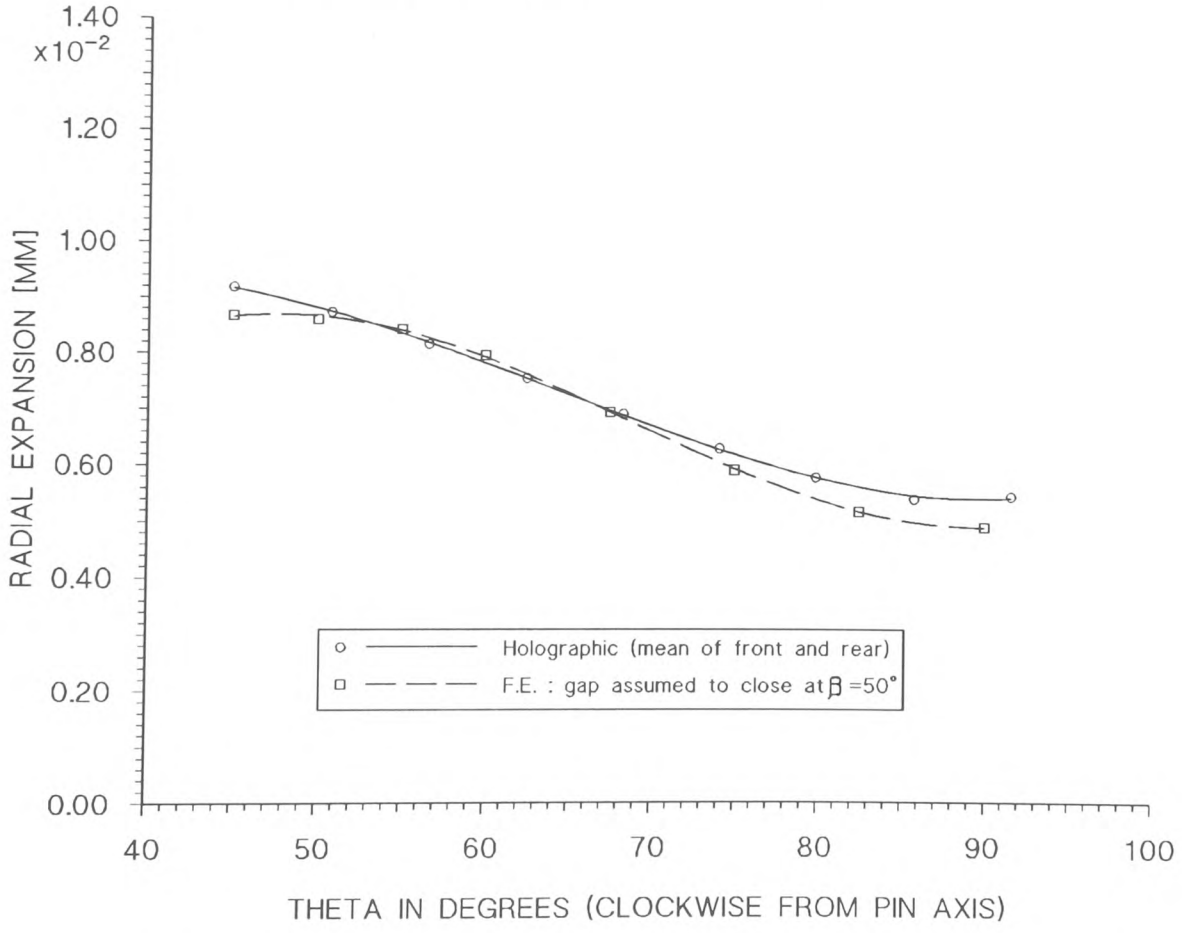

Figure 7.5. Comparison of holographic and finite element results at 10mm above pin axis (50°C to 60°C) rise

fluctuation of 0.6°C in the predicted temperatures causes a variation of 6 to 8% in the predicted deformation. Hence, quantitative comparisons between the measured and predicted expansion is also subjected to a similar variation.

The availability of measured deformation data at the front and rear surfaces enabled a more accurate comparison to be made with the predictions of the model at the top of the skirt and, hence, to determine the position of closure of the air gap with greater accuracy. The comparison is shown in Figure 7.5 in which the position of closure of the gap has now been shifted to β=50°. When Figure 7.5 and 7.2(a) are compared one will notice that the change in gradient of the predicted profile in Figure 7.5 is more gradual when compared to the previous profile. In addition, the radial displacement between the two curves agree to within 5% for about 80% of the circumference and thus forms a closer approximation to the measured profile.

The measured and predicted profiles over a 45° sector of the piston surface were plotted to provide a visual representation of the deformed surfaces (Figure 7.6(a)-(b)). The predicted profile was found to have a greater inward curvature at about mid-skirt level when compared to the measured profile. This is in agreement with the results obtained using Piston No.1. The results show a maximum difference in expansion of 15% at the bottom of the skirt along θ=90° (Figure 7.7). Along θ=50° a maximum difference of 8% occurs at mid-skirt level. At both sections of the skirt the measured profiles are less curved than those predicted by the model. As in Piston No.1 the greater curvature of the predicted profile is again attributed to the assumption that the skirt and sleeve are bonded. The predicted expansion of the skirt is therefore fully restrained by the sleeve throughout the length of the sleeve (i.e. for 40mm from the top of the skirt). The greater difference at the bottom of the skirt at θ=90° can be attributed to the effect of thermal stresses (in the model) at the interface of the two materials on this part of the skirt, which has a higher flexibility. In addition, the difference can also be due to the effects of changes in the size of the axial air gaps and the in-built stresses which have not been considered in the model because of their complexity resulting from the design and manufacturing process of the piston.

Another factor contributing to this difference could be due to inaccuracies (approximately 5-8%) in the measurement at the bottom of the skirt (see Chapter 6).

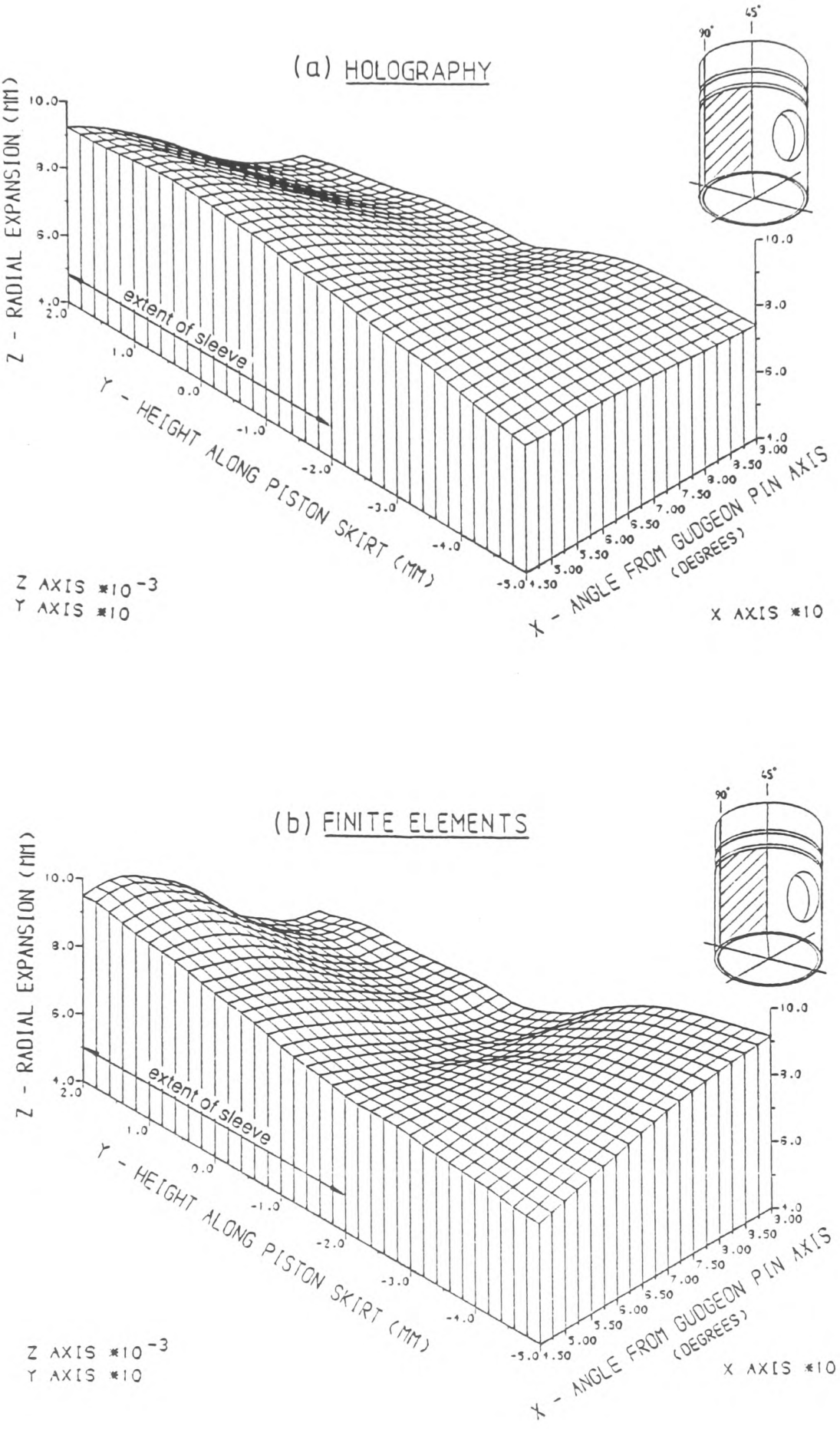

Figure 7.6. Radial expansion maps for 45° sector of piston surface for (a) holographic and (b) finite element results (50°C to 60°C)

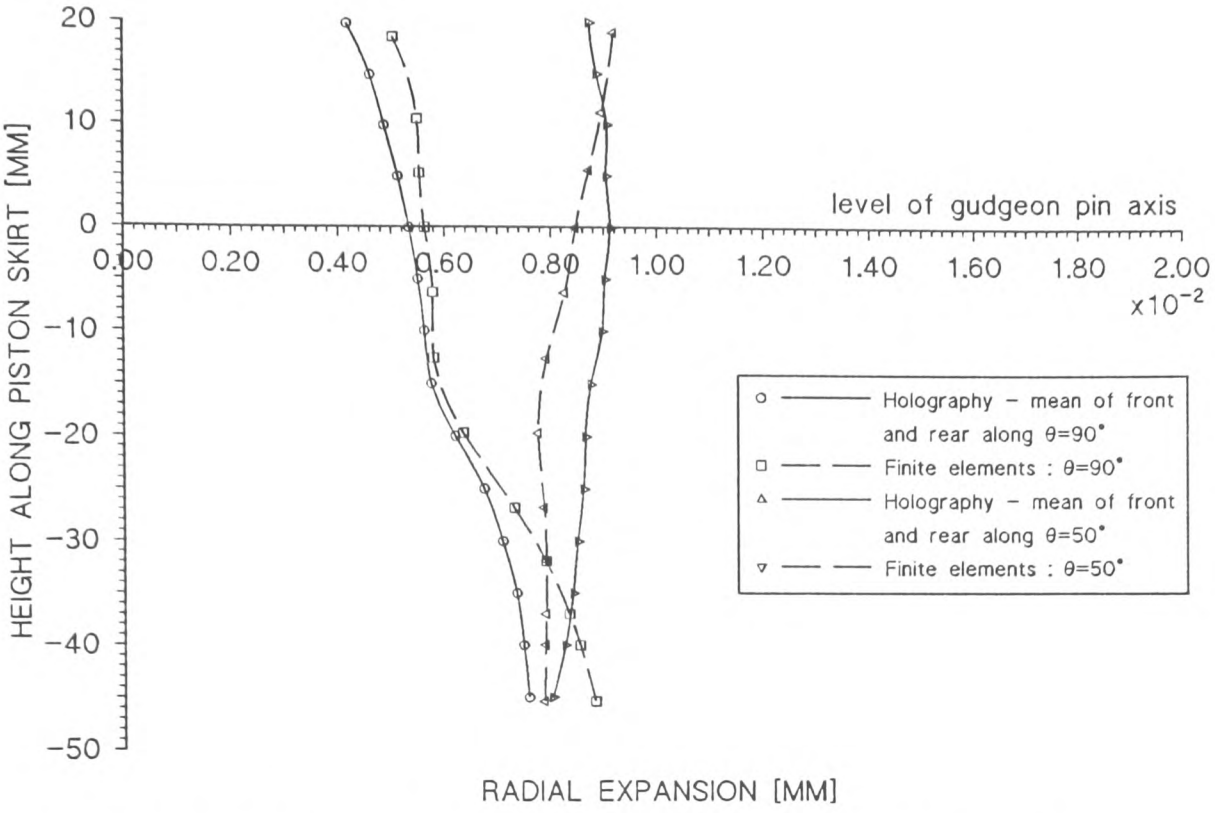

Figure 7.7. Comparison of mean of holographic measurement at front and rear surfaces with finite elements for Piston No.2 (50°C to 60°C)

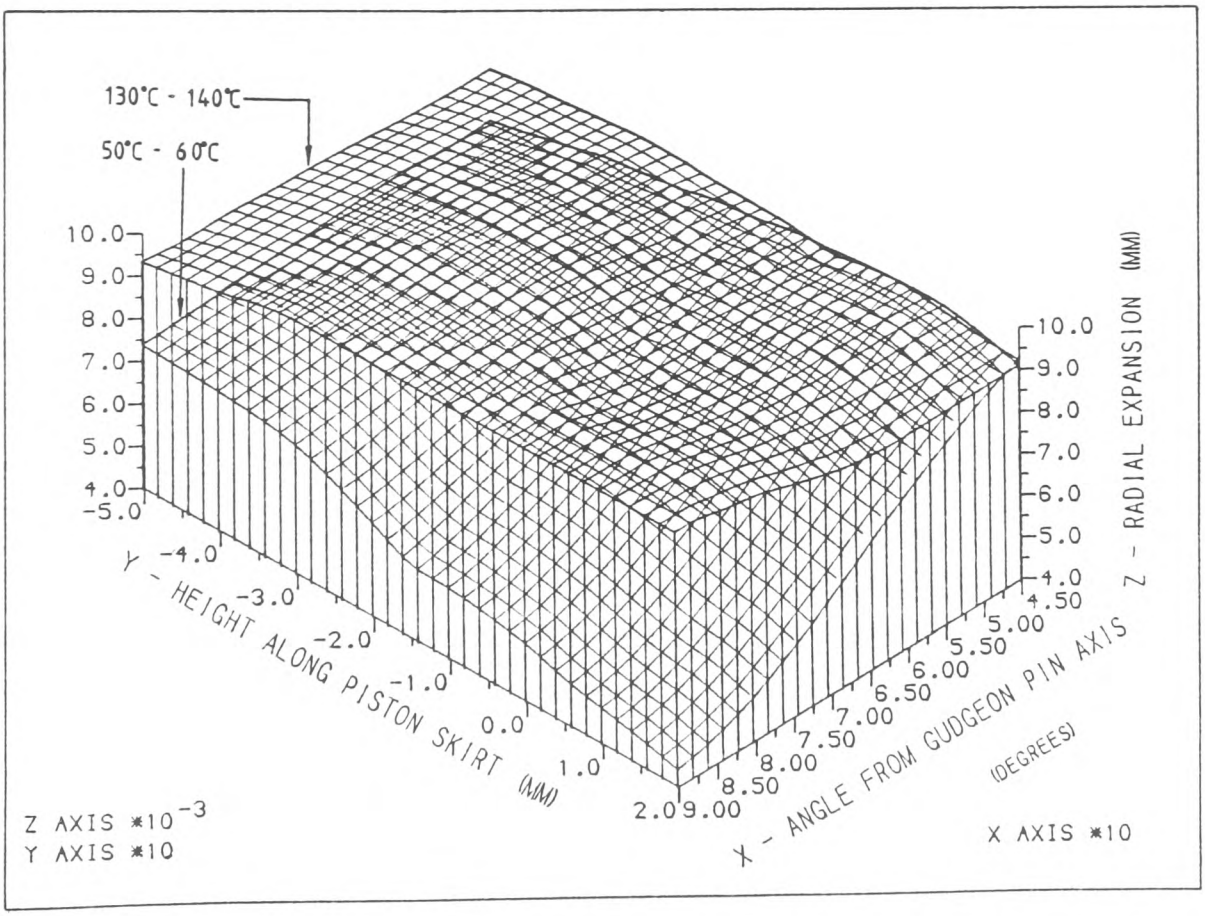

Figure 7.8. Superimposed radial displacement maps from holographic results for 50°C to 60°C and 130°C to 140°C rises

7.3 Comparison of expansion at front and rear surfaces for 130°C to 140°C rise

Superimposed radial expansion maps from the experimental results for 50°C to 60°C and 130°C to 140°C rises are shown in Figure 7.8. Along θ=90° an increase of approximately 75% in the mean radial expansion for the 130°C to 140°C range when compared to the 50°C to 60°C range was observed at the pin axis level. Along θ=50°, however, the increase is about 10% (Figures 7.7 and 7.9). At the higher temperature range the steel insert separates from the skirt and loses control of its expansion (see later discussion). This result is in agreement with the findings of Fletcher-Jones et.al.(1982) in which point-wise measurements were made and shown that abrupt increase in expansion occurs at about 130°C.

The expansion profiles along θ=90° and θ=50° predicted by the original model indicated the presence of the effects of the insert even at the higher temperature (Figure 7.9). This is because of the assumption that the insert and skirt were still bonded. The model therefore does not provide the true deformation behaviour of the piston at the higher temperature range. The measured and predicted temperatures at the 130°C to 140°C range are given in Table 7.2 in which a maximum difference of 1.5°C occurs at the thermocouple located at the top of the crown. The mean difference at the skirt is, however, about 0.2°C which was considered acceptable.

In order to confirm that a separation between the sleeve and skirt occurs at the higher temperature range, the nodes at the skirt-sleeve interface starting from θ=55° to θ=90° were decoupled and the analysis was repeated. For this purpose, the mesh was modified by deleting a few elements that made up the sleeve and redrawing them with a gap of 0.05mm between the outer surface of the sleeve and the inner surface of the skirt, for the full length of the sleeve (Figure 7.10). The results of the analysis using the modified mesh are included in Figures 7.9. When the skirt and sleeve were released a significant increase in expansion at θ=90° was observed. When compared with the holographic results, this suggests that a separation between the two surfaces has occurred during the experiment. The expansion along θ=50° was not significantly affected by the release because the skirt and sleeve are still bonded in this section.

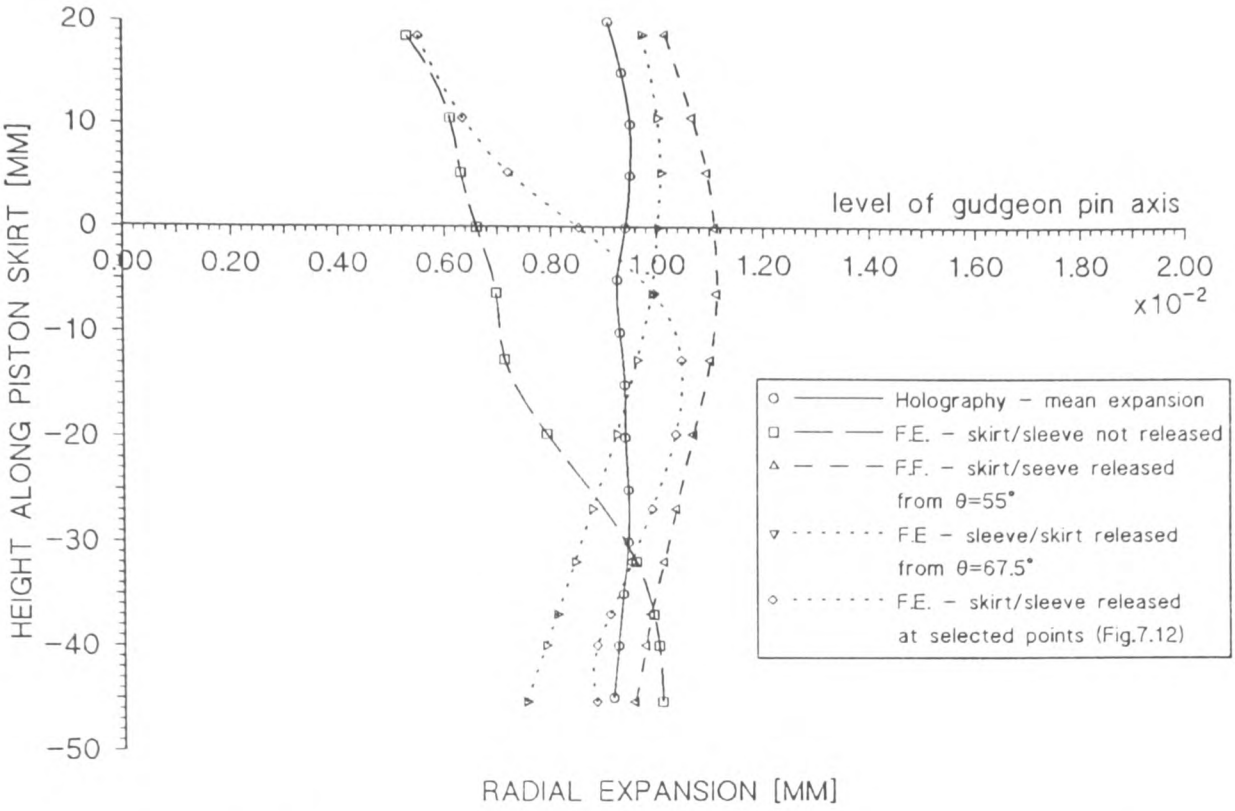

Figure 7.9. Comparison of holographic and finite element results for rise from 130°C to 140°C (Effects of releasing skirt from sleeve is included)

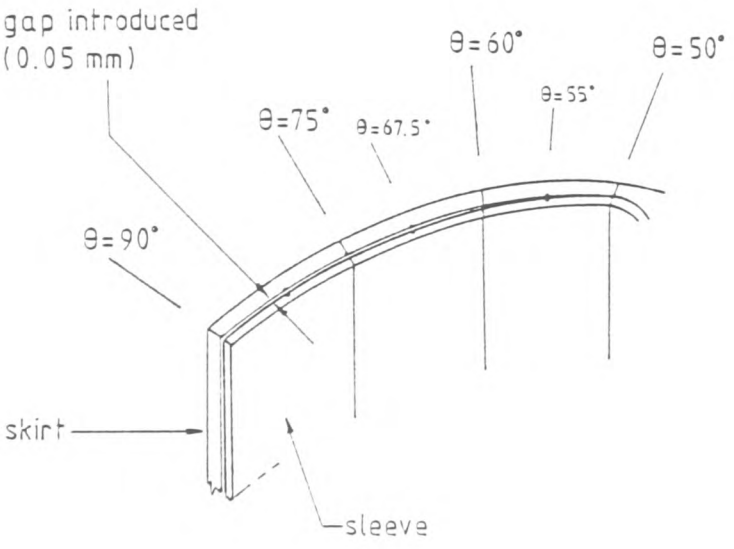

Figure 7.10. Sketch showing positions along the circumference where nodes between sleeve and skirt were decoupled

As a consequence of the separation of the sleeve from the skirt, the latter can now be expected to expand freely as a monometal piston. To check this, dial gauge measurements were taken at θ=90° and θ=270° at the level of the gudgeon pin axis while the piston was heated from room temperature (20°C) to about 150°C. The results are shown in Figure 7.11. From this figure we can see that the gradient of the expansion-temperature curve has a certain value M up to about 130°C and thereafter it increases to about 1.7xM above this temperature. On this figure theoretical expansion-versus-temperature curves for steel and the aluminium alloy have been plotted so that they can be compared with the measured results. The comparison shows that, at the lower temperatures, the skirt expansion follows that of the steel insert whereas at the higher temperature it follows the expansion of the aluminium alloy. This confirms that the steel sleeve insert has lost control over the expansion of the skirt at the higher temperatures (above approximately 130°C).

In an attempt to improve the accuracy of the model above 130°C, the positions where the nodes were decoupled was changed and the analysis was repeated. The nodes starting from θ=65.7° to θ=90° (Figure 7.10) were released so as to decrease the predicted expansion along θ=90° . The results are included in Figure 7.9. The change in the position of release of the nodes appear to have a greater effect at the bottom of the skirt along θ=90°, again due to the greater flexibility in this region. The results of the two finite element analyses suggest that the separation process is complex and it may not be uniform along the circumferential direction. In order investigate this further, the mesh was modified by releasing selected nodes at the steel-sleeve interface (Figure 7.12) and the results for this modification are included in Figure 7.9. The results of the finite elements runs on the three types of separation considered suggest that it may be impractical to modify the mesh in a manner so that the predicted and measured profiles match. The holographic measurement, however, provides the true profile of the skirt after a separation has occurred.

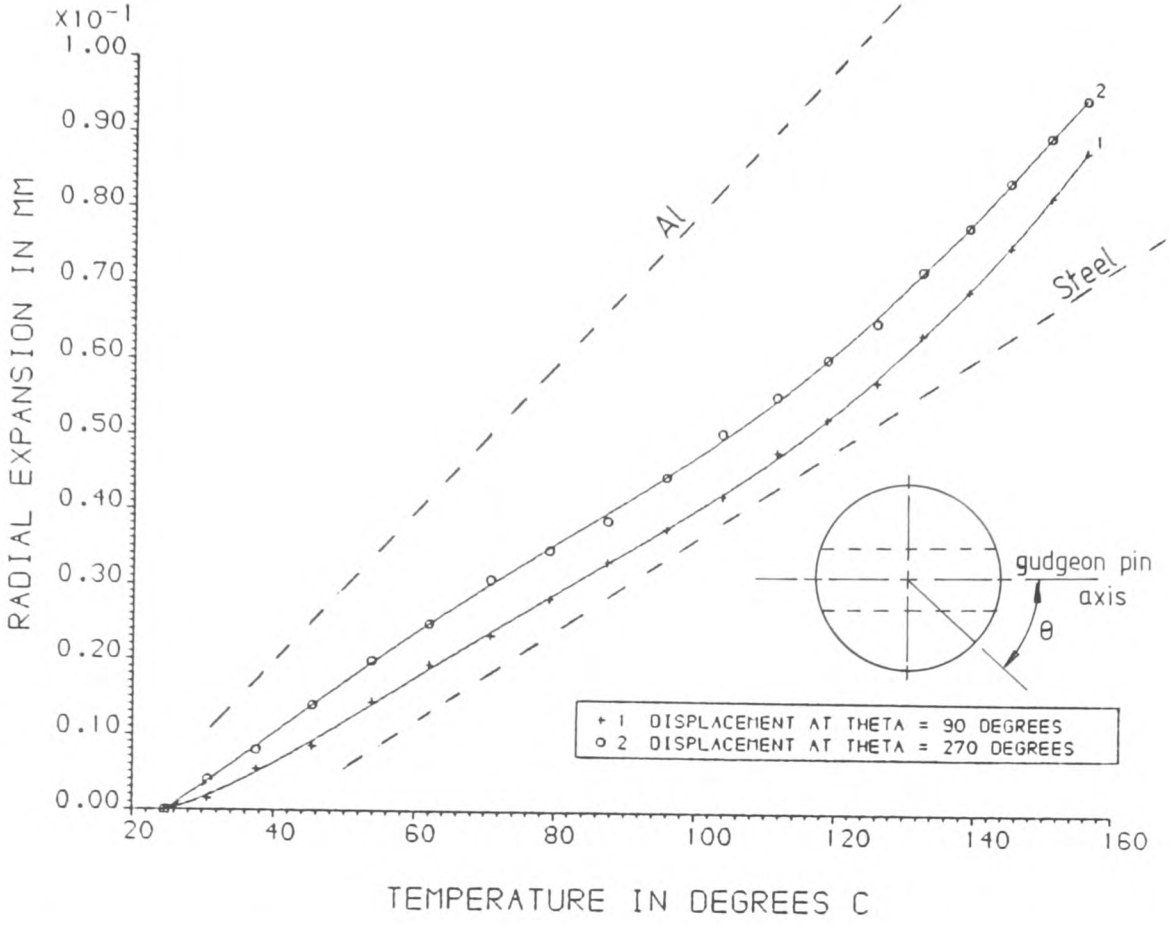

Figure 7.11. Plots of radial expansion at pin axis level against temperature along θ=90° and θ=270°

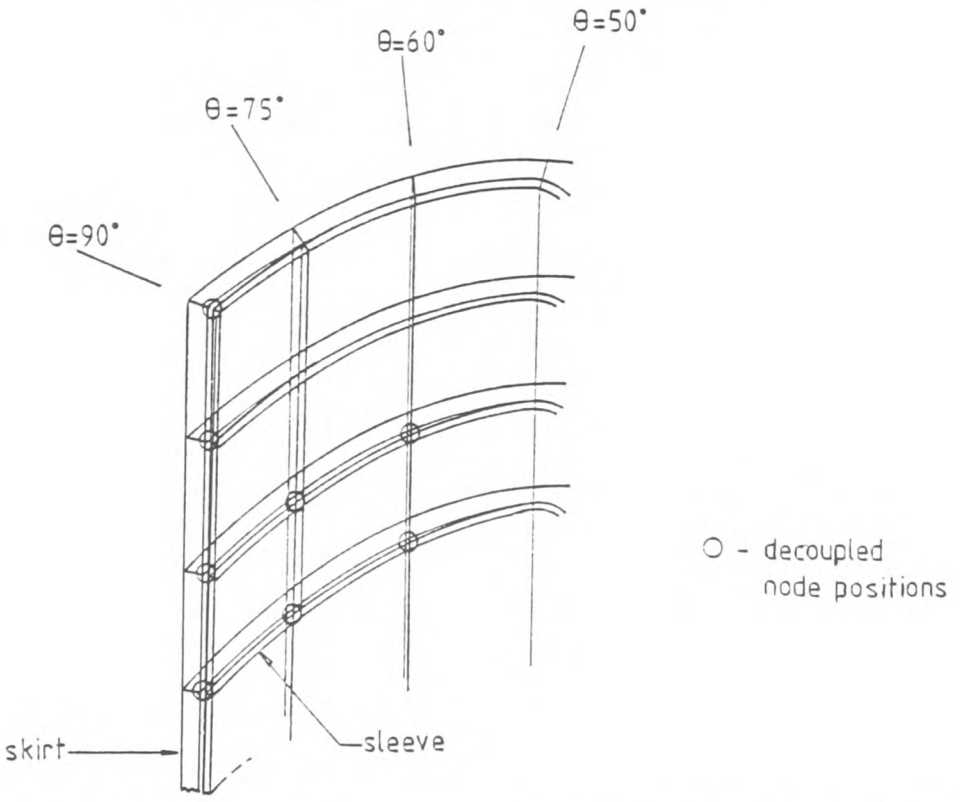

Figure 7.12. Sketch showing selected points where nodes between sleeve and skirt were decoupled

CHAPTER 8

GENERAL DISCUSSION AND CONCLUSIONS

8.1 General discussion

8.1.1 Comparison of experimental and finite element results

The assumptions made in the generation of the finite element model of an open sleeve piston resulted in predicted profiles that did not accurately represent the true deformation undergone by the piston. By using the holographic technique for direct measurement it was possible to check the effects of these assumptions and to improve the accuracy of the model. For a temperature rise below the stress free temperature of 130°C the predicted profile was found to have a greater inward curvature at mid-skirt level. This was indicative of the assumption in the model that the sleeve and skirt were bonded. In the real situation complex residual stresses exist between the two surfaces as a result of their differential contraction after casting. Although it may be possible to model these stresses by assuming a stress free temperature at 130°C, the stresses present at room temperature will depend on the initial clearance specified between the sleeve and the piston body. Since the true clearance between the sleeve and the piston may not be constant in both circumferential and axial directions (due to their complex geometries), the predicted in-built stresses at room temperature will contain a certain element of uncertainty. The predicted profile at any temperature will be subjected to similar doubts and comparison with measurements will then be necessary. The predicted and measured profiles may, however, show a closer agreement compared to the case when the residual stresses are completely ignored, but due to the complexity of the in-built stresses it may be impractical to model them accurately.

The assumption on the position of closure of the axial air gap in the circumferential direction was also found to influence the expansion profile of the skirt. Since the gap varies gradually from about 140um at 90° to the pin axis to 0um towards the pin axis, the exact position at which the skirt and sleeve regain contact cannot be established easily. The experimental results provide a guide as to where the air gap can be accurately assumed to start. From the analyses it was shown that close agreement between predicted and measured profiles occurred when the gap was assumed to start at $\theta=50°$, as opposed to the value of $\theta=40°$ recommended by the piston

manufacturer. The experimental results also take into account the effects of closure of the gap as the piston was heated. To consider this effect accurately in the modelling it will be necessary to refine the elements in the vicinity of the gap and collapse the nodes across the gap automatically as the temperature rises. This again will produce predicted profiles that are not completely free from doubts because the gap may close unevenly in the circumferential and axial directions.

The model used for predicting the expansion at 50°C to 60°C range was shown to be completely incapable of predicting the hot shape of the piston above 130°C. This is because the sleeve loses control over the expansion of the skirt which was then characteristic of a monometal piston. A separation between the sleeve and skirt occurs and this was confirmed in the finite element analysis by decoupling the nodes between the two surfaces and repeating the analysis. However, it was found that by releasing the skirt from the sleeve for a selected area it was not possible to match the two profiles. This suggests that the actual separation process is complex and could be impractical to model accurately.

8.1.2 Comparison of ESPI and holographic techniques

A detail discussion on the comparison between ESPI and holographic methods as applied to the measurement of the thermal expansion of the piston was given in Chapter 5. It was shown that both the above techniques have certain advantages and limitations. Some of the limitations of the ESPI method was found to be outweighed by the ease of obtaining and analysing the fringes. Although in the current work the ESPI results were found to be smaller than the holographic measurements, the difference can be decreased by using automatic phase-shifting and data acquisition techniques. Surface contouring techniques can be implemented to relate object surface points to the digitised points in order to improve the accuracy of the results. However, if the ESPI method is used for measuring deformation at the front and rear surfaces it will be necessary to adopt special experimental arrangement, such as the use of multiple cameras to image the two surfaces onto two TV cameras separately.

Alternatively, if a single camera is used (in a self-contained) the ESPI system can be arranged on a rotating stage (with the piston on the fixed bench) so that the camera can be rotated to image the front and rear surfaces separately with the aid of mirrors positioned behind the piston.

8.1.3 Development of the experimental methods

8.1.3.1 Simultaneous measurement of x, y and z components

The early stage of the work has lead to the design of an experimental rig and associated computer programs that can be used for measuring all three Cartesian components of displacements simultaneously. Although this rig was not subsequently used in the comparative study due to the limited laser power and problems of rigid body movement, it can be used in other applications involving continuous deformation. The accuracy of the transformation routines developed has been verified and the validity of the technique was confirmed by comparing the measurements of the expansion of a cylinder with finite element predictions. The comparison showed good agreement in the radial direction (within 7%) but a maximum difference of about 30% in the axial direction. The poorer agreement in the axial direction was attributed to lower sensitivity of the arrangement to movement in this direction. This can be overcome by positioning the cylinder at an angle to the vertical so that the axial displacement will have a larger component in the direction of the sensitivity vectors.

8.1.3.2 ESPI system for measuring radial expansion

The comparative study between holography and ESPI has lead to the development of a simple ESPI technique for measuring two displacements components simultaneously. The interferometer used is one that was designed for measuring out-of-plane displacements. A mirror concept was used to obtain two displacement vectors in the horizontal plane. The in-plane and out-of-plane displacements were

evaluated from the measured quantities. The proposed technique was verified by measuring the deflection of a cantilever and comparing the results with those from the deflection theory. This technique was subsequently used for measuring the radial deformation of the piston. A main advantage of the technique is that two fringe patterns having different sensitivities could be imaged onto a single video frame for analysis. Perspective distortions and lateral inversions in the two images were accounted for in a transformation routine.

8.1.3.3 Measurement of radial expansion in the presence of rigid body movement

The simplified holographic system developed for measuring radial expansion at the front and rear surfaces of the piston was shown to produce accurate deformation data which can be used for comparison with the predictions of a finite elements model. A model for only a quadrant of the piston is required and the loading conditions can be assumed to be symmetrical. Body displacement during the measurement was eliminated by taking the mean of the expansion at the two surfaces. The mean expansion also assumes symmetrical conditions such as heat input and piston construction.

8.1.4. Engineering implications of the results

The results of the investigation has shown that the accuracy of the finite element model of the piston can be improved based on the holographic measurement. With an improved model the piston designer can predict the expansion profile and hence the running clearance more accurately. By adopting a suitable piston design in order to achieve low running clearance it will be possible to improve the overall performance of the engine. In addition, accurate models will enable an accurate comparison of the predicted performance of pistons of various designs to be made.

8.2 Conclusions

The following conclusions can be drawn from the current work :

a) The comparison between experimental and theoretical expansion profiles indicated the effects of the assumptions and simplifications made in the generation of the finite element model of an open sleeve piston. Based on the measured data it was possible to improve the accuracy of the model.

b) The original model of the piston was found to be incapable of predicting the true deformation behaviour of the skirt above the stress free temperature. The experimental results indicated a rapid increase in expansion above this temperature, suggesting that the steel insert has lost control over the expansion of the skirt. In order to model this it was necessary to modify the original mesh by releasing the skirt from the sleeve. The predictions of the model was, nevertheless, 20% higher than the measurement. Repeated modification by releasing the skirt at selected nodes did not produce predicted profiles that matched the measured profiles. This suggests that the true separation process is complex and may not be easily modelled.

c) The following experimental techniques have been developed as a result of the comparative study :

- a simplified experimental rig to measure all three Cartesian components of displacements simultaneously using holographic interferometry. A geometrical transformation technique for relating points on the interferograms to the corresponding points on the piston surface has been developed.
- a simplified approach for measuring the horizontal in-plane and out-of-plane displacement components simultaneously using ESPI has been developed. The interferometer used is one that was designed for measuring out-of-plane displacements.
- a holographic method for measuring radial expansion in the presence of rigid body motions using multiple mirrors has been devised.

d) The comparative study between ESPI and holography has shown that some of the limitations imposed by the speckled nature of fringes in the ESPI method is outweighed by the ease of obtaining and analysing fringes to extract deformation data. Due to the high definition

fringes obtainable using the holographic method, however, it was possible to study the deformation due to a larger temperature rise, compared to that in the ESPI method, in a single stage. Although ESPI was used for studying the front surface of the piston alone, a simple technique for measuring deformation at the front and rear surfaces without using multiple cameras is proposed.

CHAPTER 9

SUGGESTIONS FOR FURTHER WORK

9.1 Introduction

The development of high resolution video systems and automatic fringe analysis techniques (review by Reid 1987) has made the process of analysing interferograms to obtain deformation data both faster and more accurate. The benefits of such techniques were not fully exploited in the current work due to lack of the relevant equipment and expertise within the department. Nevertheless, the development of automatic techniques for analysing multiple interferograms on a single video frame is considered to be outside the scope of the current study.

With the development of computer-based systems of acquiring and analysing fringes in mind, we will consider some of the ways in which the current project can be extended for future work. The possible applications of the techniques developed in the current research in an industrial environment are briefly discussed.

9.2 The 4-mirror method for measuring 3-D displacements

The simplified technique developed for measuring all three Cartesian components of displacement simultaneously can be used successfully if a high power laser (such as a Argon laser) is use for illuminating the front and rear surfaces of the piston. The reference beam should be expanded from a sufficient distance away from the holographic plate so that the expanded beam illuminates the entire plate uniformly. In order to improve the accuracy of measurement in the vertical direction (along the piston axis) the piston can be tilted so that its axis makes an angle of about 30° to the vertical. This, however, will require some modifications to the transformation routines to take into account the effects of the tilt.

A high resolution camera, such as the one proposed by Creath (1989), can be used to record all four images onto a single video frame. The interferograms at the start and end of the deformation can be digitised directly into an image processing system for analysis while recording the live fringe formation on a high band 'U-matic' video tape.

In situations where the resolution of the camera limits the density of the fringes, and hence the displacement measured, the method proposed in the current work can be adopted. In order to speed up the analysis the fringes on the photographs can be digitised into a computer using a scanner. A fringe tracking routine similar to the one developed by Robinson (1983) can be implemented to locate fringe positions. In all the above cases, however, it will still be necessary to use the transformation technique developed here to take into account the effects of perspective distortions and lateral inversions.

9.3 The ESPI technique

Future work using ESPI can be focussed on improving the accuracy of the technique developed in the current study. The incorporation of automatic phase-shifting and image acquisition methods to avoid loss of fringes due to manual phase-shifting should be considered. The fringes can be digitised directly into an image processing system instead of transfering them from a video tape (as was done here), which could result in a loss of clarity. An automatic phase-unwrapping method can be developed and implemented to determine fringe orders at specified grid points.

Since the ESPI method is a more practical method to work with in terms of time consumed, especially in a thermal problem, it could be worth considering the arrangement discussed in Section 8.1.2 for measuring deformation at the front and rear surfaces. Two images of each surfaces can be digitised simultaneously and analysed to determine the deformation at the two surfaces.

9.4 Applications

The results of the experimental work carried out suggest a need to improve the design of the open-sleeve piston for use under operating conditions, where the temperature can exceed the stress free temperature of 130°C. In order to maintain the same piston design and achieve effective control over the expansion of the skirt at all temperatures one possible approach is to use special manufacturing processes to ensure that a permanent metallic bonding occurs between the two materials. This will prevent a separation between the insert and the piston body from taking place and will enable the designer to fully exploit the advantages of the open-sleeve piston discussed in Chapter 3.

The experimental techniques employed in this work can also be extended to the study of thermal behaviour of pistons of other designs and the results can be used to improve the accuracy of the mathematical models. The wet processing holographic methods may have certain practical limitations when applied to an industrial environment but this drawback can be overcome by using thermoplastic recording materials (Hariharan 1987). With the incorporation of automatic fringe analysis techniques the holographic and ESPI methods can be effectively used by piston manufacturers to design pistons with improved thermal characteristics. In situations where the finite element method can be prohibitive to use due to cost and time consumed the optical methods provide an accurate technique of measuring the deformation of the piston. In these applications the effects of differential expansions of the various materials within the piston, on the skirt profile, can be easily established.

APPENDICES

Appendix A1 - Theory

A1.1 Holographic interferometry

A1.1.1 Real-time holographic interferometry

In the real-time holographic technique, the processed holographic plate is returned exactly to the same position in which it was exposed. When it is illuminated with the original reference beam, the virtual image coincides with the object. If the object deforms, two sets of light waves will reach the observer, one being the reconstructed wave (corresponding to the object in its original state) and the other is the directly transmitted wave from the object in its deformed state. The two wave amplitudes will add at points where the difference in optical paths is zero or a whole number of wavelengths, and cancel at some other points in between. An observer viewing the reconstructed image therefore sees it covered with a pattern of interference fringes, which contours the changes in shape of the object. These changes are observed in real-time, i.e. as they occur.

In an off-axis holographic system, the intensity at the photographic plate when the hologram is recorded is

$$I(x,y) = |r(x,y) + o(x,y)|^2 \qquad \ldots.A1.1$$

where,

$r(x,y)$ = complex amplitude due to reference beam

$o(x,y)$ = $o(x,y)\, e^{-i\Phi}$ is the complex amplitude due to the object in its original state.

Assuming that the plate has been processed so that its amplitude transmittance t is a linear function of the intensity and can be written as,

$$t(x,y) = t_o + \beta TI \qquad \ldots.A1.2$$

where,

t_o = constant background transmittance,

T = exposure time,

ß = slope of the amplitude-versus-exposure characteristic of the photographic material.

When the processed hologram is replaced in the same position in which it was recorded, it will be illuminated by the wave from the deformed object as well as the reference wave. The complex amplitude of the transmitted wave is then given by

$$u(x,y) = [o'(x,y) + r(x,y)]t(x,y) \qquad \text{....A1.3}$$

where $o'(x,y)$ is the complex amplitude of the wave from the deformed object. If the change in shape of the object is small, we can assume that only the phase distribution of the object wave is modified so that

$$o'(x,y) = o(x,y)\ e^{-i\Phi'(x,y)} \qquad \text{....A1.4}$$

The only terms of interest in the expansion of (A1.3) are those corresponding to the primary image and the directly transmitted wave (Hariharan,1986). The complex amplitude due to these is given by

$$u'(x,y) = \beta T r^2 o(x,y) + (t_o + \beta T r^2)o'(x,y) \qquad \text{....A1.5}$$

Accordingly, the resultant intensity is

$$I'(x,y) = o(x,y)^2 \{\beta^2 T^2 r^4 + (t_o + \beta T r^1)^2 + 2\beta T r^2 (t_o + \beta T r^2)\cos[\Phi'(x,y) - \Phi(x,y)]\} \qquad \text{....A1.6}$$

Since ß is negative, a dark fringe corresponds to the condition

$$\Phi'(x,y) - \Phi(x,y) = 2n\pi \qquad \text{....A1.7}$$

where n is an integer.

It should be noted that a zero-order fringe is a dark fringe in the live fringe method.

A1.1.2 Double exposure holographic interferometry

In double exposure holographic interferometry, the holographic plate is initially exposed with the object in its initial unstressed condition, and a second exposure is made with a stress applied to the object. When the processed hologram is illuminated with the original reference beam, it will reconstruct two images, one corresponding the the object in its unstressed condition and the other corresponding to the stressed object. The two wavefronts interfere to form a fringe pattern which represents the change in shape undergone by the object between the two exposures.

In this case, the intensity of the holographic plate during the first exposure is

$$I_1(x,y) = |r(x,y) + o(x,y)|^2 \qquad \text{....A1.8}$$

and that during the second exposure is

$$I_2(x,y) = |r(x,y) + o'(x,y)|^2 \qquad \text{....A1.9.}$$

The amplitude transmittance of the resulting hologram is,

$$t(x,y) = t_o + \beta T(I_1 + I_2) \qquad \text{....A1.10}$$

When the hologram is illuminated once again with the same reference wave, the transmitted amplitude is the hologram plane is

$$u(x,y) = r(x,y)t(x,y) \qquad \text{....A1.11}$$

The complex amplitude due to the two superimposed primary images in the expansion of (A1.11) is

$$u_3 = \beta T r^2\, o(x,y)\,[e^{-i\Phi} + e^{-i\Phi'}] \qquad \text{....A1.12}$$

Therefore the resultant intensity is

$$I_3(x,y) \propto o(x,y)^2\{1 + \cos[\Phi_2(x,y) - \Phi'(x,y)]\} \qquad \text{....A1.13}$$

which is maximum when

$$\Phi(x,y) - \Phi'(x,y) = 2n\pi \qquad \ldots.A1.14$$

In this case, a zero-order fringe corresponds to a bright fringe.

A1.1.3 The interferometry equation

The phase difference Φ between two wavefronts, which give rise to the fringes seen by the observer, can be determined from the change in the total optical path from the source S to the observer O (Sollid,1969). For a displacement vector L, Φ is given by

$$\Phi = \mathbf{L}.(\mathbf{k}_1 - \mathbf{k}_2) \qquad \ldots.A1.15$$

where $\mathbf{k}_1$ and $\mathbf{k}_2$ are the propagation vectors of the incident and scattered light. The magnitude of these vectors are $2\pi/\lambda$. The vector $(\mathbf{k}_1 - \mathbf{k}_2)$ is defined as the sensitivity vector and it lies along the bisector of the illumination and viewing directions.

A1.2 Electronic speckle pattern interferometry (ESPI)

The main types of measurement which are made using ESPI are :

a) in-plane displacement,
b) out-of-plane displacement,
c) shape measurement.

Since only the first two types of measurement are of concern in the current study, the discussion given here does not include the third type of measurement.

A1.2.1 In-plane displacement sensitive interferometers

In the in-plane displacement sensitive interferometer, two beams are made to illuminate the object at equal angles to the observation direction (Figure A1.1). The direction of observation is normally set

at 90° to the object surface. The in-plane displacement is given by

$$d = N\lambda/2\sin(\theta/2) \qquad \text{....A1.16}$$

where θ is the angle between the two illumination vectors. The in-plane component is at 90° to the observation direction and lies in the same plane as the two illuminating beams.

A1.2.2 Out-of-plane displacement sensitive interferometer

In an out-of-plane sensitive interferometer a smooth in-line reference beam is used and the observation and illumination directions are coincidental (Figure A1.2). The reference beam is reflected off a beam splitter positioned in the path of the observation direction so that it appears to diverge from the centre of the viewing lens aperture. The out-of-plane displacement is given by

$$d = N\lambda/2 \qquad \text{....A1.17}$$

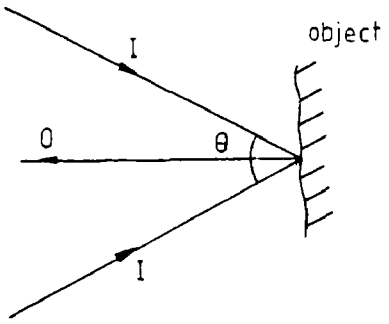

Figure A1.1 Observation and illumination directions for measuring in-plane displacement using ESPI

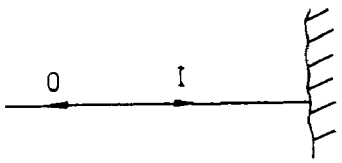

I - illumination vector
O - observation vector

Figure A1.2 Observation and illumination directions for measuring out-of-plane displacement using ESPI

A1.3 The phase-stepping method

The phase-stepping method consist of stepping one of the interferometer beams by $2\pi/k$ in (k-1) equal steps in order to obtain phase and deformation information from the fringe patterns. It is normal practise to limit k to 3,4 or even 5 as a compromise between accuracy of determination of the phase $\Phi(x,y)$ and extensive computational effort.

Mathematically it can be shown that for the two step method, where k=3, the Fourier series coefficients α_1 and β_1 are given by

$$\alpha_1 = \Sigma_{n=1,k} I_n(x,y)\cos(2\pi n/k) \qquad \ldots.A1.18$$

$$\beta_1 = \Sigma_{n=1,k} I_n(x,y)\sin(2\pi n/k) \qquad \ldots.A1.19$$

where n is the image number and $I_n(x,y)$ is the intensity (gray level) of a pixel located at (x,y) in image n. A solution for the phase Φ is then,

$$\Phi(x,y) = \tan^{-1}\,(\beta_1(x,y)/\alpha_1(x,y)) \qquad \ldots.A1.20$$

A solution for the phase in terms of pixel gray level is then,

$$\Phi(x,y) = \tan^{-1}\,[\sqrt{3}(I_1 - I_2)/(2I_3 - I_1 - I_2)] \qquad \ldots.A1.21$$

In the two step method three images are required to evaluate the phase map $\Phi(x,y)$ of the object surface image pixel-by-pixel.

Appendix A2 - Listing of computer programs

Symbols used in the programs :

CAT	- cylinder axis transformation matrix
CART	- cylinder axis reverse transformation matrix
COSOA,COSOB,COSOG	- direction cosines for observation vectors
COSIA,COSIB,COSIG	- direction cosines for illumination vectors
DL1	- distance from camera nodal point to film plane
DPL1,DPL2,DPL3,DPL4	- lengths of lines joining projected datum points
DPP	- distance from perspective plane to nodal point
DPS1,DPS2,DPS3,DPS4	- lengths of lines joining datum points in pixels
FD	- point of intersection of vector from datum point through nodal point with film plane
FN	- components of vector normal to film plane
FO,FRO	- fringe order number
FR1,FR2	- film rotation matrices
FRR1,FRR2	- reverse film rotation matrices
FTA,FTB	- film transformation matrices
FTRA,FTRB	- reverse film transformation matrices
GRL	- grey level of pixel
IC,IR	- column and row number
IORDER	- digitised datum point numbers
ILINE	- line number (used for alignment)
NGP	- number of global datum points
NP	- number of digitised points
NVIEWS	- number of views
OA,OB,OC	- global coordinates of points on laser beam to determine equation of mirror surface
R	- radius of piston
RGREY	- grey level of reference fringe
XA,YA,ZA	- global coordinates of transformed digitised points
XD,YD	- digitised coordinates of datum points
XDA,YDA,ZDA	- global coordinates of points on film after transformation of actual axis to local axis of cylinder
XDI1,YDI1,ZDI1	- first point of intersection of vectors from film plane through nodal point with cylinder
XDI2,YDI2,ZDI2	- second point of intersection of vectors from film plane through nodal point with cylinder
XF,YF,ZF	- global coordinates of point of focus
XFP,YFP,ZFP	- global coordinates of point on film before transformation
XFPT,YFPT,ZFPT	- global coordinates of point on film after transformation
XG,YG,ZG	- global coordinates of datum points
XN,YN,ZN	- global coordinates of nodal point

```
C          PROGRAM : CAMERA1.FOR
C
C          TO TRANSFORM POINTS ON A SINGLE PHOTOGRAPH CONTAINING FOUR
C          MIRROR VIEWS BACK ONTO THE CYLINDER
C
C          *** MIRROR PLANE DETERMINED BY 3 POINT LASER BEAM METHOD ***
C
           SUBROUTINE HOLO5
           DIMENSION FO(50),NP(200),XD(200,50),YD(200,50),IORDER(30),
     1   ILINE(12),XG(30),YG(30),ZG(30),XGI(30),YGI(30),ZGI(30),
     2   FN(3),FD(3),FT1(4,4),FR1(4,4),FTA(4,4),FR2(4,4),
     3   FTB(4,4),XFPT(30),YFPT(30),ZFPT(30),FRR2(4,4),FRR1(4,4),
     4   FTRA(4,4),FTR1(4,4),FTRB(4,4),XDA(200,50),YDA(200,50),
     5   ZDA(200,50),CAX(4,4),CAY(4,4),CAT(4,4),XDI1(200,50),
     6   XDI2(200,50),ZDI1(200,50),ZDI2(200,50),XDI(200,50),
     7   ZDI(200,50),YDI(200,50),FB(3),XFP(30),YFP(30),ZFP(30),
     8   CART(4,4),CARX(4,4),CARY(4,4),XA(200,50),YA(200,50),ZA(200,50)
           DIMENSION OA(3),OB(3),OC(3),XDA1(200,50),YDA1(200,50),
     1   ZDA1(200,50),S(200,50),XDRI(200,50),YDRI(200,50),ZDRI(200,50),
     2   CAT1(4,4),CAT2(4,4),CRT1(4,4),CRT2(4,4)
           CHARACTER*8 FILE1,FILE2,FILE3,OUTF
           RADIUS=55
C
C                    request names of files
C
           TYPE*,'DATA SET 1 ?'
           READ(5,5)FILE1
5          FORMAT(A8)
           TYPE*,'DATA SET 2 ?'
           READ(5,5)FILE2
           TYPE*,'DATA SET 3 ?'
           READ(5,5)FILE3
C
C                    read contents
C
           OPEN(UNIT=1,TYPE='UNKNOWN',FILE=FILE1)
           J=1
20         READ(1,*,END=40)FO(J),NP(J),(XD(I,J),I=1,NP(J))
           READ(1,*)FO(J),NP(J),(YD(I,J),I=1,NP(J))
           J=J+1
           GOTO 20
40         NUMF=J-1
           CLOSE(1)
           OPEN(UNIT=1,TYPE='OLD',FILE=FILE2)
           READ(1,*)NDP,(IORDER(I),I=1,NDP)
           READ(1,*)XN,YN,ZN
           READ(1,*)NL,(ILINE(I),I=1,2*NL)
           READ(1,*)OA(1),OA(2),OA(3)
           READ(1,*)OB(1),OB(2),OB(3)
           READ(1,*)OC(1),OC(2),OC(3)
50         CLOSE(1)
           OPEN(UNIT=1,TYPE='OLD',FILE=FILE3)
           READ(1,*)NGP,(XG(I),I=1,NGP)
           READ(1,*)NGP,(YG(I),I=1,NGP)
           READ(1,*)NGP,(ZG(I),I=1,NGP)
           CLOSE(1)
           TYPE*,'COORDINATES OF POINT OF FOCUS'
           ACCEPT*,XF,YF,ZF
C
C          coordinates of origin
C
           O1=0.0
           O2=0.0
           O3=0.0
C
C          determine image of datum points in main mirror
C
           DO 80 I=1,NGP
           CALL IMAGE1(OA,OB,OC,XG(I),YG(I),ZG(I))
           XGI(I)=XG(I)
           YGI(I)=YG(I)
           ZGI(I)=ZG(I)
80         CONTINUE
           CALL IMAGE1(OA,OB,OC,O1,O2,O3)
           O1I=O1
           O2I=O2
           O3I=O3
C
C                  determine equation of film plane
C
           DL1=183.7
           DL2=SQRT((XN-XF)**2+(YN-YF)**2+(ZN-ZF)**2)
```

```
      XC=((DL1+DL2)/DL2)*XN-(DL1/DL2)*XF
      YC=((DL1+DL2)/DL2)*YN-(DL1/DL2)*YF
      ZC=((DL1+DL2)/DL2)*ZN-(DL1/DL2)*ZF
C                    normal vector
      FN(1)=XF-XN
      FN(2)=YF-YN
      FN(3)=ZF-ZN
C           value of k in  [n].[x] = k
      FK=XC*(XF-XN)+YC*(YF-YN)+ZC*(ZF-ZN)
C
C      points of intersection of datum point vectors with film plane
C
      DO 120 I=1,NGP
      FD(1)=XN-XGI(I)
      FD(2)=YN-YGI(I)
      FD(3)=ZN-ZGI(I)
      FB(1)=XGI(I)
      FB(2)=YGI(I)
      FB(3)=ZGI(I)
      DOTNB=FN(1)*FB(1)+FN(2)*FB(2)+FN(3)*FB(3)
      DOTND=FN(1)*FD(1)+FN(2)*FD(2)+FN(3)*FD(3)
      RMU=(FK-DOTNB)/DOTND
      XFP(I)=FB(1)+RMU*FD(1)
      YFP(I)=FB(2)+RMU*FD(2)
      ZFP(I)=FB(3)+RMU*FD(3)
120   CONTINUE
C
C          translate film center to origin
C
      TX=XC
      TY=YC
      TZ=ZC
      CALL TRAN(TX,TY,TZ,FT1)
C
C       rotate about y-axis thru' alpha1 anti-clockwise
C
      ALPHA1=ABS(ATAN((XN-XF)/(ZN-ZF)))
      CALL ROT(2,-ALPHA1,FR1)
      CALL MULT(FR1,FT1,FTA)
C
C       rotate about x-axis thru' alpha2 anti-clockwise
C
      ALPHA2=ABS(ATAN((YN-YF)/(ZN-ZF)))
      CALL ROT(1,-ALPHA2,FR2)
      CALL MULT(FR2,FTA,FTB)
C
C          rotate about z-axis thru' 180 deg.
C
      PI=3.1415926
      CALL ROT(3,PI,U)
      CALL MULT(U,FTB,FTB)
C
C          apply FTB to points on film to transform 3D projected
C          datum points to 2D datum points
C
      ZFM=0.
      DO 180 I=1,NGP
      XFPT(I)=FTB(1,1)*XFP(I)+FTB(1,2)*YFP(I)+FTB(1,3)*ZFP(I)
     1 +FTB(1,4)
      YFPT(I)=FTB(2,1)*XFP(I)+FTB(2,2)*YFP(I)+FTB(2,3)*ZFP(I)
     1 +FTB(2,4)
      ZFPT(I)=FTB(3,1)*XFP(I)+FTB(3,2)*YFP(I)+FTB(3,3)*ZFP(I)
     1 +FTB(3,4)
      ZFM=ZFM+ZFPT(I)
180   CONTINUE
      ZFM=ZFM/NGP
C
C        align digitised datum points against projected datum
C
C                        scale and rotate
      SCALE=0
      THETA=0
      DO 240 I=1,NL
      GPX=XFPT(IORDER(ILINE(2*I)))-XFPT(IORDER(ILINE(2*I-1)))
      GPY=YFPT(IORDER(ILINE(2*I)))-YFPT(IORDER(ILINE(2*I-1)))
      ALG=SQRT(GPX**2+GPY**2)
      DPX=XD(ILINE(2*I),1)-XD(ILINE(2*I-1),1)
      DPY=YD(ILINE(2*I),1)-YD(ILINE(2*I-1),1)
      ALD=SQRT(DPX**2+DPY**2)
      SCALE=ALG/ALD+SCALE
C
      IF(ABS(GPX).LT.0.000001)THEN
      THETA1=3.14159/2
```

```
          GOTO 200
          END IF
          IF(ABS(GPY).LT.0.000001)THEN
          THETA1=0.
          GOTO 200
          END IF
          THETA1=ATAN(GPY/GPX)
200       IF((ABS(DPX).LT.0.000001).AND.(THETA1.LT.0.000001))THEN
          THETA2=-PI/2
          GOTO 220
          END IF
          IF((ABS(DPX).LT.0.000001).AND.(THETA1.GT.0.000001))THEN
          THETA2=PI/2
          GOTO 220
          END IF
          IF(ABS(DPY).LT.0.000001)THEN
          THETA2=0.
          END IF
          THETA2=ATAN(DPY/DPX)
220       THETA=THETA+THETA2-THETA1
240       CONTINUE
          SCALE=SCALE/NL
          THETA=THETA/NL
C
C                    scale and rotate digitised points
C
          DO 260 J=1,NUMF
          DO 260 I=1,NP(J)
          XD1=XD(I,J)*SCALE
          YD1=YD(I,J)*SCALE
          XD(I,J)=XD1*COS(THETA)+YD1*SIN(THETA)
260       YD(I,J)=-XD1*SIN(THETA)+YD1*COS(THETA)
C
C                  correct for positional errors
C
          XT=0.
          YT=0.
          DO 280 I=1,NP(1)
          XT=XT+XD(I,1)-XFPT(IORDER(I))
          YT=YT+YD(I,1)-YFPT(IORDER(I))
280       CONTINUE
          XT=XT/NP(1)
          YT=YT/NP(1)
          DO 300 J=1,NUMF
          DO 300 I=1,NP(J)
          XD(I,J)=XD(I,J)-XT
          YD(I,J)=YD(I,J)-YT
300       CONTINUE
C
C                  return film to original position
C
          CALL ROT(3,-PI,UR)
          CALL ROT(1,ALPHA2,FRR2)
          CALL MULT(FRR2,UR,FRR2)
          CALL ROT(2,ALPHA1,FRR1)
          CALL MULT(FRR1,FRR2,FTRA)
          CALL TRAN(-TX,-TY,-TZ,FTR1)
          CALL MULT(FTR1,FTRA,FTRB)
C
C                   apply FTRB to all points
C
          DO 320 J=1,NUMF
          DO 320 I=1,NP(J)
          XDA1(I,J)=FTRB(1,1)*XD(I,J)+FTRB(1,2)*YD(I,J)+FTRB(1,3)*ZFM
     1 +FTRB(1,4)
          YDA1(I,J)=FTRB(2,1)*XD(I,J)+FTRB(2,2)*YD(I,J)+FTRB(2,3)*ZFM
     1 +FTRB(2,4)
          ZDA1(I,J)=FTRB(3,1)*XD(I,J)+FTRB(3,2)*YD(I,J)+FTRB(3,3)*ZFM
     1 +FTRB(3,4)
320       CONTINUE
C
C              transform actual axes to local axes of cylinder image
C
          GAMMA1=ATAN(O2I/SQRT(O1I**2+O3I**2))
          BETA2=2*GAMMA1
          BETA1=ATAN(O1I/O3I)
          CALL ROT(2,BETA1,CAY)
          CALL ROT(1,-BETA2,CAX)
          CALL MULT(CAX,CAY,CAT1)
          O11I=CAT1(1,1)*O1I+CAT1(1,2)*O2I+CAT1(1,3)*O3I+CAT1(1,4)
          O21I=CAT1(2,1)*O1I+CAT1(2,2)*O2I+CAT1(2,3)*O3I+CAT1(2,4)
          O31I=CAT1(3,1)*O1I+CAT1(3,2)*O2I+CAT1(3,3)*O3I+CAT1(3,4)
          CALL TRAN(O11I,O21I,O31I,CAT2)
          CALL MULT(CAT2,CAT1,CAT)
C
```

```
C                apply CAT to points on film
C
          DO 340 J=1,NUMF
          DO 340 I=1,NP(J)
          XDA(I,J)=CAT(1,1)*XDA1(I,J)+CAT(1,2)*YDA1(I,J)
     1 +CAT(1,3)*ZDA1(I,J)+CAT(1,4)
          YDA(I,J)=CAT(2,1)*XDA1(I,J)+CAT(2,2)*YDA1(I,J)
     1 +CAT(2,3)*ZDA1(I,J)+CAT(2,4)
          ZDA(I,J)=CAT(3,1)*XDA1(I,J)+CAT(3,2)*YDA1(I,J)
     1 +CAT(3,3)*ZDA1(I,J)+CAT(3,4)
340       CONTINUE
C
C                apply CAT to nodal point
C
          XNA=CAT(1,1)*XN+CAT(1,2)*YN+CAT(1,3)*ZN+CAT(1,4)
        YNA=CAT(2,1)*XN+CAT(2,2)*YN+CAT(2,3)*ZN+CAT(2,4)
          ZNA=CAT(3,1)*XN+CAT(3,2)*YN+CAT(3,3)*ZN+CAT(3,4)
C
C              apply CAT to image of cylinder origin
C
C
C           project vectors from points on film thru' nodal point onto
C           cylinder to find intersection
C
C                group constants in equation
C
          DO 430 J=1,NUMF
          DO 420 I=1,NP(J)
          GRAD1=(ZDA(I,J)-ZNA)/(XDA(I,J)-XNA)
          A1=ZNA-GRAD1*XNA
          A2=1+GRAD1**2
          A3=2*GRAD1*A1
          A4=A1**2-RADIUS**2
C
C                  check if vector intersects cylinder
C
          A5=A3**2-4*A2*A4
          IF(A5.LT.0.0)GOTO 420
          XDI1(I,J)=(-A3+SQRT(A5))/(2*A2)
          XDI2(I,J)=(-A3-SQRT(A5))/(2*A2)
C
C                check if roots are equal
C
          IF(ABS(XDI1(I,J)-XDI2(I,J)).LT.0.000001)THEN
          XDI(I,J)=XDI1(I,J)
          ZDI(I,J)=A1+GRAD1*XDI(I,J)
          GOTO 400
          END IF
C
C                consider only point closer to origin
C
380       ZDI1(I,J)=A1+GRAD1*XDI1(I,J)
          ZDI2(I,J)=A1+GRAD1*XDI2(I,J)
          DIST1=SQRT((XDI1(I,J)-XNA)**2+(ZDI1(I,J)-ZNA)**2)
          DIST2=SQRT((XDI2(I,J)-XNA)**2+(ZDI2(I,J)-ZNA)**2)
          IF(DIST1.LT.DIST2)THEN
          XDI(I,J)=XDI1(I,J)
          ZDI(I,J)=ZDI1(I,J)
          GOTO 400
          END IF
          XDI(I,J)=XDI2(I,J)
          ZDI(I,J)=ZDI2(I,J)
C
C                determine y coordinate
C
400       GRAD2=(YDA(I,J)-YNA)/(ZDA(I,J)-ZNA)
          YDI(I,J)=YNA+GRAD2*(ZDI(I,J)-ZNA)
420       CONTINUE
430       CONTINUE
C
C             transform local axes to actual axes
C
          CALL TRAN(-O11I,-O21I,-O31I,CRT1)
          CALL ROT(1,BETA2,CARX)
          CALL MULT(CARX,CRT1,CRT2)
          CALL ROT(2,-BETA1,CARY)
          CALL MULT(CARY,CRT2,CART)
          DO 460 J=1,NUMF
          DO 460 I=1,NP(J)
          XDRI(I,J)=CART(1,1)*XDI(I,J)+CART(1,2)*YDI(I,J)
     1 +CART(1,3)*ZDI(I,J)+CART(1,4)
          YDRI(I,J)=CART(2,1)*XDI(I,J)+CART(2,2)*YDI(I,J)
```

```
     1 +CART(2,3)*ZDI(I,J)+CART(2,4)
           ZDRI(I,J)=CART(3,1)*XDI(I,J)+CART(3,2)*YDI(I,J)
     1 +CART(3,3)*ZDI(I,J)+CART(3,4)
460        CONTINUE
C
C               re-reflect points to obtain true coordinates
C
           DO 500 J=1,NUMF
           DO 500 I=1,NP(J)
           CALL IMAGE1(OA,OB,OC,XDRI(I,J),YDRI(I,J),ZDRI(I,J))
C          IF(NREAR.EQ.2)THEN
C          CALL IMAGE1(OA2,OB2,OC2,XDRI(I,J),YDRI(I,J),ZDRI(I,J))
C          END IF
           XA(I,J)=XDRI(I,J)
           YA(I,J)=YDRI(I,J)
           ZA(I,J)=ZDRI(I,J)
500        CONTINUE
           CALL IMAGE1(OA,OB,OC,XN,YN,ZN)
C          IF(NREAR.EQ.2)THEN
C          CALL IMAGE1(OA2,OB2,OC2,XN,YN,ZN)
C          END IF
           XNI=XN
           YNI=YN
           ZNI=ZN
C
C                              save results
C
           TYPE*,'FILE TO HOLD RESULTS ?'
           READ(5,5)OUTF
           OPEN(UNIT=1,TYPE='NEW',FILE=OUTF)
C          WRITE(1,*)NREAR
           WRITE(1,*)XNI,YNI,ZNI
           DO 520 J=1,NUMF
           WRITE(1,*)FO(J),NP(J),(XA(I,J),I=1,NP(J))
           WRITE(1,*)FO(J),NP(J),(YA(I,J),I=1,NP(J))
           WRITE(1,*)FO(J),NP(J),(ZA(I,J),I=1,NP(J))
520        CONTINUE
           RETURN
           END
C
C
C-------------------------SUBROUTINE IMAGE1(OA,OB,OC,X,Y,Z)-------------
C          determines coordinates of image of point (X,Y,Z) in a mirror
C       for three specified points A,B,C by using the three point laser
C       beam method
C
           SUBROUTINE IMAGE1(OA,OB,OC,X,Y,Z)
           DIMENSION ANO(3),OA(3),OB(3),OC(3)
           AB=SQRT((OA(1)-OB(1))**2+(OA(2)-OB(2))**2+(OA(3)-OB(3))**2)
           BC=SQRT((OB(1)-OC(1))**2+(OB(2)-OC(2))**2+(OB(3)-OC(3))**2)
           AC=SQRT((OA(1)-OC(1))**2+(OA(2)-OC(2))**2+(OA(3)-OC(3))**2)
           ALPHA=ACOS((AB**2+AC**2-BC**2)/(2*AB*AC))
           BETA=ACOS((AB**2+BC**2-AC**2)/(2*AB*BC))
           AL1=SIN(BETA/2)*AB/SIN(ALPHA+BETA/2)
           AL2=AC-AL1
           XN=(AL1*OC(1)+AL2*OA(1))/AC
           YN=(AL1*OC(2)+AL2*OA(2))/AC
           ZN=(AL1*OC(3)+AL2*OA(3))/AC
           ANO(1)=XN-OB(1)
           ANO(2)=YN-OB(2)
           ANO(3)=ZN-OB(3)
           A=ANO(1)
           B=ANO(2)
           C=ANO(3)
           D=A*(-OB(1))+B*(-OB(2))+C*(-OB(3))
           DIST=(A*X+B*Y+C*Z+D)/SQRT(A**2+B**2+C**2)
           T=SQRT(DIST**2/(A**2+B**2+C**2))
25         XM=X-A*T
           YM=Y-B*T
           ZM=Z-C*T
           X1=XM*2-X
           Y1=YM*2-Y
           Z1=ZM*2-Z
           DIST2=(A*X1+B*Y1+C*Z1+D)/SQRT(A**2+B**2+C**2)
           SIDE=DIST*DIST2
           IF(SIDE.LT.0)GOTO 30
           T=-T
           GOTO 25
30         X=X1
           Y=Y1
           Z=Z1
           RETURN
           END
```

```
      SUBROUTINE TRAN(TX,TY,TZ,A)
C
C     CALCULATE 3D AXES TRANSLATION MATRIX
C
      DIMENSION A(4,4)
      DO 2 I=1,4
      DO 1 J=1,4
      A(I,J)=0.
1     CONTINUE
      A(I,I)=1.
2     CONTINUE
      A(1,4)=-TX
      A(2,4)=-TY
      A(3,4)=-TZ
      RETURN
      END
C
C
C
      SUBROUTINE SCALE(SX,SY,SZ,A)
C
C     CALCULATES 3D AXES SCALING MATRIX
C
      DIMENSION A(4,4)
      DO 2 I=1,4
      DO 1 J=1,4
      A(I,J)=0.
1     CONTINUE
2     CONTINUE
      A(1,1)=SX
      A(2,2)=SY
      A(3,3)=SZ
      A(4,4)=1.
      RETURN
      END
C
C
C
      SUBROUTINE ROT(M,THETA,A)
C
C     CALCULATES 3D AXES ROTATION MATRIX A ABOUT DIRECTION M
C     M=1:X AXIS M=2:Y AXIS M=3:Z AXIS
C
      DIMENSION A(4,4)
      DO 2 I=1,4
      DO 1 J=1,4
      A(I,J)=0.
1     CONTINUE
2     CONTINUE
      A(4,4)=1.
      A(M,M)=1.
      M1=MOD(M,3)+1
      M2=MOD(M1,3)+1
      C=COS(THETA)
      S=SIN(THETA)
      A(M1,M1)=C
      A(M2,M2)=C
      A(M1,M2)=S
      A(M2,M1)=-S
      RETURN
      END
C
C
C
      SUBROUTINE MULT(A,B,C)
C
C     4X4 MATRIX PRODUCT
C
      DIMENSION A(4,4),B(4,4),C(4,4)
      DO 1 I=1,4
      DO 2 J=1,4
      AB=0.
      DO 3 K=1,4
      AB=AB+A(I,K)*B(K,J)
3     CONTINUE
      C(I,J)=AB
2     CONTINUE
1     CONTINUE
      RETURN
      END
C
```

```
C          PROGRAM : SOLVE1.FOR
C
C          PROGRAM TO SOLVE 4 EQUATIONS IN 3 UNKNOWNS DERIVED USING
C          THE INTERFEROMETRY EQUATION [A].[D] = [N].LAMBDA
C
           SUBROUTINE HOLO9
           DIMENSION XN(4),YN(4),ZN(4),COSOA(4),COSOB(4),COSOG(4)
     1    ,FRO(-17:17,-10:5,4),WORK(16),A(4,3),B(4),DX(-17:17,-10:5)
     2    ,DY(-17:17,-10:5),DZ(-17:17,-10:5),RO(4)
           CHARACTER*8 DATF(5)
           REAL LAMBDA
           DATA R,LAMBDA,IFAIL,NRA,TOL/55.,632.8E-6,10,4,5.E-4/
10         DO 20 NVIEW=1,4
           TYPE*,'DATA FILE',NVIEW,'?'
20         READ(5,5)DATF(NVIEW)
           TYPE*,'FILE TO HOLD RESULTS ?'
           READ(5,5)DATF(5)
5          FORMAT(A8)
C
C               initialise FRO array
C
           DO 40 NVIEW=1,4
           DO 40 J=-10,5
           DO 40 I=-17,17
40         FRO(I,J,NVIEW)=-1001
C
C             read data
C
           DO 80 NVIEW=1,4
           OPEN(UNIT=1,TYPE='UNKNOWN',ERR=65,FILE=DATF(NVIEW))
           READ(1,*)XN(NVIEW),YN(NVIEW),ZN(NVIEW)
60         READ(1,*,END=70,ERR=66)IC,IR,FRO(IC/5,IR/5,NVIEW)
           GOTO 60
65         TYPE*,'FILE DOES NOT EXIST OR INCORRECT FILE'
           GOTO 10
66         TYPE*,'DATA IN ERROR - CHECK CONTENTS OF FILE'
           GOTO 600
70         CLOSE(1)
80         CONTINUE
           TYPE*,'ILLUMINATION SOURCE ORIGIN - XI,YI,ZI ?'
           ACCEPT*,XI,YI,ZI
           DO 400 J=-10,5
           DO 400 I=-17,17
           DO 300 NVIEW=1,4
           IF(FRO(I,J,NVIEW).LT.-1000)GOTO 400
           THETA=I*5/R
           X=-R*SIN(THETA)
           Y=J*5
           Z=R*COS(THETA)
           RX=XN(NVIEW)-X
           RY=YN(NVIEW)-Y
           RZ=ZN(NVIEW)-Z
           RO(NVIEW)=SQRT(RX**2+RY**2+RZ**2)
           COSOA(NVIEW)=(XN(NVIEW)-X)/RO(NVIEW)
           COSOB(NVIEW)=(YN(NVIEW)-Y)/RO(NVIEW)
           COSOG(NVIEW)=(ZN(NVIEW)-Z)/RO(NVIEW)
           RI=SQRT((XI-X)**2+(YI-Y)**2+(ZI-Z)**2)
           COSIA=(X-XI)/RI
           COSIB=(Y-YI)/RI
           COSIG=(Z-ZI)/RI
           A(NVIEW,1)=COSOA(NVIEW)-COSIA
           A(NVIEW,2)=COSOB(NVIEW)-COSIB
           A(NVIEW,3)=COSOG(NVIEW)-COSIG
           B(NVIEW)=FRO(I,J,NVIEW)*LAMBDA
300        CONTINUE
C
C               call NAG Fortran subroutine to solve equations
C
           CALL F04JAE(4,3,A,NRA,B,TOL,SIGMA,IRANK,WORK,16,IFAIL)
           DX(I,J)=B(1)
           DY(I,J)=B(2)
           DZ(I,J)=B(3)
400        CONTINUE
           OPEN(UNIT=1,TYPE='NEW',FILE=DATF(5))
           DO 500 J=-10,5
           DO 500 I=-17,17
           IF(FRO(I,J,1).LT.-1000)GOTO 500
           WRITE(1,550)I*5,J*5,DX(I,J),DY(I,J),DZ(I,J)
500        CONTINUE
550        FORMAT(2(1X,I5),3X,3(2X,F10.6))
600        RETURN
           END
```

```
C          PROGRAM : TRANSGPO.FOR
C
C       TO TRANSFORM GRID POINTS INTO PIXEL COORDINATES (DIRECT VIEW)
C
           DIMENSION X(-9:5,9),Y(-9:5,9),Z(-9:5,9),XP(-9:5,9),YP(-9:5,9)
           DIMENSION XD(4),YD(4),ZD(4),XDP(4),YDP(4)
           DIMENSION XDS(4),YDS(4),DPS(4),DPD(4)
           REAL XNS,YNS,XN,YN,ZN,R
           CHARACTER*8 DTF,SDTF,OUTF
C
C          data for nodal point coordinates and radius of piston
           DATA XN/-28.0/,YN/-24/,ZN/699/,R/49.2/
C
C          data for screen point coordinates of lens centreline
           DATA XNS/299/,YNS/322/
C
           WRITE(5,*)'DATUM POINT FILE?'
           READ(5,'(A8)')DTF
           OPEN(1,STATUS='OLD',FILE=DTF)
           DO 20 I=2,5
20         READ(1,*)XD(I),YD(I),ZD(I)
           CLOSE(1)
           DO 60 I=2,5
           XD(I)=XD(I)-XN
           YD(I)=YD(I)-YN
           ZD(I)=ZD(I)
60         CONTINUE
           DP=200
           DO 100 I=2,5
           XDP(I)=DP*XD(I)/(ZN-ZD(I))
           YDP(I)=DP*YD(I)/(ZN-ZD(I))
100        CONTINUE
           WRITE(5,*)'SCREEN COORS. OF DATUM POINT FILE?'
           READ(5,'(A8)')SDTF
           OPEN(1,STATUS='OLD',FILE=SDTF)
           DO 120 I=2,5
           READ(1,*)XDS(I),YDS(I)
120        CONTINUE
C
C          determine lengths of lines joining projected datum points
C
           DPL1=SQRT((XDP(3)-XDP(2))**2+(YDP(3)-YDP(2))**2)
           DPL2=SQRT((XDP(5)-XDP(4))**2+(YDP(5)-YDP(4))**2)
           DPL3=SQRT((XDP(2)-XDP(4))**2+(YDP(2)-YDP(4))**2)
           DPL4=SQRT((XDP(3)-XDP(5))**2+(YDP(3)-YDP(5))**2)
C
C          determine lengths of lines joining screen datum points
C          in pixels
C
           DSL1=SQRT((XDS(3)-XDS(2))**2+(YDS(3)-YDS(2))**2)
           DSL2=SQRT((XDS(5)-XDS(4))**2+(YDS(5)-YDS(4))**2)
           DSL3=SQRT((XDS(2)-XDS(4))**2+(YDS(2)-YDS(4))**2)
           DSL4=SQRT((XDS(3)-XDS(5))**2+(YDS(3)-YDS(5))**2)
C
C          determine x and y scaling factor
C
           SCLY=(DSL1/DPL1+DSL2/DPL2)/2
           SCLX=(DSL3/DPL3+DSL4/DPL4)/2
           WRITE(5,*)'FILE TO HOLD RESULT ?'
           READ(5,'(A8)')OUTF
           OPEN(UNIT=1,STATUS='NEW',FILE=OUTF)
           DO 210 I=-9,5
           DO 200 J=1,9
           THETA=5*(J-1)/49.2
           X(I,J)=-R*SIN(THETA)-XN
           Y(I,J)=I*5-YN
           Z(I,J)=R*COS(THETA)
           XP(I,J)=XNS+(DP*X(I,J)/(ZN-Z(I,J)))*SCLX
           YP(I,J)=YNS-(DP*Y(I,J)/(ZN-Z(I,J)))*SCLY
           WRITE(1,*)I*5,(J-1)*5,XP(I,J),YP(I,J)
200        CONTINUE
210        CONTINUE
           CLOSE(1)
           END
```

```
C           PROGRAM : TRANSGPI.FOR
C
C           TO TRANSFORM GRID POINTS INTO PIXEL COORDINATES (REFLECTED VIEW)
C
            DIMENSION X(-9:5,9),Y(-9:5,9),Z(-9:5,9),XP(-9:5,9),YP(-9:5,9)
            DIMENSION XD(4),YD(4),ZD(4),XDP(4),YDP(4),A(3),B(3),C(3)
            DIMENSION XDS(4),YDS(4),DPS(4),DPD(4)
            REAL XNS,YNS,XN,YN,ZN,R
            CHARACTER*8 OUTF
            DATA XN/-28.0/,YN/-24/,ZN/699/,R/49.2/
            DATA XNS/299/,YNS/322/
C
C           data to determine mirror position
C
            DATA A(1)/111.4/,A(2)/-27/,A(3)/495.1/
            DATA B(1)/-100.6/,B(2)/-27/,B(3)/146.2/
            DATA C(1)/140.7/,C(2)/-27/,C(3)/123.8/
C
C           read global coordinates of datum points
C
            OPEN(1,STATUS='OLD',FILE='DP.DAT')
            DO 20 I=2,5
            READ(1,*)XD(I),YD(I),ZD(I)
            CALL IMAGE1(A,B,C,XD(I),YD(I),ZD(I))
20          CONTINUE
            CLOSE(1)
            DO 60 I=2,5
            XD(I)=XD(I)-XN
            YD(I)=YD(I)-YN
            ZD(I)=ZD(I)
60          CONTINUE
            DPP=200
            DO 100 I=2,5
            XDP(I)=DPP*XD(I)/(ZN-ZD(I))
            YDP(I)=DPP*YD(I)/(ZN-ZD(I))
100         CONTINUE
C
C           read screen coordinates of datum points (in pixels)
C
            OPEN(1,STATUS='OLD',FILE='SPI.DAT')
            DO 120 I=2,5
            READ(1,*)XDS(I),YDS(I)
120         CONTINUE
            DPL1=SQRT((XDP(3)-XDP(2))**2+(YDP(3)-YDP(2))**2)
            DPL2=SQRT((XDP(5)-XDP(4))**2+(YDP(5)-YDP(4))**2)
            DPL3=SQRT((XDP(4)-XDP(2))**2+(YDP(4)-YDP(2))**2)
            DPL4=SQRT((XDP(5)-XDP(3))**2+(YDP(5)-YDP(3))**2)
            DPS1=SQRT((XDS(3)-XDS(2))**2+(YDS(3)-YDS(2))**2)
            DPS2=SQRT((XDS(5)-XDS(4))**2+(YDS(5)-YDS(4))**2)
            DPS3=SQRT((XDS(4)-XDS(2))**2+(YDS(4)-YDS(2))**2)
            DPS4=SQRT((XDS(5)-XDS(3))**2+(YDS(5)-YDS(3))**2)
C
C           determine x and y scaling factor
C
            SCLX=(DPS3/DPL3+DPS4/DPL4)/2
            SCLY=(DPS1/DPL1+DPS2/DPL2)/2
            WRITE(5,*)'FILE TO HOLD RESULT ?'
            READ(5,'(A8)')OUTF
            OPEN(UNIT=1,STATUS='NEW',FILE=OUTF)
            DO 210 I=-9,5
            DO 200 J=1,9
            THETA=5*(J-1)/49.2
            X(I,J)=-R*SIN(THETA)
            Y(I,J)=I*5
            Z(I,J)=R*COS(THETA)
            CALL IMAGE1(A,B,C,X(I,J),Y(I,J),Z(I,J))
            X(I,J)=X(I,J)-XN
            Y(I,J)=Y(I,J)-YN
            XP(I,J)=XNS+(DPP*X(I,J)/(ZN-Z(I,J)))*SCLX
            YP(I,J)=YNS-(DPP*Y(I,J)/(ZN-Z(I,J)))*SCLY
            WRITE(1,*)I*5,(J-1)*5,XP(I,J),YP(I,J)
200         CONTINUE
210         CONTINUE
            CLOSE(1)
            END
```

```
C       PROGRAM : GETORDO.FOR
C
C       TO GET ORDER NUMBER AT GRID POINTS (DIRECT VIEW)
C       (LINKED TO DATA TRANSLATION SUBROUTINES)
C
        DIMENSION IGR(1),IP(10),PX(-9:5,9),PY(-9:5,9),ORD(-9:5,9)
        INTEGER XMIN,YMIN,XMAX,YMAX
        REAL ORD,UORD
        DATA XMIN/268/,YMIN/70/,XMAX/418/,YMAX/468/,RGREY/125.7/
        CALL ISINIT
        OPEN(1,STATUS='OLD',FILE='OBJPIX.DAT')
        DO 20 I=-9,5
        DO 20 J=1,9
        READ(1,*)M,N,PX(I,J),PY(I,J)
C
C       check if point is inside region
C
        IF((PX(I,J).LT.XMIN).OR.(PX(I,J).GT.XMAX))GOTO 20
        IF((PY(I,J).LT.YMIN).OR.(PY(I,J).GT.YMAX))GOTO 20
        NPX=PX(I,J)-2
        NPY=PY(I,J)
        CALL ISGPOS(NPY,NPX)
        CALL ISARC(1,NPY,NPX+2,360)
        WRITE(5,*)'UPPER ORDER NUMBER -',I,J
        READ(5,*)UORD
C
C       determine grey level at point
C
        CALL ISGETP(1,NPY,NPX+2,1,IGR)
        GRL=IGR(1)
        ORD(I,J)=UORD-GRL/255.0-(255-RGREY)/255
        WRITE(6,*)ORD(I,J),I,J
20      CONTINUE
        CLOSE(1)
C
C       save results
C
        OPEN(1,STATUS='NEW',FILE='ORD.DAT')
        DO 40 I=-9,5
        DO 40 J=1,9
        WRITE(1,*)I*5,(J-1)*5,ORD(I,J)
40      CONTINUE
        CALL ISEND
        END


C       PROGRAM : GETORDI.FOR
C
C       TO GET ORDER NUMBER AT GRID POINTS (REFLECTED VIEW)
C
        DIMENSION IGR(1),IP(10),PX(-9:5,9),PY(-9:5,9),ORD(-9:5,9)
        INTEGER XMIN,YMIN,XMAX,YMAX
        REAL ORD,UORD
        DATA XMIN/112/,YMIN/71/,XMAX/242/,YMAX/464/,RGREY/44.5/
        CALL ISINIT
        OPEN(1,STATUS='OLD',FILE='IMGPIX.DAT')
        DO 20 I=-9,5
        DO 20 J=1,9
        READ(1,*)M,N,PX(I,J),PY(I,J)
        IF((PX(I,J).LT.XMIN).OR.(PX(I,J).GT.XMAX))GOTO 20
        IF((PY(I,J).LT.YMIN).OR.(PY(I,J).GT.YMAX))GOTO 20
        NPX=PX(I,J)-2
        NPY=PY(I,J)
        CALL ISGPOS(NPY,NPX)
        CALL ISARC(1,NPY,NPX+2,360)
        WRITE(5,*)'UPPER ORDER NUMBER -',I,J
        READ(5,*)UORD
        CALL ISGETP(1,NPY,NPX+2,1,IGR)
        GRL=IGR(1)
        ORD(I,J)=UORD-GRL/255.0-(255-RGREY)/255
        WRITE(6,*)ORD(I,J)
20      CONTINUE
        CLOSE(1)
        OPEN(1,STATUS='NEW',FILE='ORD.DAT')
        DO 40 I=-9,5
        DO 40 J=1,9
        WRITE(1,*)I*5,(J-1)*5,ORD(I,J)
40      CONTINUE
        CALL ISEND
        END
```

```
C       PROGRAM SOLVE2.FOR
C
C       PROGRAM TO SOLVE A.D = N.LAMBDA (ESPI)

        DIMENSION ORO(-9:5,9),ORI(-9:5,9),DX(-9:5,9),DZ(-9:5,9)
        DIMENSION COSO(2,2),COSI(2,2)
        DATA XN/-26/,ZN/699/,XI/-86/,ZI/665/,W/632.8E-6/
C       data for image of nodal point in global coordinates
        DATA XNI/-646.2/,ZNI/405.4/
        DO 5 I=-9,5
        DO 5 J=1,9
        DX(I,J)=-1000
        ORO(I,J)=-1000
5       ORI(I,J)=-1000
        OPEN(1,STATUS='OLD',FILE='ORDOBJ')
10      READ(1,*,END=20)M,N,ORO(M/5,N/5+1)
        GOTO 10
20      CLOSE(1)
        OPEN(1,STATUS='OLD',FILE='ORDIMG')
30      READ(1,*,END=40)M,N,ORI(M/5,N/5+1)
        GOTO 30
40      CLOSE(1)
        DO 60 I=-9,5
        DO 60 J=1,9
        IF((ORO(I,J).LT.0.0001).OR.(ORI(I,J).LT.0.0001))GOTO 60
        THETA=(J-1)*5/49.2
        XA=-49.2*SIN(THETA)
        ZA=49.2*COS(THETA)
        RIAO=SQRT((XA-XI)**2+(ZA-ZI)**2)
        RANO=SQRT((XN-XA)**2+(ZN-ZA)**2)
        RIAI=RIAO
        RANI=SQRT((XNI-XA)**2+(ZNI-ZA)**2)
C
C       determine direction cosines of illumination and observation
C       vectors
C
        COSI(1,1)=(XA-XI)/RIAO
        COSI(1,2)=(ZA-ZI)/RIAO
        COSI(2,1)=COSI(1,1)
        COSI(2,2)=COSI(1,2)
        COSO(1,1)=(XN-XA)/RANO
        COSO(1,2)=(ZN-ZA)/RANO
        COSO(2,1)=(XNI-XA)/RANI
        COSO(2,2)=(ZNI-ZA)/RANI
        A1=COSO(1,1)-COSI(1,1)
        A2=COSO(1,2)-COSI(1,2)
        A3=COSO(2,1)-COSI(2,1)
        A4=COSO(2,2)-COSI(2,2)
C
C       solve equations
C
        D1=(A2*ORI(I,J)-A4*ORO(I,J))*W
        D2=(A2*A3-A4*A1)
        DX(I,J)=D1/D2
        DZ(I,J)=(ORO(I,J)*W-A1*DX(I,J))/A2
60      CONTINUE
        OPEN(1,STATUS='NEW',FILE='SOLN.DAT')
        WRITE(1,*)'DISPLACEMENT FOR RISE FROM 55 TO 60 DEG.C'
        WRITE(1,*)'DATE OF EXPT. =  22-2-90'
        WRITE(1,*)'      '
        WRITE(1,*)'         ROW           COL.        DX                DZ'
        DO 80 I=-9,5
        DO 80 J=1,9
        IF(DX(I,J).LT.-100)GOTO 80
        WRITE(1,*)I*5,(J-1)*5,DX(I,J),DZ(I,J)
80      CONTINUE
        END
```

Appendix A3 - Analysis of errors due to camera misalignment

A3.1 Estimation of errors at front surface of piston

The following calculations are based on point located at (0,0,49.3) that was used as a reference point P to count number of fringes crossing on the recording of live fringes.

For the observation-illumination geometry shown in Figure A3.1, the piston surface point P is assumed to have moved to P' through a distance d. The path length of the illumination is therefore shortened by l_a and that of observation by l_b where,

$$l_a = d\cos\beta \quad \text{and}$$
$$l_b = d\cos\gamma \qquad \text{....A3.1}$$

If n if the number of fringes caused by the shortened path length, then,

$$n\lambda = l_a + l_b = d(\cos\beta + \cos\gamma)$$

i.e. $$n = d(\cos\beta + \cos\gamma)/\lambda \qquad \text{....A3.2}$$

If the misalignment causes γ to change to $\gamma \pm \Delta\gamma$ where $\Delta\gamma$ is given by

$$\Delta\gamma = \tan^{-1}(B/L) \qquad \text{....A3.3}$$

(where L = distance from P to the camera lens nodal point and B is the lateral misalignment between the video and plate cameras), then the % error in fringe order will be given by,

$$\Delta n = \frac{\cos\gamma - \cos(\gamma \pm \Delta\gamma)}{\cos\beta + \cos\gamma} \times 100 \qquad \text{....A3.4}$$

For the holographic arrangment used $\beta=10.2°$, L is approximately 600mm and from the experimental result discussed in Chapter 5 $\gamma=0.83°$. Allowing for a 20mm lateral misalignment in the position of the two cameras (i.e. B=20mm), therefore the maximum error in n,

$$\Delta n = 0.05\%$$

For the reflected view γ=52.9° and β=10.2°. Hence from (A3.4) the maximum error in n is,

$$\Delta n = 1.7\%$$

A3.2 Estimation of errors at rear surface of piston

The analysis was based on a point located at (-34.8,0,-34.8) at the rear surface that was used as a reference for counting the fringes. For the single reflection,

$$\gamma = \tan^{-1}721.3/345.4 = 64.4°$$
$$\gamma = \tan^{-1}20/800 = 1.4°$$
$$\beta = 24.9°$$

thus, $\Delta n = 1.6\%$

For the double reflection,

$$\gamma = \tan^{-1}266.5/787.3 = 18.7°$$
$$\gamma = \tan^{-1}20/831.2 = 1.4°$$
$$\beta = 24.9°$$
$$\Delta n = 0.4\%$$

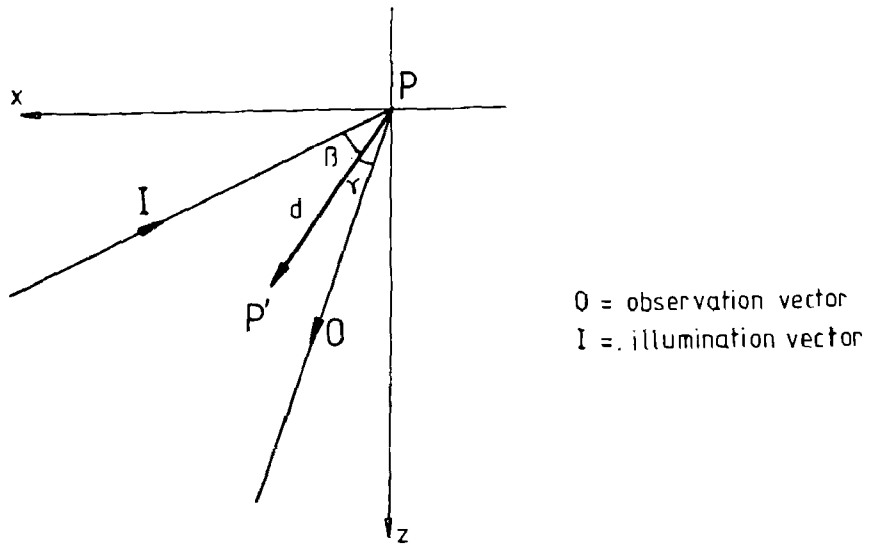

Figure A3.1 Observation-illumination geometry for estimating errors due to camera misalignment

Appendix A4 - Effects of errors in fringe orders on displacement

The following analyses were carried out to determine the effects of errors in fringe orders on displacement:

a) Analysis A1 : Effect of increasing order numbers on direct and reflected views on front surface by 1.0.
b) Analysis A2 : Effect of increasing order numbers on single and double reflection views on rear surface by 1.0.
c) Analysis B1 : Effect of decreasing order numbers on direct and reflected views on front surface by 1.0.
d) Analysis B2 : Effect of decreasing order numbers on single and double reflection views on rear surface by 1.0.
e) Analysis C1 : Effect of decreasing order numbers on direct view by 0.5 and increasing order numbers on reflected view by 0.5 on front surface.
f) Analysis C2 : Effect of increasing order numbers on direct view by 0.5 and decreasing order numbers on reflected view by 0.5 on front surface.
g) Analysis D1 : Effect of decreasing order numbers on single reflection view by 0.5 and increasing order numbers on double reflection view by 0.5.
h) Analysis D2 : Effect of increasing order numbers on single reflection view by 0.5 and decreasing order numbers on double reflection view by 0.5.

The results of the above analyses are summarised in Table A4.1.

Analysis	Y	θ°	Based on original order nos.		Based on adjusted order nos.		% change in d	change in Φ°
			d(μm)	Φ°	d(μm)	Φ°		
A1	15	45	9.29	-4.9	9.58	-3.8	3.1	1.2
		90	4.45	18.5	4.79	18.9	7.6	0.4
	-45	45	8.04	-19.0	8.30	-17.5	3.2	1.6
		90	5.85	18.8	6.16	19.6	5.3	0.8
A2	15	225	9.28	-1.6	9.59	-0.5	3.3	1.1
		270	5.26	43.4	5.60	38.9	6.1	4.5
	-45	225	8.51	8.1	8.97	7.9	5.4	2.7
		270	9.49	46.5	9.78	41.1	3.1	5.4
B1	15	45	9.29	-4.9	9.01	-6.1	3.0	1.2
		90	4.45	18.5	4.12	18.0	7.4	0.5
	-45	45	8.04	-19.0	7.85	-20.9	2.4	1.9
		90	5.85	18.8	5.49	19.0	6.2	0.2
B2	15	225	9.28	-1.6	8.93	-2.4	3.8	0.8
		270	5.29	43.4	4.90	41.4	6.8	2.0
	-45	225	8.51	8.1	8.26	6.4	2.9	1.7
		270	9.49	46.5	9.09	42.7	4.2	3.8
C1	15	45	9.29	-4.9	8.95	-1.3	3.7	3.6
		90	4.45	18.5	4.45	27.1	0.0	8.6
	-45	45	8.04	-19.0	7.59	-15.6	5.7	3.4
		90	5.85	18.8	5.82	25.9	0.5	7.1
C2	15	45	9.29	-4.9	9.68	-8.3	4.2	3.4
		90	4.45	18.5	4.56	10.0	2.5	8.5
	-45	45	8.04	-19.0	8.58	-22.2	6.7	3.2
		90	5.85	18.8	5.91	12.8	1.0	6.0
D1	15	225	9.28	-1.6	9.45	-4.0	1.8	2.4
		270	5.26	43.4	5.09	35.3	3.2	8.1
	-45	225	8.51	8.1	8.75	4.3	2.8	3.8
		270	9.49	46.5	9.25	39.3	2.5	7.2
D2	15	225	9.28	-1.6	9.08	1.2	2.2	2.8
		270	5.26	43.4	5.44	44.5	3.4	1.1
	-45	225	8.51	8.1	8.51	10.1	0.0	2.0
		270	9.49	46.5	9.63	44.4	1.5	2.1

Table A4.1. Analyses to determine effects of errors in order numbers on displacement (Y=height from pin axis, d=absolute displacement)

Appendix A5 - Estimation of rigid body movement

The body displacement vector is determined from the following analysis:

From Figure A5.1,

$$d = d_x i + d_z k$$
$$e_r = e_{rx} i + e_{rz} k$$
$$h_r = h_{rx} i + h_{rz} k$$
$$e_f = e_{fx} i + e_{fz} k$$
$$h_f = h_{fx} i + h_{fz} k \quad .$$

Now, for the front surface,

$$h_f = e_f + d \qquad \text{....A5.1}$$

from which the following equation can be obtained,

$$h_{fx} = e_{fx} + d_x \qquad \text{....A5.2(a)}$$
$$h_{fz} = e_{fz} + d_z \qquad \text{....A5.2(b)}$$

Similarly for the rear surface,

$$h_{rx} = e_{rx} + d_x \qquad \text{....A5.3(a)}$$
$$h_{rz} = e_{rz} + d_z \qquad \text{....A5.3(b)}$$

Along $\theta=50°$,

$$e_{fx} \approx - e_{rx}$$

and $$e_{fz} \approx - e_{rz}$$

Equations A5.2(a) + A5.3(a),

$$h_{fx} + h_{rx} = e_{fx} + e_{rx} + 2d_x \ ,$$
$$d_x = (h_{fx} + h_{rx})/2 \qquad \text{....A5.3(a)}$$

Similarly, equations A5.2(b) + A5.3(b),

$$d_z = (h_{rz} + h_{rz})/2 \qquad \text{....A5.3(b)}$$

From the three repeated experiments, the mean values of d_x and d_z at 45mm below pin axis are:

$$d_x = -0.001751\text{mm}$$
$$d_z = -0.000295\text{mm}$$

and the corresponding values at 15mm above pin axis are:

$$d_x = -0.000573\text{mm}$$
$$d_z = 0.000182\text{mm}$$

The absolute body displacements are:

$d_{-45} = 0.00178$mm at $\Phi = 80.4°$ and
$d_{15} = 0.000602$mm at $\Phi = 72°$,

where Φ is the angle made by d with the z-axis.

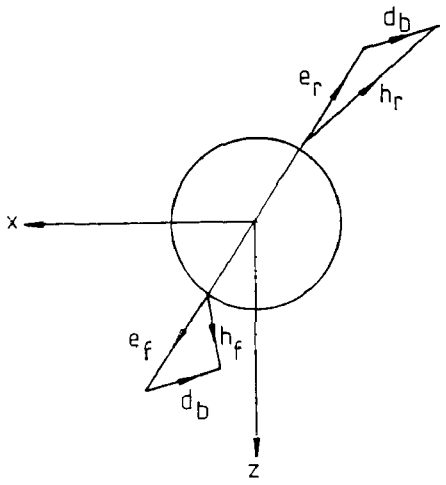

KEY:
e_f, e_r - thermal expansion
h_f, h_r - holographic measuremer
d_b - body displacement

Figure A5.1 Vector diagram to evaluate body displacement

Appendix A6 - List of publications and presentations associated with the thesis

A6.1 Publications

1. 'Measurement of thermal expansion of a piston using holographic and electronic speckle pattern interferometry' - Accepted for publication in Optical Engineering (March 1991).

2. 'Holographic investigation of the expansion control characteristics of steel inserts in pistons' - Accepted for publication in Experimental Mechanics (April 1991).

3. 'Comparison of measurement of piston deformation using holographic interferometry and finite elements' - Accepted for publication in Experimental Mechanics (June 1991).

A6.2 Presentations

1. 'The measurement of thermal expansion of a diesel engine piston using holographic and electronic speckle pattern interferometry' - Applied Optics and Opto-electronics Conference, Nottingham (September 1990).

2. 'Comparison of measurement of piston deformation using holographic interferometry and finite elements' - Conference on Internal Combustion Engine Research, IMechE, London (January 1991) (poster presentation)

3. 'Comparison of the displacement profiles of a heated isoformic diesel engine piston using finite elements and holographic interferometry' - Second International Conference on Ultraprecision in Manufacturing Engineering, Braunschweig (May 1991) (poster presentation).

REFERENCES

References

Abramson,N.,Bjelkhagen,'Sandwich hologram interferometry :Measurement of in-plane displacement and compensation of rigid body motion' Applied Optics,v 18,n 16(1979), p2870-2880.

Abramson,N.,The Making and Evaluation of Holograms, Academic Press, London, 1981.

Asundi,A.,Cheung,M.T.,Lee,C.S.,'Moire' interferometry for simultaneous measurement of u,v w',Experimental Mechanics, v 29,n 3(1989),p258-260.

Aswendt,P.,Hofling,R.,Totzaver,W.,'Digital speckle pattern interferometry applied to thermal strain measurement of metal-ceramic components', Optics and Laser Technology, v 22, n 4(1990),p278-282.

Briers,J.D.,'The interpretation of holographic interferograms - A review',Optical and Quantum Electronics, v 8(1976),p469-501.

Chen,T.Y.,Taylor,C.E.,'Computational analysis in photomechanics',Experimental Mechanics,v 29,n 3(1989) ,p323-329.

Creath,K.,'Holographic contour and deformation measurement using a 1.4 million element detector array',Applied Optics,v 28, n 11(1989),p2170- 2175.

Creath,K.,'Phase shifting speckle interferometry',Applied Optics, v 24,n 18(1985),p3053-3058.

Dally,J.W.,Riley,W.F.,Experimental stress analysis,3rd edition(1991), McGraw-Hill,Inc.,New Jersey.

Dandliker,R.,Thalmann,R.,'Heterodyne and quasi-heterodyne holographic interferometry',Optical Engineering,v 24,n 5(1985), p824-831.

Dhir,S.K.,Sikora,J.P.,'An improved method for obtaining the general displacement field from a holographic interferogram', Experimental Mechanics,v 12(1972),p323-327.

Ennos,A.E.,Robinson,D.W.,Williams,D.C.,'Automatic fringe analysis in holographic interferometry',Optica Acta, v 32,n 2(1985),p135-145.

Evans,W.T.,Russell,R.M.,'Application of holographic interferometry to piston deformation',Proc. 1st Int.Conf. on Lasers in Manufacturing,Brighton(1983),p181-192.

Evans,W.T.,Russell,R.M.,White,A.,'Application of holographic interferometry to cylinder deformation',Journal of Strain Analysis,v 22,n 2(1987), p63-74.

Evans,W.T.,Premier,G.C.,'Holographic analysis of the deformation of a diesel engine piston', Experimental Mechanics,v 29,n 4 (1989), p455-459

Fletcher-Jones,D.,Griffiths,W.J.,Munro,R.,'New piston features for truck, off-highway and industrial engines',AE Symposium(1982), paper no.7.

Gilbert,J.A.,Vedder,D.T.,'Development of holographic technique to study thermally induced deformation', Experimental Mechanics, v21(1981),p138-144.

Goldberg,J.L.,'A holographic interferometer for the measurement of vector displacement of a slowly deforming rough surface',Japan J. of Appl. Physics, v 14(1975)., Suppl.14-1.

Goldberg,J.L.,'A method of three-dimensional strain measurement of non-ideal objects using holographic interferometry',Experimental Mechanics,v 23,n 1,p59-73.

Hansche,B.D.,Murphy,C.G.,'Holographic interferogram analysis from a single view',Applied Optics,v13, n3(1974),p630-635.

Hariharan,P.,Oreb.,B.F.,Brown,N,'A digital phase measurement system for real time holographic interferometry',Optics Communication, v 46,n 6,(1982), p393-396.

Hariharan,P.,Oreb,B.F.,Brown,N.,'Real time holographic interferometry :a microcomputer system for the measurement of vector displacements',Applied Optics,v 22,n 6(1983),p876-880.

Hariharan,P.,'Quasi-heterodyne hologram interferometry', Optical Engineering,v 24,n4,(1985), p632-638.

Hariharan,P.,Optical Holography,Cambridge University Press (1986).

Hsu,T.R.,Moyer,R.G.,'Application of holography in high temperature displacement measurement',Experimental Mechanics(1972),p431-432.

Hsu,T.R.,Lewak,R.,'Measurement of thermal distortion of composite plate by holographic interferometry', Experimental Mechanics, v 16(1976),p182-187.

Hsu,T.R.,Lewak,R.,Wilkins,B.J.S.,'Measurement of crack growth in a solid at elevated temperature by holographic interferometry', Experimental Mechanics, v 18(1978),p297-302.

Hsu,T.R.,Lewak,R.,'On the sensitivity of fringe interpretation technique in laser holographic interferometry',Experimental Mechanics,v 24,n 1(1984), p40-43.

Hu,C.P.,Turner,J.L.,Taylor,G.E.,'Holographic interferometry :compensation for rigid body motion',Applied Optics, v 15,n 6(1976),p1558-1564.

Johns,T.J.,Eck,D.L.,Bollman,'An economical design analysis of pistons for internal-combustion engines', ASME paper 73-DGP-16(1973).

Jones,R.,'The design and application of a speckle pattern interferometer for total plane strain field measurement', Optics and Laser Technology,Oct.1976,p215-219.

Jones,R.,Wykes,C.,Holographic and speckle interferometry, 2nd edition(1989),Cambridge Univerity Press,Cambridge.

Kakunai,S.,Iwata,K.,Nagata,R.,Sekiguchi,H.,'Measurement of three components of displacement vectors using heterodyne holographic interferometry',Optics and Laser in Engineering, v 6(1985),p213-223.

Kakunai,S.,Hsegawa,M.,'Pattern measurement of displacement vectors using phase shifting holographic interferometry',Bull. Japan Soc. of Prec. Eng.,v 21, n 4(1987),p296-298.

Kerr,D.,Tyrer,J.,'Use of high resolution real-time image processing techniques in generation and analysis of ESPI fringe pattern', Optics and Lasers in Engineering, v 8(1988), p109-121.

Kerr,D.,Mendoza Santoyo,F.,Tyrer,J.R.,'Manipulation of the Fourier components of speckle fringes as part of an interferometric analysis process',J of Modern Optics, v 36,n 2(1989),p192-203.

Kerr,D.,Mendoza Santoyo,F.,Tyrer,J.R.,'Extraction of phase data from electronic speckle pattern interferometric using a single-phase-step method: A novel approach', J. Opt. Soc. Am., v 7,n 5(1990), p820-826.

Krishnakumar,S.,Foster,C.G.,'Whole-field optical examination of cylindrical shell deformation', Experimental Mechanics,v 29, n 1(1989),p16-22.

Kurtoglu,A.,Abramson,N.,Carlson,T.,'Holographic investigation of an industrial robot',Applied Optics, v 27,n 14(1989),p3035-3038.

Lokberg,O.J.,Malmo,J.T.,'Long-distance electronic speckle pattern interferometry', Optical Engineering, v 27,n 2(1988), p150-156.

Lokberg,O.J.,Malmo,J.T.,'Detection of defects in composite materials by TV holography', NDT Int., v 21,n4(1988), p223-228.

Lokberg,O.J.,'Electronic speckle pattern interferometry',SPIE V 673(1986), p346-352.

Lu,Y.G.,Jiang,L.Z.,L.X.Zou,'The inspection of solder joints on printed circuit boards by phase-shift holographic interferometry',NDT Int.,v 23, n 3(1990),p157-160.

Maji,A.K.,Shah,P.,'Measurement of mixed-mode crack profile by holographic interferometry',Experimental Mechanics,v 30,n 2(1990), p201-207.

Matthys,D.R.,Gilbert,J.A.,Dudderar,T.D.,Koenig,K.W., 'A windowing technique for the automated analysis of holographic interferograms',Optics and Lasers in Engineering, v 8(1988),p123-126.

Matsumoto,T.,Iwata,K.,Nagata,R.,'Distortionless recording in double exposure holographic interferometry',Applied Optics,v 12, n 7(1973), p1660-1662.

Matsumoto,T.,Iwata,K.,Nagata,R.,'Measuring accuracy of three dimensional displacement in holographic interferometry', v 12,n 5(1973),p961-967.

Matsumoto,T.,Iwata,K.,Nagata,R.,'Measurement of deformation in a cylindrical shell by holographic interferometry',Applied Optics, v 13,n 5(1974),p1080-1084.

Malmo,J.T.,Lokberg,O.J.,Slettemoen,G.A.,'Interferometric testing at very high temperature by TV holography (ESPI)',Experimental Mechanics,v 28,n 3(1988), p315-321.

Michael,H.,'Quantitative deformation measurement of diffusely reflecting objects with the aid of holography',Applied Optics, v 12,n 6, (1973), p1111-1113.

Miller,R.A.,Shah,S.P.,Bjelkhagen,'Crack profiles in mortar measured by holographic interferometry',Experimental Mechanics,v 28,n 4(1988),p388-394.

Miniatt,E.C.,Waas,A.M.,'An experimental study of stress singularities of a sharp corner in a contact problem',Experimental Mechanics, v 30,n 3(1990),p281-285.

Moore,A.J.,Tyrer,J.R.,'An electronic speckle pattern interferometer for complete in-plane displacement measurement',Measurement Science and Technology,V 1, (1990),p1024-1030.

Munro,R.,'Some diesel piston features in design analysis and experiment',SAE Special Publication SP449(1979), p131-143.

Nobis,D.,Vest,C.M.,'Statistical analysis of errors in holographic interferometry',Applied Optics,v17,n14(1978), p2198-2204.

O'Toole,B.J.,Santare,M.H.,'Photoelastic investigation of crack-inclusion interaction',Experimental Mechanics,v 30,n 3,p253-257.

Parker,R.J,Jones,D.G.,'The use of holographic interferometry for turbomachinery fan evaluation during rotation tests',J.of Turbomachinery,v 110 (1983), p393-400.

Parker,R.J.,Jones,D.G.,'Holography in an industrial environment',Optical Engineering,v 27,n 1(1988),p55-66.

PetersIII,W.H.,Sutton,M.A.,Ranson,W.F.,Poplin,W.P., Walker,D.M.,'Whole-field experimental displacement analysis of composite cylinder',Experimental Mechanics, v 29,n 1(1989),p58-62.

Pirodda,L.,'Conjugate wave holographic interferometry for the measurement of in-plane deformation', Applied Optics, V 28,n 10(1989),p1842-1844.

Pryputniewicz,R.J.,'Holographic strain analysis :an experimental implementation of the fringe vector theory',Applied Optics, v 17,n 22(1978), p3613-3618.

Pruputniewicz,R.J.,Stetson,K.A.,'Determination of sensitivity vectors in hologram interferometry from two known rotations of the object',Applied Optics,v 19,n 13(1980),p2201-2205.

Reid,G.T.,'Automatic fringe pattern analysis: a review',Optics and Lasers in Engineering,v 7,n 1(1986),p37-68.

Reipart,P.,Buchta,R.,'New design methods for pistons',SAE Special Publication SP 494(1981),p19-26.

Rhodes,M.L.P.,'Pistons for petrol and small diesel engines:part 1',AE Symposium (1978),Paper No.5,p5.1-5.9.

Röhrle,M.D.,'Determination of stresses and deformation in pistons by means of computer programs and photoelasticity',ASME Paper 75-DGP-18(1974).

Robinson,D.W.,'Automatic fringe analysis with a computer image processing system',Applied Optics, v 22, n 14(1983),p2168-2176.

Ruddy,B.L.,Kinsella,F.H.,'Computer aided engineering for pistons, rings and pins',Proc. of IMechE,Part D(1990),v 204,n 3D,p199-202.

Sciammarella,C.A.,'The moire' method - a review',Experimental Mechanics,v 22,n 11(1982),p418-433.

Sharp,B.,'Electronic speckle pattern interferometry',Optics and Lasers in Engineering,v 11 (1989), p241-255.

Shellabear,M.C.,Tyrer,J.R.,'Three dimensional analysis of volume vibration by electronic speckle pattern interferometry', Proc. of SPIE, v 1084(1989).

Shibayama,K.,Uchiyama,H.,'Measurement of three dimensional displacement by hologram interferometry',Applied Optics, v 10, n 9(1971),p2150-2154.

Sollid,J.E.,'Holographic interferometry applied to measurement of small static displacements of diffusely reflecting surfaces', Applied Optics, v 8,n 8(1969).

Stetson,K.A.,'Fringe interpretation for hologram interferometry of rigid body motions and homogeneous deformations',J.Opt.Soc.Am., v 64, n 1(1974),p1-11.

Stetson,K.A.'Use of sensitivity vector variations to determine absolute displacements in double exposure hologram interferometry',Applied Optics,v 29,n 4,(1990), p502-504.

Stimpfling,A.,Smigielski,'New method for compensating and measuring any motion of three dimensional objects in holographic interferometry',Optical Engineering, v 24, n 5(1985), p821-823.

Tatasciore,Ph.,Schumann,W.,'An approach to applying holographic interferometry for the determination of large deformations',J.Physics D: Applied Physics, v 21(1988),p1692-1700.

Tyrer,J.R.,'The use of TV holography (ESPI) for loudspeaker chassis and cabinet modal analysis',J.Audio Eng.Soc., v 36,n 5(1988), p345-348.

Vest,C.M.,'Comment on :Holographic interferometry applied to measurement of small static displacement of diffusely reflecting surfaces',Applied Optics,v 12,n 3(1973),p612-613.

Vest,C.M.,Holographic interferometry,John Wiley and Sons (1979),USA.

Weathers,J.M.,Foster,W.A.,Swinson,W.F.,Turner,J.L.,'Integration of laser-speckle and finite element techniques of stress analysis', Experimental Mechanics,v 25,n 1(1985),p60-64.

Winther,S.,'3D strain measurement using ESPI',Optics and Lasers in Eng.,v 8(1988),p45-57.

Wykes,C.,'A theoretical approach to the optimisation of electronic speckle pattern interferometry fringes with limited laser power',J.of Modern Optics,v 34,n 4(1987), p539-544.

Wykes,C.,'Use of electronic speckle pattern interferometry in the measurement of static and dynamic surface displacement',Optical Eng.,v 21,n 3(1982),P400-406.

Yoon,S.H.,Hong,C.S.,'Interlaminar fracture toughness of graphite/epoxy composite mixed-mode deformation',Experimental Mechanics, v 30,n 3(1990),p234-239.